

# Electromagnetic Simulation of CERN Accelerator Components and Experimental Applications

THÈSE N° 5737 (2013)

PRÉSENTÉE LE 18 JUIN 2013

À LA FACULTÉ DES SCIENCES DE BASE  
LABORATOIRE DE PHYSIQUE DES ACCÉLÉRATEURS DE PARTICULES  
PROGRAMME DOCTORAL EN PHYSIQUE

ÉCOLE POLYTECHNIQUE FÉDÉRALE DE LAUSANNE

POUR L'OBTENTION DU GRADE DE DOCTEUR ÈS SCIENCES

PAR

Carlo ZANNINI

acceptée sur proposition du jury:

Prof. V. Savona, président du jury  
Prof. L. Rivkin, Dr G. Rumolo, directeurs de thèse  
Dr M. Barnes, rapporteur  
Dr M. T. Tran, rapporteur  
Prof. U. van Rienen, rapporteur



ÉCOLE POLYTECHNIQUE  
FÉDÉRALE DE LAUSANNE

Suisse  
2013



# Contents

<b>Acknowledgments</b>	<b>v</b>
<b>Abstract</b>	<b>vii</b>
<b>Sintesi</b>	<b>ix</b>
<b>Introduction</b>	<b>1</b>
<b>1 Wakefields and Impedance</b>	<b>5</b>
1.1 The electromagnetic problem . . . . .	5
1.1.1 Longitudinal plane . . . . .	5
1.1.2 Transverse planes . . . . .	9
1.1.3 Effect on the beam dynamics . . . . .	13
1.2 EM simulations of wakefields and impedances . . . . .	14
1.2.1 CST Studio Suite . . . . .	14
1.2.2 Resistive wall . . . . .	16
1.2.3 Pillbox Cavity . . . . .	23
1.2.4 Step-in and step-out . . . . .	30
<b>2 Impedance model of ferrite kickers</b>	<b>41</b>
2.1 Simple model of SPS ferrite loaded kickers . . . . .	41
2.1.1 Theoretical transverse impedance of the SPS kickers . . . . .	41
2.1.2 EM simulations of SPS kickers . . . . .	45
2.2 A Spectral Method for Impedance Calculation . . . . .	55
2.2.1 C-Magnet model . . . . .	55
2.2.2 A simplified C-Magnet model for impedance calculations . . . . .	56
2.3 Effect of the TEM mode . . . . .	68
2.3.1 Theoretical model . . . . .	69
2.3.2 Comparison With 3-D Simulations . . . . .	71
2.3.3 Effect of the external circuits . . . . .	71
2.4 Realistic model of SPS kickers . . . . .	73
2.4.1 Effect of the longitudinal segmentation . . . . .	74
2.4.2 SPS extraction kicker: effect of the serigraphy . . . . .	75
2.4.3 Simulation of a kicker loaded by a coaxial cable . . . . .	79
	iii

## Contents

---

2.4.4	SPS kicker impedance model . . . . .	81
<b>3</b>	<b>Resistive wall impedance calculations</b>	<b>85</b>
3.1	A TL model for wall impedance calculation . . . . .	85
3.1.1	Description of the model . . . . .	86
3.1.2	Benchmark with ReWall . . . . .	89
3.1.3	Application to the SPS wall impedance model . . . . .	92
3.2	Impedance of the LHC beam-screen . . . . .	95
3.2.1	The scaling technique . . . . .	96
3.2.2	Electromagnetic simulation of the LHC beam-screen including the weld	97
<b>4</b>	<b>Experimental applications</b>	<b>101</b>
4.1	Bench measurements: the wire method . . . . .	101
4.1.1	Numerical investigation of the wire method . . . . .	102
4.1.2	Comparing wire measurements and impedance models . . . . .	103
4.2	Observations with beam . . . . .	106
4.2.1	Tune shifts measurements . . . . .	106
4.2.2	MKE heating . . . . .	110
4.3	EM characterization of materials . . . . .	126
4.3.1	Methods for measuring the material properties . . . . .	126
4.3.2	The Coaxial line method . . . . .	127
4.3.3	Air gap . . . . .	132
4.3.4	Measurement results . . . . .	133
	<b>Conclusions</b>	<b>137</b>
<b>A</b>	<b>EM simulations of CLIC components</b>	<b>141</b>
A.1	EM simulations of CLIC crab cavities . . . . .	141
A.1.1	Introduction and motivation . . . . .	141
A.1.2	CST 3D EM simulation studies . . . . .	142
<b>B</b>	<b>Spectral model for the calculation of the transverse impedance of an abrupt transition</b>	<b>147</b>
B.1	The analytical approach . . . . .	147
B.1.1	Projection of Maxwell equation in $r$ and $\varphi$ . . . . .	148
B.1.2	Field matching . . . . .	149
B.2	Impedance derivation . . . . .	150
B.2.1	Numerical results . . . . .	150
<b>C</b>	<b>Calculation of <math>\zeta_m</math>: transmission line model</b>	<b>153</b>
<b>D</b>	<b>List of Publications</b>	<b>155</b>
	<b>Curriculum Vitae</b>	<b>171</b>

# Acknowledgments

I am very proud to have worked under the supervision of Giovanni Rumolo. I met Giovanni in November 2008 when I started my experience at CERN as Technical Student. I immediately appreciated his knowledge and skill. He guided me, and was always open to my initiatives. Giovanni Rumolo went well beyond his duty of thesis co-director: he has been a mentor and a friend, always suggesting to me the best for my research after examining my work with critical look day by day.

A special thanks to my thesis director Leonid Rivkin, who gave me the unique opportunity to join EPFL as a Doctoral Student. In addition, in spite of the distance and his time constraints, he provided me with help and support on numerous occasions.

I am also very grateful to Gianluigi Arduini and Elias Métral, my section leaders during the PhD research. Elias and Gianluigi always supported my initiatives.

I would like to thank Prof. Vittorio Vaccaro for the continuous cooperation and exchange that we had during these three years of research. Furthermore, I cannot forget that Prof. Vaccaro together with Iulia Masullo introduced me to the fascinating field of accelerator physics.

Thanks to many colleagues for useful discussions and fruitful collaborations. In particular I would like to thank: Mike Barnes, Hannes Bartosik, Nicolò Biancacci, Rama Calaga, Fritz Caspers, Hugo Day, Alessandro D'Elia, Alexej Grudiev, Giovanni Iadarola, Elias Métral, Andrea Mostacci, Nicolas Mounet, Raphael Mutzner, Tatiana Pieloni, Benoit Salvant, Bruno Spataro, Mauro Taborelli, Riccardo Zennaro.

A special thanks to Giovanni De Michele for the close collaboration on RF measurements.

Many thanks to the RF colleagues Theodoros Argyropoulos, Thomas Bohl and Elena Shaposhnikova. Thanks, to Miranda Van Stenis and Thomas Schneider for the machining of the coaxial samples for measurements of material properties and to Serge Lebet for technical assistance.

Thanks to the unofficial CERN Italian team that never made me feel alone: Federico Aglietti, Stefano Cengarle, Alessandro Danisi, Salvatore Danzeca, Ivan De Cesaris, Giovanni De Michele, Giovanni Iadarola, Cinzia Luzzi, Michele Martino, Giovanni Spiezia.

Thanks to Tatiana Libera Rijoff for supporting me in the daily life during the writing up of the thesis and for the LATEX support.

Infine un grazie particolare alla mia famiglia ai mie fratelli e ai miei genitori; questa tesi la dedico a loro.



# Abstract

Wakes and impedances of single accelerator elements can be obtained by means of theoretical calculation, electromagnetic (EM) simulations or bench measurements. Since theoretical calculations apply only to simple structures and bench measurements have some intrinsic limitations, EM simulations can be used as a reliable tool to determine wakes and impedances. This thesis will focus on the use of time domain 3D CST Particle Studio EM simulations to calculate wakes and/or impedances.

First, the results of the EM simulations are compared with the known analytical solutions and other codes. In this exercise, the driving and the detuning terms of the wakes/impedances, in the transverse plane, are disentangled for both symmetric and asymmetric geometries. The sensitivity of the simulations results to the numerical parameters is discussed, as well as the limits of validity of the wake formalism and its extension to the nonlinear regime.

Using the CST Wakefield Solver, the SPS kicker impedance contribution is then estimated. The simulation model was improved step by step, and successfully benchmarked with existing and new theoretical models, giving confidence in the numerical results and allowing a better understanding of the EM problems.

In the case of the resistive wall impedance of simple chamber geometries a handy theoretical model has been proposed. In order to calculate the resistive wall impedance of a round chamber, a theoretical approach based on the transmission line (TL) theory, is demonstrated to be valid and practical to use. By means of appropriate form factors the method is then extended to rectangular or elliptical chambers.

Moreover the method was successfully benchmarked with the most recent codes based on the field matching technique developed at CERN and was used to construct the SPS wall impedance model. For more complicated geometries (asymmetries, small inserts, holes etc.), a theoretical estimation without involving EM simulation becomes unworkable. An example of interest is the LHC beam-screen, for which CST 3D simulations were used to estimate the impedance. In order to allow the simulator to cover the whole frequency range of interest (few KHz to several tens of MHz) a novel scaling technique was developed and applied.

Where possible, the EM models developed throughout this thesis were also successfully benchmarked with bench measurements (wire methods) and observations with beam. On the specific subject of bench measurements, a numerical investigation of coaxial wire measurements has been also presented.

Finally, in order to verify the adopted EM models of the materials both in theoretical calculations and 3D simulations, an experimental setup for measuring EM properties (permittivity

## Abstract

---

and permeability) of materials has been presented. The method is based on fitting the measured reflection transmission coefficients through a coaxial line filled with the material to be probed, with the outcome of EM simulations or theoretical models. It was successfully applied for measuring NiZn ferrites and dielectric material (e.g. SiC).

**Keywords:** accelerator, collective effects, wake functions, impedance, CST Particle Studio, EM simulations, kickers, resistive wall, SPS, LHC, impedance measurements, coaxial wire, tune shift, power loss, beam induced heating, materials properties, complex permittivity, complex permeability.



## Sintesi

Funzioni scia e impedenze di accoppiamento degli elementi di un acceleratore possono essere ottenute tramite calcoli teorici, simulazioni elettromagnetiche (EM) o misure da banco. Tuttavia, dato che i calcoli teorici sono disponibili solo per strutture semplici e che le misure da banco hanno alcune limitazioni intrinseche, le simulazioni EM possono essere usate come uno strumento affidabile per determinare campi scia e impedenze di accoppiamento. Questa tesi si concentra sull'utilizzo di simulazioni EM 3D nel dominio del tempo per il calcolo di campi scia e impedenze di accoppiamento, realizzate con 'CST Particle Studio'.

Come primo passo, i risultati delle simulazioni EM sono confrontati con soluzioni analitiche e altri codici. In questo esercizio i termini dipolare e quadrupolare delle funzioni scia o equivalentemente delle impedenze di accoppiamento, nel piano trasverso, sono stati separati sia per strutture simmetriche che asimmetriche. La sensibilità dei risultati delle simulazioni rispetto ai parametri numerici viene discussa, cosiccome i limiti di validità del formalismo delle funzioni scia e la sua estensione al regime non lineare.

Usando il risolutore di campi scia di 'CST Particle Studio', è stata stimata l'impedenza di accoppiamento dei kicker di SPS. Il modello di simulazione è stato migliorato passo dopo passo e verificato con esistenti e nuovi modelli teorici, conferendo affidabilità ai risultati numerici e permettendo una migliore comprensione del problema.

Nel caso dell'impedenza delle pareti resistive delle camere da vuoto dell'acceleratore, per semplici geometrie della camera, viene proposto un semplice modello teorico. Tale modello, basato sulla teoria delle linee di trasmissione (TL) permette di calcolare l'impedenza delle pareti resistive per camere a sezione circolare ed è stato dimostrato essere valido e facile da usare. Mediante l'uso di fattori di forma il metodo può essere applicato a camere rettangolari o ellittiche.

Inoltre il metodo è stato confrontato con i codici più recenti sviluppati al CERN ed è stato usato per costruire il modello d'impedenza delle pareti di SPS. Per geometrie più complicate (asimmetrie, piccoli inserti, pareti con fori etc.), una stima teorica dell'impedenza senza l'uso di simulazioni EM diventa impraticabile. Un esempio di interesse, in questo senso, è il 'beam screen' di LHC dove simulazioni 3D CST sono state usate per valutare l'impedenza. In modo tale da consentire al simulatore di coprire l'intero intervallo di frequenze di interesse (da alcuni kHz a decine di MHz) è stata sviluppata, verificata per un caso semplice ed applicata una nuova tecnica di scalatura in frequenza.

Il modello è risultato in buon accordo con le misure da banco (metodi del filo) e osservazioni effettuate con il fascio di particelle. Sul soggetto specifico di misure da banco, è stata presen-

tata un'investigazione numerica delle misure con il filo.

Infine, allo scopo di verificare i modelli adottati per le proprietà EM dei materiali, sia per i calcoli teorici che per le simulazioni 3D, è stato presentato un setup sperimentale per misurare le proprietà EM (permeabilità magnetica e permittività elettrica) degli stessi. Il metodo si basa sulla convergenza tra i coefficienti di trasmissione o riflessione misurati su una linea coassiale riempita con il materiale da caratterizzare, e i risultati di simulazioni EM o modelli teorici. Questo metodo è stato applicato con successo per misurare le proprietà EM di ferriti NiZn e materiali dielettrici (p.es. SiC).

**Keywords:** acceleratore, effetti collettivi, funzioni scia, impedenza, CST Particle Studio, simulazioni EM, calciatori, pareti resistive, SPS, LHC, misure di impedenza, filo coassiale, tune shift, perdita di potenza, riscaldamento indotto dal fascio, proprietà dei materiali, permittività complessa, permeabilità complessa.

# Introduction

In particle accelerators, the electromagnetic interaction between beam particles and their surroundings have attracted the attention of physicists and engineers since the beginning of the systematic study of coherent instabilities. The strength of the interaction is characterized by the impedances (and wake fields) of the accelerator components. Impedances (and wake fields) play a key role because they usually limit the performance of existing accelerators and need to be taken into account in the design of new machines. A small perturbation in the ideal configuration of the beam can become a source of electromagnetic (EM) fields which enhances the perturbation itself; this is illustrated in Fig. 1.

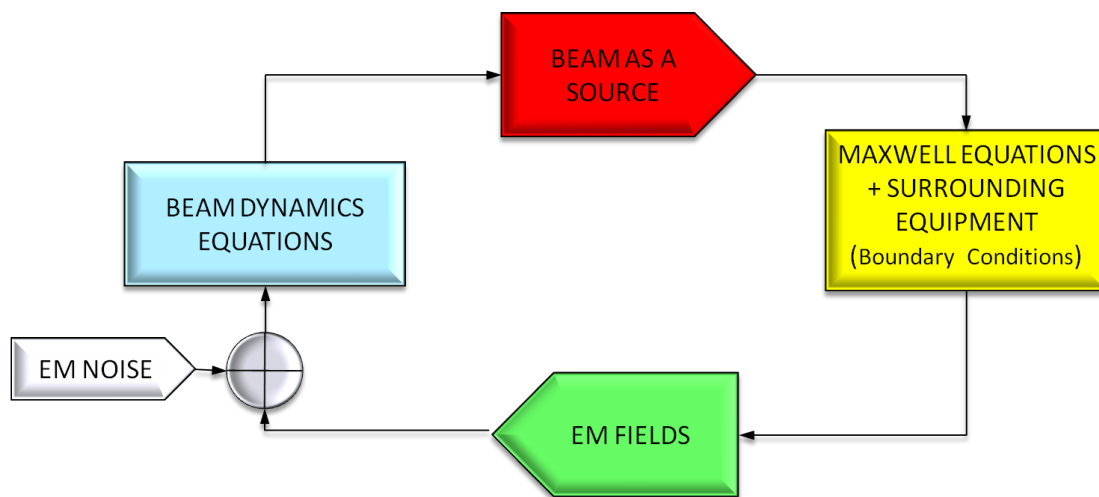


Figure 1: Flow chart of the EM problem.

The effect of impedances ideally becomes significant when the beam intensity inside an accelerator is pushed beyond a certain threshold. When an unstable beam motion is triggered and allowed to grow without damping mechanism (active or passive), the beam is quickly degraded or even lost.

Impedances are usually responsible for tune shift, instabilities, emittance growth and beam loss. To predict tune shift and instability thresholds we need to be able to quantify the total impedance of a machine. Therefore, theoretical analysis, computer simulations, and experimental measurements of impedances of accelerator components are critical tasks in accelerator research, design, and development. Electromagnetic simulations are necessary

to calculate the contribution to the total impedance of single accelerator components. Time domain simulations are of special interest, because the wake fields they provide can be fed directly into macroparticle simulations in order to predict their effects on the beam in realistic conditions.

The main goal of this PhD project is to establish a solid technique through which the results from electromagnetic simulation codes, both in time and frequency domain, can be easily coupled to beam dynamics to solve complex accelerator physics problems involving collective effects. Therefore, the procedures to be followed are outlined in detail and the limits of applicability are explored.

First, the characterization from the electromagnetic point of view of some selected components of the CERN accelerators (from the PSB to LHC) with variable degrees of complexity is necessary to determine the beam coupling impedances and the wake fields. For each of these devices the goal is to calculate and disentangle longitudinal and transverse components of the wake, driving and detuning, linear and nonlinear. The impedances and the wake fields thus calculated can be subsequently input into the general impedance database, and their impact on the particle beam can be evaluated by means of beam dynamics equations or simulations (e.g. particle tracking with collective effects, i.e. HEADTAIL code). Special attention is devoted to the impedance of the kickers, whose evaluation is complex and which are also believed to be among the most significant contributors to the global impedances of the CERN machines. In the frame of the upgrade of the existing machines and the construction of new machines, another interesting application of the electromagnetic simulations can be to test the coupling impedances of devices under design and predict their impact on the total impedance budget of the accelerator in which they are planned to be installed (e.g. CLIC (see Appendix A)).

Electromagnetic simulations can also be used to benchmark and understand bench measurements of different types, which are based on the scattering parameters. This is an important step to learn how to use the results of bench measurements to derive inputs for beam dynamics simulations. For example, impedance measurements based on the wire(s) method or permittivity/permeability measurements based on the waveguide or coaxial line method, can be reproduced numerically and provide an important tool to define the relationships between the measured quantities and the desired ones.

The work of this PhD thesis has been subdivided into 4 Chapters and can be summarized as follows:

- In **Chapter 1**, the key concepts of wake function and beam coupling impedance are introduced and the use of 3D EM simulations to obtain them is discussed. In particular to assess the validity of the adopted method, the simulation results are compared with the known analytical solutions and other codes. Throughout the chapter, the sensitivity of the simulation results to the numerical parameters is discussed, as well as the limits of validity of the wake formalism and its extension to the nonlinear regime.
- **Chapter 2** describes step by step the simulation and theoretical studies performed to build the SPS kicker impedance model.
- **Chapter 3** focuses on the studies of the resistive wall impedance. A theoretical model

for resistive wall impedance calculation based on the transmission line (TL) theory is presented. The model is benchmarked with existing models based on the Field Matching Technique developed at CERN (ReWall and ImpedanceWake2D [1]) and is used to construct the SPS wall impedance model. However, analytical models apply only to simple structures. For more complicated geometries (asymmetries, small insert, holes etc.), a theoretical estimation involving EM simulation becomes necessary. In the second part of the Chapter we present an example of interest in this sense: the LHC beam screen. The resistive wall impedance contribution of this structure is obtained by means of CST 3D simulations.

- In **Chapter 4** some noteworthy experimental applications of the impedance models described in Chapters 2 and 3 are presented. The benchmarks consist of bench measurements (wire(s) method) and observation with beam (tune shift and beam induced heating measurements). Finally, an experimental setup for measuring EM properties (permittivity and permeability) of materials is also presented.



# 1 Wakefields and Impedance

In this chapter, we first introduce the concept of wake function and beam coupling impedance treating separately the longitudinal and transverse planes. In the longitudinal plane we also discuss the relationship between the beam coupling impedance and the energy loss by a bunch of particles. Moreover we also briefly discuss the effect of wakes/impedance on the beam dynamics introducing the concept of effective impedance.

In the second part of the chapter we discuss the use and the full validation of CST Particle Studio 3D EM simulations to calculate wakes and/or impedances. The steps are to compare their results with the known analytical solutions or other codes as well as disentangle, in the transverse plane, the driving and the detuning terms of the wakes/impedances. Throughout this part of the chapter, the sensitivity of the simulations results to the numerical parameters is discussed, as well as the limits of validity of the wake formalism and its extension to the nonlinear regime.

## 1.1 The electromagnetic problem

The wake functions describe the interaction of the beam with the surrounding environment. The electromagnetic (EM) problem is posed setting the Maxwell's equations with the beam as source term and boundary conditions given by the structure in which the beam propagates. Wake fields (time domain) and Impedances (frequency domain) allow describing in a sufficiently general way the effects of the self-induced fields on the beam. A particle  $q_0$  going through a device of length  $L$ ,  $s(0, L)$ , leaves behind an oscillating field and a probe charge  $q$  at distance  $z$  will feel a force as a result (see Fig. 1.1). The integral of this force over the device defines the wake function and its Fourier transform is called the impedance of the device of length  $L$ . The particles are assumed to move with the same velocity  $v = \beta c$ , where  $c$  is the speed of light and  $\beta$  is the relativistic factor.

### 1.1.1 Longitudinal plane

The longitudinal wake function of an accelerator component is basically its Green function in the time domain [2] (i.e., its response to a pulse excitation) and is defined as follow:

$$W_{\parallel}(x, y, x_0, y_0, z) [V/C] = -\frac{1}{q_0 q} \int_0^L F_{\parallel}(x, y, s, x_0, y_0, z) ds \quad (1.1)$$

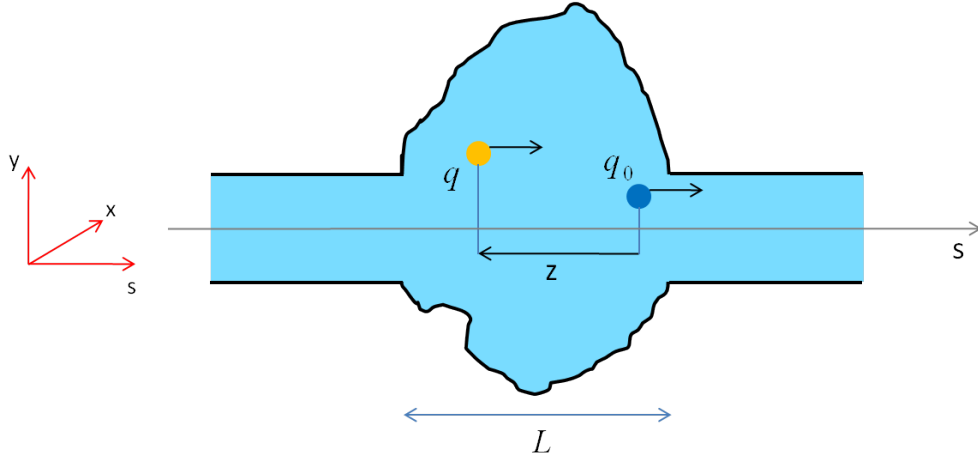


Figure 1.1: Device of arbitrary cross section along an accelerator.

where  $F_{\parallel}(x, y, s, x_0, y_0, z) = q e_s(x, y, s, x_0, y_0, z)$  is the longitudinal component of Lorentz's force,  $e_s(x, y, s, x_0, y_0, z)$  is the longitudinal component of the electric field  $\vec{e}(x, y, s, x_0, y_0, z)$  induced by the source charge  $q_0$ ;  $(x_0, y_0)$  and  $(x, y)$  define respectively the transverse offset of source and test particle with respect to the geometric center of the structure.

The wake function of Eq. 1.1 can be expanded into a power series in the offset of source and test particle [3]. The classical longitudinal wake function is defined as the zeroth order term of this series. This definition leads to a longitudinal wake function independent of the offsets of both source and test particle. In axisymmetric structures (or simply with left/right and top/bottom symmetry), if both source and test particle are in the center of symmetry of the accelerator element:  $(x_0, y_0) = (0, 0)$  and  $(x, y) = (0, 0)$ , the longitudinal wake function reduces exactly to the zeroth order term.

The definition of wake function is very useful for macroparticle models and simulations, because it can be used to describe the driving terms in the single particle equations of motion. We can also describe it as a transfer function in the frequency domain [4, 5]. This is the definition of longitudinal beam coupling impedance of the element under study:

$$Z_{\parallel}(\omega) [\Omega] = \int_{-\infty}^{\infty} W_{\parallel}(z) e^{-\frac{j\omega z}{v}} \frac{dz}{v} \quad (1.2)$$

Here  $j$  is the imaginary unit and  $\omega = 2\pi f$  is the angular frequency conjugate variable of the time delay  $\tau = \frac{z}{v}$ .

The impedance can be defined also directly in frequency domain as follows [1]:

$$Z_{\parallel}(x, y, x_0, y_0, \omega) [\Omega] = -\frac{1}{q_0} \int_0^L E_s(x, y, s, x_0, y_0, \omega) e^{jks} ds \quad (1.3)$$

where  $E_s(x, y, s, x_0, y_0, \omega)$  is the longitudinal component of the electric field in frequency domain and  $k = \frac{\omega}{v}$  is the wave number. EM fields in frequency domain will be indicated with



capital letter to be distinguished from the fields in time domain, indicated by the respective low-case letters.

The value of the wake function in 0,  $W_{\parallel}(0)$ , is related to the energy lost by the source particle in the creation of the wake:

$$W_{\parallel}(0) = -\frac{\Delta E_1}{q^2} \quad (1.4)$$

$W_{\parallel}(0) > 0$  since  $\Delta E_1 < 0$ .  $W_{\parallel}(z)$  is discontinuous in  $z = 0$  and it vanishes for all  $z < 0$  in case of ultra-relativistic approximation ( $\beta = 1$ ). In the global energy balance, the energy lost by the source splits into: electromagnetic energy of modes that propagate down the beam chamber (above cut-off), which will be eventually lost on surrounding lossy materials, and electromagnetic energy of the modes that remain trapped in the object. In the second case two scenarios are possible: 1) this energy can be dissipated on lossy walls or purposely designed HOM absorbers; 2) it keeps ringing without damping (perfect electric conducting (PEC) walls), but can also be transferred to following particles (or the same over several turns), possibly feeding into an instability.

### Energy loss

Let us consider a bunch of particles with line density  $\lambda(z)$  (normalized to unity) passing once through an accelerator device generating a wake function  $W_{\parallel}(z)$ . The energy kick  $\Delta E(z)$  on the witness slice  $eN_{\text{bunch}}\lambda(z)dz$  ( $e$  is charge of the particle and  $N_{\text{bunch}}$  is the number of particles in the bunch) is the integral of the contributions from the wakes left behind by all the preceding  $eN_{\text{bunch}}\lambda(z')dz$  slices (sources) (see Fig. 1.2).

The total energy loss  $\Delta E$  of the bunch can then be obtained by integrating  $\Delta E(z)$  over the full bunch extension:

$$\Delta E = \int_{-\hat{z}}^{\hat{z}} \lambda(z) \Delta E(z) dz \quad (1.5)$$

with:

$$\Delta E(z) = e^2 N_{\text{bunch}}^2 \int_z^{\hat{z}} \lambda(z') W_{\parallel}(z - z') dz' \quad (1.6)$$

Transforming Eq. (1.5) into the frequency domain yields:

$$\Delta E = \frac{e^2 N_{\text{bunch}}^2}{2\pi} \int_{-\infty}^{\infty} |\bar{\lambda}(\omega)|^2 \text{Re}[Z_{\parallel}(\omega)] d\omega \quad (1.7)$$

Considering a bunch of particles that passes many times through the accelerator structure the total energy loss  $\Delta E$  of the bunch can still be obtained by integrating  $\Delta E(z)$  over the full bunch

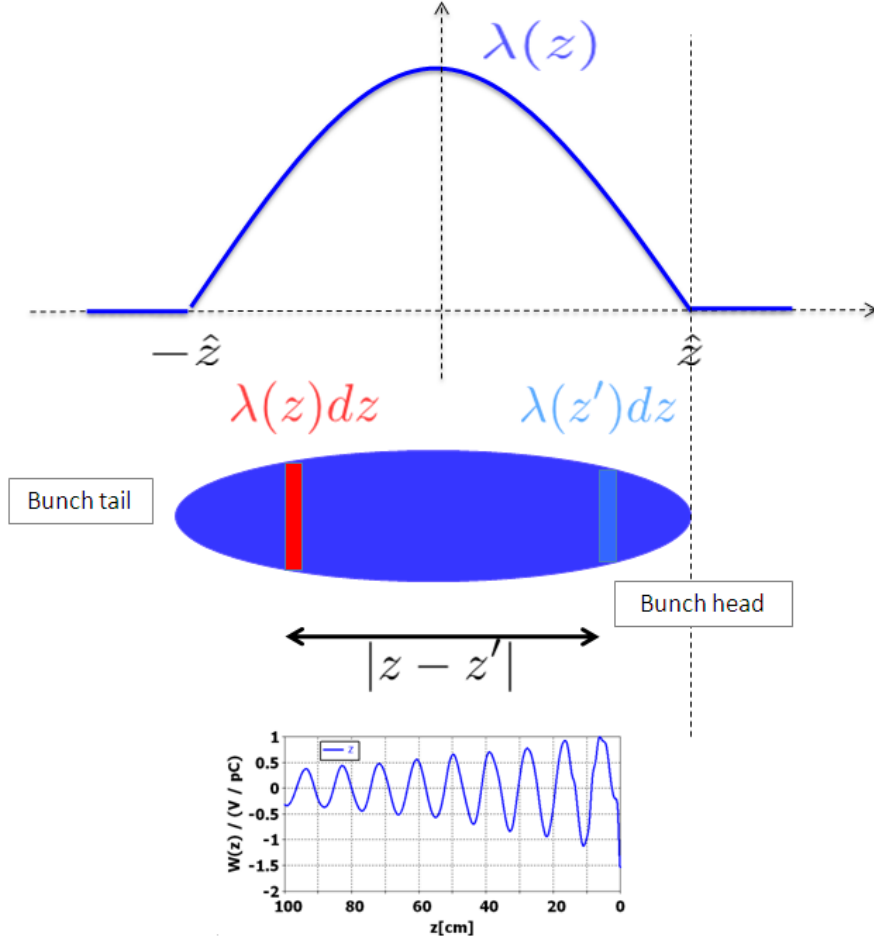


Figure 1.2: Bunch spatial distribution (at the top). The bunch is divided in slices (in the center). Each slice leaves behind a wake-field (at the bottom).

extension.  $\Delta E(z)$  this time also includes the contributions from all previous turns, spaced by multiples of the ring circumference  $C$ :

$$\Delta E = \frac{e^2 N_{\text{bunch}}^2}{2\pi} \int_{-\infty}^{\infty} \lambda(z) dz \int_{-\infty}^{\infty} \lambda(z') \sum_{k=-\infty}^{\infty} W_{\parallel}(kC + z - z') dz' \quad (1.8)$$

Considering the following relationship:

$$\sum_{k=-\infty}^{\infty} W_{\parallel}(kC + z - z') = \frac{c}{C} \sum_{p=-\infty}^{\infty} Z_{\parallel}(p\omega_0) e^{-\frac{ip\omega_0(z-z')}{c}} \quad (1.9)$$

we obtain:

$$\Delta E = \frac{e^2 N_{\text{bunch}}^2 \omega_0}{2\pi} \sum_{p=-\infty}^{\infty} |\bar{\lambda}(p\omega_0)|^2 \text{Re}[Z_{\parallel}(p\omega_0)] \quad (1.10)$$

where  $\bar{\lambda}(p\omega_0)$  is the Fourier transform of  $\lambda(z)$  evaluated in  $p\omega_0$ .

The formula can be easily extended to the case of a beam of any number of bunches  $n_{\text{bunches}}$ , that passes many times through the structure, by replacing the bunch spectrum  $\bar{\lambda}(p\omega_0)$  with the beam spectrum  $\bar{\Lambda}(p\omega_0)$  and the intensity of the bunch  $N_{\text{bunch}}$  with the intensity of the beam  $N_{\text{beam}} = n_{\text{bunches}} N_{\text{bunch}}$  (total number of particles in the beam). The power loss on the device  $\Delta E f_0$ , where  $f_0$  is the revolution frequency of particles in the ring of circumference  $C$ , is an important quantity since it directly relates to the beam induced heating.

### 1.1.2 Transverse planes

In an axisymmetric structure (or simply with a top-bottom and left-right symmetry) a source particle traveling on axis cannot induce net transverse forces on a witness particle also following on axis. We need to introduce a breaking of the symmetry to drive transverse effect, i.e. offset the source or the witness. The transverse wake functions are defined as:

$$W_{x,y}(x, y, x_0, y_0, z) [V/C] = -\frac{1}{q_0 q} \int_0^L F_{x,y}(x, y, s, x_0, y_0, z) ds \quad (1.11)$$

where  $F_{x,y}(s, z) = \left[ q \left( \vec{e}(x, y, s, x_0, y_0, z) + \vec{v} \times \vec{b}(x, y, s, x_0, y_0, z) \right) \right]_{x,y}$  are the transverse components of Lorentz's force;  $\vec{b}(x, y, s, x_0, y_0, z)$  is the magnetic induction field. Similarly to its longitudinal counterpart the transverse wake functions of Eq. (1.11) can be expanded into a power series in the offset of source and test particle [3]. Since no transverse effects can appear when both source and test particle are in the center of symmetry, the zeroth order term of the power series is null. Considering only the first order terms and disregarding possible coupling between transverse planes we can write:

$$\begin{aligned} W_x &= W_x^{\text{driv}} x_0 + W_x^{\text{det}} x \\ W_y &= W_y^{\text{driv}} y_0 + W_y^{\text{det}} y \end{aligned} \quad (1.12)$$

where  $W_{x,y}^{\text{driv}} \left[ \frac{V}{mC} \right]$  is the horizontal/vertical driving (also called dipolar) wake function and  $W_{x,y}^{\text{det}} \left[ \frac{V}{mC} \right]$  is the horizontal/vertical detuning (also called quadrupolar) wake function. As will be show in the subsection 1.2.2, for small offsets of both source and test particle, Eq. (1.12) is a very good approximation of the transverse wakes. From Eq. (1.12) we find the following

relationship to disentangle driving and detuning contributions:

$$\begin{aligned}
 W_x^{\text{driv}}(z) &= \frac{W_x(z)}{x_0} \Big|_{x=0} \\
 W_x^{\text{det}}(z) &= \frac{W_x(z)}{x} \Big|_{x_0=0} \\
 W_y^{\text{driv}}(z) &= \frac{W_y(z)}{y_0} \Big|_{y=0} \\
 W_y^{\text{det}}(z) &= \frac{W_y(z)}{y} \Big|_{y_0=0}
 \end{aligned} \tag{1.13}$$

The sum of driving and detuning contributions define the generalized terms  $W_{x,y}^{\text{gen}}$ .

The transverse wake function of an accelerator component can be viewed as basically its Green function in the time domain (i.e., its response to a pulse excitation). It is very useful for macroparticle models and simulations, because it relates source perturbations to the associated kicks on trailing particles:

$$\begin{aligned}
 \Delta x' &\propto W_x(z) = W_x^{\text{driv}}(z) x_0 + W_x^{\text{det}}(z) x \\
 \Delta y' &\propto W_y(z) = W_y^{\text{driv}}(z) y_0 + W_y^{\text{det}}(z) y
 \end{aligned} \tag{1.14}$$

Moreover, from Maxwell's equations and the definitions of wake functions one can derive the general relation [3]:

$$\frac{\partial W_x(z)}{\partial x} = -\frac{\partial W_y(z)}{\partial y} \tag{1.15}$$

from which it follows that:

$$W_x^{\text{det}}(z) = -W_y^{\text{det}}(z) \tag{1.16}$$

Likewise to the longitudinal case the transverse beam coupling impedance of the element under study is defined as the Fourier transform of the respective wake function:

$$\begin{aligned}
 Z_{\perp}^{\text{driv}}(\omega) [\Omega/m] &= j \int_{-\infty}^{\infty} W_{\perp}^{\text{driv}}(z) e^{-\frac{j\omega z}{v}} \frac{dz}{v} \\
 Z_{\perp}^{\text{det}}(\omega) [\Omega/m] &= j \int_{-\infty}^{\infty} W_{\perp}^{\text{det}}(z) e^{-\frac{j\omega z}{v}} \frac{dz}{v}
 \end{aligned} \tag{1.17}$$

Furthermore, as for the longitudinal case we can define the transverse impedance directly in

the frequency domain:

$$\begin{aligned} Z_x(x, y, x_0, y_0, \omega) [\Omega] &= \frac{j}{q_0} \int_0^L [E_x - \beta Z_0 H_y](x, y, s, x_0, y_0, \omega) e^{jks} ds \\ Z_y(x, y, x_0, y_0, \omega) [\Omega] &= \frac{j}{q_0} \int_0^L [E_y + \beta Z_0 H_x](x, y, s, x_0, y_0, \omega) e^{jks} ds \end{aligned} \quad (1.18)$$

where  $Z_0$  is the free space impedance ( $120\pi\Omega$ ). Analogously to its equivalent in the time domain the impedance of Eq. (1.18) can be expanded into a power series in the offsets of source and test particle:

$$\begin{aligned} Z_x &= Z_x^{\text{driv}} x_0 + Z_x^{\text{det}} x \\ Z_y &= Z_y^{\text{driv}} y_0 + Z_y^{\text{det}} y \end{aligned} \quad (1.19)$$

In this section we have defined longitudinal and transverse wakes as the response to a pulse excitation (single particle, the so called wake function). If the source is a bunch of particles the resulting wake will be given by the convolution of the wake function by the charge density of the bunch  $\lambda(z)$  and is called wake potential. Applying the convolution theorem, the beam coupling impedance as defined in Eq. (1.2) can be calculated as the Fourier transform of the wake potential divided by the Fourier transform of the line density.

### Effect of an asymmetric chamber or offset beam

The definitions of Eq. (1.12) hold only for a device with left/right and top/bottom symmetry and centered beam. Assuming now that a transverse effect is also possible between the source and test particles on their nominal orbits:

$$\begin{aligned} W_x(z) \Big|_{x=x_0=0} &= A_x(z) \\ W_y(z) \Big|_{y=y_0=0} &= A_y(z) \end{aligned} \quad (1.20)$$

Eq. 1.12 has to be rewritten as:

$$\begin{aligned} W_x(z) &= A_x(z) + W_x^{\text{driv}}(z) x_0 + W_x^{\text{det}}(z) x \\ W_y(z) &= A_y(z) + W_y^{\text{driv}}(z) y_0 + W_y^{\text{det}}(z) y \end{aligned} \quad (1.21)$$

where  $(x_0, y_0)$  and  $(x, y)$  are the offsets with respect to the nominal orbit and driving and

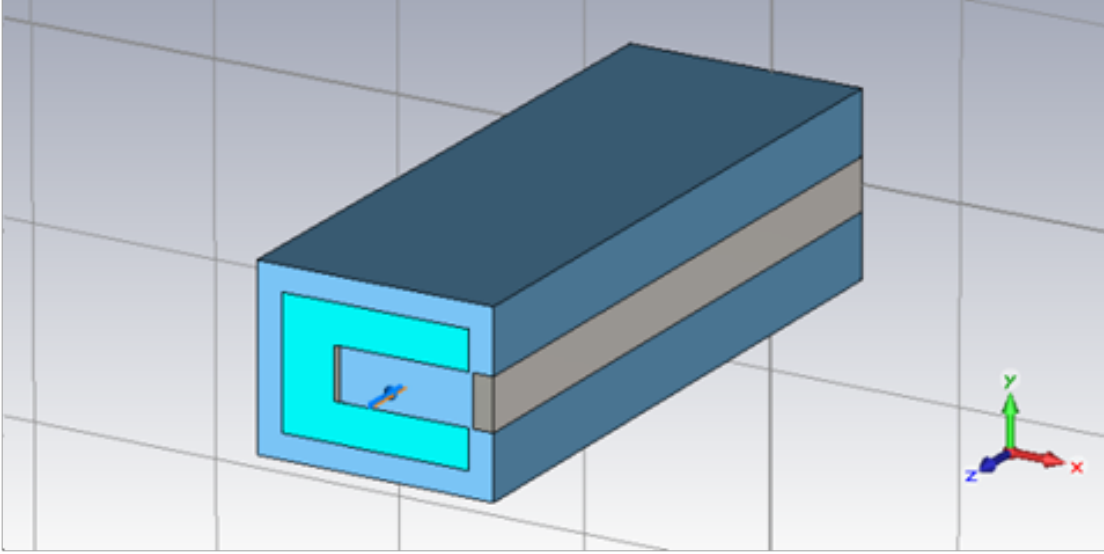


Figure 1.3: Simplified model of a kicker magnet: Vacuum in blue, ferrite in light green and Perfect Electric Conductor (PEC) in gray.

detuning wakes must be defined with respect to it:

$$\begin{aligned}
 W_x^{\text{driv}}(z) &= \frac{W_x(z) - A_x(z)}{x_0} \Big|_{x=0} \\
 W_x^{\text{det}}(z) &= \frac{W_x(z) - A_x(z)}{x} \Big|_{x_0=0} \\
 W_y^{\text{driv}}(z) &= \frac{W_y(z) - A_y(z)}{y_0} \Big|_{y=0} \\
 W_y^{\text{det}}(z) &= \frac{W_y(z) - A_y(z)}{y} \Big|_{y_0=0}
 \end{aligned} \tag{1.22}$$

Similarly, we can apply the same concept for the transverse impedances, which are the Fourier transforms of the wakes:

$$\begin{aligned}
 Z_x(f) &= a_x(f) + Z_x^{\text{driv}}(f) x_0 + Z_x^{\text{det}}(f) x \\
 Z_y(f) &= a_y(f) + Z_y^{\text{driv}}(f) y_0 + Z_y^{\text{det}}(f) y
 \end{aligned} \tag{1.23}$$

In structures with left/right and top/bottom symmetries the constant terms are exactly zero. An example of asymmetric structure of interest is the SPS C-shaped kicker magnet sketched in Fig. 1.3. This structure is not symmetric with respect to the y-z plane.

A constant term also appears when the beam passes off axis in a symmetric geometry. In general we can define the constant term as the transverse impedance when both source and test particle are on the nominal beam axis. If the nominal beam axis is in the geometrical centre of the structure the constant term appears only for asymmetric geometry.

### 1.1.3 Effect on the beam dynamics

The wakes play an important role in the beam dynamics and can give rise to both single-bunch and coupled bunch collective phenomena. If the wake potential induced by a bunch vanishes before the arrival of the next bunch (broad-band impedance), it only affects the single-bunch dynamics (head-tail phenomena). When the decay time of the wake field is larger than the time spacing between the bunches (narrow-band impedance) the coupling between subsequent bunches cannot be neglected. In the following we briefly describe the role of the impedance in the single bunch dynamics.

#### The effective impedance

For bunched beams the impedance is sampled at an infinite number of discrete frequencies given by the mode spectrum. An "effective coupling impedance" can then be defined as the sum over the product of the coupling impedance and the normalized spectral density. The "effective coupling impedance" is required for the calculation of both longitudinal and transverse complex tune shifts of bunched beam and can be defined as [6, 7, 8]:

$$\left(\frac{Z_{\parallel}}{\omega}\right)_{\text{eff}} = \frac{\sum_{p=-\infty}^{p=\infty} \frac{Z_{\parallel}(\omega')}{\omega'} h_l(\omega')}{\sum_{p=-\infty}^{p=\infty} h_l(\omega')} \quad (1.24)$$

$$(Z_{\perp})_{\text{eff}} = \frac{\sum_{p=-\infty}^{p=\infty} Z_{\perp}^{\text{gen}}(\omega' + \omega_{\beta}) h_l(\omega' + \omega_{\beta} - \omega_{\xi})}{\sum_{p=-\infty}^{p=\infty} h_l(\omega' + \omega_{\beta} - \omega_{\xi})} \quad (1.25)$$

Here  $h_l(\omega)$  is the power spectral density,  $\omega_{\beta}$  is the betatron angular frequency,  $\omega_{\xi}$  is the chromaticity frequency shift and  $\omega' = \omega_0 p + l\omega_s$  where  $\omega_0$  is the revolution angular frequency,  $\omega_s$  is the synchrotron frequency and  $l$  determines the type of oscillations (the case  $l = 0$  describes the single-bunch head-tail instabilities). For a Gaussian bunch  $h_l(\omega)$  can be written as:

$$h_l(\omega) = \left(\frac{\omega\sigma_z}{c}\right)^{2l} e^{-\frac{\omega^2\sigma_z^2}{c^2}} \quad (1.26)$$

where  $\sigma_z$  is the standard deviation of the Gaussian bunch profile (root mean square (RMS) bunch-length). The real and the imaginary parts of the "effective impedance"  $(Z/\omega)_{\text{eff}}$  give the growth rate and the frequency shift of the mode under consideration [8, 9, 10, 11].

For a broad-band impedance,  $(Z_{\parallel}/\omega)_{\text{eff}}$  is purely imaginary because the real part of the impedance is an even function of  $\omega$ ; the growth rate vanishes and there is no instability.

For the transverse effective impedance of Eq. (1.25) the mode  $l = 0$  is now allowed. Due to the spectral shift the real part of  $(Z_{\perp})_{\text{eff}}$  no longer vanishes even for broad-band impedances; the

mode frequency has an imaginary part. If the real part of  $(Z_{\perp})_{\text{eff}}$  is negative, the beam can become unstable.

### 1.2 Using CST Particle Studio simulations to obtain wake fields and impedances of accelerator structures

CST Particle Studio [12] 3D EM simulations have been used to calculate wakes and/or impedances of simple accelerator structures. The first steps are to compare their results with the known analytical solutions or other codes as well as disentangle, in the transverse plane, the dipolar and the quadrupolar components of the wakes/impedances. Throughout this section, the sensitivity of the simulations results to the numerical parameters is discussed, as well as the limits of validity of the wake formalism and its extension to the nonlinear regime. The objective of the present work is to test the method of using EM simulations with CST Particle Studio to derive impedances and wakes of typical accelerator structures, like cavities or chambers with Perfectly Electrical Conducting (PEC) boundaries (geometric), as well as in the presence of lossy materials (finite electrical conductivity and/or with complex permeability/permittivity). To assess the validity of the proposed model, with its physical and numerical limits, we have first simulated simple structures (cylindrical and rectangular chamber with longitudinally constant cross-section and conductive walls) and we have studied the general behaviour of the code when dealing with this type of elements. The advantage of these simple cases is that their results can be readily benchmarked against theoretical predictions. Secondly, we have simulated pillbox cavities and step transition to further compare with theoretical results. The main interest of simulating accelerator structures in time domain lies in the fact that the output of the simulation in terms of wake function may be directly used in particle tracking simulations to study the impact of these elements on the beam stability. In particular, wake functions in form of tables can be fed as an input into the HEADTAIL code [13], which is typically used for studying collective effects in beam dynamics. Since the wake functions are needed, the source bunch used in CST simulations should be short enough to be consistent with the length of the bunch slices simulated in HEADTAIL. This obviously limits the analysis to a maximum frequency defined by the bunch slicing, but it can be applied when no higher frequency mechanisms are expected in the given beam dynamics problem.

#### 1.2.1 CST Studio Suite

The software used in this work, CST Studio Suite, is a commercial 3-D electromagnetic Computer Aided Design (CAD) software. In particular, the Wakefield solver of Particle Studio (PS), solves Maxwell's equations in time domain (TD), using a particle bunch as excitation of the structure under study. Standard outputs of the code are the wake potentials produced by the exciting Gaussian bunch (called 'source') as a function of the time delay  $\tau$  with respect to the passage of the source (i.e. the integrated electromagnetic force felt by a witness charge that goes through the structure a time  $\tau$  behind the source) and its equivalent in frequency domain (FD), the Fourier transform normalized to the bunch spectrum, the beam coupling impedance. Besides, since the code allows defining separately the transverse position of the exciting bunch and that of the computation point, we can also separately simulate the driving



and the detuning terms of the transverse wake potentials.

### Wakefield solver: settings

To set up the calculations efficiently in terms of accuracy of the results and computing time, a wise choice of some numerical and physical parameters of the solver becomes crucial. Here follows a list of the most relevant ones.

- $\sigma_z$ : the standard deviation of the source Gaussian bunch (RMS bunch-length) is crucial both for TD (Wake-field) and FD (Impedance) results. In general, since for beam dynamics purpose we are interested in the wake functions, we would like to have a bunch length  $\sigma_z$  comparable with the thickness of the slices needed for the beam dynamics calculation (which can become very small for some special application, e.g. CLIC bunches [14]). Decreasing  $\sigma_z$ , also the wavelength decreases by the same factor. This allows for a larger range of frequencies to be explored but also requires a proportional increase of mesh cells to keep the lines of mesh per wavelength constant. The choice of a value for  $\sigma_z$  turns out to be a trade-off between the special needs of the simulation. Concerning impedance studies the choice of  $\sigma_z$  is determined by the range of frequency that we are interested to analyze.
- WL: the simulated wake length limits the calculation of the wakes to a distance WL from the source and plays an important role on the accuracy of the impedance results. Its effect will be detailed in the subsection 1.2.3.
- LW: the reliability of the EM simulation is related to the accuracy of the discretization of the computational domain. Concerning this aspect the main parameter for the user is the number of mesh lines per wavelength (LW). The stability of the results for the device under test (DUT) must be checked with respect to this parameter to set up its value according to the demanded accuracy of the results. The time of the calculation significantly increases with the density of the mesh since the time step is directly related to the minimum mesh step width used in the discretization of the structure.
- Source offsets: for the simulation of transverse wakes (driving and detuning) it is important to use an offset from the source small enough to stay in the region where the linear approximation of the wake functions made in Eq. (1.12) remains valid (the topic will be treated in the subsection 1.2.2). Otherwise, it is important to mention that the use of a very small displacement for the calculation of the transverse impedance can lead to numerical issues (the transverse kick tends to zero when the displacement goes to zero).
- Integration method: the wake potentials by default are calculated by integrating the electromagnetic force along the z-axis (direct integration scheme). Indirect integration schemes are also available: the indirect test-beam and interfaces. These methods can be more accurate, but require some extra conditions. The indirect test-beam method computes the wake potential by recording the longitudinal field values on the extruded shell of the beam tube in the discontinuous region and has been found very helpful for

the simulation of cavities and resistive wall. The application of this scheme requires an ultra-relativistic beam and equal DUT cross sections at the entry and exit boundary (e.g., it cannot be applied to simulate a step). In the ultra-relativistic case, if the cross section of the DUT varies at the entry and the exit boundary, the indirect interfaces integration can be used.

- **Boundary conditions:** to be properly defined, depending on the DUT. The CST Wakefield solver allows for different boundary conditions: Electric (tangential component of the electric field  $\vec{E}_t = 0$ ), Magnetic (tangential component of the magnetic field  $\vec{H}_t = 0$ ), conductive wall (infinitely thick dissipative wall), periodic and Perfect Matching Layer (PML). For the simulation of the wakes and impedance we typically use Electric or conductive boundary in  $x$  and  $y$ , and periodic or PML boundaries in  $z$ .
- **Symmetry conditions:** when the geometry of the problem makes it possible, to speed up the simulations, symmetry conditions of the fields can be enforced reducing up to a factor 4 the number of mesh cells for Wakefield simulations.

### 1.2.2 Resistive wall

#### Simulation model

In the first simulations made with CST Particle Studio we have used the chamber models depicted in Fig. 1.4 with Electric boundary conditions in  $x$  and  $y$ , and PML boundaries in  $z$ . Type and thickness of the chamber material also need to be specified as inputs, and the total integration volume includes both the inner chamber volume and the chamber itself. Resorting to the conductive wall boundary condition in  $x$  and  $y$ , the rectangular chamber can be simulated without having to define the surrounding material.

#### Procedure for the simulation

Using one of the standard outputs of CST PS we have simulated the longitudinal and transverse wake potentials. Besides, we have disentangled the driving and the detuning terms for the transverse case. The CST PS wake field solver allows defining the position of the source beam and that of the test particle (as observation or computation point). Therefore, we can separately calculate the driving and the detuning terms. The transverse driving kicks are obtained by displacing the beam transverse location to  $(x, y) = (a, 0)$  for the horizontal wake, and  $(x, y) = (0, a)$  for the vertical wake, while leaving the wake integration transverse location on the chamber axis,  $(x, y) = (0, 0)$ . Similarly, the detuning terms are obtained by displacing the wake integration path to the transverse location  $(x, y) = (a, 0)$  and  $(x, y) = (0, a)$ , respectively for horizontal and vertical component, while leaving the beam transverse location on the chamber axis,  $(x, y) = (0, 0)$ . This procedure is illustrated in Fig. 1.5. Offsetting both the source beam and the test particle by the same amount, it is possible to simulate the generalized term and, therefore, verify that it is the sum of the two contributions given by the driving and the detuning terms. The longitudinal wake potential was simulated by placing both beam and wake integration locations on the axis,  $(x, y) = (0, 0)$ .

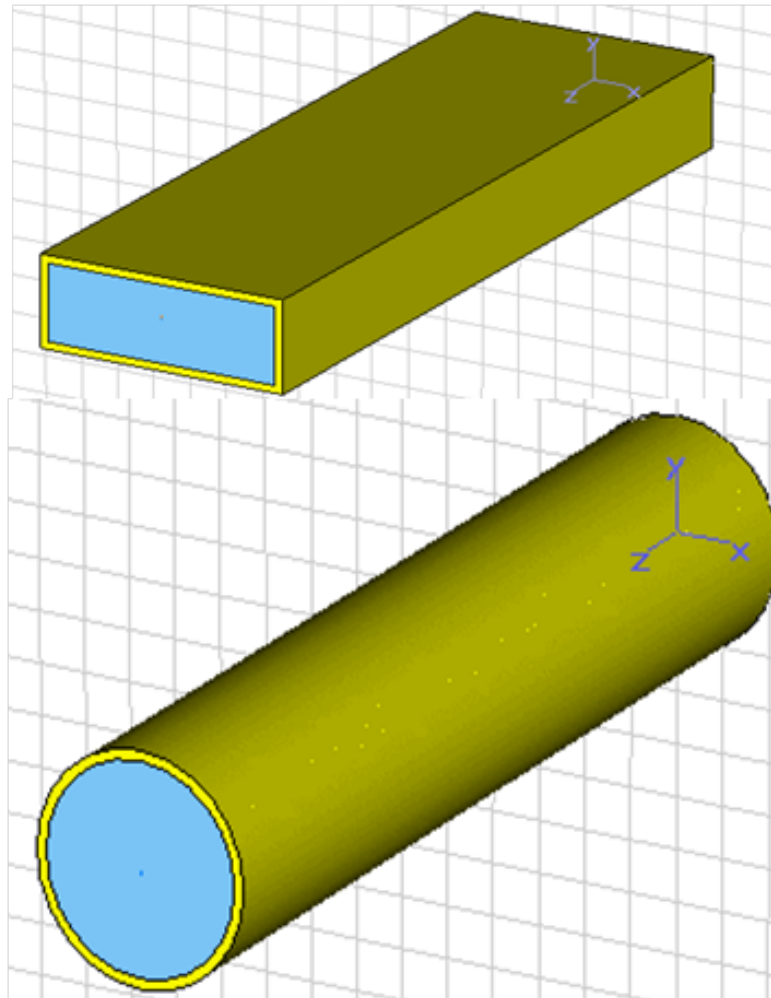


Figure 1.4: Simulation models of chambers of rectangular (top) and circular (bottom) cross section made of resistive material: yellow (Copper), blue (Vacuum).

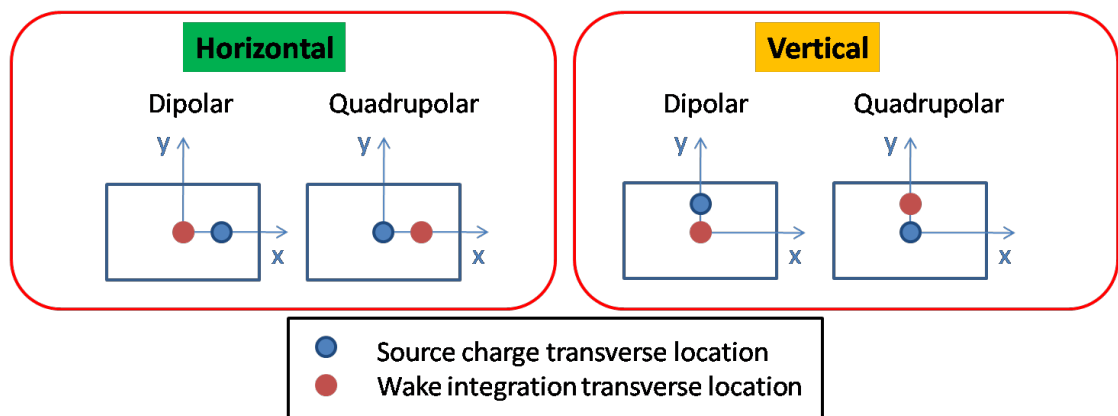


Figure 1.5: Procedure to obtain the driving (dipolar) and detuning (quadrupolar) transverse wake potentials from 3D time domain simulations with a simulated beam.

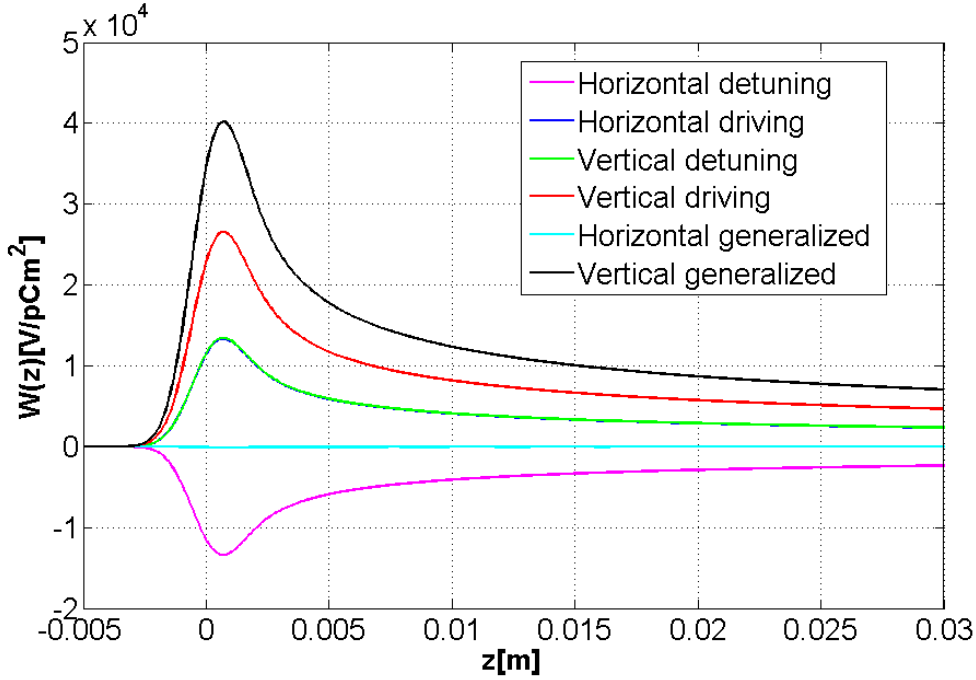


Figure 1.6: Simulated wake potentials (all terms) for a rectangular vacuum chamber with half height  $b = 1$  mm, half width  $a = 3$  mm and electrical conductivity of the walls  $\sigma_{el} = 10^6$  S/m.

### Separating the driving and detuning terms in the rectangular shape

Using the procedures outlined above we can calculate longitudinal and transverse wake potentials, separating the driving and the detuning terms for the transverse part. The goal of the simulations is to compare the CST simulated results with the known theoretical results. Fig. 1.6 displays the results obtained separating the transverse terms for a chamber with the rectangular boundary (horizontal and vertical driving and detuning wake potentials).

We can see that, as predicted by the theory [15], the detuning terms in  $x$  and  $y$  have opposite signs (the vertical detuning term is superimposed upon the horizontal driving term), the horizontal generalized term is zero and the vertical driving term is twice the horizontal driving term. However, comparing these results with the theoretical formulae [16], we observed that theoretical values systematically differed from the simulated values by a factor in the range 4.4 – 4.8 [17]. This discrepancy was investigated in detail [18]. The outcome of this study seemed to point to a problem with the integration method, which was later confirmed and fixed by the CST development team in the version of CST released in 2010. We report here the formula for the longitudinal wake function of an ultrarelativistic particle as quoted for example in Ref. [16]:

$$W_{\parallel}(\tau) = -\frac{FL}{4\pi b} \sqrt{\frac{Z_0}{\pi c \sigma_{el}}} \tau^{-3/2} \quad (1.27)$$

## 1.2. EM simulations of wakefields and impedances

---

This is defined as the response to a pulse excitation: the wake potential from a Gaussian pulse of finite length should asymptotically tend to  $W_{||}(\tau)$  when the length of the bunch tends to zero or equivalently for  $z$  much larger than the bunch-length  $\sigma_z$ . In Eq. (1.27),  $F$  is the geometrical form factor with respect to the cylindrical geometry [15],  $L$  is the device length,  $b$  is the radius (circular case) or the half height (rectangular case),  $\sigma_{el}$  is the electrical conductivity,  $Z_0$  is the free space impedance. Figure 1.7 shows a comparison between the analytically calculated wake function and the simulated wake potential. As expected the wake function is significantly different from the wake potential on the scale of the exciting pulse (see upper picture, log-scale on x-axis), but the two converge for  $z \gg \sigma_z$  (lower picture). The simulation result exhibits a good agreement with the theory in terms of long range wake potential ( $z$  much larger than the bunch-length  $\sigma_z$ ).

For the transverse wake function we have used the formula (for instance, [16]):

$$W_{x,y}^{\text{driv/det}}(\tau) = \frac{F_{x,y}^{\text{driv/det}} L}{\pi b^3} \sqrt{\frac{c Z_0}{\pi \sigma_{el}}} \tau^{-1/2} \quad (1.28)$$

where  $F_{x,y}^{\text{driv/det}}$  are the transverse geometrical form factor [15] with respect to the driving transverse wake function of the cylindrical case. For an axisymmetric structure, such as a cylindrical chamber, there is no difference between the horizontal and vertical planes. Moreover, since the longitudinal component of the electric field induced by a source charge placed in the centre of symmetry does not have radial dependence, the detuning term is zero. Comparing CST 3D simulation results, obtained with the 2010 version, a good agreement with the theory is found for the long range behaviour also for the transverse wakes (see Fig. 1.8). As observed above, so far we have compared the simulated wake of a Gaussian bunch with the theoretical wake of a point charge and focused on their long range behaviours. We could also proceed to a full comparison by making the convolution between the theoretical wake function and the source bunch (or equivalently, in frequency domain, multiply their spectra and then Fourier transform back to the time domain). By doing this, we obtain the wake potentials illustrated in Fig. 1.9. The agreement between the analytical and simulated wakes is very good.

### Form Factor

In order to investigate the rectangular form factor typically used for resistive wall calculation we analyzed the rectangular structure shown in Fig. 1.10:

The aspect ratio  $q$  of the geometry is defined as [16]:

$$q = \frac{a - b}{a + b} \quad (1.29)$$

Therefore, the geometry of the resistive chamber has been first of all simulated for three different  $q$  values and then the wake form factors (only driving for the transverse plane) have been plotted versus the aspect ratio (see Fig. 1.11).

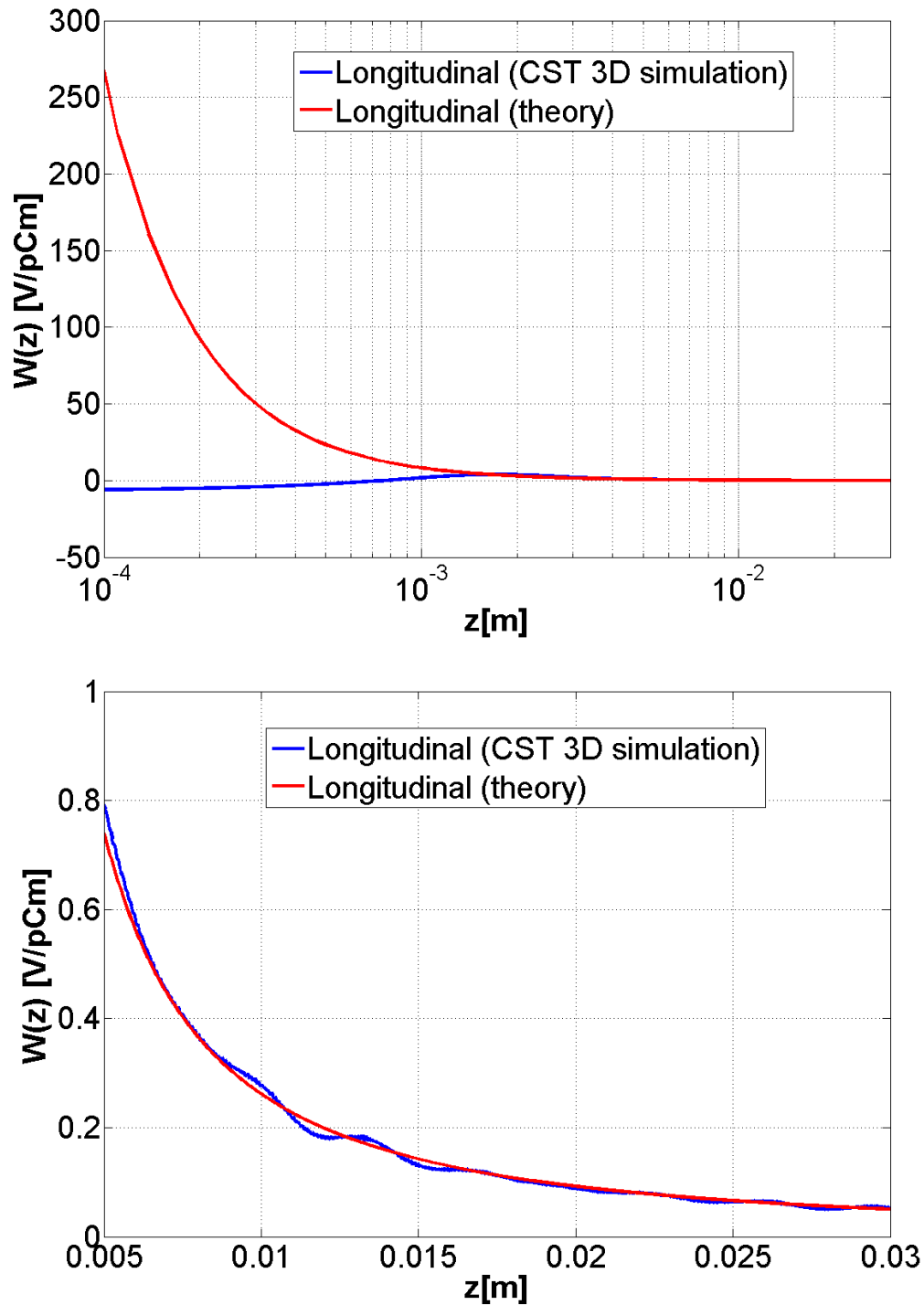


Figure 1.7: Comparing longitudinal theoretical wake function and simulated wake potential ( $\sigma_z = 1$  mm) for a rectangular vacuum chamber with half height  $b = 1$  mm, half width  $a = 3$  mm and electrical conductivity of the walls  $\sigma_{el} = 10^6$  S/m. The bottom picture shows a zoom on the long range behaviour.

## 1.2. EM simulations of wakefields and impedances

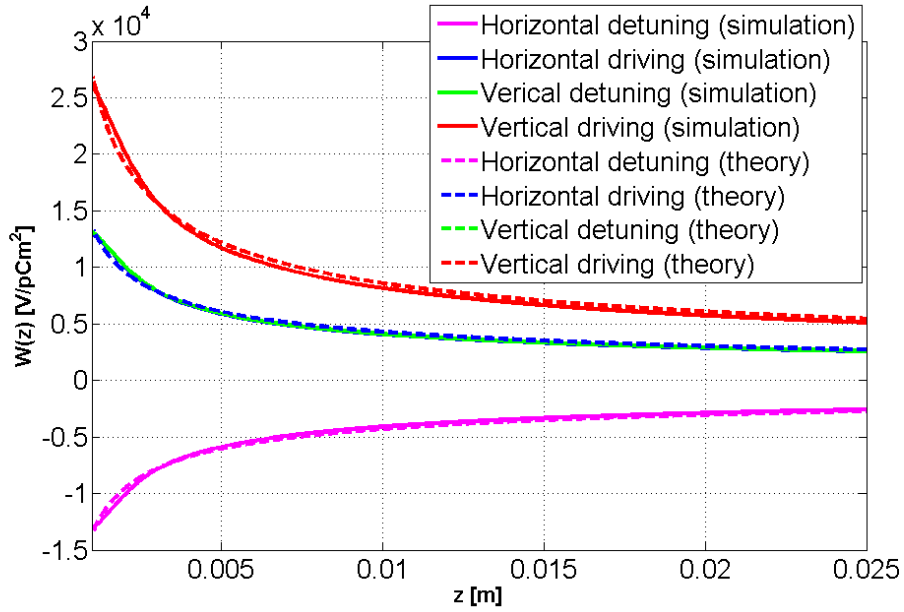


Figure 1.8: Comparing transverse theoretical wake functions and simulated wake potentials ( $\sigma_z = 1$  mm) for a rectangular vacuum chamber with half height  $b = 1$  mm, half width  $a = 3$  mm and electrical conductivity of the walls  $\sigma_{el} = 10^6$  S/m.

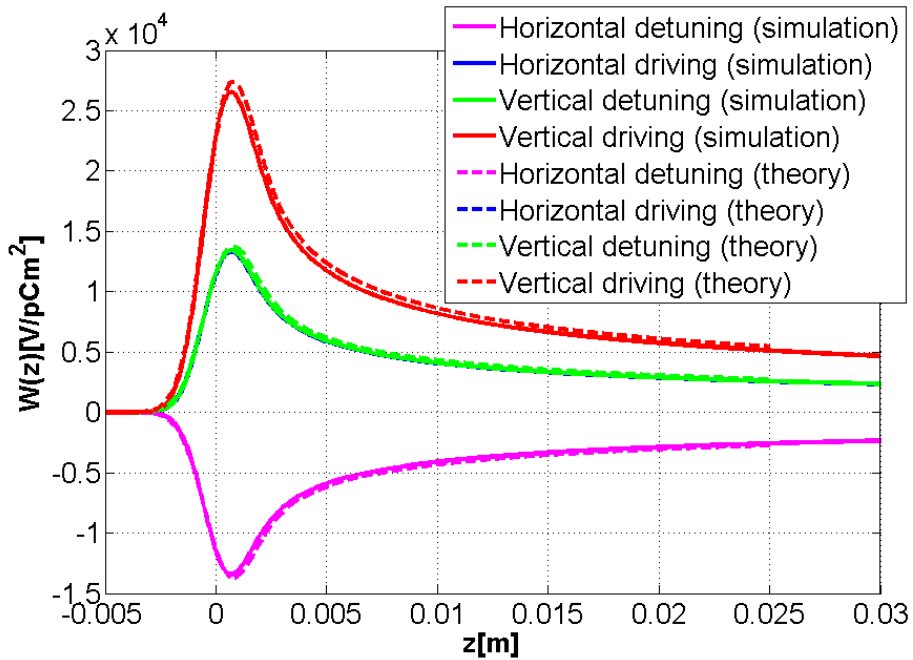


Figure 1.9: Comparing transverse theoretical and simulated wake potentials ( $\sigma_z = 1$  mm) for a rectangular vacuum chamber with half height  $b = 1$  mm, half width  $a = 3$  mm and electrical conductivity of the walls  $\sigma_{el} = 10^6$  S/m.

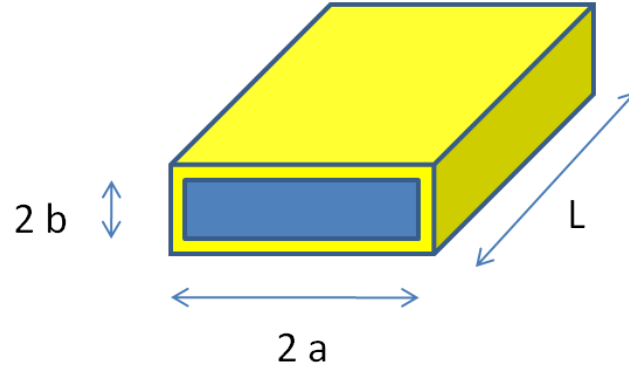


Figure 1.10: Simulated geometry: vacuum in light blue and copper in yellow.

The simulated values of the transverse wake form factors are obtained as the ratio of the simulated transverse driving wake for the rectangular geometry and theoretical transverse driving wake for cylindrical geometry (Eq. (1.28) with  $F_{x,y} = 1$ ):

$$\begin{aligned}
 F_x^{\text{driv}} &= \frac{W_{\perp}^{\text{driv/cyl}}}{W_x^{\text{driv/rect}}} \\
 F_y^{\text{driv}} &= \frac{W_{\perp}^{\text{driv/cyl}}}{W_y^{\text{driv/rect}}}
 \end{aligned} \tag{1.30}$$

The theoretical values are given by the following formulae [16]:

$$\begin{aligned}
 F_x^{\text{driv}}(\lambda) &= \frac{\pi^3}{8} \left[ \sum_{\substack{n=1, \\ \text{odd}}}^{\infty} \frac{n^2}{\sinh^2\left(\frac{n\pi}{2\lambda}\right)} + \lambda^3 \sum_{\substack{n=2, \\ \text{even}}}^{\infty} \frac{n^2}{\cosh^2\left(\frac{n\pi}{2}\right)} \right] \\
 F_y^{\text{driv}}(\lambda) &= \frac{\pi^3}{8} \left[ \lambda^3 \sum_{\substack{n=1, \\ \text{odd}}}^{\infty} \frac{n^2}{\sinh^2\left(\frac{n\pi}{2}\right)} + \sum_{\substack{n=2, \\ \text{even}}}^{\infty} \frac{n^2}{\cosh^2\left(\frac{n\pi}{2\lambda}\right)} \right]
 \end{aligned} \tag{1.31}$$

where  $\lambda = \frac{b}{a}$ . With respect to that reported in Ref. [16], the formula for  $F_y^{\text{driv}}$  has been adequately corrected to yield the proper result. The simulated values lie within 5% of the theoretical curves.

### Nonlinear and coupling terms

Both in theoretical approaches, and in the HEADTAIL code [13], developed by G. Rumolo, the wake is assumed to have a linear and uncoupled (between transverse planes) dependence on the positions of both source and test particles. This linear approximation holds for small particle amplitudes. However, for larger particle amplitudes, we might have to include coupling and/or higher order terms. By means of CST PS simulations we have addressed the question



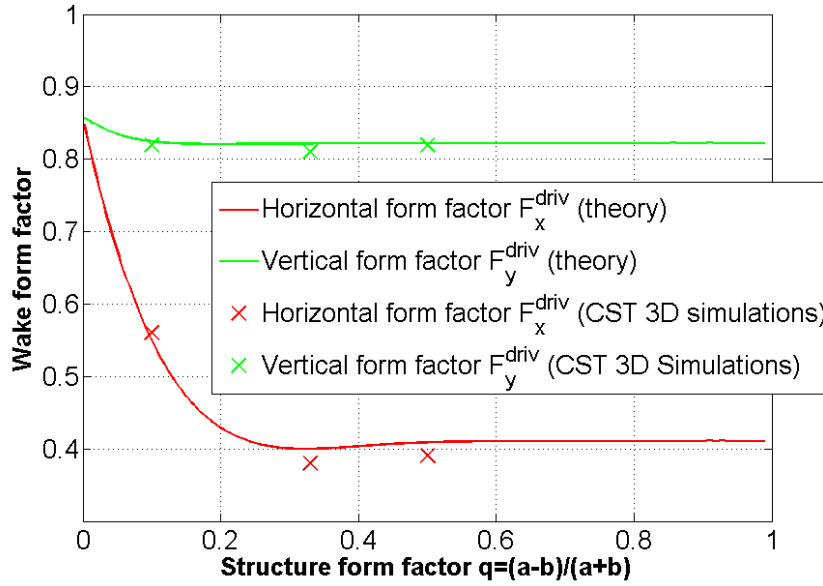


Figure 1.11: Comparing theoretical and simulated wake form factors.

of the limits of validity of the linear and uncoupled approximation. While analytical formulae are generally valid only in the linear regime [16], i.e. for offsets in close proximity of the axis of the structure, EM simulations allow exploring also regions far off axis, in which the linear approximation does not hold anymore. From this analysis, it is possible to obtain information about the nonlinear terms of the wakes and the coupling terms between transverse planes. Figure 1.12 illustrates the results of the simulations performed to investigate this issue.

These first results are difficult to explain without involving nonlinear or coupled dependence of the wake on the transverse location. The threshold for the onset of a nonlinear or coupled dependence is found to be quite low in  $b$  units ( $\delta = 0.1b$ ). The illustrations in Figs. 1.13 and 1.14 give a more quantitative analysis, defining displacement regions in which one or more coupling or nonlinear terms need to be taken into account for a more correct description of the wake. The contribution of nonlinear uncoupled terms is studied in the vertical plane and the contribution of nonlinear coupled terms in the horizontal plane at a displacement of 10% of the pipe aperture.

### 1.2.3 Pillbox Cavity

#### PEC Pillbox

Since the wake-field solver works in the time domain, it directly calculates the wake and then computes the impedance via FFT. The code would need, in principle, a vanishing wake to make correctly the FFT. The frequency resolution attainable with this procedure is therefore limited by the length of the simulated wake. For example, the width of a narrow band resonator cannot be correctly identified if the time domain signal is not long enough to fully show its decaying behaviour. In the case of a pillbox cavity with PEC walls, in which we do not have dissipation,

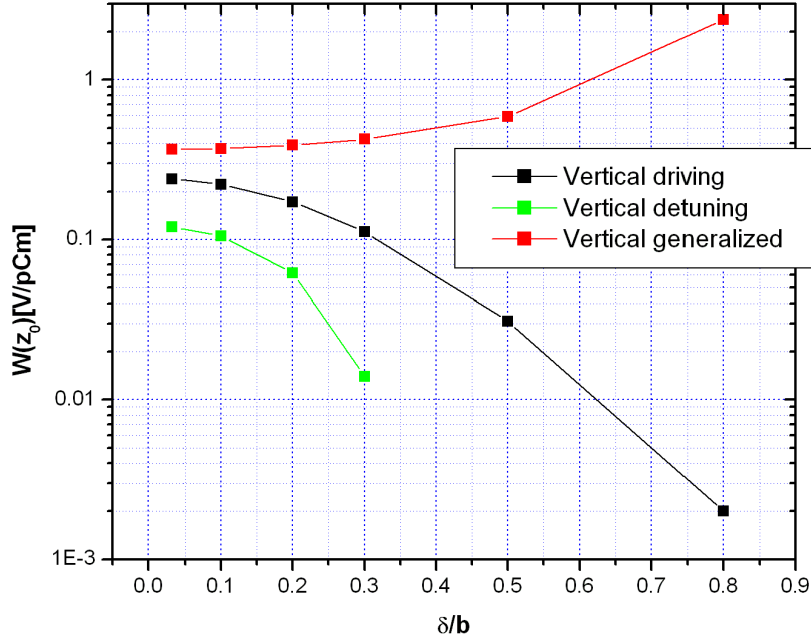


Figure 1.12: Wake potential at a fixed  $z_0$  as function of the displacement  $\delta$ . The displacement is along the diagonal of the rectangular chamber  $\delta_y/b = \delta_x/a$  and the wake is normalized to the displacement.

the wake does not decay (see Fig. 1.15) and so the time windowing to perform the FFT will introduce a significant error. Increasing the wake length (WL), we notice that the peaks below the cut-off frequency of the beam chamber attached to the cavity tend to a Dirac delta in the real part of the impedance and to its derivative,  $\delta'$ , in the imaginary part (see Fig. 1.16). This was expected from theory, as no dissipation is possible at these frequencies (no propagation and perfectly conductive walls). The WL sets the resolution in the frequency domain and determines an upper limit for the simulated quality factor  $Q_{\text{sim}}$ . In the ultra-relativistic case (relativistic factor  $\beta = 1$ ) we have:

$$Q_{\text{max}} = \frac{f_r}{\Delta f_{\text{min}}} \quad (1.32)$$

where  $\Delta f_{\text{min}} = \frac{c}{\text{WL}}$  and  $f_r$  is the frequency of resonance. In the PEC case, the simulated quality factor of the peaks below cut-off will be exactly  $Q_{\text{max}}$ : when WL goes to infinity also  $Q_{\text{sim}}$  will go to infinity (see Fig. 1.17).

The same behaviour can be observed also with other EM codes. We have focused the attention on ABCI [19]. ABCI is a computer program that solves the Maxwell equations directly in the time domain when a bunched beam goes through an axisymmetric structure on or off axis.

## 1.2. EM simulations of wakefields and impedances

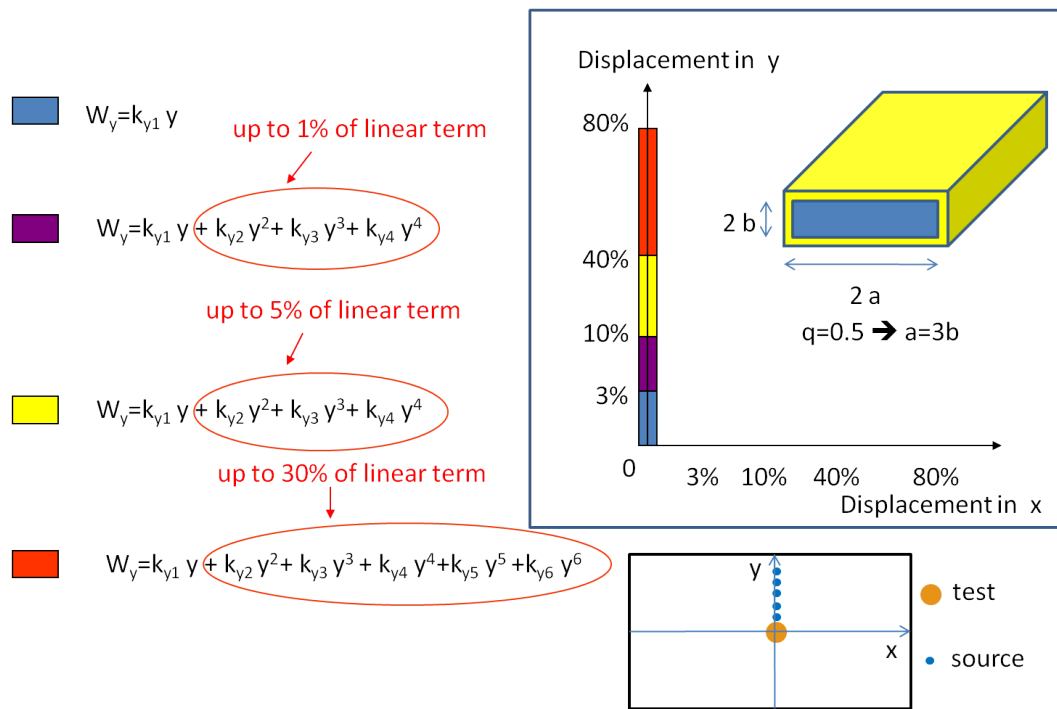


Figure 1.13: Contributions of linear and nonlinear uncoupled terms in the vertical plane.

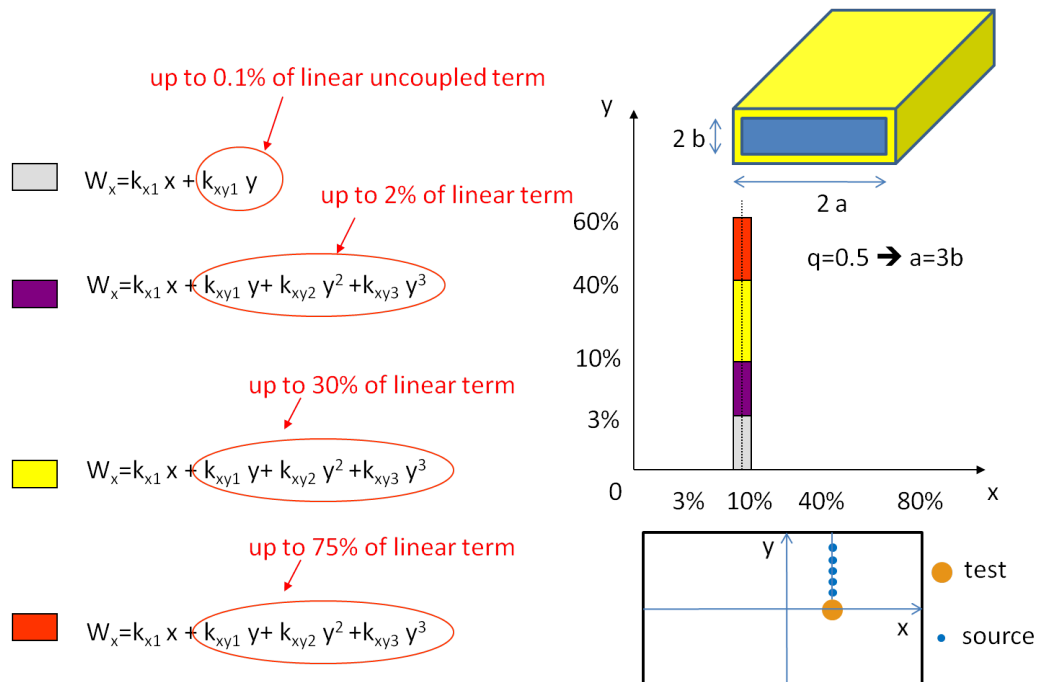


Figure 1.14: Contributions of linear and nonlinear coupled terms in the horizontal plane for a displacement of 10% of the pipe width.

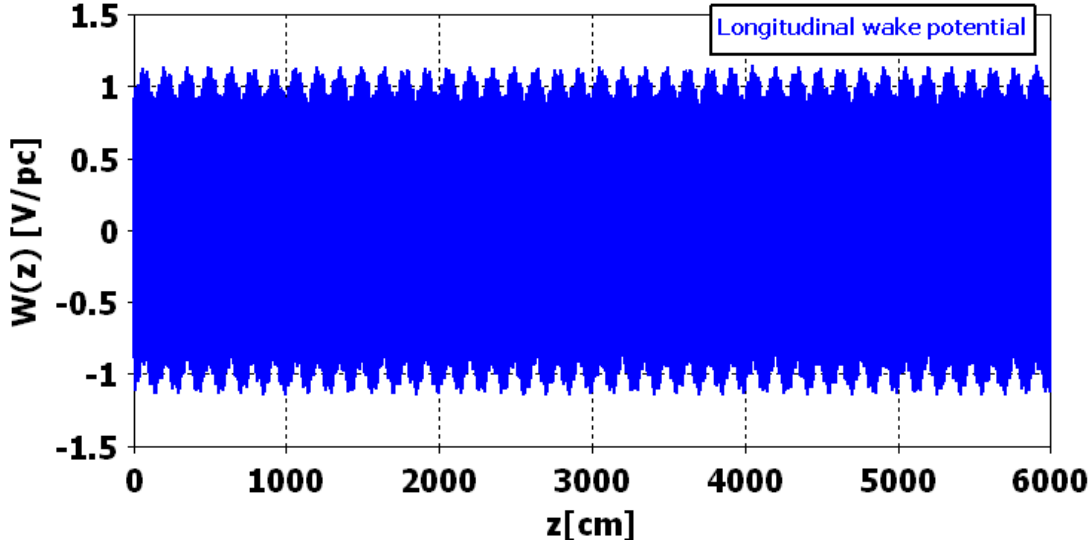


Figure 1.15: Longitudinal wake potential of a PEC pillbox.

An arbitrary charge distribution can be defined by the user (default=Gaussian) [19]. The two codes show a good agreement for the simulations of a PEC pillbox (see Figs. 1.18 and 1.19). Here we define as normalized wave number the term  $kb$ , where  $k = \frac{\omega}{c}$  is the propagation constant and  $b$  is the radius of the pipe.

It is interesting to observe the difference between the impedance peaks above and below the cut off frequency of the beam pipe ( $kb = 2.4$ ). For  $kb > 2.4$  EM energy can be lost via propagation in the beam chamber and consequently the peaks exhibit finite width and finite quality factors. When  $kb < 2.4$  only the lower frequency cavity eigenmodes can be excited and the corresponding peaks tend to be Dirac deltas, as the energy stored in these modes cannot be dissipated and the corresponding wakes are never damped.

### Pillbox with resistive walls

A pillbox with resistive walls allows for dissipation of the EM energy even below the cut-off frequency of the beam pipe. The wake decays with time (see Fig. 1.20) and the time constant of the decay is proportional to the electrical conductivity  $\sigma_{el}$ . Increasing the WL, the accuracy in the frequency domain improves. The accuracy is fundamental if we are interested to estimate properly the quality factor  $Q$  and the peak value of the impedance. Otherwise, to determine only the resonant frequency of the modes, it is sufficient to simulate a very short wake because it is important only to excite the modes. Figure 1.21 shows that to obtain an accurate value of  $Q$  and impedance peak value it could be necessary to simulate very long wakes with respect to the geometrical dimensions of the pill-box, thereby increasing enormously the time of simulation. In this specific case, we cannot be sure to have converged even for WL=300 m. Figure 1.22 shows the direct comparison between the real part of the longitudinal impedance calculated for a pillbox cavity with PEC walls or with walls having finite conductivity. Above the cut-off frequency of the beam pipe, the two spectra are almost indistinguishable, suggesting

## 1.2. EM simulations of wakefields and impedances

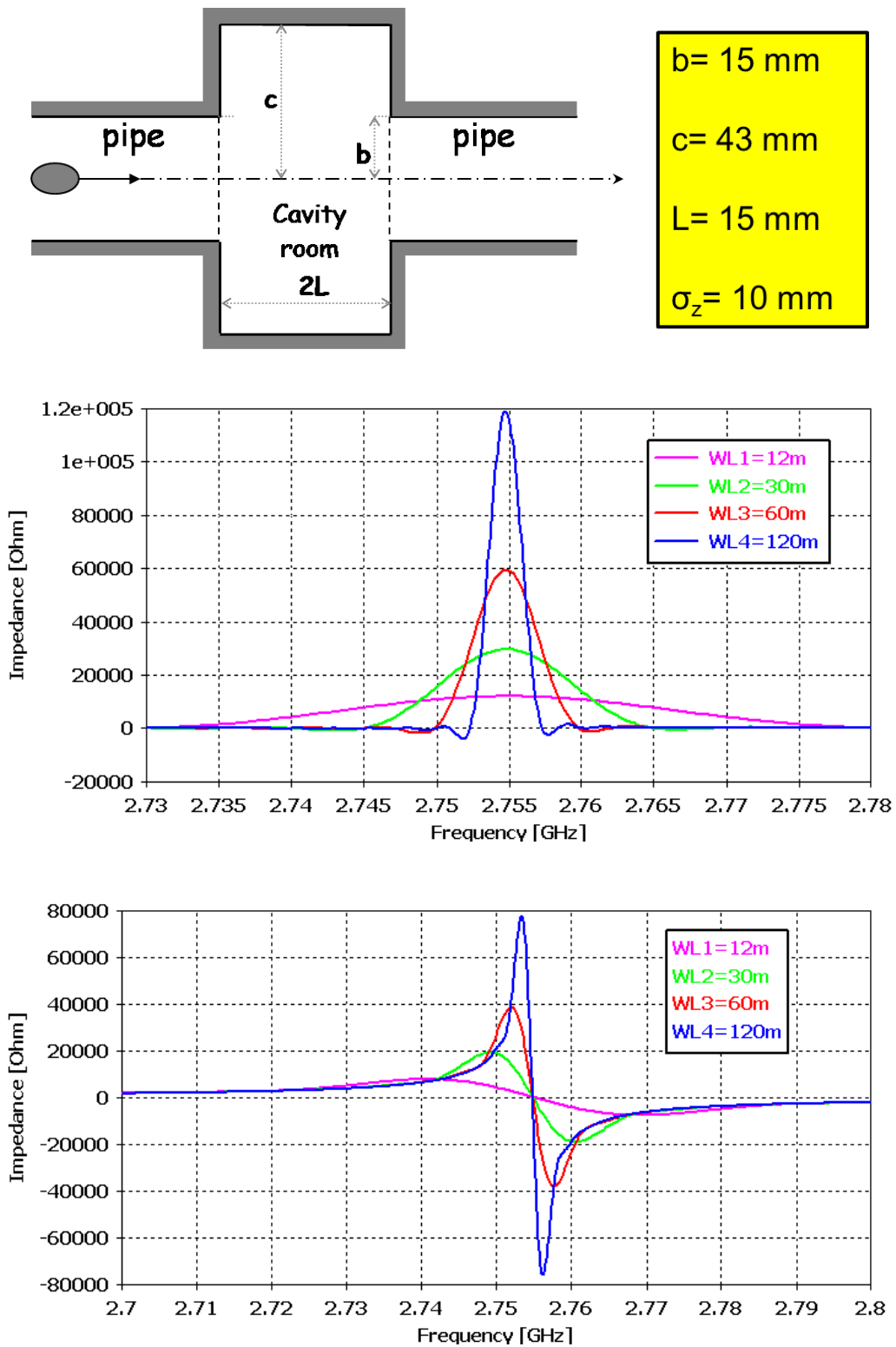


Figure 1.16: Above: simulated geometry,  $\sigma_z$  represents the RMS length of the Gaussian bunch. Below: Real and imaginary part of the longitudinal impedance of the first resonance changing the WL.

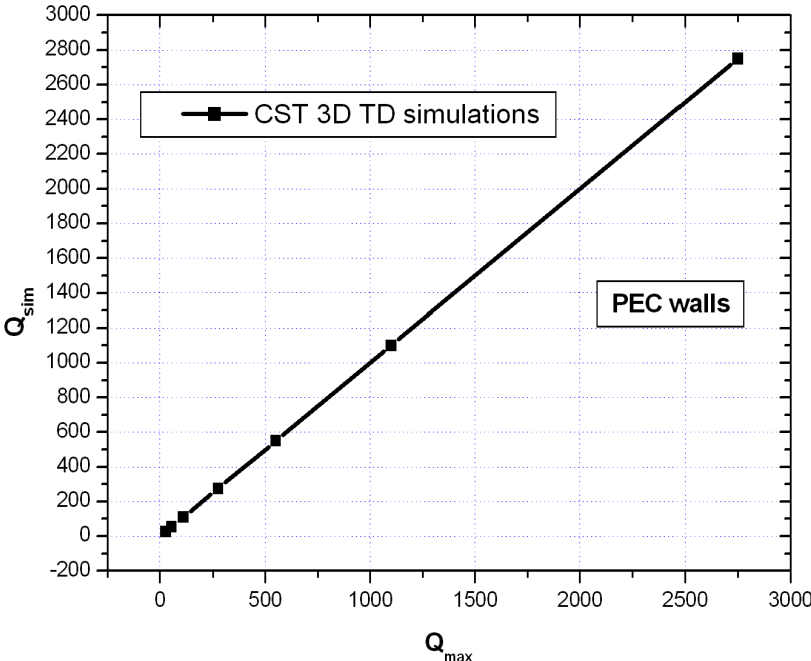


Figure 1.17: Displayed  $Q$  of a time domain simulation versus  $Q_{\max}$  for a PEC pillbox.

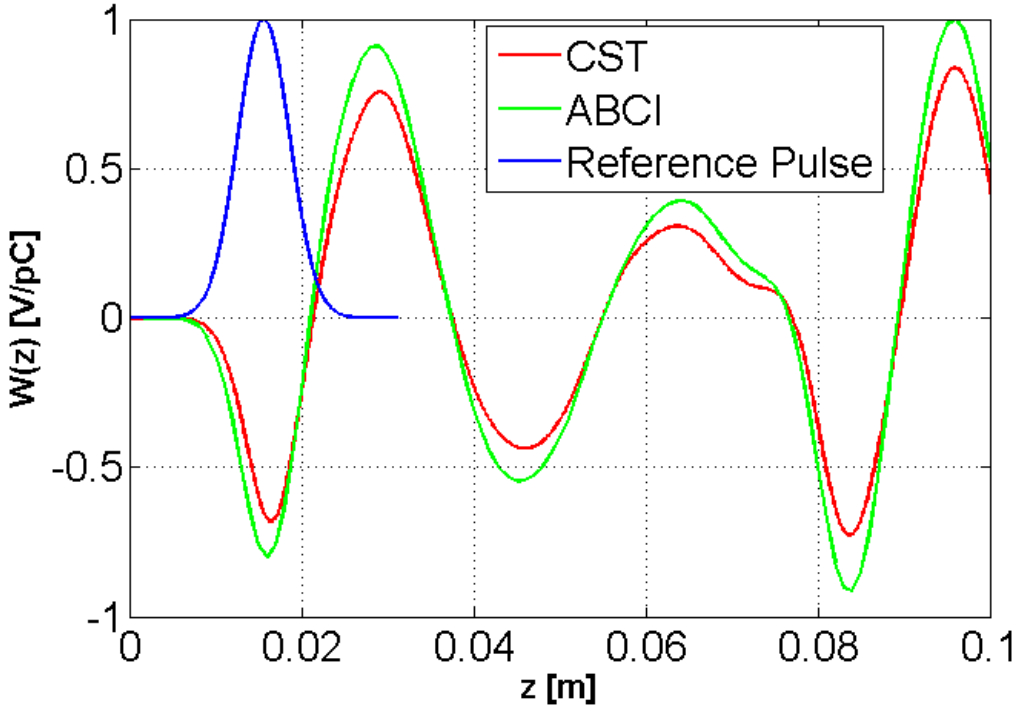


Figure 1.18: Comparing longitudinal wake potential from CST and ABCI for a PEC pillbox.

## 1.2. EM simulations of wakefields and impedances

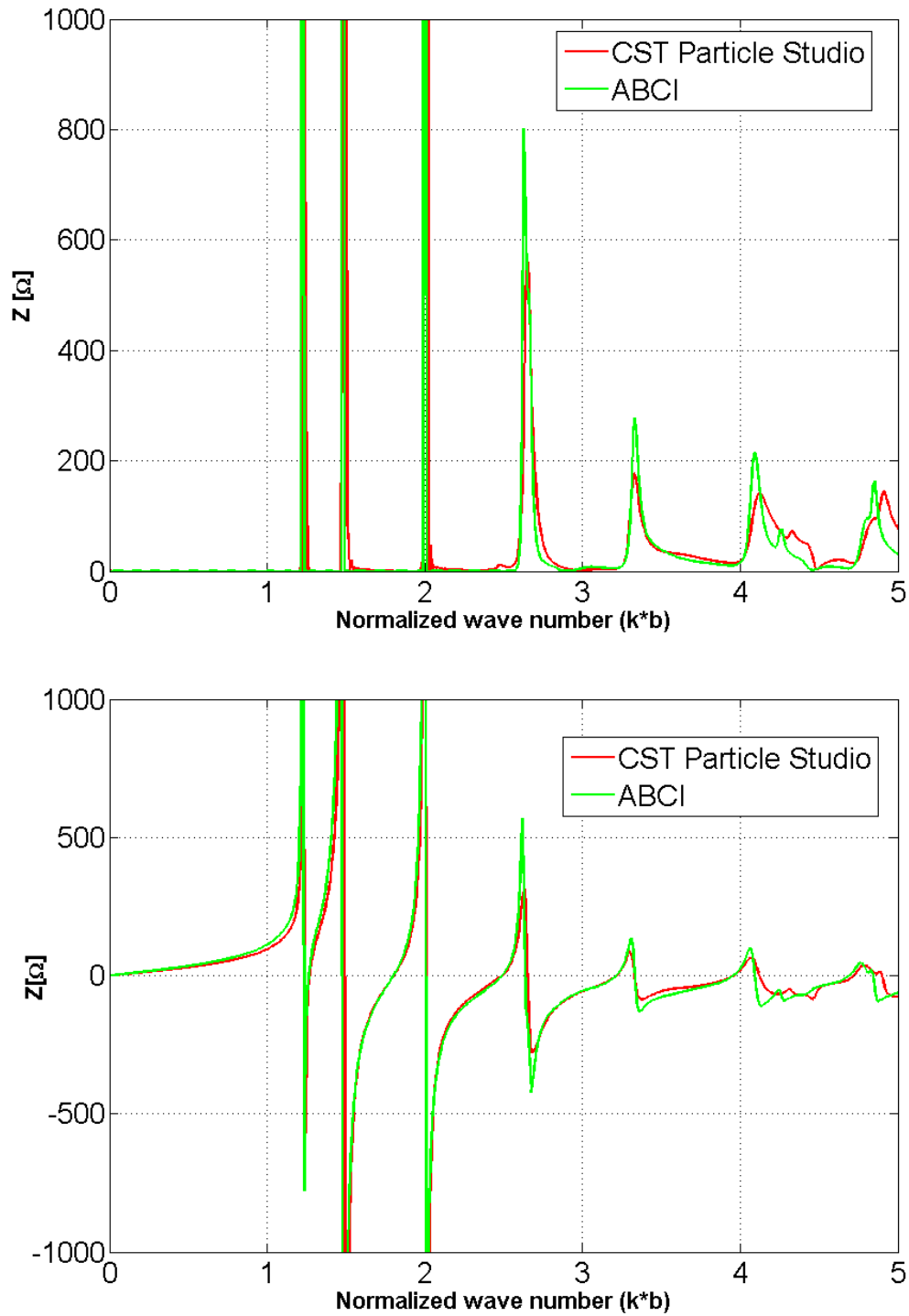


Figure 1.19: Comparing real (at the top) and imaginary (at the bottom) part of the longitudinal impedance from CST and ABCI for a PEC pillbox.

that here losses are dominated by propagation in the beam pipe. Below cut-off the situation is different. In fact below the pipe cut-off we cannot have propagation losses but only losses on the wall. Thus we can expect that the width of the resonant peak only strictly depends on the conductivity of the walls. It is not easy to see these differences using a time domain code, as normally these resonances are characterized by a very high  $Q$  value (high conductivity of the walls). The displayed quality factor  $Q_{\text{sim}}$  of the peaks below cut-off will be limited to  $Q_{\text{max}}$ . The results of Fig. 1.22 were obtained using a WL of  $120m$  ( $Q_{\text{max}} = 1100$ ). We analyzed in detail, in terms of  $Q$  value, the first resonance below cut-off of Fig. 1.22. The  $Q$  value is calculated directly from the displayed impedance by the definition:

$$Q = \frac{f_r}{\Delta f_r} \quad (1.33)$$

where  $\Delta f_r$  is the bandwidth of the resonance at half maximum. In the PEC case, coherently with what expected, we obtain  $Q_{\text{sim}} = 1100 : Q_{\text{real}} = \infty$ , then  $Q_{\text{sim}} = Q_{\text{max}} = 1100$ . In the lossy case we found  $Q_{\text{sim}} = 760$ . Moreover, for the lossy pillbox, using the 2D frequency domain (FD) code SUPERFISH [20] we simulated the real value of  $Q$  obtaining  $Q_{\text{real}} = 1420$ . Empirically, an approximate estimation of the simulated quality factor  $Q_{\text{sim}}$  can be obtained from the parallel combination of the real value of the quality factor  $Q_{\text{real}}$  and  $Q_{\text{max}}$ :

$$Q_{\text{sim}} = \frac{Q_{\text{max}} Q_{\text{real}}}{Q_{\text{max}} + Q_{\text{real}}} \quad (1.34)$$

Note that we will obtain exactly the  $Q_{\text{real}}$  only when  $Q_{\text{max}} = \infty$  that it means  $WL = \infty$ . This implies that theoretically we cannot obtain the  $Q_{\text{real}}$  with a time domain code. Anyway we can display the  $Q$  for different WL to see if we are approaching a convergence of the simulated value  $Q_{\text{sim}}$  as illustrated in Fig. 1.23 where  $Q_{\text{sim}}$  is plotted as function of  $Q_{\text{max}} = \frac{f_r WL}{c}$ . We expect to see a convergence of the simulated value in the case of a vanishing wake. For a low loss pillbox the wake-field vanishes for very large value of WL and the simulation becomes time and memory consuming. In these cases we can simulate the structure for some values of WL, and then extrapolate the real value. All these studies aim to point out that extrapolating typical frequency domain quantities (e.g.  $R_s$  and  $Q$  of resonant peaks) from time domain codes is not straightforward and attention has to be paid to the results in order to obtain significant numbers.

### 1.2.4 Step-in and step-out

In this section we will discuss the behaviour of the real longitudinal impedance in a step-in and in a step-out and benchmark the results obtained with the numerical codes CST Microwave Studio and ABCI.



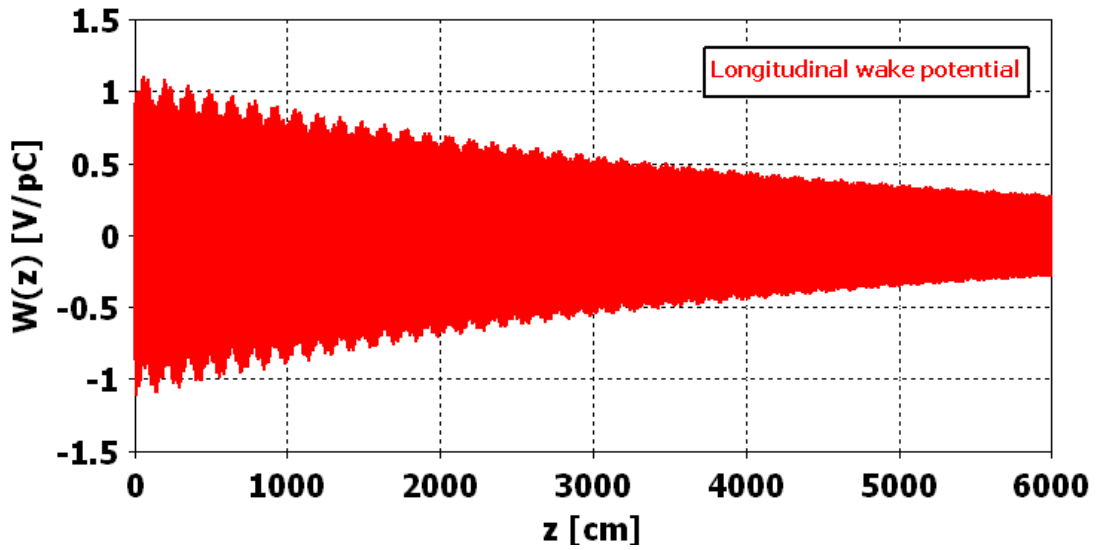


Figure 1.20: Longitudinal wake potential of the lossy pillbox of Fig. 1.16 with an electrical conductivity  $\sigma_{el} = 6 \times 10^5$  S/m.

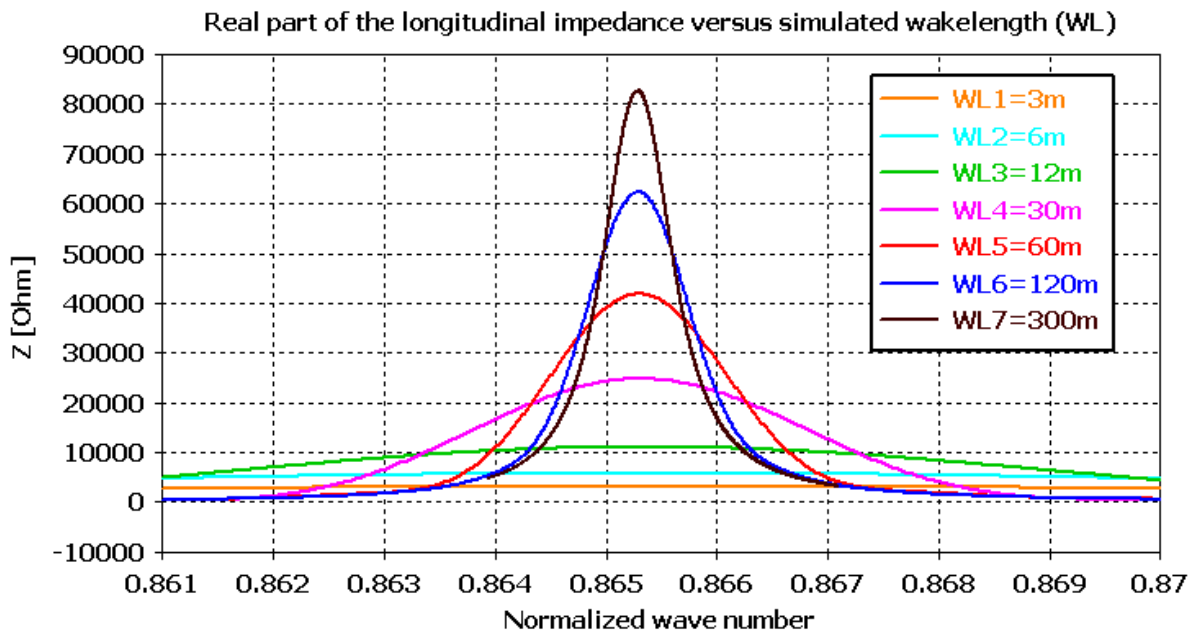
#### Step-in step-out transition: simulations and qualitative theory

The step-in is defined as an abrupt transition in which the beam goes from a pipe with larger radius into a pipe with smaller radius. A step-in transition is shown in Fig. 1.24.

In Fig. 1.25 we show the real part of the longitudinal impedance of a step-in structure calculated with the electromagnetic codes CST Microwave Studio (3D simulations) and ABCI (2D simulations). The results obtained with the two codes exhibit a good agreement.

At low frequency the real part of the impedance is negative. The first peak corresponds to the cut-off frequency of the larger pipe and above this frequency the real part of the impedance tends to vanish. From Eqs. (1.7) and (1.10) it can be seen that a negative real part of the impedance at low frequencies means that the bunch gains energy. This behavior can be intuitively explained in the following way: below the cut-off frequency of the larger pipe the structure cannot lose energy (PEC walls and no radiative losses because there is no propagation), therefore, the electromagnetic energy stored in the part of the field that is "cut" after the passage into a smaller pipe can be only translated into an increase of kinetic energy of the beam. A quadratic dependence of the low frequency impedance on the ratio  $d/b$  has been observed in the simulations as shown in Fig. 1.26. Considering the interpretation given above, we can understand this behaviour, because increasing the ratio  $d/b$  the amount of "scraped" electromagnetic energy increases and therefore the energy gained by the beam also increases. In the step-out case the beam passes from the region with smaller radius to a region with larger radius as shown in Fig. 1.27. We show the real part of the longitudinal impedance of a step-out structure calculated with CST Microwave Studio and ABCI in Fig. 1.28. The results are again in good agreement.

Now, when the charge crosses the discontinuity, the self field restoring the boundary con-



WL [m]	Time [s]	Memory [Mb]	$Q_{sim}$	$Q_{max}$
12	120	46	107	110
30	480	88	253	275
60	1440	157	461	550
120	4680	296	761	1100
300	25920	711	1149	2750

Figure 1.21: Above: Real longitudinal impedance changing WL: first peak of resonance of the pill-box cavity of Fig. 1.16 with an electrical conductivity  $\sigma_{el} = 6 \times 10^5$  S/m. Below: Table that specifies for each simulation  $Q_{sim}$  and  $Q_{max}$  together with the CPU times and memory.

## 1.2. EM simulations of wakefields and impedances

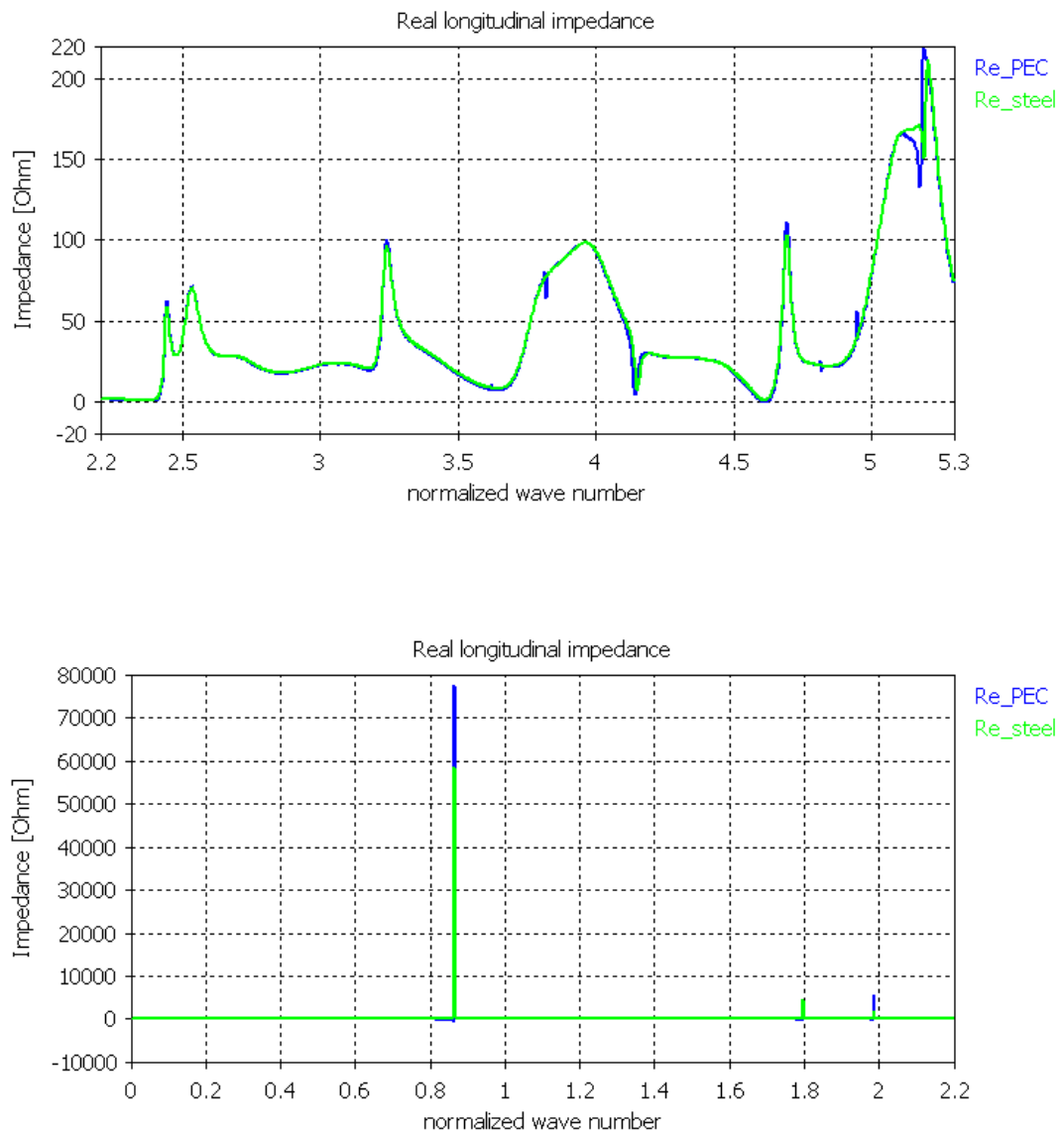


Figure 1.22: Real longitudinal impedance in case of infinite (PEC) and finite conductivity (a bad conductor with  $\sigma_{el} = 6 \times 10^5$  S/m) above the cut-off frequency (at the top) and below the cut-off frequency (at the bottom).

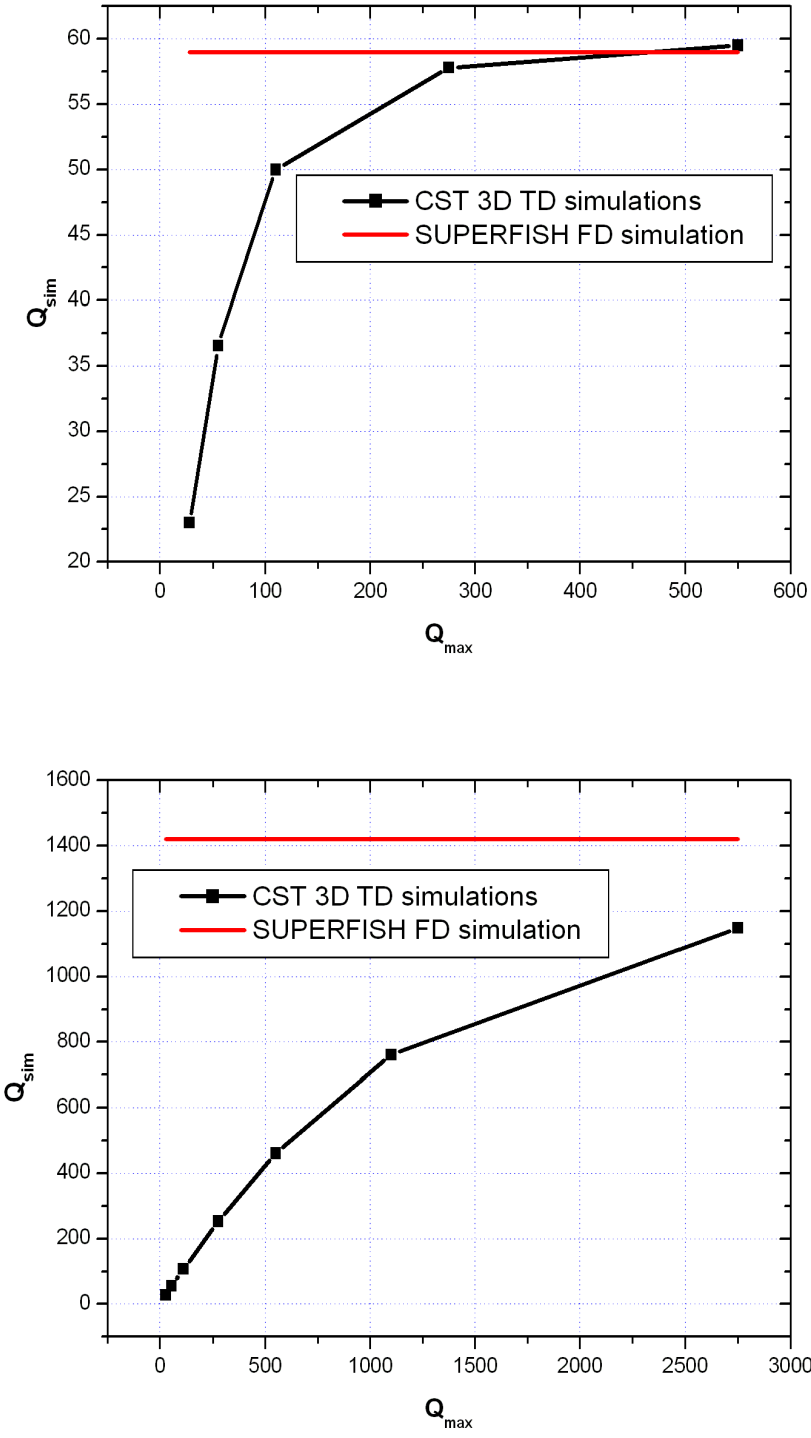


Figure 1.23: Displayed  $Q$  of a time domain simulation versus  $Q_{max}$ . First picture: case of a pillbox with conductive material of  $\sigma_{el} = 1000$  S/m; Second picture: case of a pillbox with conductivity  $\sigma_{el} = 6 \times 10^5$  S/m.

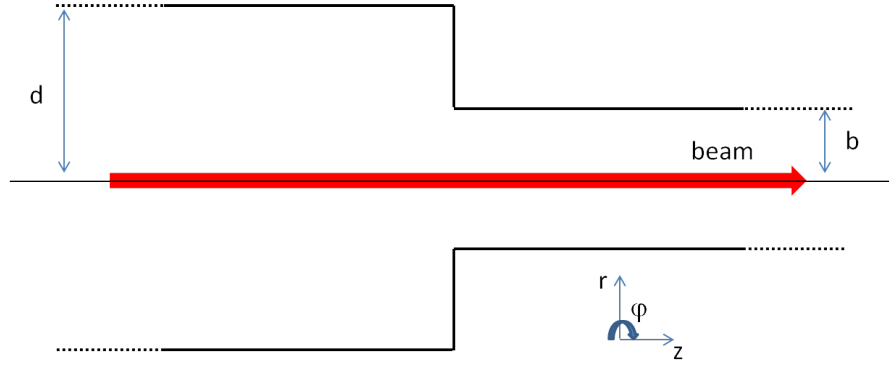


Figure 1.24: Step in transition.

ditions, has to fill the extra space  $b < r < d$  between the two pipes, while diffracted fields propagate into the pipes (if they are above cut-off). Both these effects lead to an energy loss that can be put as [16]:

$$\Delta E^{\text{step-out}} = U(b < r < d) + E_{\text{rad}} \quad (1.35)$$

where  $E_{\text{rad}}$  is the energy radiated at the edges and  $U(b < r < d)$  is the energy necessary to fill the region  $b < r < d$ . In the step-in case, the radiated energy is reflected back with respect to the particle motion [16]:

$$\Delta E^{\text{step-in}} = -U(b < r < d) + E_{\text{rad}} \quad (1.36)$$

We recall that for a real bunch  $E_{\text{rad}}$  depends on the bunch length. In particular, if the bunch spectrum does not significantly cover the frequency region above the pipe cut-off, there is no radiation [16]. Below the cut-off of the pipe with larger radius  $E_{\text{rad}} = 0$  and then accordingly to Eqs. (1.35) and (1.36) the static impedances in step-in and step-out case must be opposite in sign. From Eqs. (1.35) and (1.36) we can derive the following relations between the step-in and step-out longitudinal impedance:

$$\begin{aligned} Z_{\parallel}^{\text{step-out}} &= Z_{\parallel}^{\text{step-in}} - 2Z_{\parallel}^{\text{step-in}}(0) \\ Z_{\parallel}^{\text{step-in}} &= Z_{\parallel}^{\text{step-out}} - 2Z_{\parallel}^{\text{step-out}}(0) \end{aligned} \quad (1.37)$$

where  $Z_{\parallel}^{\text{step-in}}(0) = -Z_{\parallel}^{\text{step-out}}(0)$  is the static impedance of a step-in. The above relations have been verified with CST 3D simulations (see Fig. 1.29).

Contrary to the longitudinal impedance, the simulation of the transverse impedance of a step-transition is very critical. For these reasons we developed an analytical method based on the mode matching technique for the calculation of this impedance contribution (see Appendix B).

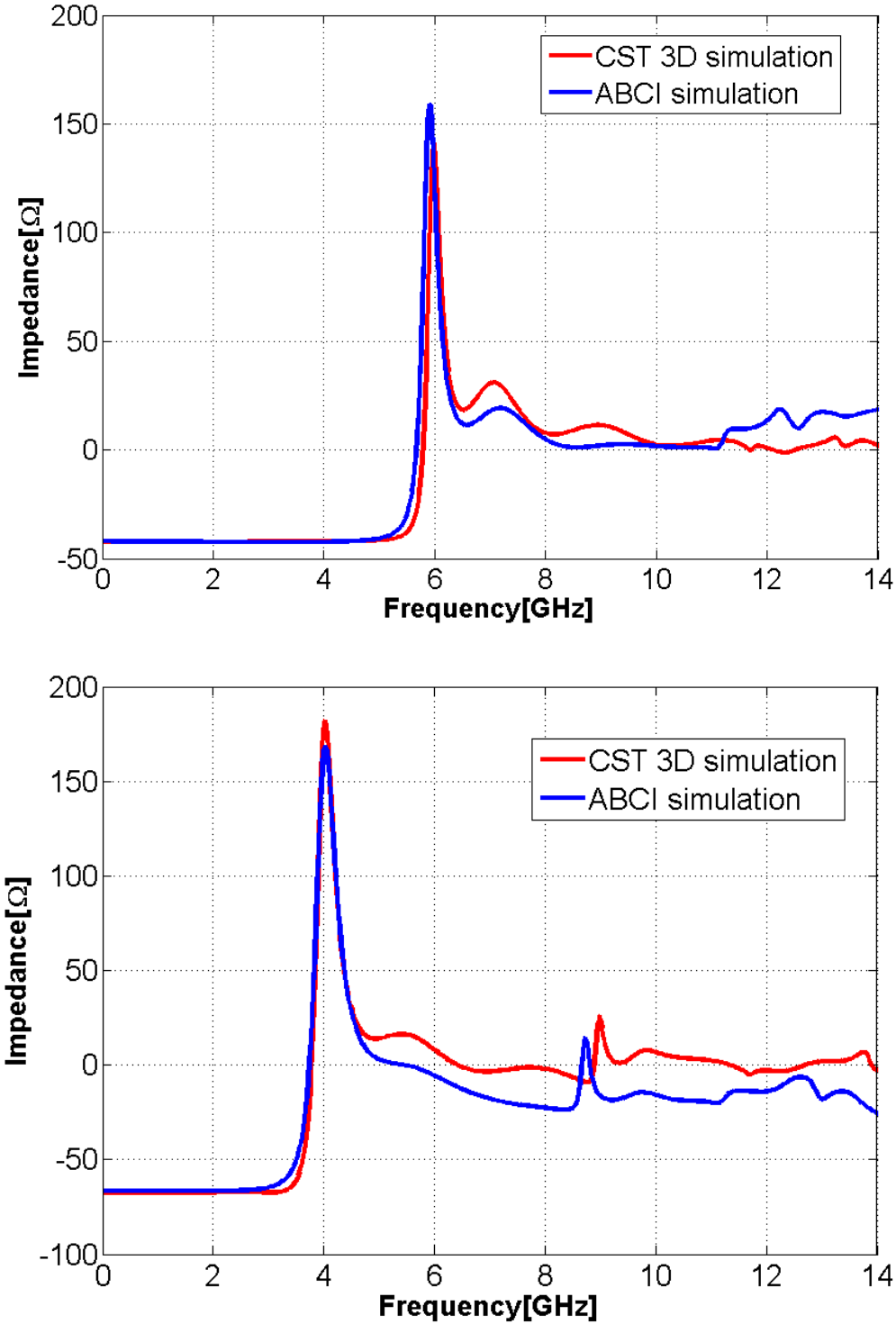


Figure 1.25: Real part of the longitudinal impedance of a step-in transition with  $b = 1$  cm and  $d = 2$  cm (at the top) and  $d = 3$  cm (at the bottom).

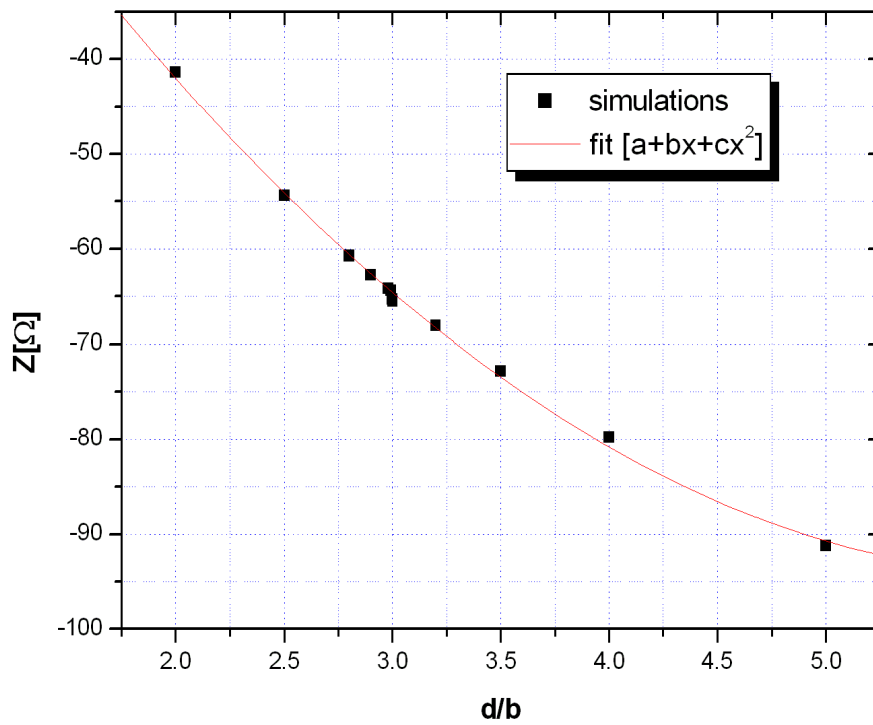


Figure 1.26: Real part of the longitudinal impedance of a step-in transition versus  $d/b$  at  $f = 0$ .

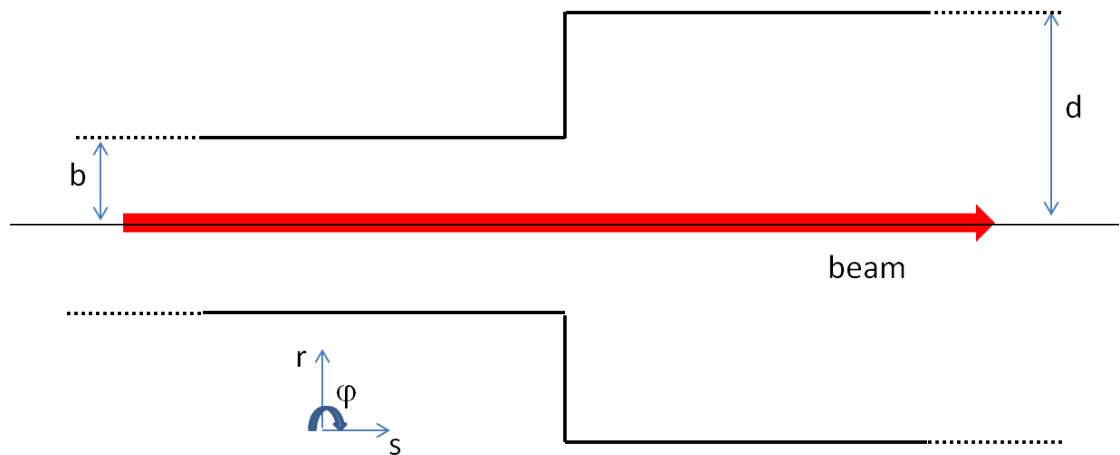


Figure 1.27: Step-out transition.

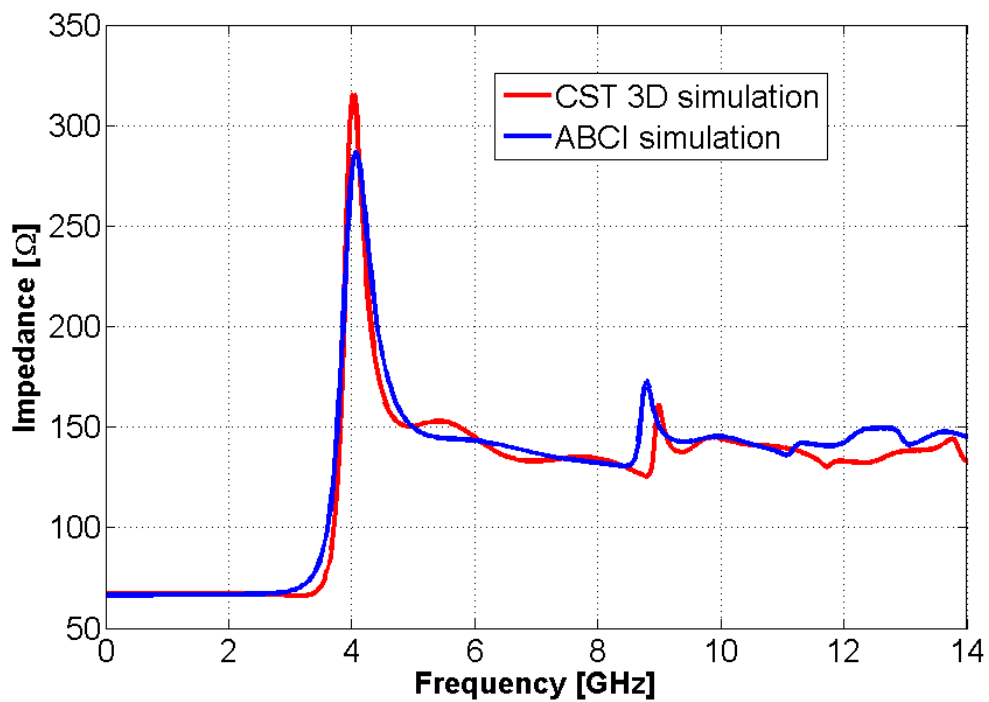
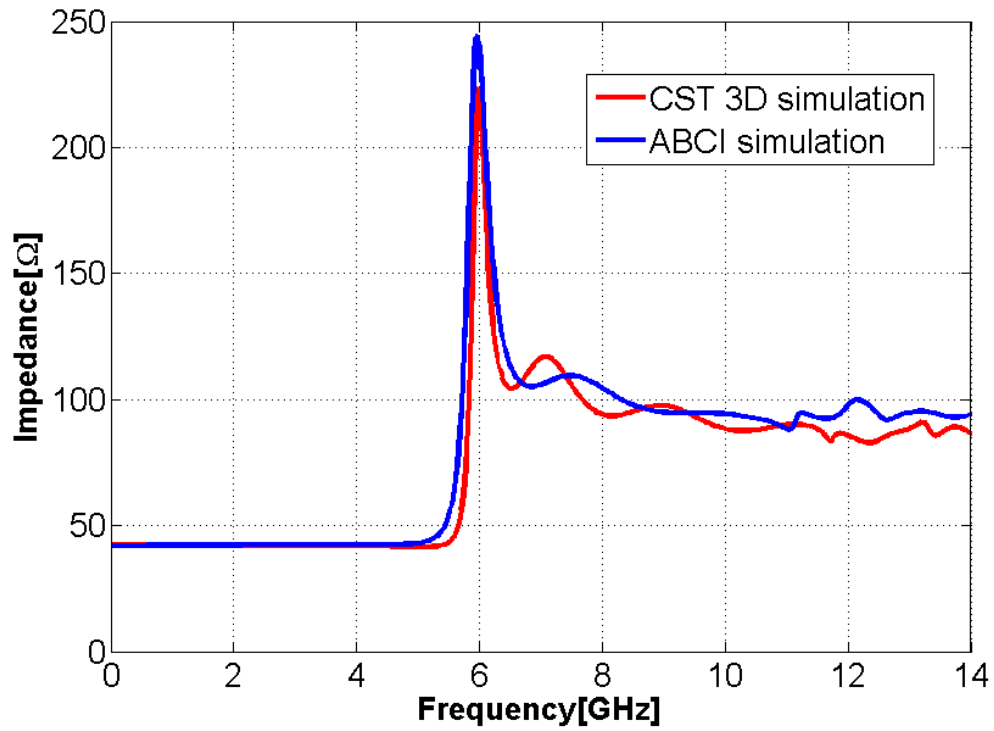


Figure 1.28: Real part of the longitudinal impedance of a step-out transition with  $b = 1$  cm and  $d = 2$  cm (at the top) and  $d = 3$  cm (at the bottom).



## 1.2. EM simulations of wakefields and impedances

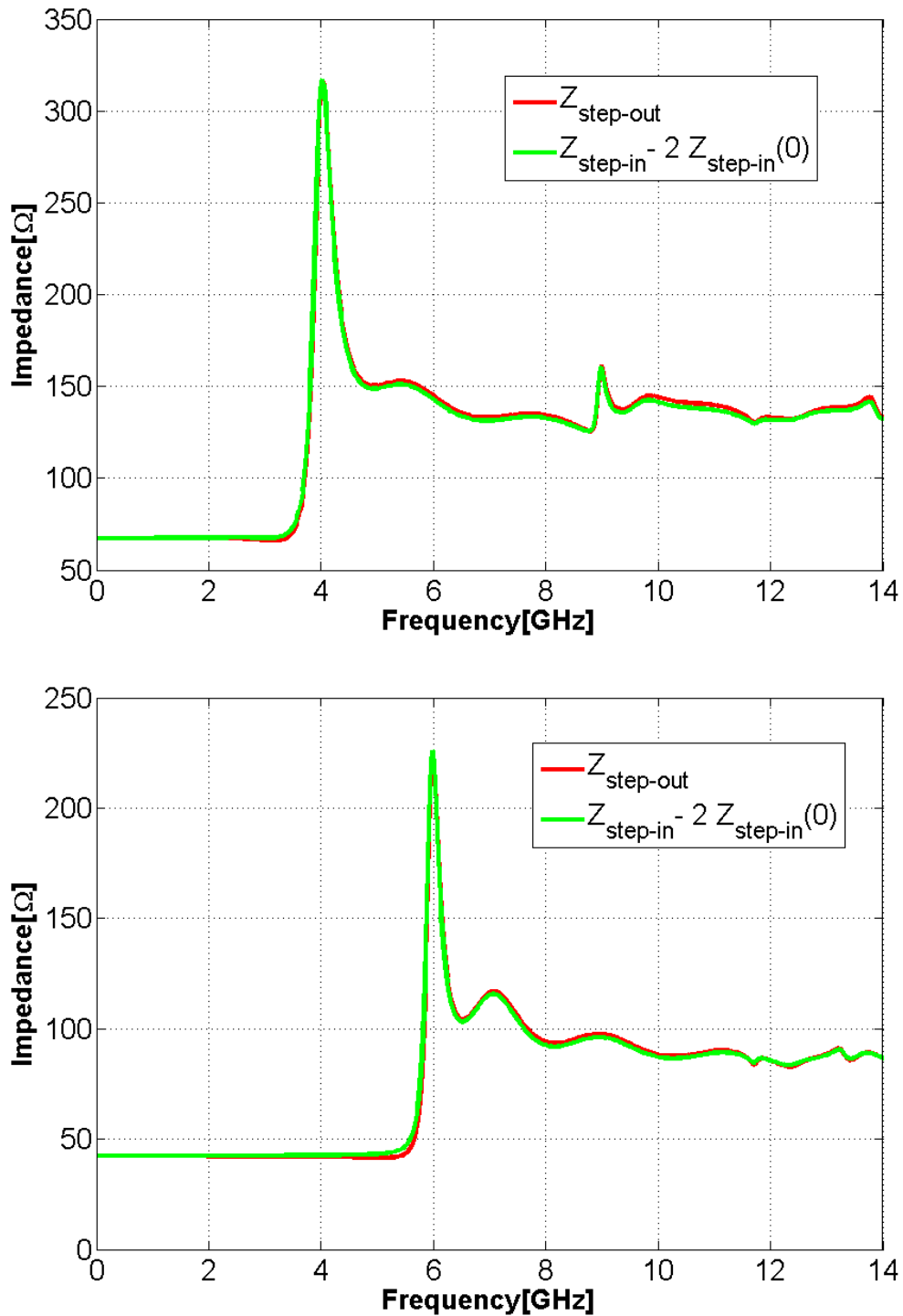


Figure 1.29: Real part of the longitudinal impedance of a step-out transition with  $b = 1$  cm and  $d = 2$  cm (at the top) and  $d = 3$  cm (at the bottom) from the simulation of a step-out (in red) and from the simulation of the symmetric step-in using Eq. 1.37 (in green).



## 2 Impedance model of ferrite loaded kickers

In the frame of the SPS upgrade an accurate impedance model is needed in order to predict the instability threshold and if necessary to start a campaign of impedance reduction. Special attention has to be devoted to the estimation of the impedance contribution of the kicker magnets, which are suspected to be the most important transverse impedance source in the SPS. The aim of this Chapter is a stepwise description of the simulation studies performed to build the SPS kicker impedance model.

### 2.1 Simple model of SPS ferrite loaded kickers

#### 2.1.1 Theoretical transverse impedance of the SPS kickers

##### The SPS kickers

A kicker is a special type of magnet designed to abruptly deflect the beam off its previous trajectory, to inject the beam into a ring or extract it to a transfer line or to a beam dump. Among all the SPS elements, the kickers are suspected to contribute to a significant amount of the transverse impedance of the SPS [21]. There are several types of kickers installed in the SPS as reported in Tab. 2.1: injection kickers (MKP), extraction kickers to LHC transfer lines (MKE), extraction kickers to the SPS dump (MKDH, MKDV) and tune measurement kickers (MKQH, MKQV). In Tab. 2.1 the beta functions at the kicker locations are also reported for both the standard Q26 optics and the new low  $\gamma$ -transition Q20 optics (Q stands for tune and the number indicates the integer part of the transverses tune  $Q_{x,y} = \frac{\omega_{\beta}}{\omega_0}$ ). The Q20 has been introduced to increase the beam stability in the intensity range required by the LHC injectors upgrade project [22]. In October 2012 the Q20 has become operationally used in the SPS. The location of these kickers in the SPS ring is schematically shown in Fig. 2.1.

In order to be able to compute the impedance of the kickers analytically with the field matching technique it is necessary to make some approximations. First, the complicated geometry of each of the SPS kickers will be modeled as a flat chamber made of two infinite blocks of ferrite (see for instance the MKE geometry in Fig. 2.2). We therefore neglect many features of the kicker magnets at this stage: hot and cold conductors on either side of the aperture, C-shape magnetic yoke, cell longitudinal structure, transitions between the ferrite blocks and the SPS beam pipe, external coupling circuits and geometry outside of the ferrite yoke. Besides, the MKDH kickers have been built with laminated silicon steel yokes instead of ferrite yokes [23]. Since relevant high frequency properties for this laminated silicon steel are not

## Chapter 2. Impedance model of ferrite kickers

Kicker name	s	$\beta_x$ (Q20)	$\beta_y$ (Q20)	$\beta_x$ (Q26)	$\beta_y$ (Q26)	a	b	L
MKQH.11653	524.68	72.28	48.36	64.52	37.19	0.0575	0.01615	0.768
MKQV.11679	535.77	45.41	76.71	33.88	70.08	0.051	0.028	1.133
MKDV.11731	550.62	37.40	91.61	25.68	88.28	0.0375	0.028	2.314
MKDV.11736	553.81	42.85	81.09	31.21	75.44	0.0415	0.028	2.314
MKDH.11751	556.02	47.14	74.31	35.78	67.28	0.048	0.028	1.28
MKDH.11754	557.92	51.16	68.83	40.19	60.75	0.048	0.028	1.28
MKDH.11757	559.82	55.49	63.66	45.04	54.67	0.0525	0.03	1.28
MKPA.11931	615.09	38.09	89.96	26.33	85.78	0.05	0.0305	2.738
MKPA.11936	618.72	44.43	78.25	32.83	71.59	0.05	0.0305	2.738
MKPC.11952	620.70	48.36	72.33	37.07	64.52	0.05	0.0305	1.424
MKP.11955	624.32	56.44	62.36	46.07	52.83	0.07	0.027	2.738
MKE.41631	3973.35	94.57	35.87	91.97	24.04	0.07385	0.0175	1.658
MKE.41634	3975.66	86.75	39.48	82.33	27.58	0.07385	0.0175	1.658
MKE.41637	3977.97	79.38	43.55	73.34	31.77	0.0675	0.016	1.658
MKE.41651	3980.29	72.47	48.07	65.00	36.63	0.0675	0.016	1.658
MKE.41654	3982.60	66.02	53.06	57.33	42.14	0.07385	0.0175	1.658
MKE.61631	6277.18	95.45	35.73	92.09	24.12	0.07385	0.0175	1.658
MKE.61634	6279.50	87.52	39.36	82.42	27.70	0.07385	0.0175	1.658
MKE.61637	6281.81	80.05	43.45	73.42	31.95	0.0675	0.016	1.658

Table 2.1: SPS kickers parameter list: Kicker name, longitudinal coordinate along the accelerator  $s$ , horizontal and vertical beta functions  $\beta_x$  and  $\beta_y$  at this location for both Q20 and Q26 optics, horizontal and vertical half apertures  $a$  and  $b$  and length of the kicker magnet  $L$  (in m). The thickness of the ferrite is assumed to be 6 cm for all kickers. It is important to note that all the kickers are designed to deflect the beam horizontally (i.e. the magnetic field is vertical and the ferrite blocks are aligned horizontally as in Fig. 2.2), apart from 3 vertical kickers (MKQV and MKDVs) in which the ferrite blocks are rotated by  $\pi/2$  to produce a horizontal magnetic deflecting field.

readily available, we will assume for now that all the kickers are made of ferrite. The model for the ferrite permeability  $\mu$  as a function of frequency  $f$  was obtained from a first order dispersion fit on measured data up to 1.8 GHz [24]:

$$\mu = \mu_0 \cdot \mu_r = \mu_0 \left( 1 + \frac{\mu_i}{1 + jf2\pi\tau_u} \right) \quad (2.1)$$

with  $\mu_i = 460$  and  $\frac{1}{2\pi\tau_u} = 20\text{MHz}$ .

## 2.1. Simple model of SPS ferrite loaded kickers



Figure 2.1: Physical locations of the SPS kickers (red dots). We can observe that the SPS kickers are not evenly distributed along the ring but are clustered around the injection zone (4 MKP), extraction zones to TI2 and TI8 (5+3 MKE), the tune measurement zone (MKDH+MKQH), and the beam dump (3 MKDV + 2MKDH). Courtesy M. Barnes.

The ferrite dielectric properties are characterized by a complex permittivity  $\epsilon$ :

$$\epsilon = \epsilon_0 \cdot \epsilon_r = \epsilon_0 \left( \epsilon_r' - \frac{j \sigma_{el}}{2\pi f \epsilon_0} \right) \quad (2.2)$$

with  $\sigma_{el} = 10^{-6}$  S/m and  $\epsilon_r' = 12$ .

The ferrite used for the measurements of the ferrite EM properties was of type 4A4 made by Philips Components (now Ferroxcube). Most SPS kickers are made of Ferroxcube ferrite type 8C11 [25]. Contrary to ferrites of type 4A4, it is not possible to obtain a simple analytical dispersion model fitting the existing measured data for ferrites of type 8C11 up to 1.8 GHz.

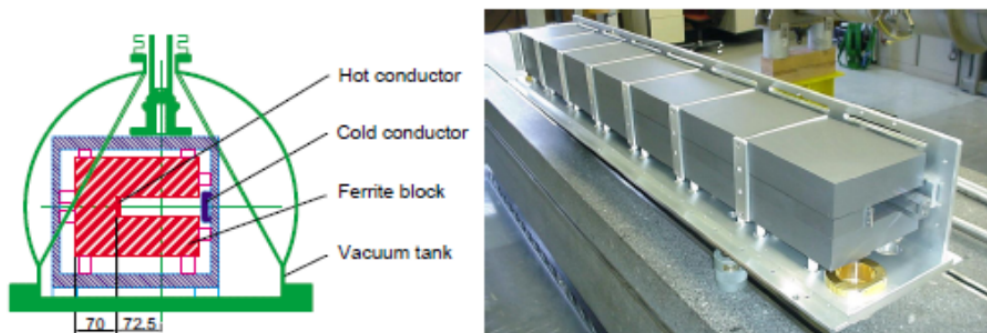


Figure 2.2: Drawing showing the transverse cross-section of an SPS MKE kicker (left) and the longitudinal segmentation into seven assembled ferrite cells mounted with the hot and cold conductors (right). Courtesy T. Kroyer.

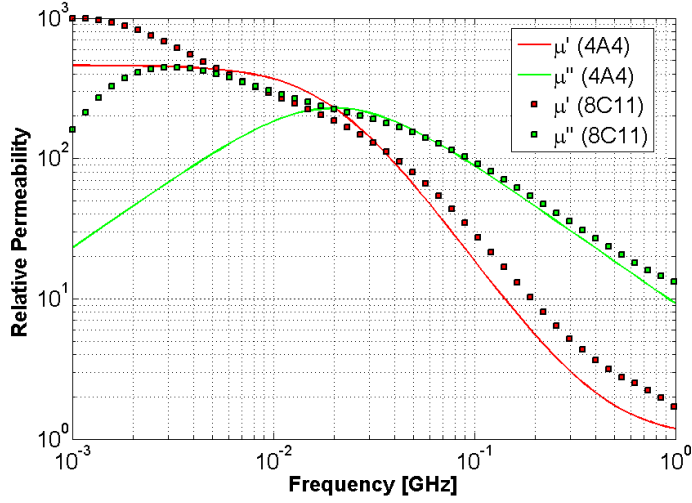


Figure 2.3: Comparing real (red) and imaginary (green) part of the relative permeability  $\mu_r = \mu' - j\mu''$  for the ferrite 4A4 (solid lines) and 8C11 (dotted curves).

Consequently, to simulate this material with CST is not straightforward. In Fig. 2.3 we show the measured data for the ferrite 8C11 comparing them with the permeability model of the ferrite 4A4. A significant difference between the models is visible at low frequency (below 10 MHz). In spite of this difference, recent studies [26] - which will be discussed in the next section - have shown that the beam coupling impedance models obtained for kicker type structures made of ferrites 4A4 and 8C11 are actually very similar.

### Kicker analytical models

In the past, the impedance of the SPS kickers was obtained using the Zotter/Métral model [27, 28] for a cylindrical beam pipe made of ferrite and applying the Yokoya form factors [15] to transform the cylindrical geometry into a flat chamber. However, the Yokoya factors were obtained for resistive chamber under the assumption that the beam is ultra-relativistic, the beam pipe is longitudinally uniform, and the skin depth is much smaller than both the dimensions of the beam pipe and the thickness of the material [15]. In our case the third hypothesis is not true and it could be expected that the Yokoya factors are not valid. In the following we use Tsutsui's theory to model ferrite loaded kickers instead of Zotter/Métral's theory. In order to refine the model for the kickers, H. Tsutsui derived a field matching theory to obtain the longitudinal [29, 30] and transverse dipolar [31] impedance of a geometrical model made of two ferrite blocks inserted inside a metallic chamber, for an ultra-relativistic beam. Fig. 2.4 shows an overview on the kicker impedance models so far described, for which analytical solutions are available. Tsutsui's theoretical impedance calculations were compared to HFSS simulations and subsequently to measurements of PS and SPS kickers in references [32, 33, 34]. In his paper [31], H. Tsutsui only derived the transverse dipolar impedances, while the quadrupolar part was first derived in [35].

The analytical calculations of the beam impedance using, for instance, the models of Zot-

## 2.1. Simple model of SPS ferrite loaded kickers

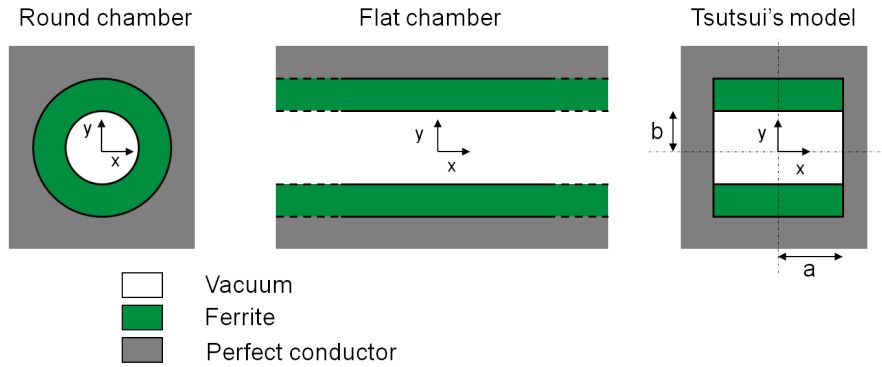


Figure 2.4: Geometric models for theoretical impedance calculations. The impedance for a multilayer cylindrical model (left) can be obtained with the field matching formalism by Zotter and Métral. The impedance for a multilayer flat chamber model (center) can be obtained under certain assumptions by applying the Yokoya factors to the impedance of the cylindrical model. H. Tsutsui derived a formalism to obtain the impedance of a model that accounts for perfect conducting plates on both sides of the ferrite plates (right). The beam travels perpendicularly to the drawing.

ter/Métral and Tsutsui are unfortunately restricted to simplified geometrical models so that the equations can be solved analytically. Real accelerator devices are in general designed with complicated shapes optimized to give the best operating performance. The next subsection will illustrate 3D simulations of kickers. We will gradually move from the simplified models to more realistic, and hence complicated, structures.

### 2.1.2 EM simulations of SPS kickers

First of all, we have performed CST Particle Studio Wakefield simulations of simple 3D models of kickers [26, 36]. Here we describe the benchmark of the simulated impedance of Tsutsui's kicker geometrical model and the available theoretical computations. It is important to note that Tsutsui's model can only be applied to the kickers as installed in the machine in 2006, because, from 2007 on, a campaign to shield the MKE kickers with serigraphed conducting stripes has been implemented in order to reduce their longitudinal beam coupling impedance [37]. Applying the field matching formula we can obtain the impedance for several structures made of blocks of ferrite 4A4 with variable thickness. Figure 2.5 shows the scan of the ferrite layer thickness from 1 mm to infinity. We notice that the impact of increasing the ferrite thickness above 6 cm is negligible in the frequency range of interest (red and green curve are perfectly superimposed), and that we may equally use an infinitely thick layer or at least 6 cm thick ferrite layer.

#### Simulation setup

The cross-sectional view of the geometrical model described by H. Tsutsui was already shown in Fig. 2.4. The corresponding model generated with CST STUDIO SUITE is presented in Fig. 2.6. The dispersion model for the ferrite type 4A4 was presented in the subsection 2.1.1.

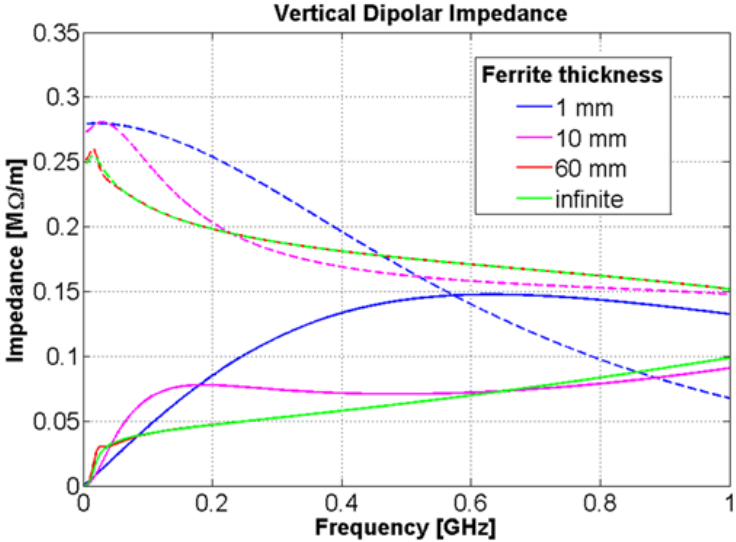


Figure 2.5: Vertical dipolar impedance of Tsutsui’s models of SPS extraction kickers (MKE) with various ferrite thicknesses. Real parts of impedance are full lines, Imaginary parts are dashed lines.

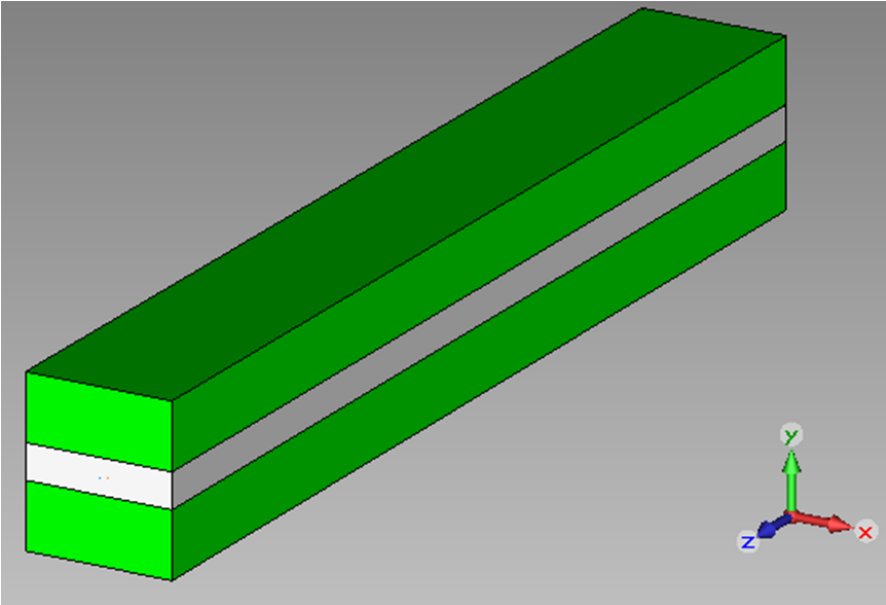


Figure 2.6: 3D model of the geometrical kicker model described by Tsutsui: vacuum chamber (white); 2 ferrite blocks (green) transversely surrounded by PEC (electric boundary conditions).



## 2.1. Simple model of SPS ferrite loaded kickers

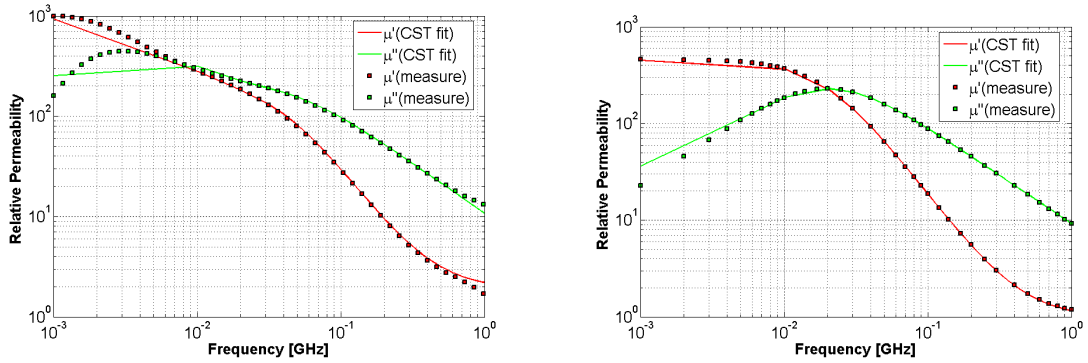


Figure 2.7: Comparing CST's fit and measurements of real and imaginary relative permeability for the ferrite 8C11 (left) and 4A4 (right).

When a material in CST is described through the measured data of its EM properties, the actual data are fitted using the pre-defined dispersion model that best matches the frequency behaviour of both permeability and permittivity. As already mentioned, this is the reason why modeling the EM properties of ferrites 8C11 is difficult (all existing models are rather far from the measured data). An acceptable fit can be obtained in both cases, as shown in Fig. 2.7 where we compare the measured and the CST fitted data for the ferrites 8C11 and 4A4. Differences between the measured and the fitted results only appear below 10MHz.

Next, using only the theoretical formulae for the impedance, we show the expected difference between the impedance of a kicker made of ferrite 4A4 and 8C11 (see Fig. 2.8). The input data for Tsutsui's theory were the same as for Fig. 2.7. Since the results are very close, we can conclude that the low frequency differences between ferrite 4A4 or 8C11 do not play a major role in the impedance calculation, at least up to almost 2 GHz.

The boundary conditions are set to electric around the ferrite. At the beam entrance and exit planes, the boundary condition is set to an absorbing Perfect Matching Layer. A parameter study shows that the simulated impedance exhibits a nonlinear behaviour with the length of the kicker [36]. In Fig. 2.9 we plot the vertical dipolar impedance normalized to the simulated length,  $Z_y(f)/L$  against the simulated length at a given frequency. If the impedance of the kicker was a linear function of the kicker length, we would expect to obtain a constant normalized impedance value, i.e.  $Z_y(f)/L = Z_{ny}(f)$ . In Fig. 2.9 we can see that this is not true, especially for kicker lengths below 1 m. The simulated normalized impedance exhibits a second order exponential decay with the length and tends asymptotically to a certain value. The limit value for infinite length can be extrapolated thanks to the second order exponential fit, or equivalently, directly simulated using periodic boundary conditions in the longitudinal plane. The two methods are found to give very similar results. Figure 2.10 shows the percentage increase of impedance  $(\frac{Z_y(f)/L}{Z_{ny}(f)} - 1) \times 100$ , due to the finite length effect [38, 39], together with the second order exponential fit used to extrapolate the expected value for infinite length for the cases of Fig. 2.9. We can see that, given the physical length of the MKE in Tab. 2.1, the finite length effect is below the 3% for the cases under test. Anyway it is important to underline the importance of simulating the physical length of the magnet, as the effect of finite length can

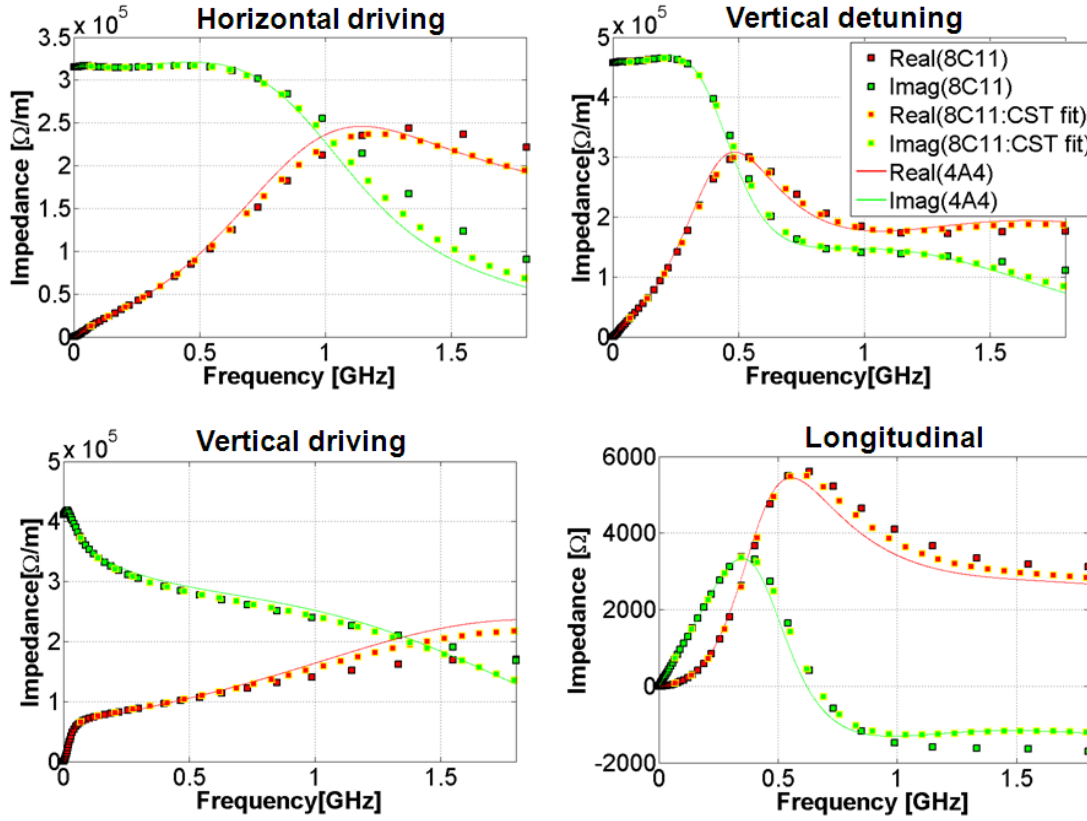


Figure 2.8: Longitudinal and transverse dipolar and quadrupolar impedance of a SPS extraction kicker (MKE) for ferrite 4A4, 8C11 and 8C11 CST fit as calculated from Tsutsui formalism. The horizontal quadrupolar impedance is not shown (it is equal but opposite in sign to the vertical quadrupolar according to Eq. (1.16)).

become much larger depending on kicker dimensions. Simulating shorter length to reduce the computational efforts can lead to inaccurate results (e.g. for the MKE with  $L = 20$  cm the error on the real part of the dipolar vertical impedance is about the 40%). For these reasons we choose to simulate the physical length of each kicker as given in Tab. 2.1.

An average of 5 million hexahedral mesh cells was used for the simulations (around 1.3 mm between 2 consecutive mesh points). Five simulations per kicker were performed with the transverse aperture given in Tab. 2.1 to obtain the longitudinal wake potential, as well as the driving and detuning transverse wake potentials following the procedure illustrated in Fig 1.5. The detuning wake potentials by definition must be exactly opposite in sign (see Eq. (1.14)). In all the cases we simulated both contributions to have a further cross-check of the consistence of the results.

### Simulation results and comparison with Tsutsui's theory

As an example, the simulated transverse wake potentials for a model of MKE kicker (MKE.41651) are presented in Fig. 2.11. Figure 2.12 shows the impedance derived from these simulated

## 2.1. Simple model of SPS ferrite loaded kickers

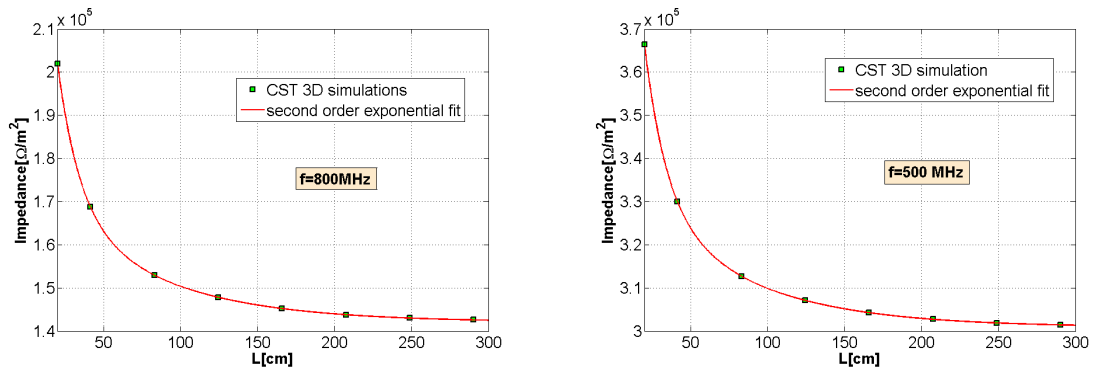


Figure 2.9: Vertical driving impedance per unit length for the SPS extraction kicker MKE.41651 versus simulated length at a fixed frequency: real part (left), imaginary part (right).

wake potentials with a DFT normalized to the bunch spectrum. Since the wakes vanish before the other bunch passing in SPS (7.5 m for 25 ns spacing), the kicker wakes as calculated with the Tsutsui model play a role only for single bunch dynamics. In Fig. 2.13 these simulations are compared to the theoretical impedance obtained by H. Tsutsui for the driving contribution, and the new theoretical formulae for the detuning impedance derived in [35] from Tsutsui's formalism. The agreement is very good. Due to the different methods to obtain these impedance contributions, this successful benchmark confirms: 1) the robustness of CST PS when simulating the impedance of kicker type structure; 2) the formulae for the dipolar and quadrupolar impedance contributions derived in Refs. [31, 35]; 3) the validity of the general method to obtain the driving and detuning contributions of the impedance with CST Particle Studio. We have compared simulations and theory for the same kicker using always Tsutsui's formulae [29, 30] also for the longitudinal impedance (see Fig. 2.14), obtaining again an excellent agreement.

All the others SPS kickers approximated with the simplified Tsutsui's structures have been also simulated with CST-PS. The total impedance contribution from all the kickers can be obtained

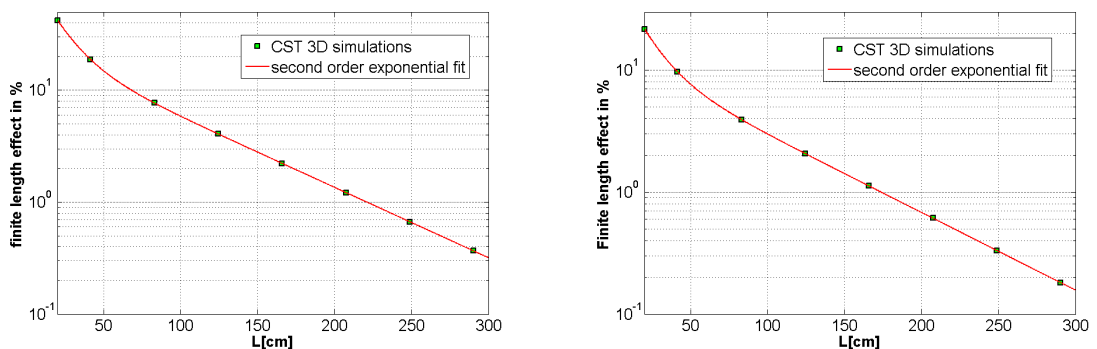


Figure 2.10: Finite length effect in percentage for the cases of Fig. 2.9: real part (left), imaginary part (right).

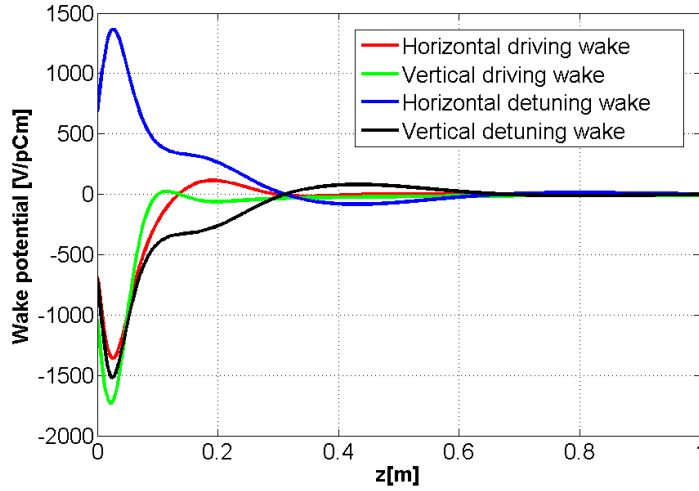


Figure 2.11: Simulated transverse wake potentials for the SPS extraction MKE.41651 with Tsutsui's kicker geometry model.

by summing up the impedance of each kicker weighted by the respective beta function at the kicker location  $\beta_{x,y}$ , and dividing the sum by the average beta function of the accelerator  $\langle \beta \rangle_{x,y}$ . Comparing the total kicker impedance contribution as obtained from theoretical calculations and EM simulations, we can see that the behaviour is very similar up to 2 GHz, as shown in Fig. 2.15.

In order to be able to use the simulated wake functions as inputs of HEADTAIL for single bunch dynamics studies, it is important to have an accurate description of the wake at a distance  $z$  significantly smaller than the RMS bunch-length, which means that the impedance calculation needs to be accurate up to very high frequency (depending on the accelerator we consider, from a few GHz to the range of THz). To go up in frequency we need to decrease the simulated bunch length,  $\sigma_z$ , and then increase the number of mesh cells so that the number of lines per wavelength (LW) remains high enough to produce accurate results. Therefore,

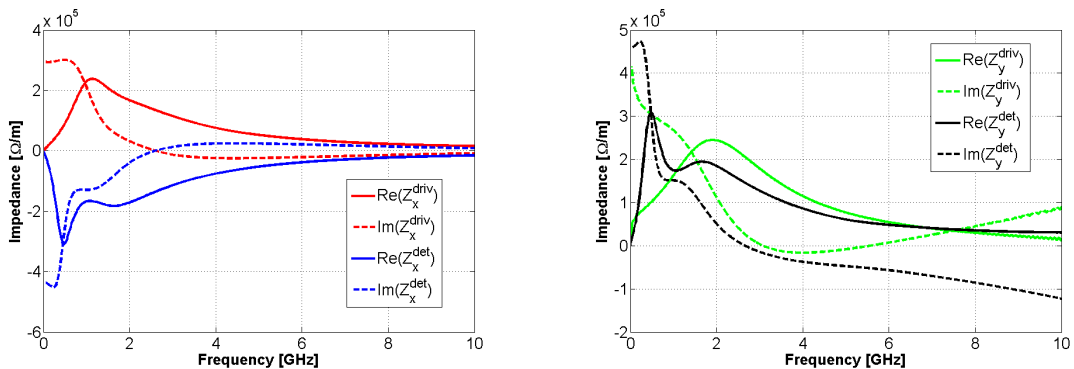


Figure 2.12: Simulated transverse impedances for the SPS extraction kicker MKE.41651 with Tsutsui's kicker geometry model: horizontal (left) and vertical (right).

## 2.1. Simple model of SPS ferrite loaded kickers

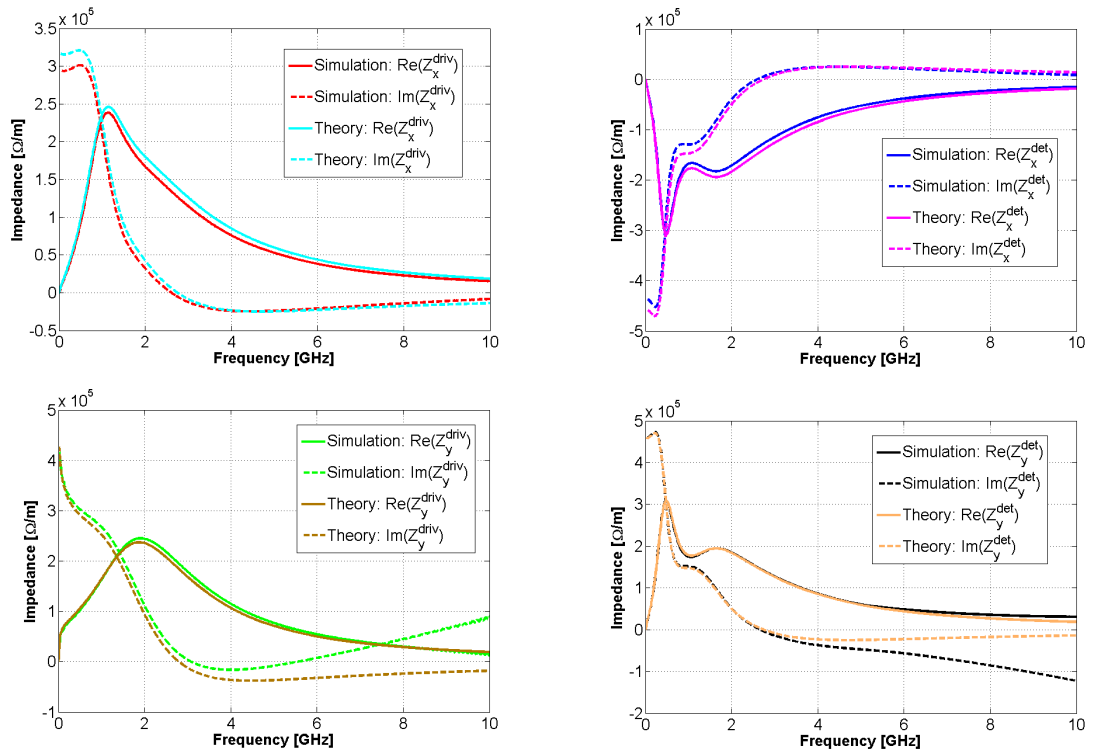


Figure 2.13: Comparison between theoretical and simulated transverse impedances for the SPS extraction kicker MKE.41651 with Tsutsui's kicker geometry model: horizontal driving (top left), vertical driving (bottom left), horizontal detuning (top right) and vertical detuning (bottom right). Real parts of the impedance are full lines, imaginary parts are dashed lines.

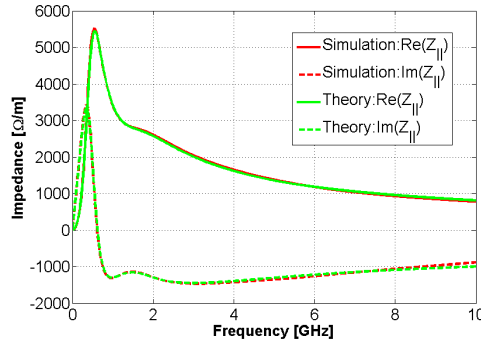


Figure 2.14: Comparison between theoretical and simulated longitudinal impedance for the SPS extraction kicker MKE.41651 with Tsutsui's kicker geometry model. Real parts of the impedance are full lines, imaginary parts are dashed lines.

these simulations can be time consuming and require a lot of memory. As a trade-off for the SPS case, we choose to use a RMS bunch length  $\sigma = 1.5$  cm (more than a factor 10 smaller with respect to the RMS bunch-length of SPS at injection energy).

In comparison with Tsutsui's theory for a single kicker (MKE.41651) made of ferrite 4A4, we

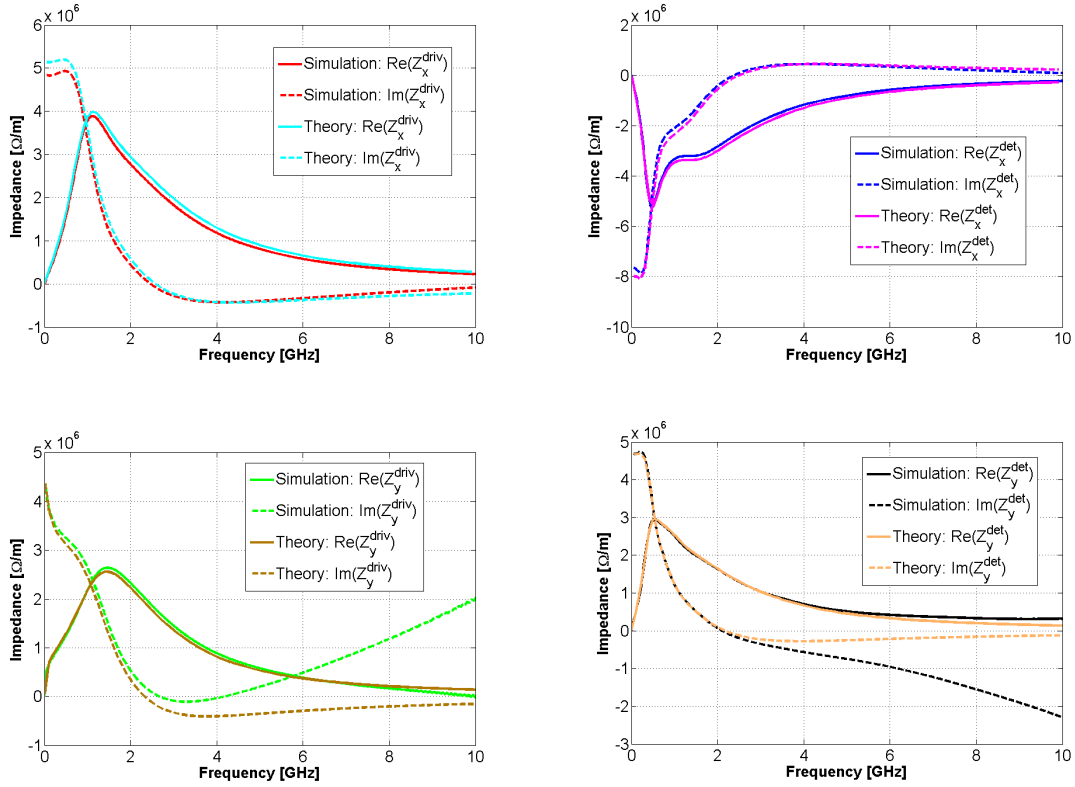


Figure 2.15: Comparison between theoretical and simulated total impedance from all SPS kickers with Tsutsui's kicker geometry model: horizontal driving (top left), vertical driving (bottom left), horizontal detuning (top right) and vertical detuning (bottom right). Real parts of the impedance are full lines, imaginary parts are dashed lines.

observe that both horizontal and vertical impedances agree very well, except for a discrepancy in the vertical imaginary driving and detuning impedance above 4GHz (see Fig. 2.13, bottom line). However, if we sum the two contributions we obtain a generalized vertical impedance in agreement with theory (see Fig. 2.16). The high frequency discrepancy between theoretical model and numerical simulations for the vertical imaginary driving and detuning impedance has been investigated in detail [40]. The differences seem to be of numerical nature: related to the transverse offset of the wake integration path with respect to the source. Fixing the source and test offset at the same value respectively for the calculation of driving and detuning impedance (see Fig. 1.5), according to Fig. 2.16, we introduce on these impedance contributions equal errors, but opposite in sign. Figure 2.17 shows the dipolar imaginary vertical impedance as a function of the source offset. It is evident that increasing the beam offset we tend to converge to the analytical behaviour also for higher frequencies (see Fig. 2.18), on the other hands we can also notice that below 3GHz, probably due to nonlinear contributions, the impedance slightly increases with the displacement. The simulation results obtained following this approach provide a plausible explanation for the high frequency discrepancy found between theory and simulations for the vertical imaginary impedance (see Fig. 2.19).

## 2.1. Simple model of SPS ferrite loaded kickers

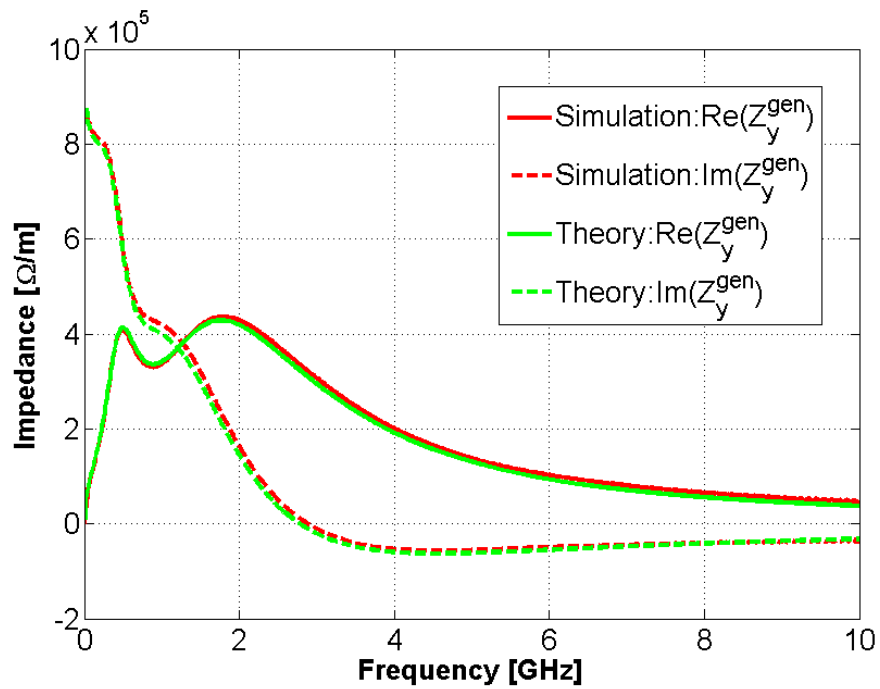


Figure 2.16: Comparison between theoretical and simulated vertical generalized impedance for the SPS extraction kicker MKE.41651 with Tsutsui's kicker geometry model. Real parts of the impedance are full lines, imaginary parts are dashed lines.

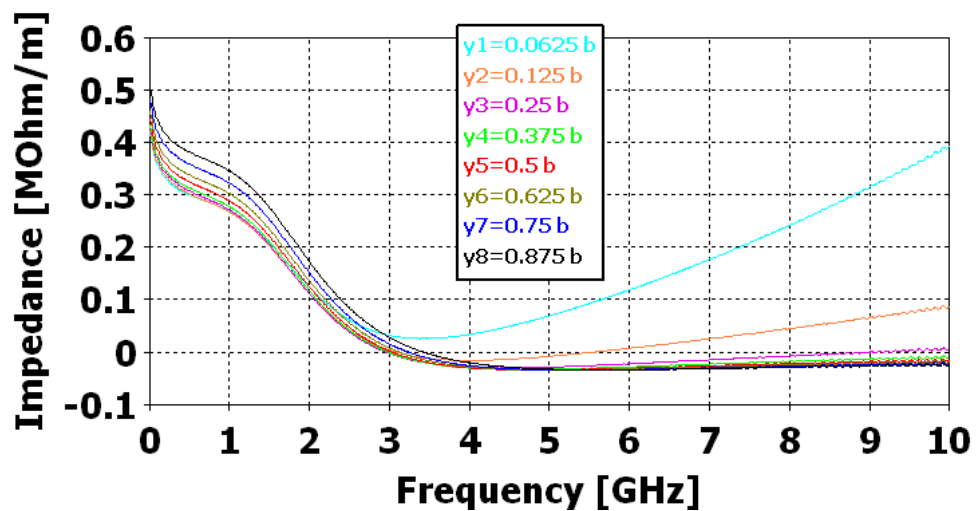


Figure 2.17: CST 3D simulations of the imaginary vertical driving impedance of the MKE.41651 kicker for different beam offsets.

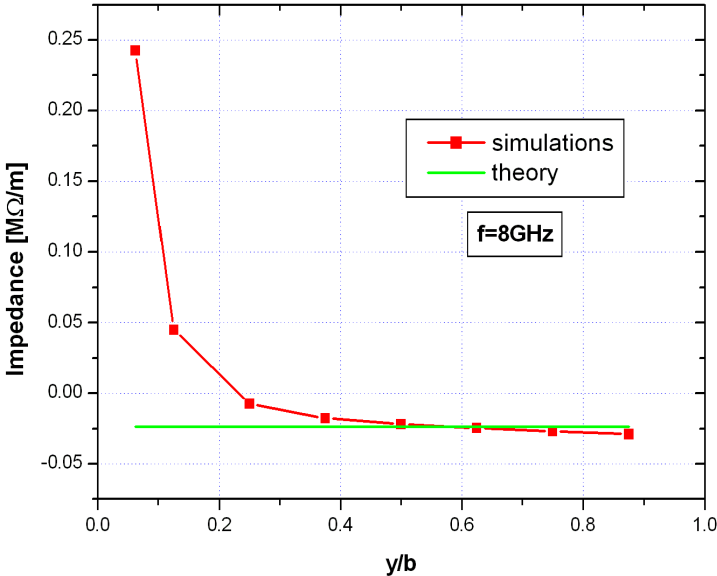


Figure 2.18: Imaginary vertical driving impedance of the MKE.41651 at 8 GHz versus the beam offset.

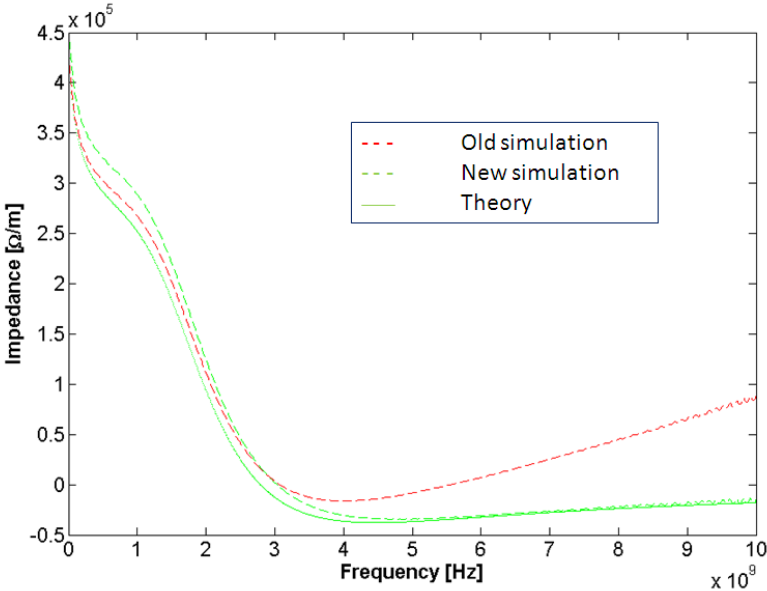


Figure 2.19: Comparing the Tsutsui's theory and CST simulations for a MKE kicker. New simulations (green dashed line) are the results obtained with a larger displacement in order to solve the high frequency discrepancy.



## 2.2 A Spectral Method for Impedance Calculation of a C-shaped ferrite loaded kicker

### 2.2.1 C-Magnet model

#### Introduction

A first approximate SPS impedance model includes the impedance contributions of the kickers by means of the Tsutsui model [29, 31] (see Fig. 2.4). Despite its simplicity, the large detuning (also called quadrupolar) term of these kickers could explain both the "negative" total horizontal impedance observed in bench measurements [41] and the positive horizontal tune shift measured with beam in SPS [42]. However in this simple model several features of the kicker magnets have been neglected. When the field penetration in the ferrite becomes comparable to the magnetic circuit length (e.g. below few hundreds of MHz for typical SPS kicker sizes), it is reasonable to expect that the connection of the top and bottom ferrite plates plays an important role in determining the kicker impedance. Therefore, to estimate correctly the kicker impedance contributions in this range of frequencies we need to use a C-Magnet or Frame-Magnet model (see Fig. 2.20). For the ferrites 4A4 and 8C11 used in SPS kickers [43] the penetration depth can be calculated and is displayed in Fig. 2.21. It is evident that below few hundreds of MHz the Tsutsui model cannot be applied: the penetration depth increases to several centimeters and becomes comparable with the distance between the two ferrite plates. Consistently with this observation, Fig. 2.22 shows a CST simulation of the driving horizontal impedance. In this Figure we can clearly see that Tsutsui and C-Magnet model are in perfect agreement above few hundreds of MHz but significantly differ at lower frequencies. A resonance is observed at 45 MHz. A much less pronounced peak is also observed in the longitudinal and in the vertical impedances at the same frequency [44]. The small peak in the longitudinal impedance was also observed in bench measurements for the MKP kickers [45] (see section 4.1.2). The C-Magnet model has no left/right symmetry. This complicates the calculation due to the constant impedance contribution [46] that has to be taken into account. In order to simplify the theoretical analysis, we can symmetrize the C-Magnet model converting it into a Frame-Magnet model. Figure 2.22 shows the comparison of the real driving horizontal impedance obtained by CST EM simulations with the two models.

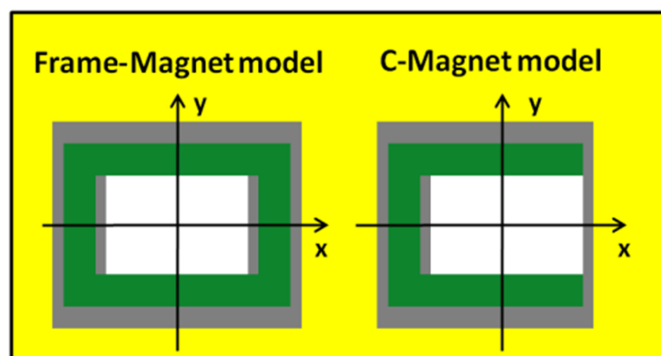


Figure 2.20: Geometric models for impedance calculation: ferrite in green, PEC in gray and vacuum in white.

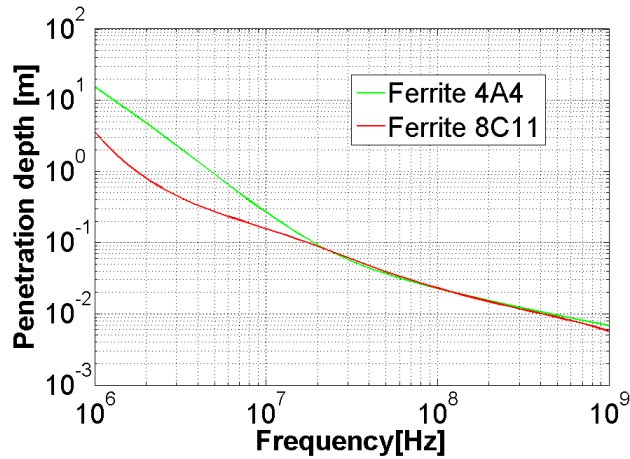


Figure 2.21: Penetration depth in ferrites 4A4 and 8C11.

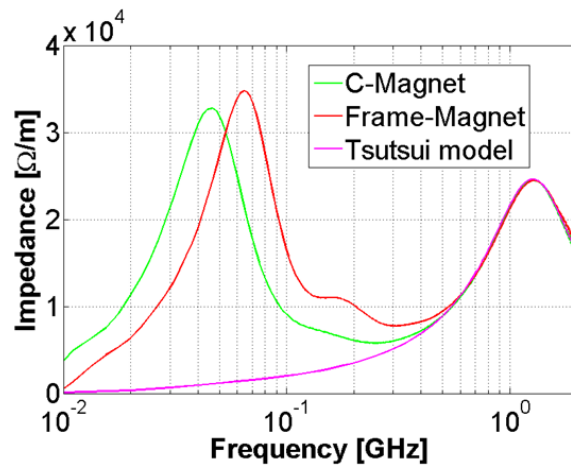


Figure 2.22: CST Simulations of the real part of the driving horizontal impedance for an MKP-L (SPS Injection kicker) module using different models.

### 2.2.2 A simplified C-Magnet model for impedance calculations

It is very interesting to calculate analytically the impedance contribution using the C-Magnet or the Frame-Magnet model. As a first step we calculate analytically the impedance of a C-Magnet kicker without the High Voltage (HV) conductor and approximating the kicker as shown in Fig. 2.23 [47]. From 3D time domain EM simulations we first checked the consistency of the round approximation of a C-Magnet [48].

#### Analytical calculation of the fields

From Maxwell's equations we can derive the EM fields for the simplified model of a C-Magnet. The model is assumed to be indefinite in the longitudinal direction. The analysis is performed in the FD and all the fields have the same behaviour in the longitudinal direction. The source term of the EM problem is point-like with charge  $q_0$ . In the TD the charge density of a source

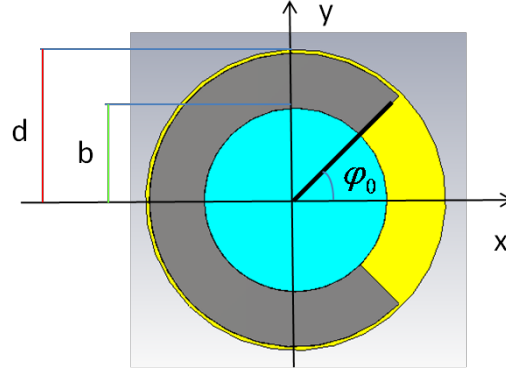


Figure 2.23: Geometric model for analytical derivation of the C-Magnet impedance: vacuum in light blue, ferrite in gray and PEC in yellow.

particle moving in the  $s$  coordinate with a velocity  $v$  placed in  $x = x_1$  and  $y = y_1$  can be written as follows:

$$\rho(x, y, s, t) = q_0 \delta(x - x_1) \delta(y - y_1) \delta(s - vt) \quad (2.3)$$

In the frequency domain we obtain:

$$\rho(x, y, s, \omega) = \frac{q_0}{v} \delta(x - x_1) \delta(y - y_1) e^{-jks} \quad (2.4)$$

The current density  $\vec{J}$  can than be written as:

$$\vec{J}(x, y, s, \omega) = q_0 \delta(x - x_1) \delta(y - y_1) e^{-jks} \vec{i}_s \quad (2.5)$$

$\vec{i}_s$  being the unit vector along the  $s$  axis. In cylindrical coordinates  $(r, \varphi, s)$  defining  $r_1$  and  $\varphi_1$  such that  $x_1 = r_1 \cos \varphi_1$  and  $y_1 = r_1 \sin \varphi_1$  the product  $\delta(x - x_1) \delta(y - y_1)$  must be replaced with  $\frac{1}{r_1} \delta(r - r_1) \delta_p(\varphi - \varphi_1)$ ,  $\delta_p$  is the  $2\pi$ -periodic Dirac distribution. Writing the equation of the propagation in vacuum:

$$\nabla^2 \vec{A} + k_0^2 \vec{A} = -\mu \vec{J} \quad (2.6)$$

$k_0 = \frac{\omega}{c}$  is the propagation constant in free space, with the following potential vector:

$$\vec{A}(x, y, s, \omega) = A_{\perp}(x, y, \omega) e^{-jks} \vec{i}_s \quad (2.7)$$

## Chapter 2. Impedance model of ferrite kickers

---

It can be shown that Eq. (2.6) is valid when:

$$\nabla^2 A_{\perp} + (k_0^2 - k^2)A_{\perp} = -\mu\rho(x, y) \quad (2.8)$$

being  $\rho(x, y) = \delta(x - x_1)\delta(y - y_1)$ . It is worth noting in Eq. (2.8) that transverse modes in vacuum are in cut-off ( $k_0^2 - k^2 < 0$ ). From the definition of the potential vector we find that also the EM fields have the dependence  $e^{-jk_s}$  (the magnetic field  $\vec{H}$  is the curl of the potential vector divided by the vacuum permeability  $\mu_0$ , the electric field  $\vec{E}$  is related to the magnetic field with the law of Ampere-Maxwell).

Using Maxwell's equations all the components of the fields are derived from the longitudinal fields of TE and TM modes. Since the current density  $\vec{J}$  is different from zero only for  $x = x_1$  and  $y = y_1$  (see Eq. (2.5)), excluding the point where is placed the source we can write Maxwell's equations in vacuum as follow:

$$\begin{aligned} \nabla \times Z_0 \vec{H}^{\nu} &= j k_0 \vec{E}^{\nu} \\ \nabla \times \vec{E}^{\nu} &= -j k_0 Z_0 \vec{H}^{\nu} \end{aligned} \quad (2.9)$$

where  $\vec{E}$ ,  $\vec{H}$  are respectively the electric and the magnetic field and  $Z_0$  is the impedance in the free space. Expanding the curl in cylindrical coordinates we obtain:

$$\begin{aligned} \frac{1}{r} \frac{\partial}{\partial \varphi} H_s^{\nu} + j k H_{\varphi}^{\nu} &= j k_0 Y_0 E_r^{\nu} \\ -\frac{\partial}{\partial r} H_s^{\nu} - j k H_r^{\nu} &= j k_0 Y_0 E_{\varphi}^{\nu} \\ \frac{1}{r} \frac{\partial}{\partial \varphi} E_s^{\nu} + j k E_{\varphi}^{\nu} &= -j k_0 Z_0 H_r^{\nu} \\ \frac{\partial}{\partial r} E_s^{\nu} + j k E_r^{\nu} &= j k_0 Z_0 H_{\varphi}^{\nu} \end{aligned} \quad (2.10)$$

and after some manipulation we finally obtain:

$$\begin{aligned} -k_0 Z_0 \frac{\partial}{\partial r} H_s^{\nu} + k \frac{1}{r} \frac{\partial}{\partial \varphi} E_s^{\nu} &= -j \frac{k_0^2}{\beta^2 \gamma^2} E_{\varphi}^{\nu} \\ -k Z_0 \frac{\partial}{\partial r} H_s^{\nu} + k_0 \frac{1}{r} \frac{\partial}{\partial \varphi} E_s^{\nu} &= j \frac{k_0^2}{\beta^2 \gamma^2} Z_0 H_r^{\nu} \\ k_0 \frac{\partial}{\partial r} E_s^{\nu} + k \frac{Z_0}{r} \frac{\partial}{\partial \varphi} H_s^{\nu} &= -j \frac{k_0^2}{\beta^2 \gamma^2} Z_0 H_{\varphi}^{\nu} \\ k \frac{\partial}{\partial r} E_s^{\nu} + k_0 \frac{Z_0}{r} \frac{\partial}{\partial \varphi} H_s^{\nu} &= -j \frac{k_0^2}{\beta^2 \gamma^2} E_r^{\nu} \end{aligned} \quad (2.11)$$

Here  $\beta$  and  $\gamma$  are the relativistic factors and  $k = \frac{k_0}{\beta}$ .

## 2.2. A Spectral Method for Impedance Calculation

Expanding in the same way Maxwell's equations in the ferrite:

$$\begin{aligned}\nabla \times Z_F \vec{H}^f &= j k_F \vec{E}^f \\ \nabla \times \vec{E}^f &= -j k_F Z_F \vec{H}^f\end{aligned}\quad (2.12)$$

we obtain the relations in the medium:

$$\begin{aligned}\frac{1}{r} \frac{\partial}{\partial \varphi} H_s^f + j k H_\varphi^f &= j k_F Y_F E_r^f \\ -\frac{\partial}{\partial r} H_s^f - j k H_r^f &= j k_F Y_F E_\varphi^f \\ \frac{1}{r} \frac{\partial}{\partial \varphi} E_s^f + j k E_\varphi^f &= -j k_F Z_F H_r^f \\ \frac{\partial}{\partial r} E_s^f + j k E_r^f &= j k_F Z_F H_\varphi^f\end{aligned}\quad (2.13)$$

and after some manipulation:

$$\begin{aligned}k_F Z_F \frac{\partial}{\partial r} H_s^f - k \frac{1}{r} \frac{\partial}{\partial \varphi} E_s^f &= -j k^2 (\beta^2 \epsilon_r \mu_r - 1) E_\varphi^f \\ k Z_F \frac{\partial}{\partial r} H_s^f - k_F \frac{1}{r} \frac{\partial}{\partial \varphi} E_s^f &= j k^2 Z_F (\beta^2 \epsilon_r \mu_r - 1) H_r^f \\ k_F \frac{\partial}{\partial r} E_s^f + k \frac{Z_F}{r} \frac{\partial}{\partial \varphi} H_s^f &= j k^2 Z_F (\beta^2 \epsilon_r \mu_r - 1) H_\varphi^f \\ k \frac{\partial}{\partial r} E_s^f + k_F \frac{Z_F}{r} \frac{\partial}{\partial \varphi} H_s^f &= j k^2 (\beta^2 \epsilon_r \mu_r - 1) E_r^f\end{aligned}\quad (2.14)$$

Here  $\epsilon_r$  and  $\mu_r$  are respectively the relative permittivity and permeability of the ferrite and:

$$\begin{aligned}Z_F &= Z_0 \sqrt{\frac{\mu_r}{\epsilon_r}} \\ k_F &= k_0 \sqrt{\epsilon_r \mu_r}\end{aligned}\quad (2.15)$$

In vacuum the EM fields are expanded in TE and TM cut-off waves expressed by modified Bessel functions of the first kind of integer order  $m$ :

$$\begin{aligned}E_s^v(r, \varphi) &= Q \sum_m A_m I_E \cos(m\varphi) \\ H_s^v(r, \varphi) &= \frac{Q}{Z_0} \sum_m B_m I_E \sin(m\varphi)\end{aligned}\quad (2.16)$$

## Chapter 2. Impedance model of ferrite kickers

---

where:

$$Q = j \frac{q_0 k_0 Z_0}{2\pi \beta^2 \gamma^2} \quad (2.17)$$

and

$$I_E = I_m \left( \frac{k_0}{\beta \gamma} r \right) \quad (2.18)$$

The other components of the fields in vacuum are derived from the Eq. (2.11) starting from the expressions of  $E_s^v(r, \varphi)$  and  $H_s^v(r, \varphi)$ :

$$\begin{aligned} E_r^v(r, \varphi) &= j \frac{\beta^2 \gamma^2 Q}{k_0} \sum_m \left[ \frac{m}{r} B_m I_E + \frac{k_0}{\beta^2 \gamma} A_m I'_E \right] \cos(m\varphi) \\ H_r^v(r, \varphi) &= j \frac{\beta^2 \gamma^2 Q}{k_0 Z_0} \sum_m \left[ \frac{m}{r} A_m I_E + \frac{k_0}{\beta^2 \gamma} B_m I'_E \right] \sin(m\varphi) \\ E_\varphi^v(r, \varphi) &= -j \frac{\beta^2 \gamma^2 Q}{k_0} \sum_m \left[ \frac{m}{r \beta} A_m I_E + \frac{k_0}{\beta \gamma} B_m I'_E \right] \sin(m\varphi) \\ H_\varphi^v(r, \varphi) &= j \frac{\beta^2 \gamma^2 Q}{k_0 Z_0} \sum_m \left[ \frac{m}{r \beta} B_m I_E + \frac{k_0}{\beta \gamma} A_m I'_E \right] \cos(m\varphi) \end{aligned} \quad (2.19)$$

In the ferrite the EM fields are expanded in TE and TM forward and backward radial waves. They can be expressed by Bessel function of order  $\nu = \frac{\pi}{2\pi - 2\varphi_0} (2n + 1)$ :

$$\begin{aligned} E_s^f(r, \varphi) &= Q \sum_m C_m J_E \sin(\nu(\varphi - \varphi_0)) \\ H_s^f(r, \varphi) &= \frac{Q}{Z_F} \sum_m D_m J_H \cos(\nu(\varphi - \varphi_0)) \end{aligned} \quad (2.20)$$

with:

$$\begin{aligned} J_E &= J_\nu(k_+ r) - Y_\nu(k_+ r) \frac{J_\nu(k_+ d)}{Y_\nu(k_+ d)} \\ J_H &= J_\nu(k_+ r) - Y_\nu(k_+ r) \frac{J'_\nu(k_+ d)}{Y'_\nu(k_+ d)} \end{aligned} \quad (2.21)$$

Eq. (2.20) satisfies the boundary conditions on  $r = d$ . Working in an analogous way the other components of the fields in ferrite are derived from the Eq. (2.14) starting from the expression

of  $E_s^f(r, \varphi)$  and  $H_s^f(r, \varphi)$ :

$$\begin{aligned}
 E_r^f(r, \varphi) &= \frac{jk_0Q}{k_+^2} \sum_m \left[ \begin{array}{l} \frac{\nu\sqrt{\epsilon_r\mu_r}}{r} D_m J_{H^-} \\ + \frac{k_+}{\beta} C_m J_E' \end{array} \right] \sin(\nu(\varphi - \varphi_0)) \\
 H_r^f(r, \varphi) &= \frac{jk_0Q}{k_+^2 Z_F} \sum_m \left[ \begin{array}{l} \frac{\nu\sqrt{\epsilon_r\mu_r}}{r} C_m J_{E^-} \\ + \frac{k_+}{\beta} D_m J_H' \end{array} \right] \cos(\nu(\varphi - \varphi_0)) \\
 E_\varphi^f(r, \varphi) &= \frac{jk_0Q}{k_+^2} \sum_m \left[ \begin{array}{l} -\frac{\nu}{r\beta} C_m J_{E^+} \\ + k_+ \sqrt{\epsilon_r\mu_r} D_m J_H' \end{array} \right] \cos(\nu(\varphi - \varphi_0)) \\
 H_\varphi^f(r, \varphi) &= \frac{jk_0Q}{k_+^2 Z_F} \sum_m \left[ \begin{array}{l} \frac{\nu}{r\beta} D_m J_{H^-} \\ + k_+ \sqrt{\epsilon_r\mu_r} C_m J_E' \end{array} \right] \sin(\nu(\varphi - \varphi_0))
 \end{aligned} \tag{2.22}$$

with:

$$k_+^2 = k_0^2 \epsilon_r \mu_r - \frac{k_0^2}{\beta^2} \tag{2.23}$$

and:

$$\begin{aligned}
 J_E' &= J_\nu'(k_+ r) - Y_\nu'(k_+ r) \frac{J_\nu(k_+ d)}{Y_\nu(k_+ d)} \\
 J_H' &= J_\nu'(k_+ r) - Y_\nu'(k_+ r) \frac{J_\nu'(k_+ d)}{Y_\nu'(k_+ d)}
 \end{aligned} \tag{2.24}$$

Equation (2.23) derives from writing the equation of propagation (Eq. (2.6)) in the ferrite.

### Matching conditions and solutions of the problem

The matching conditions are imposed on the interface between ferrite and vacuum by requiring the continuity of tangential fields and normal induction fields:

$$\begin{aligned}
 E_s^{SC} + E_s^\nu &= E_s^f & \varphi_0 \leq \varphi \leq 2\pi - \varphi_0 \\
 H_s^\nu &= H_s^f & r = b \\
 B_r^\nu &= B_r^f \\
 D_r^{SC} + D_r^\nu &= D_r^f
 \end{aligned} \tag{2.25}$$

where with the apex *SC* we represent the source fields. Resorting to the Ritz-Galerkin method, the functional equations (2.25) are transformed into an infinite set of linear equations using

the following projection matrix:

$$\begin{aligned}
 (M_H^v)_{m,n} &= \int_{\phi_0}^{2\pi-\phi_0} \cos[v(\phi-\phi_0)] \sin[m\phi] d\phi \\
 (M_E^v)_{m,n} &= \int_{\phi_0}^{2\pi-\phi_0} \sin[v(\phi-\phi_0)] \cos[m\phi] d\phi \\
 (M_H^f)_{m,n} &= \int_{\phi_0}^{2\pi-\phi_0} \cos[v_n(\phi-\phi_0)] \cos[v_m(\phi-\phi_0)] d\phi \\
 (M_E^f)_{m,n} &= \int_{\phi_0}^{2\pi-\phi_0} \sin[v_n(\phi-\phi_0)] \sin[v_m(\phi-\phi_0)] d\phi
 \end{aligned} \tag{2.26}$$

After some manipulation we can write the final set of equations as follows:

$$\begin{aligned}
 M_{11}\hat{A} + M_{12}\hat{B} &= N_1 \\
 M_{21}\hat{A} + M_{22}\hat{B} &= N_2 \\
 \begin{pmatrix} M_{11} & M_{12} \\ M_{21} & M_{22} \end{pmatrix} \begin{pmatrix} \hat{A} \\ \hat{B} \end{pmatrix} &= \begin{pmatrix} N_1 \\ N_2 \end{pmatrix}
 \end{aligned} \tag{2.27}$$

where:

$$\begin{aligned}
 \hat{B} &= B I_E \\
 \hat{A} &= A I_E
 \end{aligned} \tag{2.28}$$

are the unknown vectors, and:

$$\begin{aligned}
 M_{11} &= \frac{2}{k_0 b} \left[ \beta^2 \gamma^2 M_H^v D_M - \frac{k_F^2}{k_+^2} D_N M_E^v \right] \\
 M_{12} &= \left[ \gamma M_H^v (I_E^- + I_E^+) I_E^{-1} + \frac{\mu_r k_0}{\beta k_+} (J_H^- - J_H^+) J_H^{-1} M_H^v \right] \\
 M_{21} &= \left[ \gamma M_E^v (I_E^- + I_E^+) I_E^{-1} + \frac{\epsilon_r k_0}{\beta k_+} (J_E^- - J_E^+) J_E^{-1} M_E^v \right] \\
 M_{22} &= \frac{2}{k_0 b} \left[ \beta^2 \gamma^2 M_E^v D_M - \frac{k_F^2}{k_+^2} D_N M_H^v \right]
 \end{aligned} \tag{2.29}$$



where:

$$\begin{aligned}
 (D_M)_{m,n} &= m \\
 (D_N)_{m,n} &= v \\
 (J_E^-)_{m,n} &= I_{m-1} \left( \frac{k_0}{\beta\gamma} r \right) \\
 (J_E^+)_{m,n} &= I_{m+1} \left( \frac{k_0}{\beta\gamma} r \right) \\
 (J_E^-)_{m,n} &= \left( J_{v-1}(k_+ r) - Y_{v-1}(k_+ r) \frac{J_v(k_+ d)}{Y_v(k_+ d)} \right) \\
 (J_E^+)_{m,n} &= \left( J_{v+1}(k_+ r) - Y_{v+1}(k_+ r) \frac{J_v(k_+ d)}{Y_v(k_+ d)} \right) \\
 (J_H^-)_{m,n} &= \left( J_{v-1}(k_+ r) - Y_{v-1}(k_+ r) \frac{J'_v(k_+ d)}{Y'_v(k_+ d)} \right) \\
 (J_H^+)_{m,n} &= \left( J_{v+1}(k_+ r) - Y_{v+1}(k_+ r) \frac{J'_v(k_+ d)}{Y'_v(k_+ d)} \right)
 \end{aligned} \tag{2.30}$$

The projection matrices of the fields in ferrite disappear in the final set because:

$$M_E^f = M_H^f = (\pi - \phi_0) I \tag{2.31}$$

To overcome numerical limitations the modified Bessel function I is expressed as a finite sum of zeros:

$$\begin{aligned}
 I_n(z) &= \frac{z^n}{2^n n!} \prod_{k=1}^{\infty} \left[ 1 + \left( \frac{z}{j_{nk}} \right)^2 \right] \\
 z \frac{I'_n(z)}{I_n(z)} &= z \frac{d}{dz} [\ln I_n(z)] = n + 2 \sum_{k=1}^{\infty} \frac{z^2}{j_{nk}^2 + z^2}
 \end{aligned} \tag{2.32}$$

By means of an ad-hoc truncation of matrices and vectors the linear set of Eq. (2.27) can be solved. We get the following expressions for the unknown vectors:

$$\begin{aligned}
 \hat{B} &= [M_{22} - M_{21} M_{11}^{-1} M_{12}]^{-1} [N_2 - M_{21} M_{11}^{-1} N_1] \\
 \hat{A} &= [M_{11} - M_{12} M_{22}^{-1} M_{21}]^{-1} [N_1 - M_{12} M_{22}^{-1} N_2]
 \end{aligned} \tag{2.33}$$

where  $N_1$  and  $N_2$  are related to the source fields. The sources are represented by linear currents placed at the points  $P_n(r_n, \varphi_n)$  (Eq. (2.5) in cylindrical coordinates). The longitudinal field is computed in the points  $P(r, \varphi)$ . The longitudinal electric field created by a cylindrically shaped source placed in  $P_n(r_n, \varphi_n)$  with charge density uniformly distributed on its surface in

## Chapter 2. Impedance model of ferrite kickers

---

the limit of  $r_n \rightarrow 0$  can be written in the following way:

$$E_s^{SC}(r, r_n, \varphi, \varphi_n) = Q \sum_n K_0 \left( \frac{k_0 R_n}{\beta \gamma} \right) \quad (2.34)$$

where  $K_0$  is the modified Bessel function of order 0 and:

$$R_n = \sqrt{r^2 + r_n^2 - 2rr_n \cos(\varphi - \varphi_n)} \quad (2.35)$$

The other components of the source fields are derived from the Eq. (2.10). We get:

$$\begin{aligned} H_\varphi^{SC}(r, \varphi) &= j \frac{Q\beta\gamma}{Z_0} \sum_n K'_0 \left( \frac{k_0 R_n}{\beta \gamma} \right) \\ E_r^{SC}(r, \varphi) &= jQ\gamma \sum_n K'_0 \left( \frac{k_0 R_n}{\beta \gamma} \right) \end{aligned} \quad (2.36)$$

### Impedance derivation

The structure analyzed has no left/right symmetry. Therefore the transverse horizontal impedance is different from zero even when the beam passes in the geometric center. Thus beside the classical longitudinal and transverse (driving and detuning) impedance [49], also a so called constant term [50] must be derived. For the longitudinal impedance the source will consist of only one linear current placed on axis. From Eq. (2.34) we obtain the following expression of the source field:

$$E_s^{SC}(r, 0, \varphi, 0) = QK_0 \left( \frac{k_0 r}{\beta \gamma} \right) \quad (2.37)$$

The other components of the source fields are derived from the Eqs 2.35 and 2.36. We obtain:

$$\begin{aligned} H_\varphi^{SC}(r, \varphi) &= j \frac{Q\beta\gamma}{Z_0} K'_0 \left( \frac{k_0 r}{\beta \gamma} \right) \\ E_r^{SC}(r, \varphi) &= jQ\gamma K'_0 \left( \frac{k_0 r}{\beta \gamma} \right) \end{aligned} \quad (2.38)$$

Applying the matching conditions (2.25) and writing the system (2.27) we obtain the following expression for  $N_1$  and  $N_2$  :

$$\begin{aligned} N_1 &= \frac{2}{k_0 b} \frac{k_F^2}{k_+^2} D_N M_E^v K_0 \left( \frac{k_0 b}{\beta \gamma} \right) \\ N_2 &= -2\gamma M_E^v K'_0 \left( \frac{k_0 b}{\beta \gamma} \right) - \varepsilon_r \frac{k_0}{k_+} \frac{1}{\beta} (J_E^- - J_E^+) J_E^{-1} M_E^v K_0 \left( \frac{k_0 b}{\beta \gamma} \right) \end{aligned} \quad (2.39)$$

## 2.2. A Spectral Method for Impedance Calculation

and from  $E_s^v$  calculated in  $r = 0$  and  $\varphi = 0$  the classical longitudinal impedance per unit length is obtained (see Eq. (1.3)):

$$\frac{Z_{//}}{L} = \frac{Q}{q_0} A_0 \quad (2.40)$$

For the driving impedance the source will consist of two linear currents placed in the points  $P_1(r_1, 0)$  and  $P_2(r_1, \pi)$  for the horizontal impedance and  $P_1(r_1, \frac{\pi}{2})$  and  $P_2(r_1, \frac{3\pi}{2})$  for the vertical impedance. From the theorem of Gegenbauer [51] we can write:

$$\begin{aligned} K_0(R) &= K_0(r) I_0(r_n) + \\ &+ 2 \sum_m K_m(r) I_m(r_n) \cos[m(\varphi - \varphi_n)] \quad r \geq r_n \\ K_0(R) &= 2 \sum_m K_m(r_n) I_m(r) \cos[m(\varphi - \varphi_n)] \quad r \leq r_n \end{aligned} \quad (2.41)$$

Then we write the longitudinal source field for the driving horizontal (Eq. (2.42)) and vertical (Eq. (2.43)) impedance in the following way:

$$\begin{aligned} E_s^{SC+}(r, r_1, \varphi, 0) &= Q K_0(r) I_0(r_1) + \\ &+ 2Q \sum_m K_m\left(\frac{k_0 r}{\beta\gamma}\right) I_m\left(\frac{k_0 r_1}{\beta\gamma}\right) \cos[m(\varphi)] \\ E_s^{SC-}(r, r_1, \varphi, \pi) &= -Q K_0(r) I_0(r_1) - \\ &+ 2Q \sum_m (-1)^m K_m\left(\frac{k_0 r}{\beta\gamma}\right) I_m\left(\frac{k_0 r_1}{\beta\gamma}\right) \cos[m(\varphi)] \end{aligned} \quad (2.42)$$

$$\begin{aligned} E_s^{SC+}\left(r, r_1, \varphi, \frac{\pi}{2}\right) &= Q K_0(r) I_0(r_1) + \\ &+ 2Q \sum_m K_m\left(\frac{k_0 r}{\beta\gamma}\right) I_m\left(\frac{k_0 r_1}{\beta\gamma}\right) \cos\left[m\left(\varphi - \frac{\pi}{2}\right)\right] \\ E_s^{SC-}\left(r, r_1, \varphi, \frac{3\pi}{2}\right) &= -Q K_0(r) I_0(r_1) - \\ &+ 2Q \sum_m (-1)^m K_m\left(\frac{k_0 r}{\beta\gamma}\right) I_m\left(\frac{k_0 r_1}{\beta\gamma}\right) \cos\left[m\left(\varphi - \frac{\pi}{2}\right)\right] \end{aligned} \quad (2.43)$$

From the sum of the field we get the following equations respectively for horizontal and vertical driving impedance:

$$\begin{aligned} E_s^{SC+}(r, r_1, \varphi, 0) + E_s^{SC-}(r, r_1, \varphi, \pi) &= \\ = 2Q \sum_m [1 - (-1)^m] K_m\left(\frac{k_0 r}{\beta\gamma}\right) I_m\left(\frac{k_0 r_1}{\beta\gamma}\right) \cos[m(\varphi)] \end{aligned} \quad (2.44)$$

$$\begin{aligned}
 E_s^{SC+} \left( r, r_1, \varphi, \frac{\pi}{2} \right) + E_z^{SC-} \left( r, r_1, \varphi, \frac{3\pi}{2} \right) &= \\
 = 2Q \sum_m [1 - (-1)^m] K_m \left( \frac{k_0 r}{\beta \gamma} \right) I_m \left( \frac{k_0 r_1}{\beta \gamma} \right) \cos \left[ m \left( \varphi - \frac{\pi}{2} \right) \right] &
 \end{aligned} \tag{2.45}$$

By taking the limit for  $r_1 \rightarrow 0$  keeping constant the following quantity:

$$Q_p = j \frac{p k_0 Z_0}{2\pi \beta^2 \gamma^2} \tag{2.46}$$

with  $p = q_0 2r_1$  we obtain the longitudinal source fields for horizontal (Eq. (2.47)) and vertical driving impedance (Eq. (2.48)):

$$E_s^{SC/hor} (r, \varphi) = Q_p \frac{k_0}{\beta \gamma} K_1 \left( \frac{k_0 r}{\beta \gamma} \right) \cos \varphi \tag{2.47}$$

$$E_s^{SC/ver} (r, \varphi) = Q_p \frac{k_0}{\beta \gamma} K_1 \left( \frac{k_0 r}{\beta \gamma} \right) \sin \varphi \tag{2.48}$$

From the Eq. (2.11) we write the other components of the source fields respectively for horizontal and vertical driving impedance:

$$\begin{aligned}
 H_\varphi^{SC/hor} (r, \varphi) &= j \frac{Q_p k_0}{Z_0} K_1' \left( \frac{k_0 r}{\beta \gamma} \right) \cos \varphi \\
 E_r^{SC/hor} (r, \varphi) &= j Q_p \frac{k_0}{\beta} K_1' \left( \frac{k_0 r}{\beta \gamma} \right) \cos \varphi
 \end{aligned} \tag{2.49}$$

$$\begin{aligned}
 H_\varphi^{SC/ver} (r, \varphi) &= j \frac{Q_p k_0}{Z_0} K_1' \left( \frac{k_0 r}{\beta \gamma} \right) \sin \varphi \\
 E_r^{SC/ver} (r, \varphi) &= j Q_p \frac{k_0}{\beta} K_1' \left( \frac{k_0 r}{\beta \gamma} \right) \sin \varphi
 \end{aligned} \tag{2.50}$$

Then applying the matching conditions of Eq. (2.25) and writing the set (2.27) for the driving horizontal impedance we obtain the following expression for  $N_1$  and  $N_2$  :

$$\begin{aligned}
 N_1 &= \frac{2}{b \beta \gamma} \frac{k_F^2}{k_+^2} D_N M_E^v K_1 \left( \frac{k_0 r}{\beta \gamma} \right) \\
 N_2 &= -2 \frac{k_0}{\beta} M_E^v K_1' \left( \frac{k_0 b}{\beta \gamma} \right) - \epsilon_r \frac{k_0^2}{k_+} \frac{1}{\beta^2 \gamma} (J_E^- - J_E^+) J_E^{-1} M_E^v K_1 \left( \frac{k_0 b}{\beta \gamma} \right)
 \end{aligned} \tag{2.51}$$

## 2.2. A Spectral Method for Impedance Calculation

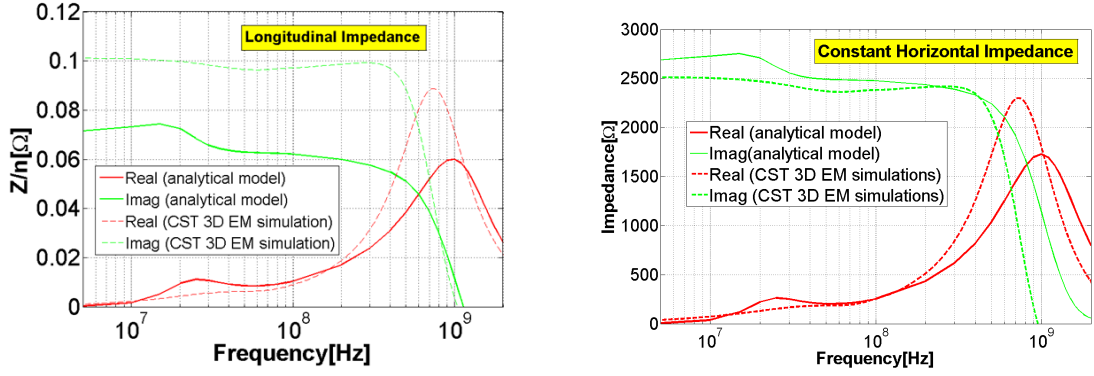


Figure 2.24: Comparison between the analytical model and CST 3D EM simulation for the longitudinal impedance (left) and horizontal constant impedance (right) ( $b=0.02$  cm,  $d=0.04$  cm,  $\varphi_0 = \pi/4$ ).

Similarly it is possible to obtain the same quantities for the vertical impedance. The driving horizontal transverse impedance is then calculated as follows (see Eq. (1.18)):

$$-j \frac{Z_x^{\text{driv}}}{L} = \frac{1}{p} \left[ E_r^v - \beta Z_0 H_\varphi^v \right]_{r=0} = \frac{j Q_p}{2 p \gamma} A_1 \quad (2.52)$$

For detuning and constant impedance the source is the same as for the longitudinal impedance. We obtain the following expressions respectively for detuning and constant impedance:

$$\frac{Z_\perp^{\text{det}}}{L} = \frac{Q k_0}{4 q_0 \beta \gamma^2} (A_0 + A_2) \quad (2.53)$$

$$\frac{Z_\perp^{\text{const}}}{L} = \frac{Q}{2 q_0 \gamma} A_1 \quad (2.54)$$

### Numerical results

For one case ( $\varphi_0 = \pi/4$ ) we show all the impedances compared with the results obtained from the 3D EM code CST Particle Studio (see Figs. 2.24 and 2.25). The longitudinal impedance is normalized to the revolution frequency of the SPS. We can see that for all the impedances the analytical calculations show qualitatively the same behaviour as the CST simulations with some quantitative differences (20-40% for the imaginary part and a shift to higher frequency for the peak on the real part). The differences between simulations and analytical model could be due to the approximation of round structures with hexahedral meshes.

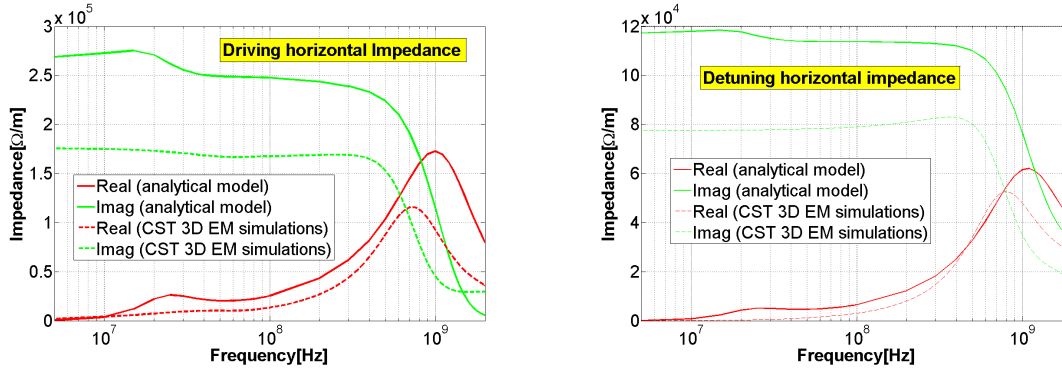


Figure 2.25: Comparison between the analytical model and CST 3D EM simulation for the horizontal driving (left) and detuning (right) impedances ( $b=0.02$  cm,  $d=0.04$  cm,  $\varphi_0 = \pi/4$ ).

### 2.3 Effect of the TEM mode on the kicker impedance

A device of finite length inserted in the vacuum tank and equipped with an inner conductor can support propagation of a Quasi-TEM mode when interacting with the beam. The device behaves as a transmission line formed by the vacuum tank and the inner conductor which are continued on the external cables and closed on the appropriate circuit terminations. The TEM mode affects the impedance below a certain frequency (when the field penetration in the ferrite becomes comparable to the magnetic circuit length). This behaviour disappears as soon as we allow for 2-D geometries (infinite in the longitudinal direction) because the transverse TEM mode arises at the discontinuities. For this reason, if we want to take into account the interaction of the beam with the TEM mode, we must resort to a 3D C-Magnet model. Following the results of the section 2.1 the calculation of the impedance contribution of kicker magnets have been based on the so called Tsutsui model [29, 30, 31]. Since this model cannot support TEM mode, it is expected to be valid only above a certain frequency (when the TEM mode has no effect because the penetration depth in the ferrite is small compared to the magnetic circuit length [47]). Contrary to the Tsutsui model the C-Magnet model (CMM) (see Fig. 2.20) can support a TEM mode but as described before its effect on the impedance disappears if we do not account for finite length. All the contributions to the impedance (constant, driving, detuning, longitudinal) of a 2-D model of the C-Magnet without inner conductor were calculated in the previous section. To take into account the TEM impedance contribution this model should be modified including the effect of the inner conductor (which complicates the field matching conditions) and the finite length resorting to a mode matching technique. Since already in [47] the calculation was very complicated and we had to find a trade-off between several numerical issues we decided to resort to a circuit model for the calculation of this TEM impedance contribution. In 1979 Sacherer and Nassibian [52] calculated the TEM impedance contribution for longitudinal and dipolar horizontal impedances for the CMM. Starting from this study we reviewed this calculation including also the non TEM contribution. We calculated all the impedance terms for the CMM and successfully benchmarked the results with EM simulations.

We also investigated the possibility of using the Laslett transmission line equations [53] to calculate the TEM contribution to the kicker impedance. In Ref. [53] Laslett treated the EM problem of a rectangular vacuum chamber that extends horizontally from  $x = 0$  to  $x = w$  and vertically between the limits  $y = \pm \frac{h}{2}$  with electrodes at  $y = \pm(\frac{h}{2} - T)$  that extend across the full width of the chamber. While this model seems to be very promising to be applied for the theoretical calculation of the beam coupling impedance of a stripline kicker, for the calculation of the TEM contribution of the ferrite loaded kicker we found the model of Sacherer and Nassibian [52] more suitable.

### 2.3.1 Theoretical model

The broadband beam coupling impedance of the CMM kicker of Fig. 2.20 is calculated using the superposition of the effects. Indeed for these devices the impedance arises from core losses and coupling to the external circuits through the kicker supply line. The first contribution can be easily calculated applying to the Tsutsui model (see Fig. 2.4). In this approximation the core losses could be underestimated because we neglect the additional ferrite block of the CMM with respect to the Tsutsui simplified structure. This effect should be negligible because at high frequency the penetration depth in the ferrite becomes so small that the Tsutsui model approximates perfectly the CMM and at low frequency the core losses become negligible as the ferrite is transparent for the beam. The second contribution due to the coupling to the external circuit, that we called TEM contribution, can be calculated by approximating the kicker as an ideal transformer as explained in [54], where a circuit model was applied for the calculation of the transverse beam coupling impedance of a frame-magnet in the kick direction. The results obtained in [54] differ from the results obtained in [52] in the imaginary part. We calculated the longitudinal and transverse impedances of a C-Magnet kicker following the same approach of Ref. [54]. The C-Magnet kicker has also a constant term [46] (the horizontal impedance is different from zero also when the beam is in the geometrical center of the structure) because it has no left/right symmetry.

#### Total impedance of a kicker

Since we separated the core losses contribution from the TEM contribution, the total impedances of the kicker (longitudinal, constant, driving and detuning) can be obtained applying the superposition of the effects as:

$$Z^{\text{kicker}} = Z_{\text{TEM}} + Z_{\text{M}} \quad (2.55)$$

where  $Z_{\text{TEM}}$  is the impedance contribution due to the TEM propagation and  $Z_{\text{M}}$  the impedance contribution due to core losses. Figure 2.26 shows the equivalent circuit of our model.

#### TEM impedance contributions

In order to have a full characterization in terms of beam coupling impedance we are interested in knowing the longitudinal and transverse (horizontal and vertical) driving and detuning impedances [46] of the kicker magnet due to the TEM propagation. As calculated in [52] the

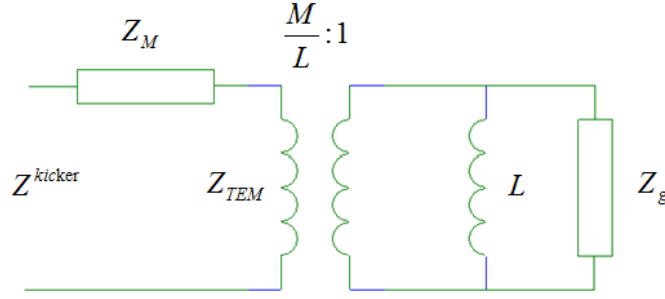


Figure 2.26: Circuit model of the kicker including cables.  $L$  is the inductance of the magnet circuit,  $Z_g$  the external impedance including cables,  $M$  the mutual inductance of the magnet.

mutual inductance  $M$  for a C-Magnet of constant gap  $2b$  is given by:

$$M = \frac{(x+a)\mu_0 l}{2b} \quad (2.56)$$

where  $x$  is the beam position,  $a$  and  $b$  are respectively the horizontal and vertical half aperture of the magnet,  $l$  is the kicker length and  $\mu_0$  is the vacuum permeability. The TEM contribution to the longitudinal impedance can be then calculated from the circuit model of Fig. 2.26:

$$Z_L = Z_{TEM}|_{x=0} = \frac{M^2}{L^2} \frac{j\omega LZ_g}{j\omega L + Z_g}|_{x=0} = \frac{1}{4} \frac{j\omega LZ_g}{j\omega L + Z_g} \quad (2.57)$$

The horizontal driving impedance is calculated from the longitudinal impedance as follows [52]:

$$Z_x = \frac{c}{\omega a^2} Z_L = \frac{c}{4\omega a^2} \frac{j\omega LZ_g}{j\omega L + Z_g} \quad (2.58)$$

The vertical driving impedance is related only to core losses since it is not coupled to the external circuit. For the same reasons also the detuning vertical and horizontal impedances are considered to be zero. The constant impedance [46] of the CMM can be calculated from the longitudinal impedance using the Panofsky-Wenzel theorem [55]:

$$Z_{\text{const}} = \frac{c}{4\omega a} \frac{j\omega LZ_g}{j\omega L + Z_g} \quad (2.59)$$

The model allows for any longitudinal boundary condition,  $Z_g$  can be changed in order to implement different boundary conditions and the effect of external cables can be easily included.



### Core losses contributions

As previously said the core losses contribution (see Fig. 2.26) to the coupling impedance is well approximated by the Tsutsui model [29]. Longitudinal, driving and detuning horizontal and vertical impedances are calculated in [29, 31, 35].

### 2.3.2 Comparison With 3-D Simulations

The model is brought into comparison with the results of the Wakefield solver of CST Microwave Studio. In the simulations, to account also for the finite length, the simulation box (vacuum tank) is longer than the kicker length and is terminated with a Perfectly Matched Layer (PML) boundary condition. Then in order to compare with the CST simulations in our model the kicker is terminated at both ends with its frequency dependent characteristic impedance:

$$Z_g = Z_0 \sqrt{\frac{\mu_{\text{eff}}}{\epsilon_{\text{eff}}}} \quad (2.60)$$

where  $Z_0$  is the free space impedance and  $\mu_{\text{eff}}$  and  $\epsilon_{\text{eff}}$  are calculated as the effective permeability and permittivity of the kicker magnet approximated as an equivalent microstrip [56]. Figure 2.27 shows the comparison between the CST simulations and our model for an MKP module in the CMM approximation. The simulation and the theoretical model are in very good agreement over the whole explored frequency range. The small difference below 200 MHz could be related to the TEM approximation of the Quasi-TEM mode supported by the kicker module. Figure 2.28 shows the longitudinal impedance of an MKP module in the CMM approximation. Also in this case our model is in very good agreement with the CST simulations. The good agreement in the low frequency peak (around 55 MHz) is remarkable. This peak is related to the contribution of the TEM mode to the longitudinal impedance (see Eq. 2.57).

### 2.3.3 Effect of the external circuits

The ejection kicker (EK) of the PSB is analyzed as an example of interest for our model. In the PSB the cables that connect the kicker to the generator are not as long as in the SPS, where the cables are roughly 200 meters, and can then determine resonances at frequencies relatively high (few MHz). The external impedance including cables can be calculated resorting to the transmission line theory. Figure 2.29 shows the dipolar horizontal impedance of the ejection kicker of the PSB calculated when the kicker is matched at one side and open circuited at the other side and when the kicker is open circuited at both sides. The first resonance appears at 1.5 and 1.65 MHz. A head-tail horizontal instability is observed in the PSB when the feedback system is switched off. The resistive wall impedance is considered a good candidate as possible source of this instability [57]. Anyway a line at 1.65 MHz had been singled out on a spectrum analyzer during instability measurements at the PSB [58]. Moreover HEADTAIL simulations with a narrow band resonator at 1.6MHz seems to reproduce much better the instability intra-bunch pattern with respect to the resistive wall [58]. Therefore the driving source of this instability could also be a low frequency narrow-band resonance. Consistently with instability

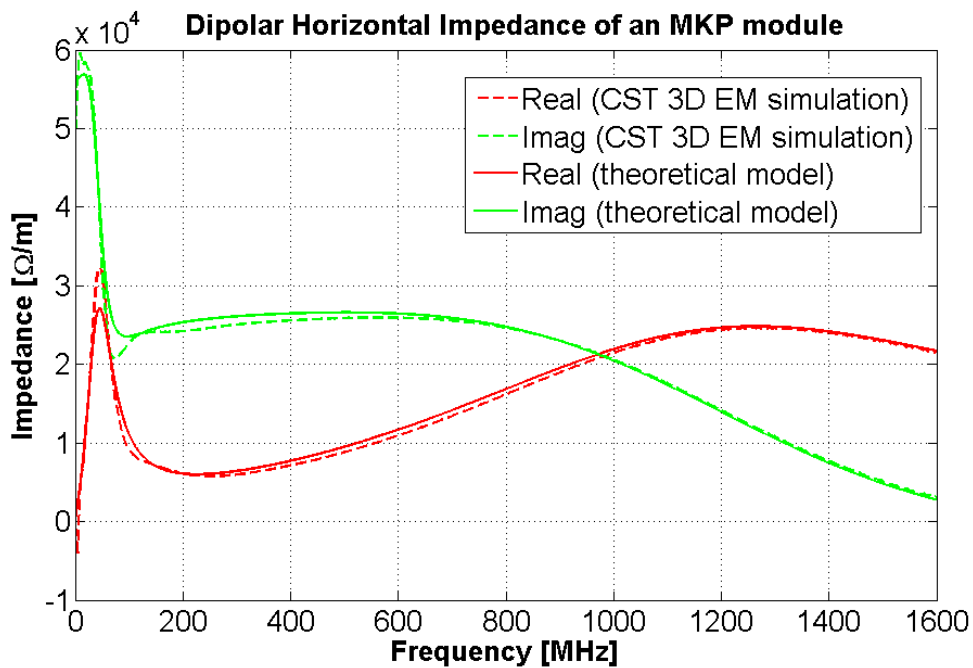


Figure 2.27: Comparison of the driving horizontal impedance for an MKP-L module of CST 3D TD simulations (dashed lines) with the theoretical model (full lines).

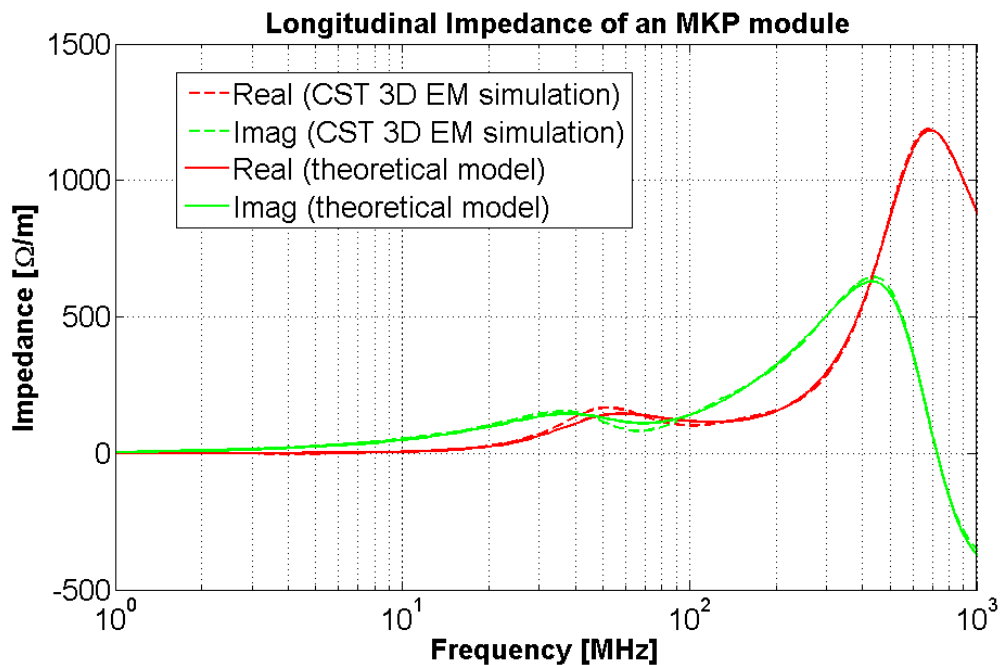


Figure 2.28: Comparison of the longitudinal impedance for an MKP-L module of CST 3D TD simulations (dashed lines) with the theoretical model (full lines).

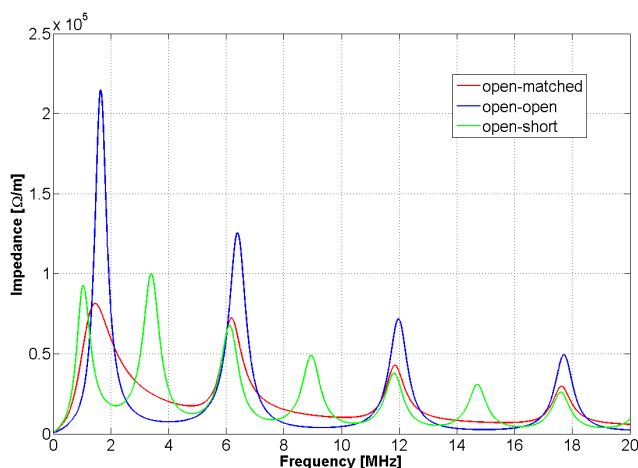


Figure 2.29: Driving horizontal impedance of the PSB EK including external cables open terminated at one end and matched, open or short terminated at the other end.

measurements, HEADTAIL simulations and theoretical predictions, the first resonance due to unmatched terminations of the ejection kicker is a good candidate. The frequency values found in the model only depend on cable length and characteristic impedance. The height and width of the peaks depend on the cable attenuation that is considered to be 0.1dB/m in the calculation.

## 2.4 Realistic model of SPS ferrite loaded kickers

The SPS consists of 19 kickers (see Tab. 2.1) divided as follows: two tune measurement kickers (MKQ), five dump kickers (MKD), four injection kickers (MKP: three of type S (smaller aperture) and one of type L (larger aperture)) and eight extraction kickers (MKE: five of type L (larger aperture) and three of type S (smaller aperture)). In a very simple approximation a SPS ferrite loaded kicker can be modelled as two parallel plates of ferrite (see Fig. 2.4). For this simple geometrical model all the impedance terms (longitudinal, driving and detuning horizontal and vertical impedances) have been calculated analytically in [29, 31, 35]. As described in section 3.1.3 CST 3D simulations were found to be in very good agreement with the existing models [29, 31] and exactly predicted the detuning (also called quadrupolar) impedance of these devices [35]. The excellent agreement between analytical model and numerical simulations also shown in [41] can be read as an important benchmark for the simulation code in the correct solution of electromagnetic problems involving dispersive materials such a ferrite. In the frame of an improvement of the kicker impedance model we performed a step by step simulation study starting from the simplest model and introducing one by one the new features that make the model gradually closer to reality. This approach allows for a good understanding of the different contributions brought to the kicker impedance by the different aspects. First, as described in section 2.2, the ferrite is assumed to be C-shaped and the whole finite length device is inserted in the vacuum tank and equipped with an inner conductor [59] (see section 2.3).

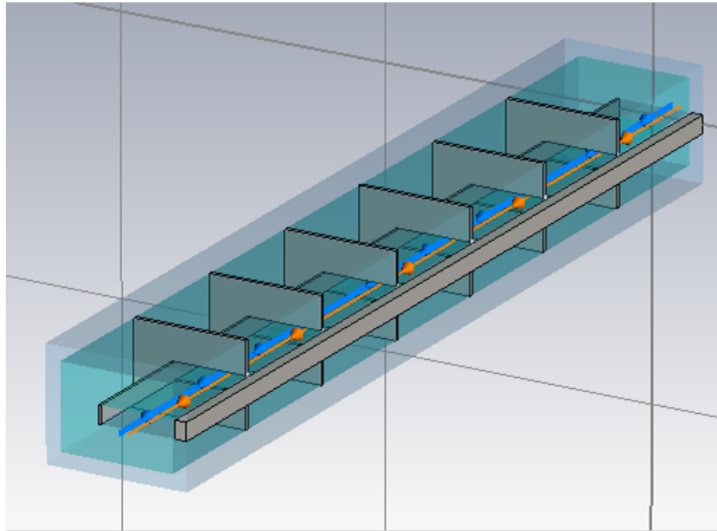


Figure 2.30: Simulation model of the SPS extraction kicker without serigraphy. The kicker is divided into 7 cells.

In order to further approach a more realistic model other aspects have to be included: the cell longitudinal structure, also called segmentation (see Fig. 2.30), the non ideal terminations, etc. An important simulation effort was devoted to the estimation of the impedance contribution of the SPS extraction kickers. Due to heating issues [60] the original design of these kickers was modified [37]. Interleaved fingers were printed by serigraphy directly on the ferrite (see Fig. 2.31). Presently only one of the 8 SPS extraction kickers (MKE) is still without serigraphy. Serigraphy represents yet one more complication in the EM modeling of this type of kickers.

### 2.4.1 Effect of the longitudinal segmentation

The first transmission-line kicker magnet was developed at CERN in the early 1960s to overcome the long rise-time [61]. A transmission-line magnet consists of several cells to approximate a broadband coaxial cable (see Fig. 2.32). C-cores ferrite magnet are sandwiched between high voltage (HV) capacitance plates. Plates connected to ground are interleaved between the HV plates: the HV and ground plates form a capacitor to ground (Fig. 2.32). One C-core, together with its HV and ground capacitance plates, is named a cell [62]. The impact of segmentation in cells on the beam coupling impedance has been studied in detail. In the frequency range of interest (from few tens of MHz up to few GHz) for the SPS impedance model, the segmentation is found to have a significant effect only on the injection kickers (MKPs). For the other kickers (MKD and MKE) the effect of the segmentation is negligible since the wavelength is sufficiently small compared to the cell length  $l$  (see Fig. 2.33). The 3-D simulation model of the SPS injection kickers (MKPs) is illustrated in Fig. 2.34. Except for the MKPC11952, divided into 17 cells, the other MKPs have modules divided into 22 cells, each of 26 mm length. In the MKP-S the cell includes a 61.2 nH series inductance, and a cell capacitance of 220 pF. There is also a resistance of approximately 47  $\Omega$  in parallel with the inductance. The cell capacitance has a parasitic inductance estimated to be 100 nH. In the

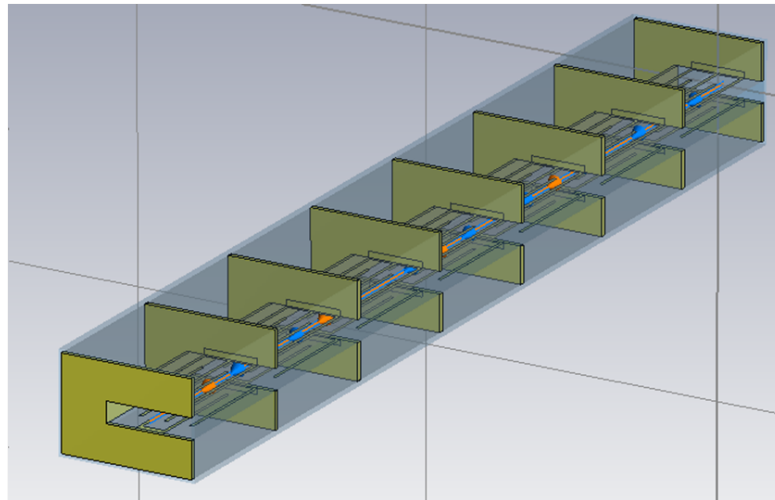


Figure 2.31: Simulation model of the SPS extraction kicker with serigraphy. The kicker is divided in 7 cells.

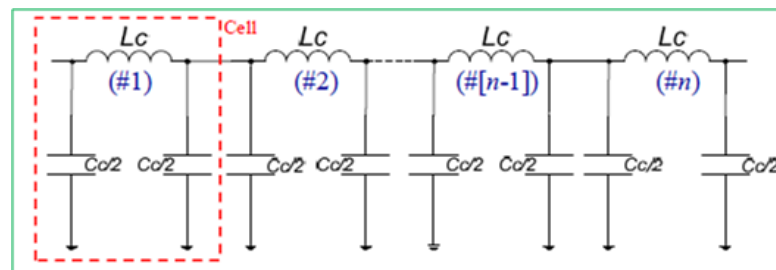


Figure 2.32: Simplified equivalent electric circuit of a transmission-line kicker magnet. Courtesy of M. Barnes.

MKP-L the cell includes a 104 nH inductance, and a cell capacitance of 668 pF. There is no resistance in parallel with the inductance. The cell capacitance has a parasitic inductance estimated to be 100 nH [63]. The effect of the longitudinal segmentation on the beam coupling impedance is expected to be significant since the wavelength has been estimated to be comparable with the cell length (see Fig. 2.35). As an example, in order to show the effect of such a dense longitudinal segmentation, in Fig. 2.36 we compared the vertical driving (dipolar) impedance with and without segmentation for the MKP11955. Using lumped elements also the internal circuit could be simulated. The effect of segmentation is very visible in the low frequency range, in which three additional broad resonant peaks appear close to 250, 500 and 800 MHz.

#### 2.4.2 SPS extraction kicker: effect of the serigraphy

The existing MKE fast extraction kicker system (as used since the late 70's until 2000 in the Super Proton Synchrotron (SPS)) has been renewed to meet the LHC and the CNGS specifications. A fast extraction kicker system has been installed in the SPS and successfully used in extraction tests in 2003 [64]. Since the beam induced heating of these devices was observed to

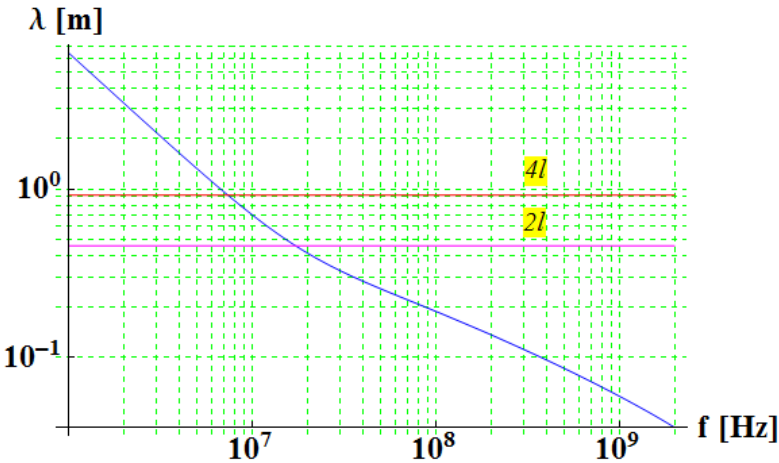


Figure 2.33: Wavelength in the microstrip approximation of a MKE (SPS extraction kicker).

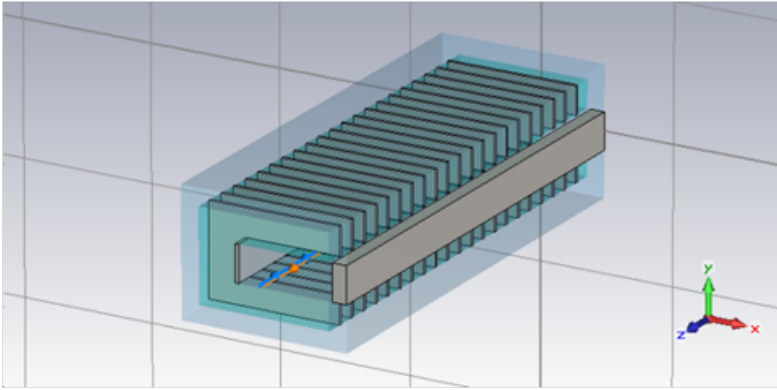


Figure 2.34: Advanced model of the MKP kicker module.

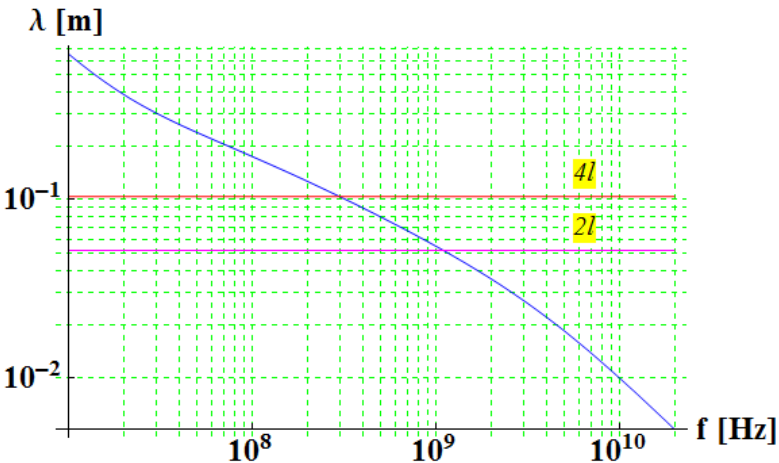


Figure 2.35: Wavelength in the microstrip approximation of a MKP (SPS injection kicker).

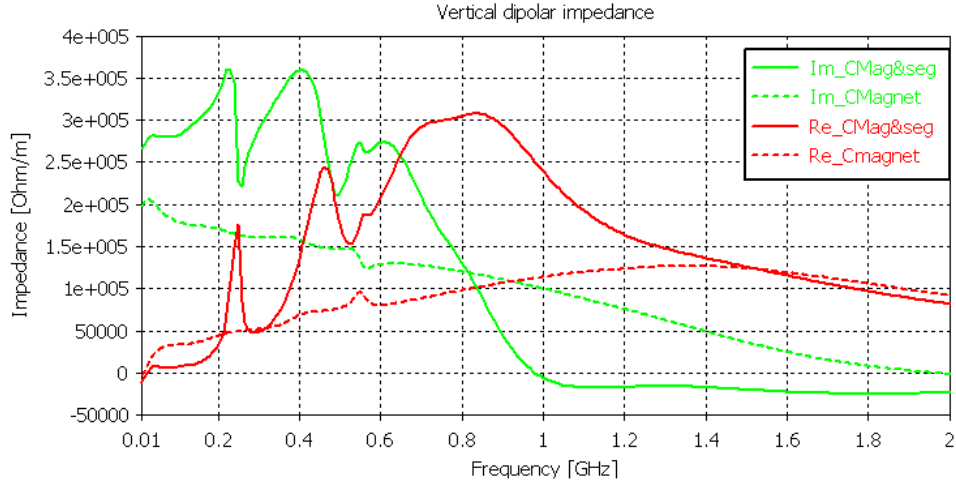


Figure 2.36: Comparing the driving vertical impedance for the MKP11955 with and without segmentation.

be critical [65], each kicker was equipped with a cooling system [60, 66]. The beam induced heating is directly related to the beam power loss through the real part of the longitudinal impedance. Impedance reduction techniques were investigated in order to solve the issue of the beam induced heating. The idea of using metalized fingers first proposed in [67] was investigated in detail [68, 69]. The final solution of using silver fingers printed by serigraphy directly on the ferrite [37] was implemented in 2007. Presently only one SPS extraction kicker out of eight is not yet serigraphed. There is a plan to serigraph this kicker in 2013 during the long shutdown of all the CERN accelerators (LS1). Figure 2.37 shows the simulated longitudinal impedance for the MKE with and without serigraphy. As expected serigraphy results in a strong reduction of the real part of the longitudinal impedance over a broad frequency range [34, 37, 68]. The broad-band peak shifts from  $\approx 600$  MHz to  $\approx 3.3$  GHz. At the same time the serigraphy introduces a clear resonance at 44 MHz. This resonance (see Fig. 2.38) was studied in detail and recognized to be a quarter wavelength resonance on the silver fingers as shown in Figure 2.39. Neglecting the capacitive effect related to the finger width at the resonance frequency we obtain:

$$\lambda = \frac{c}{f \sqrt{\epsilon_{\text{eff}}(f) \mu_{\text{eff}}(f)}} = 0.78 \text{ m} \cong 4L_{\text{finger}} \quad (2.61)$$

where  $f$  is the frequency of the resonance,  $\mu_{\text{eff}}$  and  $\epsilon_{\text{eff}}$  are calculated as the effective permeability and permittivity of the kicker magnet approximated as an equivalent microstrip [56] and  $L_{\text{finger}}$  is the finger length. The theoretical formula confirms that we have a quarter wave resonance in agreement with the CST simulations. As we will see in one of the next chapters the impedance model of the SPS extraction kicker shown in Figure 2.37 is fully consistent with the beam induced heating observed in the machine [70].

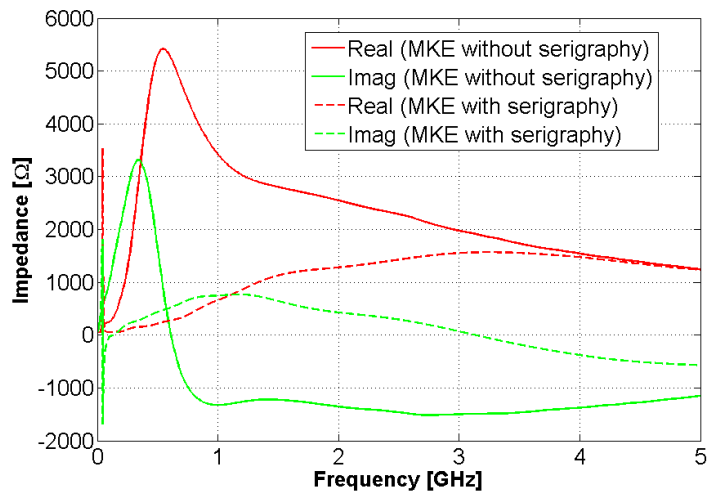


Figure 2.37: CST simulations of the longitudinal impedance for the SPS extraction kicker (MKE-L) with and without serigraphy.

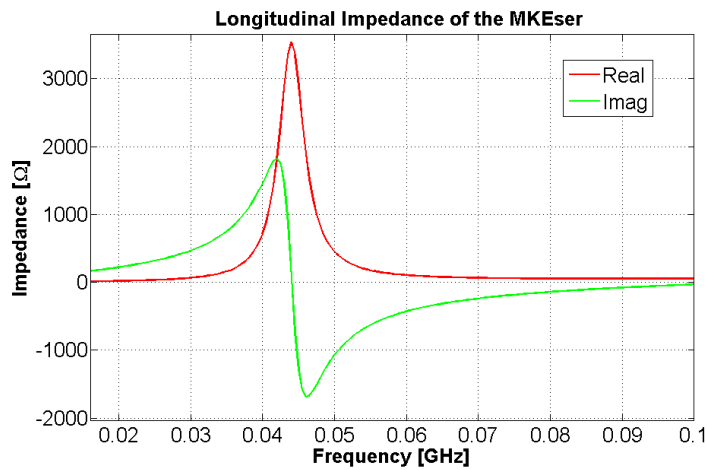


Figure 2.38: Zoom of the resonance due to the serigraphy.

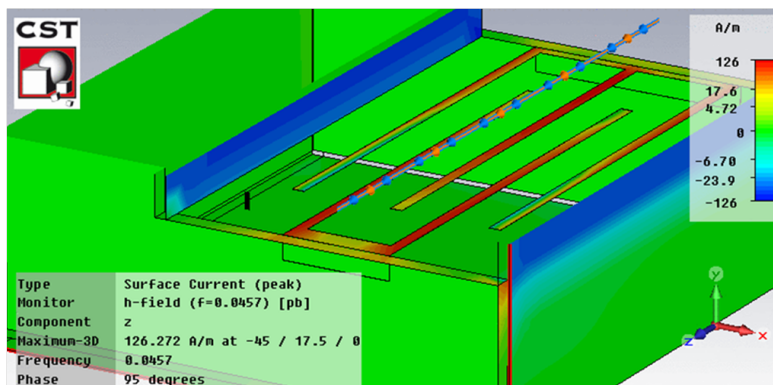


Figure 2.39: Surface currents on the serigraphed fingers.



### 2.4.3 Simulation of a kicker loaded by a coaxial cable

An open ended external cable (length  $l$ , propagation constant  $k$  and characteristic impedance  $Z_0$ ) exhibits an impedance given by the usual formula coming from the impedance transport in the classical transmission line theory:

$$Z = -jZ_0 \cot(kl) \quad (2.62)$$

Resorting to the expansion of the cotangent function as a sum of singularities we may reproduce the cable behaviour by an infinite series of lumped constant element circuits:

$$Z = \frac{Z_0}{jkl} + 2 \sum_{n=1}^{\infty} \frac{jk \ln \pi}{(n\pi)^2 - (kl)^2} \quad (2.63)$$

In the simulation model the circuit is approximated by a finite number of RLC parallel cells connected in series (see Fig. 2.40) where each cell accounts for a resonance:

$$Z = \frac{1}{G_0 + j\omega C_0} + \sum_{n=1}^{\infty} \frac{1}{G_n + j[\omega C_n - (\omega L_n)^{-1}]} \quad (2.64)$$

with:

$$\begin{aligned} G_0 &= \alpha l Y_0; & C_0 &= l \epsilon_0 \epsilon_r; \\ G_n &= \frac{\alpha l Y_0}{\pi n}; & C_n &= \frac{l \epsilon_0 \epsilon_r}{2\pi n}; & L_n &= \frac{2l \mu_0 \mu_r}{\pi n} \end{aligned} \quad (2.65)$$

Using this technique we are able to take into account the effect of external cables in CST 3D time domain Wakefield simulations. Figure 2.41 shows an example of application of this technique. Remarkable is the good agreement for the 5th resonance between the green and blue curves, which confirms the consistency of the method.

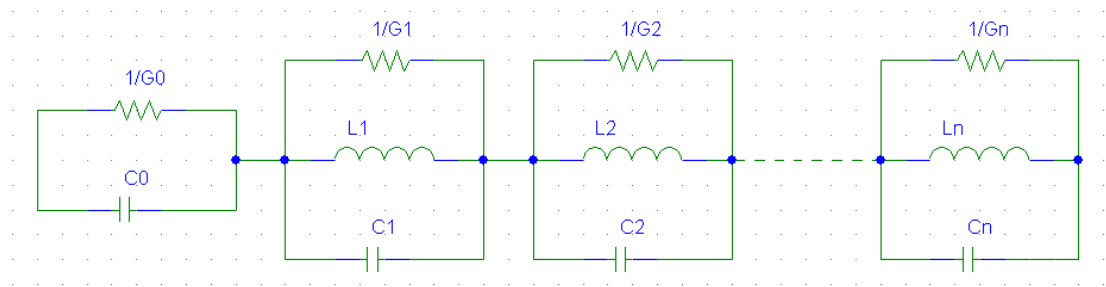


Figure 2.40: Circuit model of an open ended coaxial cable.

## Chapter 2. Impedance model of ferrite kickers

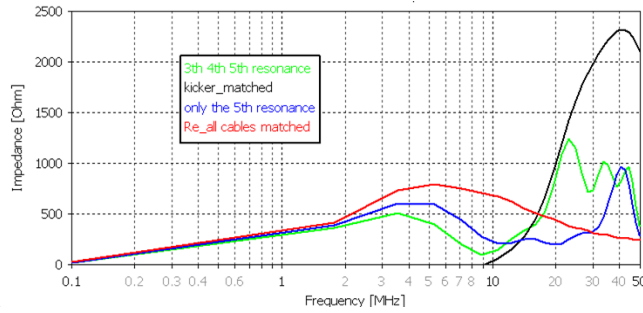


Figure 2.41: Simulation of a C-shaped kicker magnet including external circuits ( $a = 5.75$  cm,  $b = 3.5$  cm,  $L = 0.81$  m,  $l = 18$  m): the cables are considered open ended and are modeled to account the 3th, 4th and 5th resonance (green curve), only the 5th resonance (blue curve). Moreover the black curve is the standard case of a perfectly matched kicker and the red curve the case of perfectly matched cables (kicker closed on the characteristic impedance of cables).

NAME	Model
MKQH.11653	Tsutsui
MKQV.11679	Tsutsui
MKDV.11731	C-magnet
MKDV.11736	C-magnet
MKDH.11751	C-magnet
MKDH.11754	C-magnet
MKDH.11757	C-magnet
MKPA.11931	C-magnet with segmentation
MKPA.11936	C-magnet with segmentation
MKPC.11952	C-magnet with segmentation
MKP.11955	C-magnet with segmentation
MKE.41631	C-magnet with segmentation
MKE.41634	C-magnet with segmentation and serigraphy
MKE.41637	C-magnet with segmentation and serigraphy
MKE.41651	C-magnet with segmentation and serigraphy
MKE.41654	C-magnet with segmentation and serigraphy
MKE.61631	C-magnet with segmentation and serigraphy
MKE.61634	C-magnet with segmentation and serigraphy
MKE.61637	C-magnet with segmentation and serigraphy

Table 2.2: SPS kicker advanced model.

### 2.4.4 SPS kicker impedance model

The SPS kicker impedance model accounts for the contribution of all the SPS kickers (see Tab. 2.1) calculated with the closest available impedance model to the kicker geometry. For each kicker we calculated the longitudinal and the transverses impedances. The driving and detuning total SPS impedances of the advanced model (Tab. 2.2) for both Q20 and Q26 optics are shown in 2.42 and 2.43. For the Q26 optics in Fig. 2.44 we show respectively the generalized horizontal and vertical SPS kicker impedance calculated with the advanced model and Tsutsui's theoretical model. Finally the longitudinal impedance is shown in Fig. 2.45. The advanced model of kicker is significantly different from the simplified model especially in the frequency range below 2 GHz.

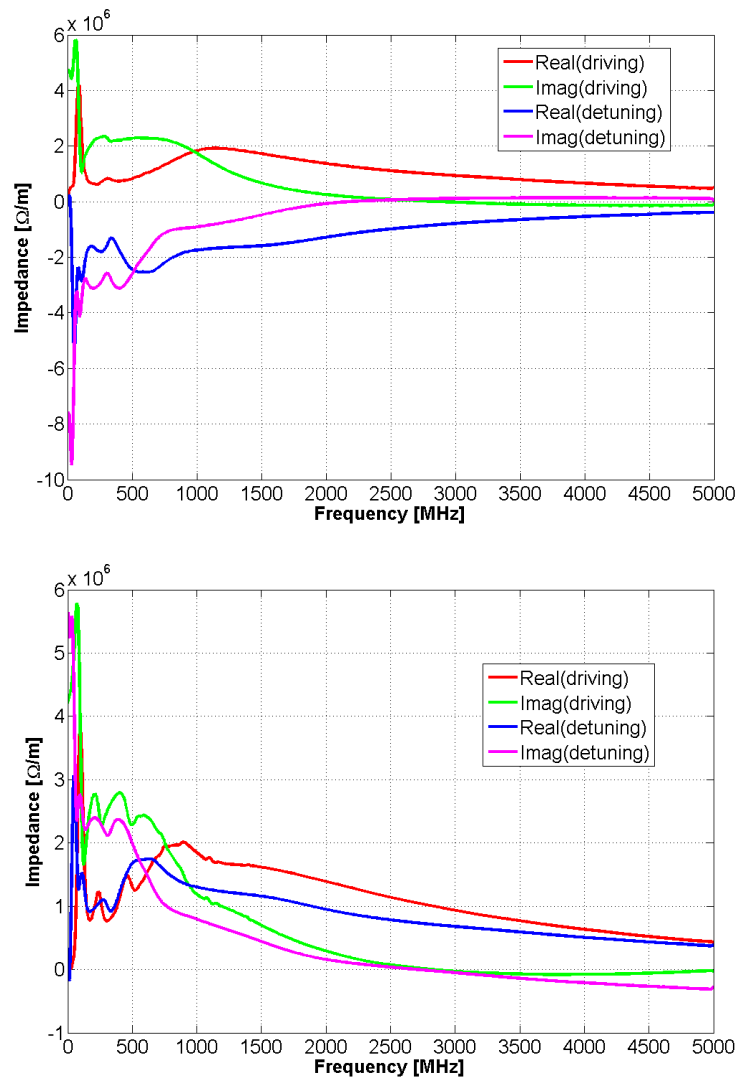


Figure 2.42: Driving and detuning impedance of the SPS kickers (advanced model) for the Q20 optics: horizontal (top), vertical (bottom).

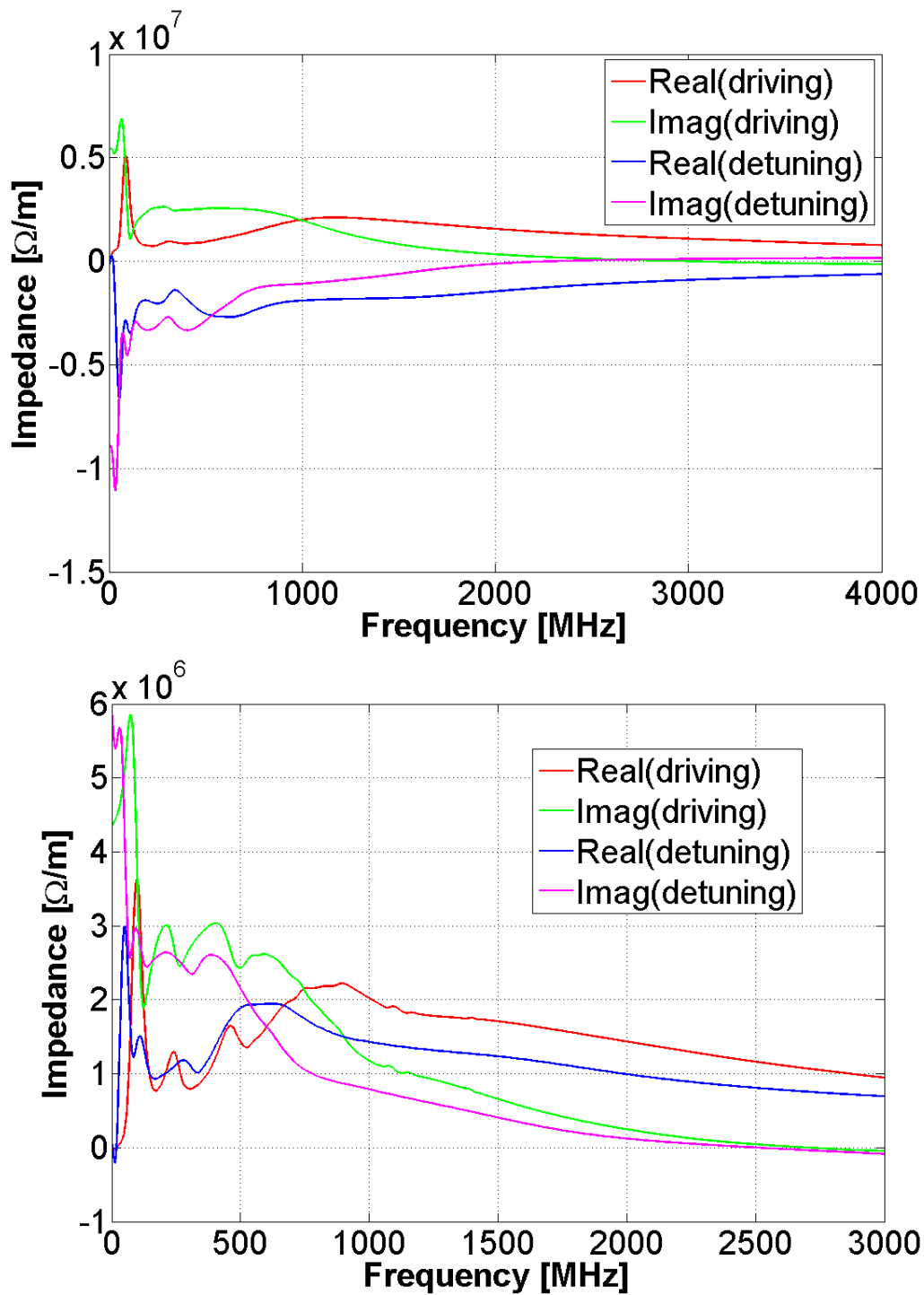


Figure 2.43: Driving and detuning impedance of the SPS kickers (advanced model) for Q26: horizontal (top), vertical (bottom).

## 2.4. Realistic model of SPS kickers

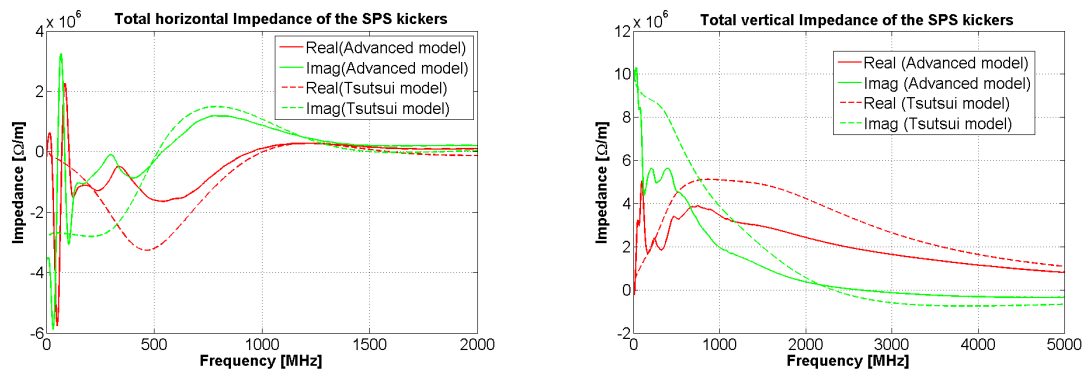


Figure 2.44: Generalized horizontal (left) and vertical (right) impedance of the SPS kickers. In full lines the advanced model (3D CST simulation of the closest available impedance model to the kicker geometry) and in dashed lines the Tsutsui model.

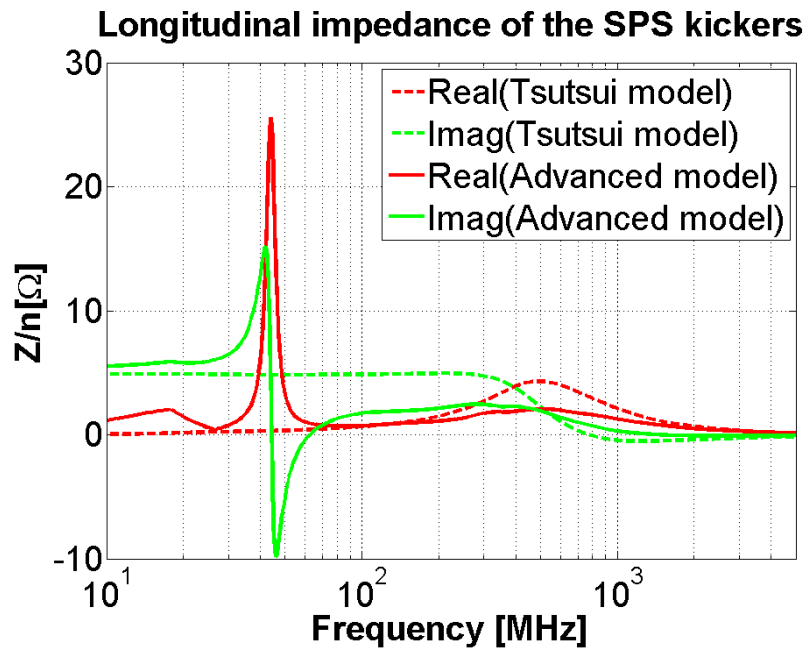


Figure 2.45: Longitudinal impedance of the SPS kickers. In full lines the advanced model (3D CST simulation of the closest available impedance model to the kicker geometry) and in dashed lines the Tsutsui model.



## 3 Resistive wall impedance calculations

In this chapter we present studies on resistive wall impedance. In general, the resistive wall impedance describes the coupling between the beam and an external chamber having finite conductivity. Analytical derivations are possible when dealing with chambers with simple geometries. Many of the existing theories are based on the field matching technique. Here we present an alternative model for resistive wall calculation based on the transmission line (TL) theory. The model has been benchmarked with the most recent codes developed at CERN (ReWall and ImpedanceWake2D [1]) and has been applied to construct the SPS wall impedance model.

For more complicated geometries (asymmetries, small inserts, holes etc.), a theoretical estimation without involving EM simulation becomes nonviable. An example of interest in this sense is the LHC beam-screen where CST 3D simulations were used for the impedance estimation [71, 72].

### 3.1 A TL model for wall impedance calculation

Presently at CERN, the resistive wall impedance of a round or flat chamber is calculated using the ReWall or ImpedanceWake2D codes based on the field matching technique [1, 27, 73, 74, 75, 76]. The ImpedanceWake2D is the translation into C-language of the ReWall code (written in "Mathematica"), which contains in addition a special FFT routine to calculate the wake functions [1]. We developed an alternative code based on the transmission line (TL) theory. The TL theory to model the resistive wall impedance was already used at CERN in 2003 by L. Vos [77]. However, after a few studies and applications [77, 78, 79] this strategy was not followed up and all the efforts were devoted to model the resistive wall using the field matching technique [1, 27, 76].

Resuming the studies of L. Vos, we developed a theoretical model based on the TL theory for the calculation of the resistive wall impedance. In spite of its simplicity, the TL theory with some modification allows modeling the resistive wall without loss of generality. The theory can be applied to calculate the wall impedance (resistive wall impedance plus the indirect space charge term [1, 28]) of a round chamber loaded by a structure made of an arbitrary number of layers of finite thickness allowing for PEC, Vacuum or Conductive Wall (lossy materials, i.e. finite electrical conductivity and/or with complex permeability/permittivity) boundary conditions. Presently, the code is implemented in Matlab and can be used to simulate the

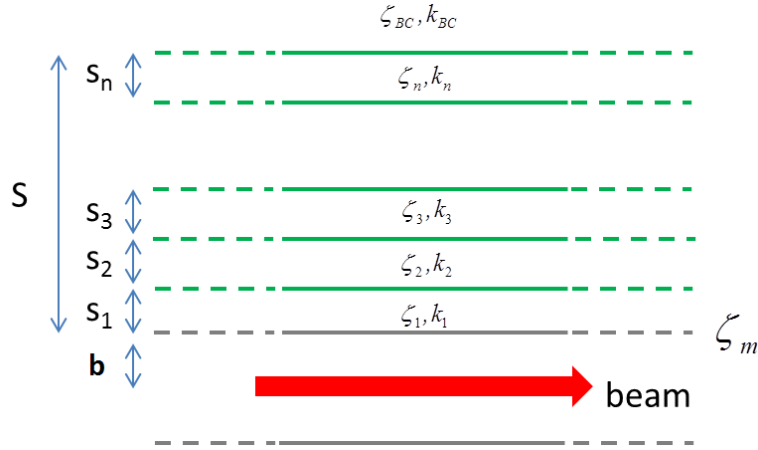


Figure 3.1: Sketch of the multilayer geometry

desired number of layers. A post-processing part, in the limits of its applicability [1, 80], can be used to calculate the impedance for rectangular and elliptical chamber by means of geometrical form factors [81]. The code has been successfully benchmarked with ReWall [1].

### 3.1.1 Description of the model

Resorting to the TL theory we model the multilayer round chamber with the planar geometry of Fig. 3.1, where each layer is characterized by its intrinsic impedance  $\zeta_n = \sqrt{\frac{\mu_n}{\epsilon_n}}$  and propagation constant  $k_n = \omega\sqrt{\epsilon_n\mu_n}$ , ( $n$  is the layer index). The last layer extends to infinity and determines the boundary condition of the EM problem, that's why its characteristic quantities are indicated with the subscript  $BC$ . Applying the TL theory we transport the intrinsic impedance of the boundary condition onto the vacuum chamber wall surface (see Appendix C for more details). This represents the surface impedance seen by the beam and is indicated with  $\zeta_m$ . In practice we can treat our multilayer wall as a single equivalent layer of surface impedance  $\zeta_m$ .

Assuming that this is also the impedance of all the directions of incidence, we can apply the Leontovich boundary condition to this equivalent structure:

$$\vec{E}_t = \zeta_m \vec{H} \times \hat{i}_n \quad (3.1)$$

where  $\vec{E}_t$  is the tangential component of the electric field and  $\hat{i}_n$  is the unity vector normal to the chamber inner wall. The approximate boundary condition given by Leontovich in [82] and reported in Eq. 3.1 applies in general to the case of a plane wave incident on an infinite plane separating two media, one of which has finite conductivity. In order for the TL formalism to be valid through all the layers beyond the first one, it is required that [83]:

$$|\epsilon_1\mu_1| \gg \epsilon_0\mu_0 \quad (3.2)$$



### 3.1. A TL model for wall impedance calculation

This condition ensures that the EM field through all the media will be a plane wave propagating in the direction normal to the separation surfaces. Note that the condition has to be imposed only for the first layer: in the case of normal incidence on the first separation surface, for symmetry, also backward and forward waves will have direction of propagation normal to the separation surface in the second medium, and so on through all the media. The longitudinal beam coupling impedance is then calculated by its definition in the frequency domain Eq. (1.3) for a source of charge  $q_0$  centered in a round chamber. Writing Maxwell's equations in cylindrical coordinates it can be demonstrated that in the ultrarelativistic case the longitudinal component of the electric field induced by a centered source charge does not have radial dependence [8]. Regarding the magnetic field, the only non zero term is the  $\varphi$  component, which has only radial dependence. Therefore the electric field to be inserted into Eq. (1.3) can be calculated directly by using the Leontovich boundary condition of Eq. (3.1). We obtain the following expression for the longitudinal component of the electric field:

$$E_s = \zeta_m H_\varphi \quad (3.3)$$

where the magnetic field  $H_\varphi = \frac{I}{2\pi b}$  has been obtained from the Ampere Law. The current  $I$  in the frequency domain associated to the source of charge  $q_0$  is simply [1]:

$$I = q_0 e^{-jks} \quad (3.4)$$

Finally, applying Eq. (1.3) with the electric field of Eq. (3.3) we find the following expression for the longitudinal beam coupling impedance of the round indefinite structure of radius  $b$  with boundary impedance  $\zeta_m$ :

$$Z_{\parallel}(\omega) = L \frac{\zeta_m(\omega)}{2\pi b} \quad (3.5)$$

In the non-ultrarelativistic case,  $\zeta_m$  is renormalized to take into account the radial dependence of the longitudinal component of the electric field induced by a centered source charge (Eqs. (2.16) and (2.18) for  $m=0$ ).

The TL theory applies to planar geometry. Using this theory for our round multilayer structure we are neglecting the attenuation due to propagation of cylindrical waves. This is a good approximation when the penetration depth is significantly smaller than the pipe radius  $b$ . This limitation in the validity of Eq.(3.5) can be overcome by including, in the definition of characteristic impedance of each layer, the attenuation due to the propagation of cylindrical waves. Including this effect, Eq. (3.3) can be rewritten as follows:

$$E_s = \zeta_m H_\varphi (1 - \alpha_m) \quad (3.6)$$

### Chapter 3. Resistive wall impedance calculations

---

where  $\alpha_m$  represents the attenuation due to propagation of cylindrical waves. Therefore, in order to account for this effect we should rewrite the characteristic impedance of each layer as follows:

$$\zeta_n^{eq} = \zeta_n \Theta_n \quad (3.7)$$

where  $\Theta_n = 1 - \alpha_n$  is the function that describes the attenuation due to propagation of cylindrical waves in the layer  $n$ . The function is close to 1 when the penetration depth in the material is much smaller than the pipe radius ( $\zeta_n^{eq} = \zeta_n$ , negligible effect of the attenuation due to the propagation of cylindrical waves) and decreases more and more with the penetration depth approaching the value of zero ( $\zeta_n^{eq} = 0$ , no propagation: the cylindrical wave is totally attenuated) when the penetration depth is much larger than the pipe radius. Since in most of the cases of interest, the wall thickness  $S$  is much smaller than pipe radius, we consider this attenuation only in the critical case of vacuum boundary. In this case, even if  $S$  is smaller than the pipe radius, neglecting the attenuation for propagation of cylindrical waves, the model will be inaccurate at frequencies such that the penetration depth is larger than  $S$ . It is worth noting that, for PEC boundary, the condition  $S \ll b$  guarantees that the attenuation due to propagation of cylindrical waves is negligible. In vacuum, for a source charge  $q_0$  centered in a round chamber, the EM fields propagate with the modified Bessel function of order 0 and argument  $k_0 b$ ,  $I_0(k_0 b)$  (see Eq. (2.16)), therefore a plausible expression for  $\Theta$  is the following:

$$\Theta = 1 - \frac{1}{I_0(k_0 b)} \quad (3.8)$$

The function  $I_0(k_0 b)$  tends to the unity when the argument goes to zero, in agreement with our expectations:  $k_n \ll 1/b$  that since  $k$  is inversely proportional to the penetration depth  $\delta$  means  $\delta \gg b$ . For large values of the argument ( $k_n \gg 1/b$ ), the modified Bessel function goes to infinity, giving  $\Theta = 1$ : the attenuation due to propagation of cylindrical waves is negligible since the penetration depth inside the material becomes much smaller than the pipe radius. Therefore, for the vacuum boundary, we use the equivalent characteristic impedances as defined in Eq. (3.7). The impedance on the inner surface obtained from the equivalent vacuum boundary characteristic impedance is called  $\zeta_m^{eq}$ . For vacuum boundary, Eq. (3.5) has to be rewritten as follow:

$$Z_{\parallel}(\omega) = L \frac{\zeta_m^{eq}(\omega)}{2\pi b} \quad (3.9)$$

The transverse impedance can be calculated from the longitudinal resistive wall impedance of Eq. (3.5) with the usual relation:

$$Z_{\perp} = \frac{2 Z_{\parallel}}{k b^2} \quad (3.10)$$

### 3.1. A TL model for wall impedance calculation

A derivation of Eq. (3.10) can be found in Ref. [52]. The relation has been obtained assuming the penetration depth smaller than the pipe radius, therefore, becomes questionable below a certain frequency, especially for Vacuum or conductive wall boundary (as in the case of longitudinal impedance for the PEC boundary, if the wall thickness  $S$  is smaller than  $b$ , the formula is valid independently of the frequency [8]). For this reason we use the more general relation introduced by L.Vos based on the concept of inductive bypass [78, 84]. L. Vos studied the coupling of an off-centered beam with a conducting pipe, finding that the differential current induced by the beam will not only face the image inductance (indirect space charge contribution) but will also act on the resistive wall impedance of the pipe related to  $\zeta_m$ . In practice due to the asymmetry introduced by the offset the differential wall current will have a preferential path lowering the beam coupling impedance. This effect becomes significant for large penetration depth and can be accounted for by including a parallel inductance. The longitudinal impedance to be inserted into Eq. (3.10) is an equivalent impedance obtained from the parallel combination of the impedance due to the wall properties (see Eq. (3.5)) and the inductive impedance  $j\omega L_1$ , where  $L_1$  is the inductance of the bypass and can be calculated as the parallel combination of vacuum and boundary inductance. For vacuum boundary one obtains  $L_1 = \mu_0/2$ . Finally we obtain the following relation for the transverse impedance:

$$Z_{\perp} = \frac{2}{k b^2} F_{\text{bypass}} \quad (3.11)$$

where  $F_{\text{bypass}}$  is:

$$F_{\text{bypass}} = \frac{j\omega L_1 L Z_{\parallel}}{j\omega L_1 L + Z_{\parallel}} \quad (3.12)$$

#### 3.1.2 Benchmark with ReWall

The code based on the model described above has been called "TL-wall" and it has been benchmarked with "ReWall" [1]. In order to have a full benchmark we show examples for different sets of boundary conditions.

The cases studied are simplified models of CERN accelerator chambers. The first two cases of study are round approximations of the LHC beam-screen [85] with PEC and Vacuum boundary conditions. ReWall does not allow to use a PEC boundary condition (the conductivity has to be finite), however it is possible to simulate a Quasi-PEC boundary condition by setting a high value for the electrical conductivity (we used  $\sigma_{el} = 10^{15} S/m$ ). However, increasing the conductivity we run into problems of numerical convergence. A comparison of longitudinal and transverse impedance is shown in Fig. 3.2. The discrepancy with respect to ReWall below 100Hz is ascribed to the fact that ReWall cannot simulate exactly a PEC boundary.

The second case of study, presented in Fig. 3.3, analyzes the same structure without the Copper coating and with a Vacuum boundary condition. In this case the agreement with ReWall is impressive over the whole range of frequencies analyzed for both longitudinal and transverse impedance. Moreover, in order to underline the importance of considering the attenuation of

### Chapter 3. Resistive wall impedance calculations

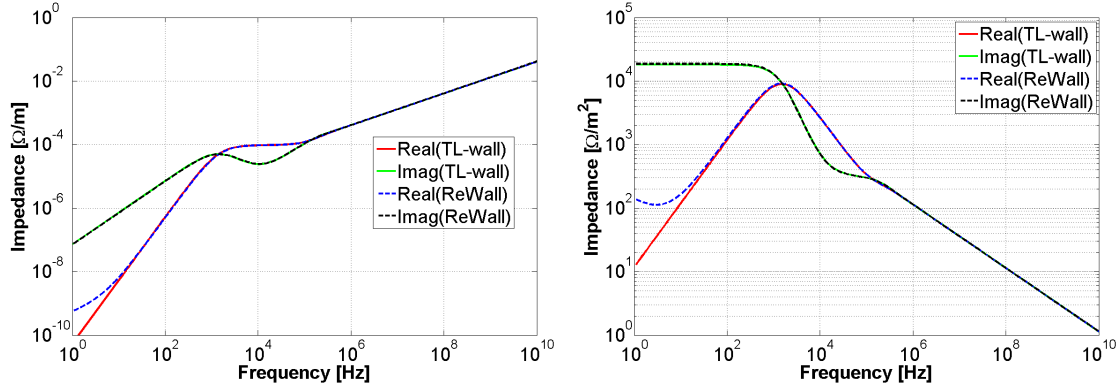


Figure 3.2: Comparing impedance from TL-wall and ReWall (longitudinal (left) and transverse (right)) for a round chamber of radius  $b = 18.4$  mm with 2 layers and a PEC or quasi-PEC boundary condition. For both layers  $\epsilon_r = \mu_r = 1$ . First layer:  $s_1 = 50 \mu\text{m}$ ,  $\sigma_{el} = 1.82 \times 10^9$  S/m; second layer:  $s_1 = 1\text{mm}$ ,  $\sigma_{el} = 1.67 \times 10^6$  S/m.

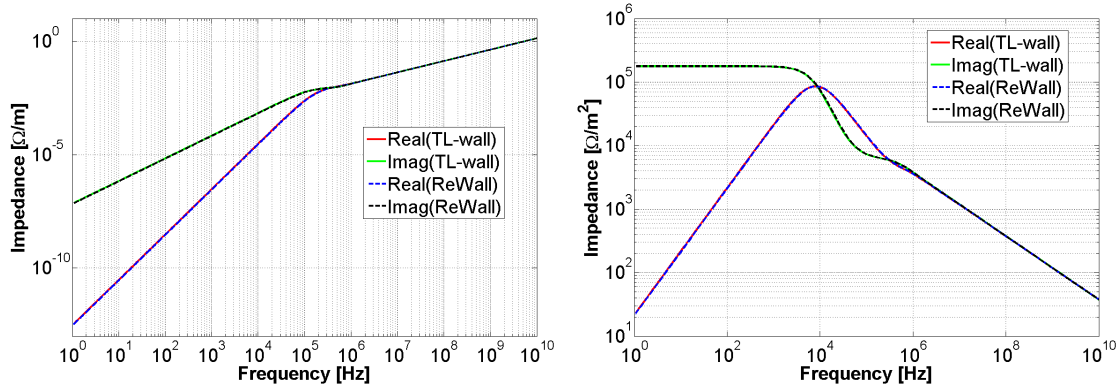


Figure 3.3: Comparing impedance from TL-wall and ReWall (longitudinal (left) and transverse (right)) for a round chamber of radius  $b = 18.4$  mm with 1 layer ( $\epsilon_r = \mu_r = 1$ ,  $s_1 = 1$  mm,  $\sigma_{el} = 1.67 \times 10^6$  S/m) and a Vacuum boundary condition.

cylindrical wave, Fig. 3.4 shows the longitudinal impedance calculated with Eq. (3.5), without applying any correction. We observe that, when neglecting this attenuation, the real part of the longitudinal impedance tends to a constant positive value at low frequency (like a DC impedance).

To complete the set of possible boundary conditions, we consider the case of an SPS bending magnet having as boundary material the "iron" (silicon-steel) of the magnet. Also in this case the agreement with ReWall is highly satisfactory (see Fig. 3.5). The dispersion model for the permeability of silicon-steel used in this calculation (Eq. (2.1) with  $\mu_i = 500$  and  $\frac{1}{2\pi\tau_u} = 10$  kHz) is shown in Fig. 3.6. The model is based on DC permeability measurements performed directly on the silicon-steel of the SPS bending magnets [86] and on published measurements of the complex permeability of silicon-steel up to 1MHz [87].

### 3.1. A TL model for wall impedance calculation

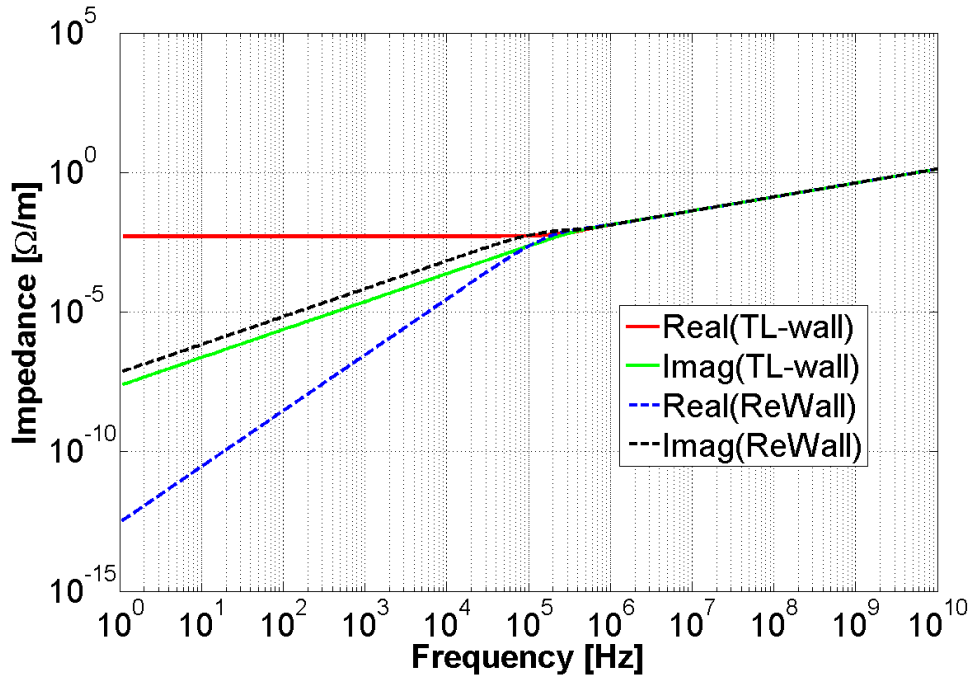


Figure 3.4: Comparing longitudinal impedance from TL-wall, without considering the attenuation due to propagation of cylindrical waves, and ReWall for a round chamber of radius  $b = 18.4$  mm with 1 layer ( $\epsilon_r = \mu_r = 1$ ,  $s_1 = 1$  mm,  $\sigma_{el} = 1.67 \times 10^6$  S/m) and a Vacuum boundary condition.

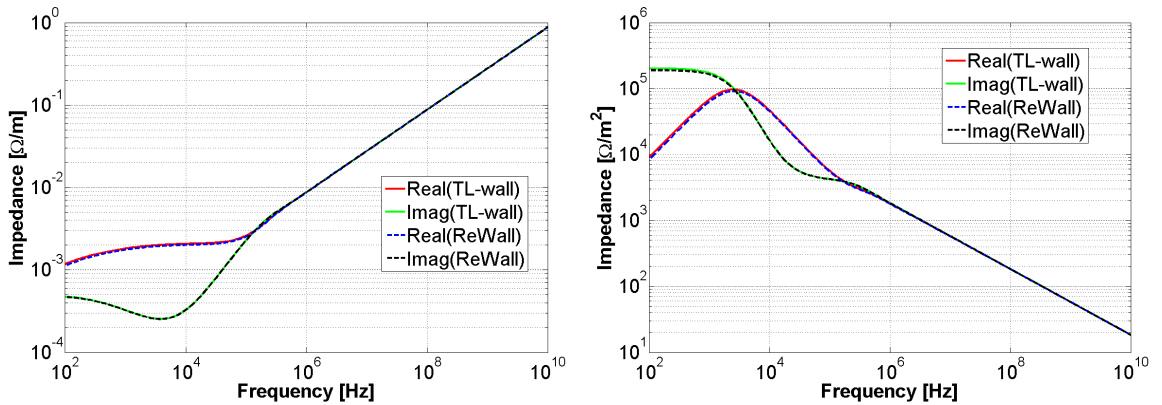


Figure 3.5: Comparing impedance from TL-wall and ReWall (longitudinal (left) and transverse (right)) for a round chamber of radius  $b = 24.25$  mm with 1 layer ( $\epsilon_r = \mu_r = 1$ ,  $s_1 = 1$  mm,  $\sigma_{el} = 1.67 \times 10^6$  S/m) and a Conductive Wall boundary condition ( $\epsilon_r = 1$ ,  $\sigma_{el} = 1 \times 10^6$  S/m and permeability model given in Fig. 3.6).

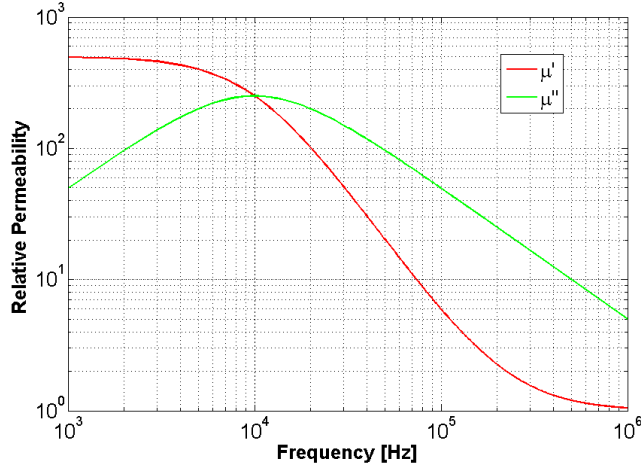


Figure 3.6: Permeability model of the 'iron' (silicon-steel) of the SPS magnet at injection energy.

### 3.1.3 Application to the SPS wall impedance model

In order to fully characterize the global impedance of the SPS the theoretical model just described was applied to estimate the SPS wall impedance model [88]. Up to now an approximate estimation was used, which was obtained assuming an uniform flat chamber around the accelerator. The calculation was performed using Zotter's theory for a round chamber with thin wall [27] for a pipe of 20 mm radius transformed into a flat chamber using the Yokoya factor [15]. Here we present a more accurate calculation that accounts for all the different SPS vacuum chambers (see Fig. 3.7) weighted by the respective length and beta function:

$$Z_{\parallel} = \sum_{i=1}^6 Z_{\parallel}^i L_i \quad (3.13)$$

$$Z_{x,y} = \frac{1}{\langle \beta_x \rangle} \sum_{i=1}^6 Z_{x,y}^i L_i \langle \beta_{x,y}^i \rangle$$

In the above formulae, obviously  $Z_{\parallel}^i$  and  $Z_{x,y}^i$  are impedances for unit longitudinal length. The chambers in the bending magnets and focusing quadrupoles can be reasonably approximated as having a rectangular geometry. The calculation is performed by weighting the impedance obtained for round chamber with the form factor of Eq. (1.31)[15, 16, 81]. Moreover, as previously described, we also consider the "iron" of the magnets. The "iron" was modeled as a silicon steel assuming the permeability model illustrated in Fig. 3.6 and an electrical conductivity  $\sigma_{el} = 10^6$  S/m.

The results obtained are presented in Fig. 3.8 for the longitudinal impedance and in Figs. 3.9 and 3.10 respectively for horizontal and vertical transverse impedances for both the Q26 and Q20 optics. The effect of the iron in the magnets becomes significant for frequencies below a few kHz as can be clearly observed in Fig. 3.11, in which we compare the case of a vacuum boundary with the case of the iron boundary.

### 3.1. A TL model for wall impedance calculation

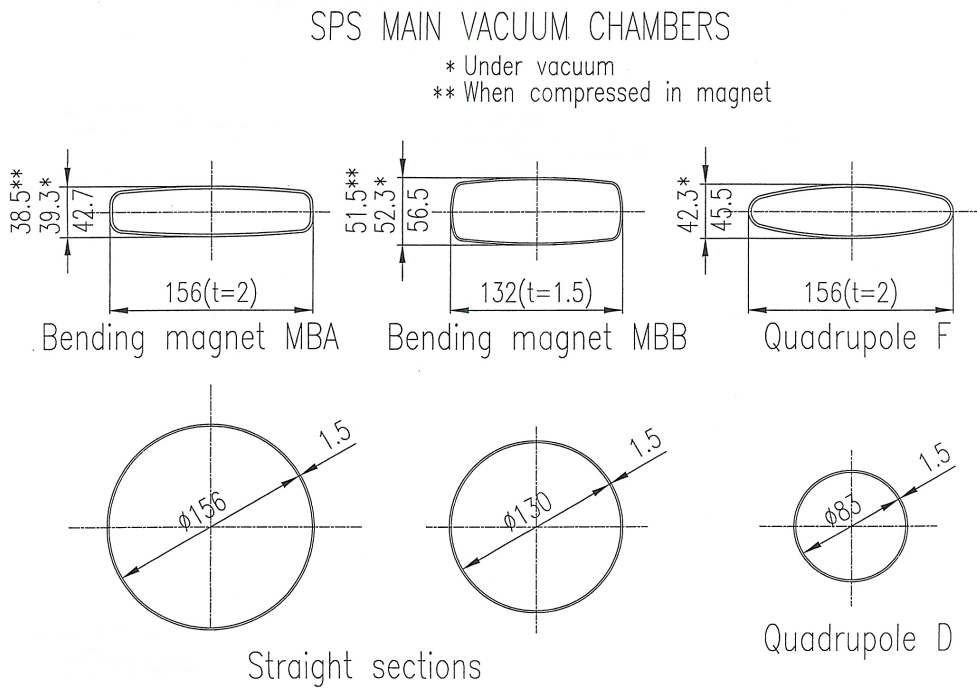


Figure 3.7: SPS vacuum chambers.

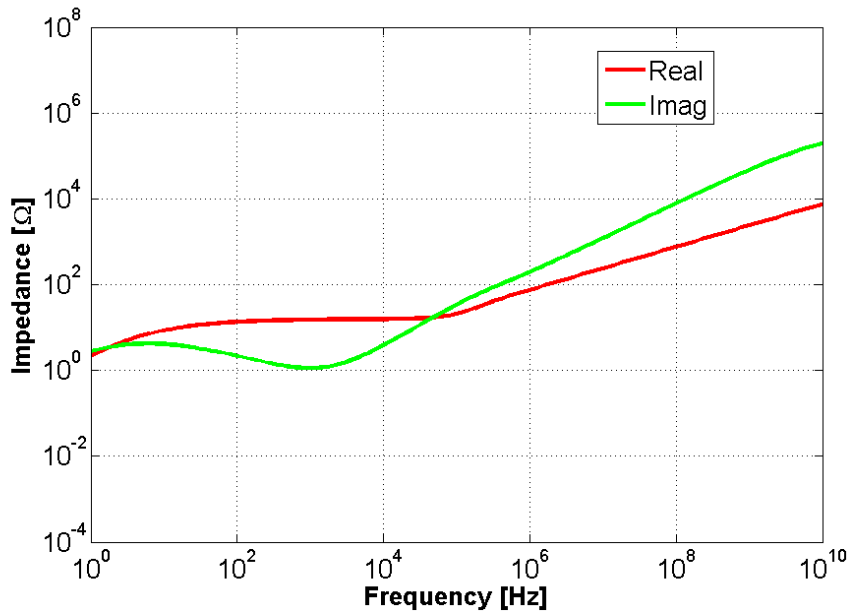


Figure 3.8: SPS wall longitudinal impedance.

### Chapter 3. Resistive wall impedance calculations

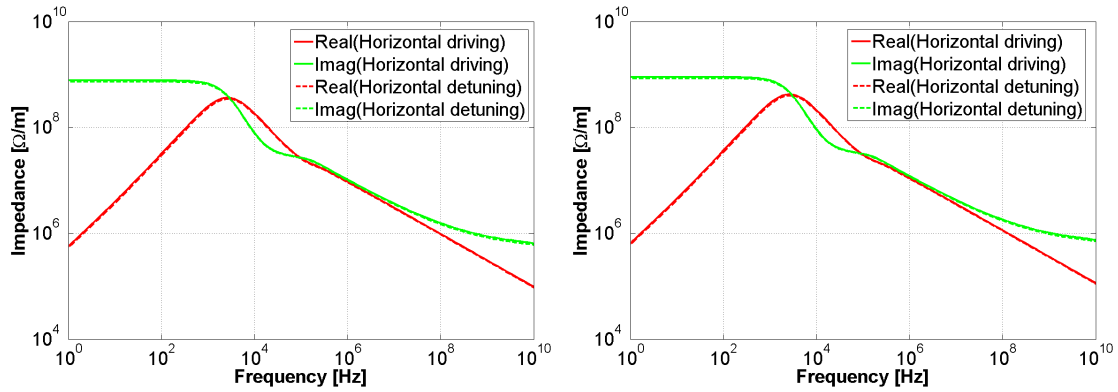


Figure 3.9: Horizontal SPS wall transverse impedance: Q20 (left) and Q26 (right). For the horizontal detuning impedance we plot  $-Z_x^{\text{det}}$ .

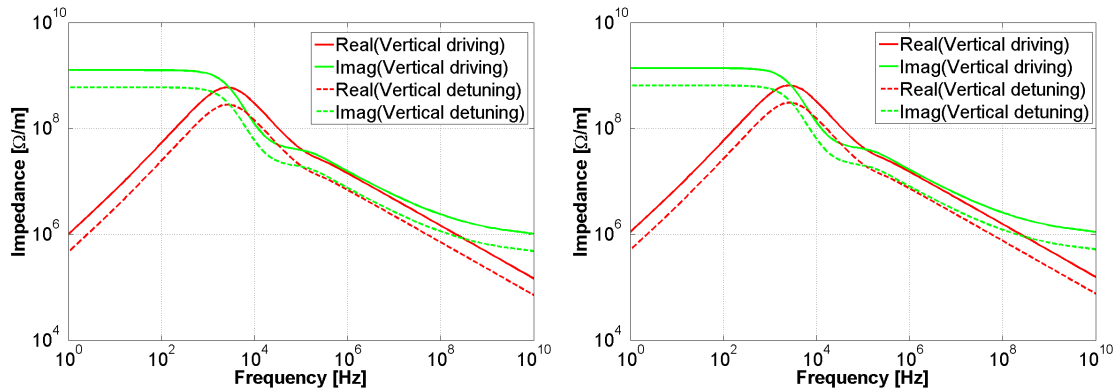


Figure 3.10: Vertical SPS wall transverse impedance: Q20 (left) and Q26 (right).

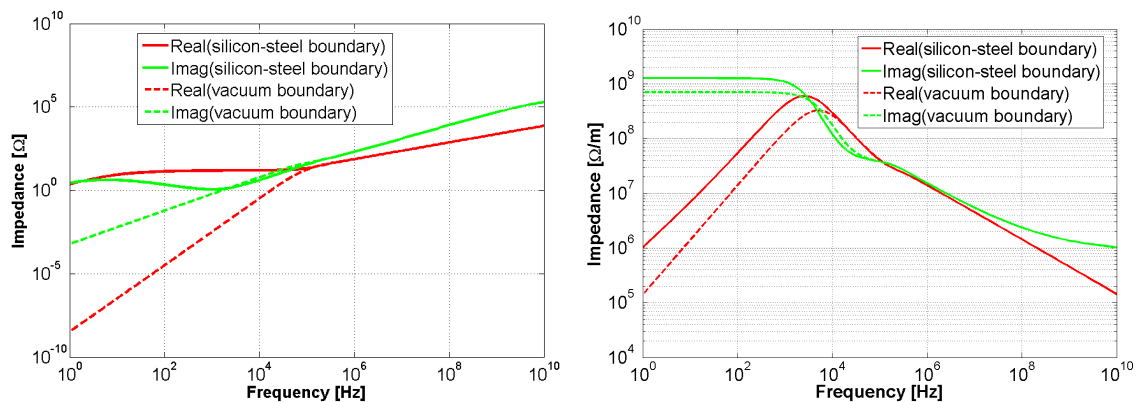


Figure 3.11: Longitudinal (left) and vertical driving (right) SPS wall impedance: Comparing vacuum and iron boundary.



### 3.2 Resistive wall impedance of the LHC beam-screen

The beam-screen used in the LHC main dipoles (see Fig. 3.12) is a pipe made of 1 mm thick ultra-low magnetic permeability stainless steel (SS) coated on its inner surface with a  $50\ \mu\text{m}$  layer of high electrical conductivity Copper (Cu) [85] to minimize resistive wall losses and other undesirable effects of beam coupling impedance [89]. The large eddy current forces created during a magnet quench require that the thickness of this Cu layer must be minimized and have excellent adherence to a high strength support structure, the beam screen body, which in turn must have an optimum thickness to maximize beam aperture. The two beam vacuum tubes, or cold bores, are the interface between the 1.9 K magnet baths of superfluid helium and the ultra high vacuum system. Besides, by shielding the 1.9 K surfaces from synchrotron radiation, gas in the beam aperture may be effectively cryopumped via holes (pumping slots) in the beam screen wall. The two stainless steel cooling tubes, which maintain the beam screen temperature between 5 K and 20 K, are positioned to optimize the available aperture [90]. The pumping slots on the flat zones of the beam screen body, representing some  $4.4\%$  of the inner surface area, have a randomized pattern which repeats every  $500 \pm 10\ \text{mm}$ .

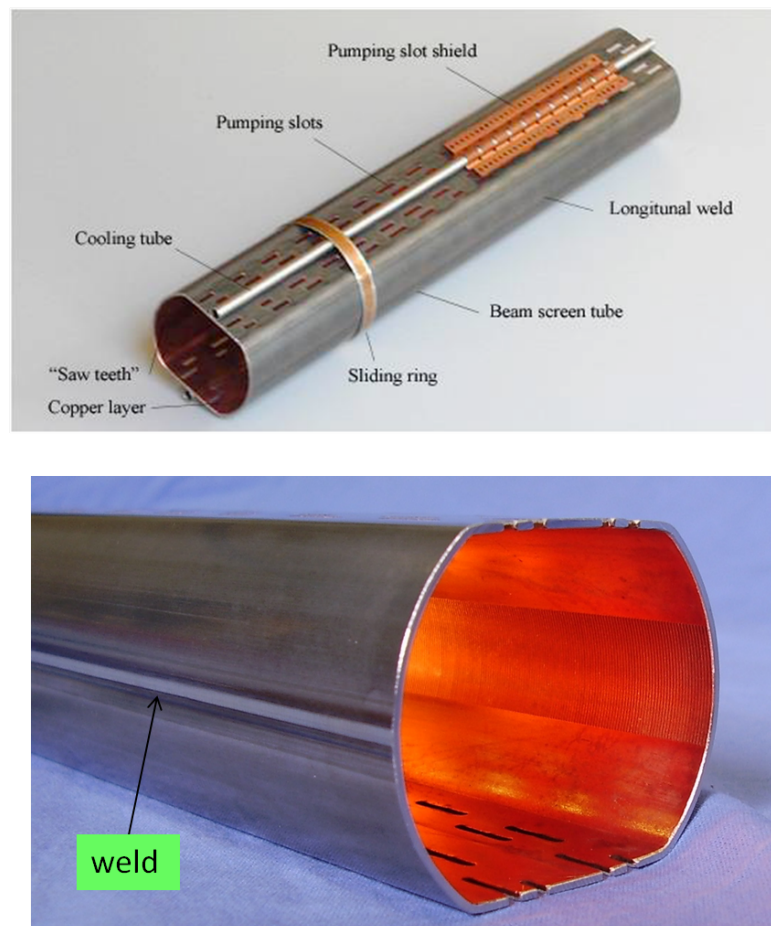


Figure 3.12: The LHC beam screen as it is built and installed. Courtesy of N. Kos.

In this section we will present some simulations to characterize the resistive wall impedance of

the LHC beam-screen. Special emphasis will be put on accurately determining the impedance spectrum in the low frequency range (down to few kHz), which could be of high interest for beam dynamics applications (coupled bunch instabilities).

### 3.2.1 The scaling technique

As already discussed in section 1.2.3 the wake length (WL) sets the resolution in the frequency domain when using TD simulations. For example, in the ultra-relativistic case  $v = c$ ,  $WL = 1$  km is required to obtain a resolution in frequency of  $\Delta f_{min} = \frac{c}{WL} = 300$  kHz. Very often the dimensions of the DUT are much smaller than the WL needed to have a good resolution below few MHz. In these cases, the classical approach becomes unworkable (very large memory consuming). To overcome this limitation we developed a novel simulation technique, which we called "the scaling technique".

The basic idea of the scaling technique is the following: if the only contribution to the impedance is given by the resistive walls, we can preserve the electromagnetic configuration by scaling all the geometrical parameters ( $a, b, L, S$ ), the source and test offsets ( $x_0, y_0, x, y$ ), the bunch-length  $\sigma_z$  and the skin depth  $\delta$  by the same factor. In the case of a good conductor, the skin depth  $\delta$  is given by the usual formula:

$$\delta(\omega) = \sqrt{\frac{2}{\omega \mu \sigma_{el}}} \quad (3.14)$$

In order to scale the skin depth by a factor  $P$ , the electrical conductivity  $\sigma_{el}$  must be scaled by a factor  $\frac{1}{P^2}$ . Since we keep the same EM configuration the longitudinal impedance per unit length must remain unchanged. As a consequence, the longitudinal impedance of the scaled setup will be  $P$  times larger than the unscaled setup. The scaling can be verified using Eq. (3.5). In fact, since the characteristic impedances of the layers scale with  $P$  and the characteristic quantities  $k s_n$  and  $k b$  do not depend on  $P$ ,  $\zeta_m$  also scales with  $P$ . Driving and detuning impedances of the scaled setup will be  $P$  times smaller than the impedances of the unscaled setup (see Eq. (3.10)). Therefore, using the scaling technique, with the same computational effort of the original configuration ( $P = 1$ ), we can simulate a wake  $P$  times longer, thus lowering the coverable frequency range by a factor  $P$ . Putting together different simulations (different ranges of frequency) we can obtain the impedance of the DUT starting from very low frequencies. In general each scaling setup will give accurate results in a certain range of frequency where the lower and upper limit are determined respectively by the wake length WL and the bunch length  $\sigma_z$ .

### A simple example of application

As a first example of application we consider a chamber of rectangular cross section made of resistive material with PEC boundaries in  $x$  and  $y$  and perfectly matched layer (PML) boundary in  $z$ . For this simple structure we can obtain the theoretical frequency behavior using the TL model described in the previous section. In Fig. 3.13 the theoretical results have

been compared with the simulation results obtained by means of the scaling technique. The excellent agreement between results from the real and the scaled setup proves the reliability of this technique.

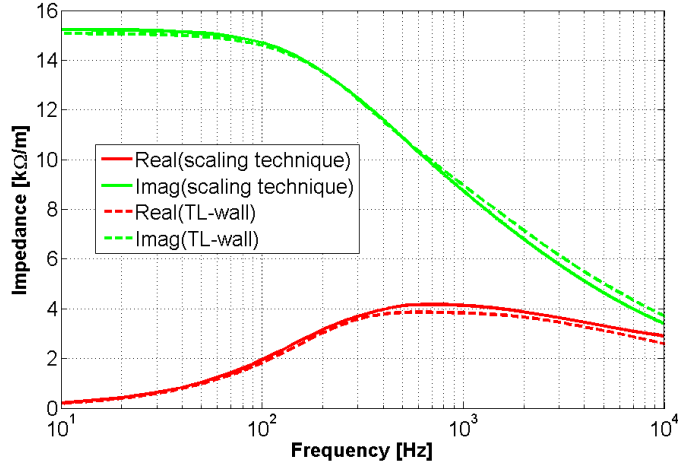


Figure 3.13: Horizontal driving impedance. Comparing theoretical and simulation results for a chamber of rectangular cross section made of resistive material ( $\sigma_{el} = 1.67 \times 10^6$  S/m) and with the following geometrical parameters:  $a = 23.2$  mm,  $b = 18.4$  mm,  $L = 200$  mm and wall thickness  $S = 40$  mm.

#### 3.2.2 Electromagnetic simulation of the LHC beam-screen including the weld

First studies on the beam screen impedance model can be found in [91]. More detailed studies were later conducted and summarized in [92]. Based on a semi-analytical analysis, it was estimated that the weld creates an increase of the power loss by 35-40% due to the higher longitudinal beam coupling impedance. The impact of the longitudinal weld (see Fig.3.12) on the transverse impedance remained an open task.

In order to study the possible effect of the resistive wall impedance on the transverse coupled-bunch instability [93], the frequency range of interest ranges between 8 kHz ( $((1 - Q_{x,y})\omega_0$  the first possible unstable betatron line in the LHC) and 40 MHz (frequency of the 25 ns bunch spacing). As already pointed out, to perform impedance simulations at these frequencies we need large values of WL in order to have enough resolution in the frequency domain. Furthermore, to make a good Fourier transform, the wake is required to vanish. The scaling technique described in the previous section seems to be a suitable tool to evaluate the transverse impedance of the LHC beam screen covering the interesting range of frequencies (i.e. down to kHz).

The aim of this study is to include properly also the effect of the weld. In this frame we approximate the beam screen with a rectangular geometry. Using a feature available from CST 2011 it is possible to define a material as coated allowing for a compact representation of the material as a surface impedance without the need of meshing the coating itself. For our purpose we defined a SS layer of 1 mm coated with Cu ( $50\mu\text{m}$  thick). In order to include the effect of

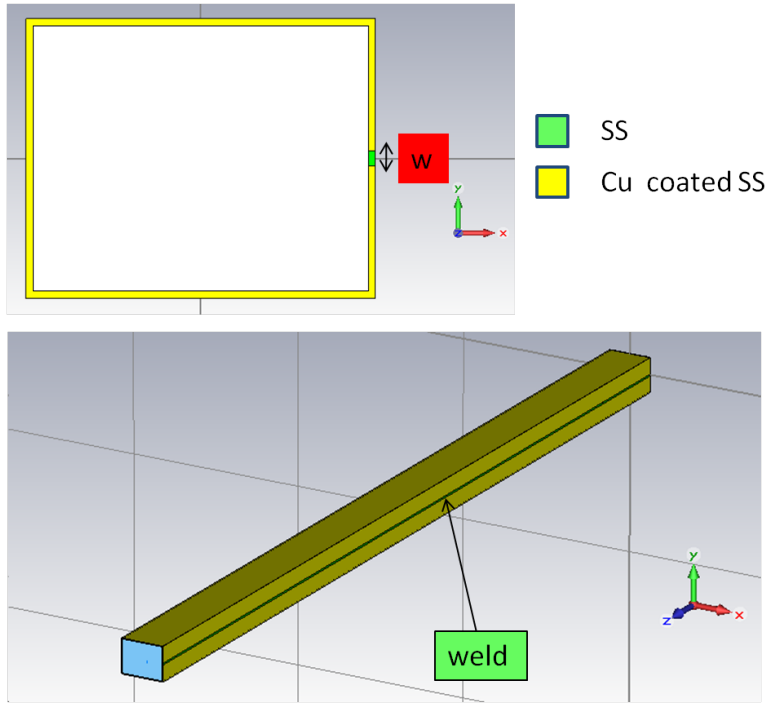


Figure 3.14: The LHC beam screen as it is simulated. Geometrical parameters:  $a = 23.2$  mm,  $b = 18.4$  mm,  $L = 1$  m,  $w = 2$  mm. The electrical conductivity at the cryogenic operating temperature is assumed to be  $1.82 \times 10^9$  S/m for Cu and  $1.67 \times 10^6$  S/m for SS [89, 91, 92].

the weld, the corresponding area is considered uncoated (see Fig. 3.14). The estimation of the relative effect of the weld, for both longitudinal and transverse impedance, is performed comparing the impedance of the beam screen, in the rectangular approximate geometry, with and without weld (the wall is made of SS coated with Cu). For a simple representation of the weld effect we introduce the factor  $G = \frac{Z_{\parallel,x,y}^{\text{weld}}}{Z_{\parallel,x,y}}$  where  $Z_{\parallel,x,y}^{\text{weld}}$  is the impedance in case of the presence of the weld and  $Z_{\parallel,x,y}$  is the impedance without weld.

The Cu coated SS could be approximated with an infinitely thick Cu layer when the skin depth  $\delta$  in Cu is much smaller than the thickness of the copper coating. In our case this turns out to be a good approximation only for frequencies above a few hundreds of kHz. To analyze accurately lower frequencies, we need to use the detailed model of Fig. 3.14.

### Simulation results

Due to the presence of the weld, the LHC beam screen is an asymmetric structure, which means that a transverse effect is also possible in the geometric center of the chamber. Therefore, to disentangle driving and detuning components of the wake, we use the procedure for asymmetric device described in 1.1.2. Resorting to the scaling technique, we were able to cover the frequency range between 1 kHz and 100 MHz. In order to explore such a large range of frequencies, five simulations with scaling factor  $P$  varying between 1 and  $10^4$  were performed (linear logarithmic step). Basically each simulation was optimized to characterize the impedance over a frequency decade. Figure 3.15 shows the  $G$  factor for longitudinal and

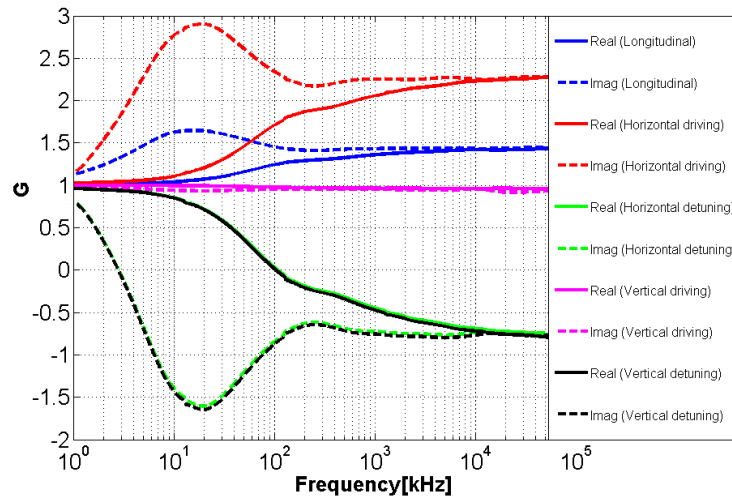


Figure 3.15:  $G$  factor for longitudinal (blue) and transverse: horizontal driving (red), horizontal detuning (green), vertical driving (magenta), vertical detuning (black). Real part are full lines and imaginary part dashed lines.

transverse impedances in the frequency range of interest. It is worth underlining that the real part of the longitudinal impedance is found to increase by 40 – 45% in very good agreement with the 35 – 40% increase found in [92]. In [92] a value of  $2 \times 10^6$  was used for the SS conductivity, which might explain the slightly higher value obtained in our analysis. The weld plays the most significant role in the horizontal driving impedance. At the moment based on these simulations a factor  $G = 2$  is considered in the LHC impedance model to account for the effect of the weld in the horizontal driving impedance [1]. For the vertical driving impedance the effect of the weld is negligible. For the detuning impedance  $G$  becomes negative meaning that the weld causes a change of the sign of the impedance. Moreover, the very similar absolute values of  $G$  for horizontal and vertical detuning is another indication of a very good relative accuracy of the simulations (should be equal according to Eq. (1.15)).



## 4 Experimental applications

In this chapter we present the dedicated measurements involving applications of the impedance models described in previous chapters 2 and 3. The applications mainly consist of benchmarks with test bench or beam measurements. Bench measurements based on the coaxial wire method have been used to verify the impedance model of single kicker magnets. Beam observables, like tune shift and beam induced heating measurements, have been used, respectively, to validate the SPS impedance model (kicker and resistive wall) and the longitudinal impedance model of the MKE with and without serigraphy. In the last part of the chapter we will also present an experimental setup for measuring EM properties (permittivity and permeability) of materials and describe the method used as well as the results obtained by applying it to some materials of our interest.

### 4.1 Bench measurements: the wire method

Ideally measurements of beam coupling impedances of a device should be done by exciting the device with the beam itself [94]. However, in most cases this solution is not possible and one must resort to bench measurement techniques in which the beam is simulated by a current pulse flowing through a wire stretched along the beam axis. For beam coupling impedance evaluations, the wire method (WM) is a common and appreciated choice. This technique was proposed in the first half of the 70's, based on intuitive considerations. By means of WM, Faltens et al. [95] measured the wall contributions to the beam coupling impedance. M. Sands and J. Rees (1974) [96] measured the energy loss of a stored beam to a cavity due to the higher mode excitation. Moreover, at BNL and at CERN, the method was employed to measure the longitudinal and transverse beam coupling impedance [52, 97] of a kicker in the frequency domain. The method of Sands and Rees requires a complex numerical manipulation to obtain the beam coupling impedance from the measured quantities, because of the presence of multiple reflections in the measuring devices [96]. An improved method of measurement that does not need this manipulation was proposed by V. G. Vaccaro [98].

Since many years it has become customary to use the coaxial wire method [96, 98] to measure the beam coupling impedance of accelerator devices (e.g. [32, 33, 34, 37, 68, 97, 99, 100, 101, 102, 103]). Nevertheless, the results obtained from wire measurements might not entirely represent the solution of our initial problem, because the presence of the stretched wire perturbs the EM boundary conditions. The most evident consequence of the presence of

another conductive medium in the center of the device under study is the fact that it artificially allows TEM propagation through the device, with zero cut-off frequency. The presence of a TEM mode among the solutions of the EM problem will have the undesired effect to cause additional losses during the measurement. Theoretical studies about the validity limits of the Sands and Rees method in relation to the presence of the central wire that simulates the beam can be found in Ref. [104], where, by means of a general theoretical approach, the effect of the central conductor with small but finite radius has been studied. As results for an example of application (pill-box cavity with a radius of 15 cm using a wire with a diameter of 1.12 mm) the longitudinal beam coupling impedance of the DUT, calculated with this approach, is very similar to the impedance obtained with the Sands and Rees formula (Fig. 2 of Ref [104]). Details about the measurement setup used in [104] can be found in [105]. However, the mode analyzed in this study is above the cut off frequency of the beam chamber. For modes below this frequency, due to the TEM propagation introduced by the wire, the WM is found to provide inaccurate results, as investigated in Ref. [106] comparing the impedance with and without a wire for a Copper pillbox, by means of the Mode Matching Technique.

### 4.1.1 Numerical investigation of the wire method

For a better understanding of the limitations of the WM, we performed numerical measurements, simulating the measurement setup with the Transient Solver of CST Microwave Studio. The main output of the simulation, which is also the physically measurable quantity, is the scattering parameter  $S_{21,DUT}$ . As example, we analyzed the case of an MKE-L with serigraphy (see Fig. 2.31) for the longitudinal impedance. Differences with respect to the real setup could arise from the losses in the wire (considered lossless in the model) and from the imperfect matching of the DUT to the network analyzer. In the simulation the kicker is perfectly matched at both ends. The longitudinal impedance is calculated from the  $S_{21,DUT}$  using the standard log formula ( e.g. Eq. (2.8) of Ref. [37]):

$$Z_{\parallel} = -2Z_{ch} \log \left( \frac{S_{21,DUT}}{S_{21,REF}} \right) \quad (4.1)$$

where  $S_{21,REF} = e^{-j\omega \frac{L}{c}}$  and  $Z_{ch}$  is the characteristic impedance of the coaxial line formed by the wire and the DUT wall.  $Z_{ch}$  is also an output of the simulation. It is worth observing that the kicker structure of Fig. 2.31 with wire can in reality support 2 TEM modes due to the presence of three conductors (wire conductor in addition to the mass (cold) and HV (hot) conductor (see Fig. 2.2)). Figure 4.1 shows a comparison of CST-Wake-field solver simulations and numerical measurements. A very good agreement is found for the broadband behaviour. On the contrary, the low frequency resonance appears to be lowered and widened, suggesting that both its quality factor and peak values are reduced by a certain factor. This is visible in the zoom displayed in Fig. 4.2. The simple example of a pillbox with resistive walls will clarify what happens. Let us consider a cavity mode below the cut-off frequency of the attached beam pipe. In the real configuration of the structure (without wire) this mode can only get dissipated on the cavity wall. Introducing a wire, the beam pipe is turned into a coaxial cable



and its cut off frequency vanishes. The mode, which would be otherwise trapped in the cavity, will be able to lose power also through propagation (TEM propagation). Therefore, defining  $Q_{WM}$  the quality factor measured with the wire,  $Q_{\Omega}$  that of the ohmic losses and  $Q_{prop}$  that associated with the propagation losses, the following relation will hold for a mode below the cut-off frequency of the beam pipe:

$$\frac{1}{Q_{WM}} = \frac{1}{Q_{\Omega}} + \frac{1}{Q_{prop}} \quad (4.2)$$

It should be noticed that assuming  $Q_{\Omega} \gg Q_{prop}$  (very well satisfied for low loss pillbox made for instance of Cu, Ag, etc.),  $Q_{WM}$  tends to be equal to  $Q_{prop}$ . In this case, the WM is only measuring the losses introduced by its own presence in the DUT. Below the pipe cutoff frequency, the WM provides reliable results only if  $Q_{\Omega} \ll Q_{prop}$ . Equation (4.2) has been verified by using CST numerical simulations. The Ohmic quality factor  $Q_{\Omega}$  of the mode can be calculated simulating the structure without wire ( $Q_{prop} = \infty$ ) and taking care of simulating a sufficiently long WL. The term  $Q_{prop}$  is computed separately considering a PEC pillbox ( $Q_{\Omega} = \infty$ ) with wire. Finally considering the structure with wire, the quality factor of the measurement setup  $Q_{WM}$  is simulated and the validity of Eq. (4.2) can be checked. Above the pipe cutoff frequency the situation is less critical since propagation losses are allowed both with and without wire. The wire acts as a perturbation and will only slightly lower the quality factor and the peak value of the resonances.

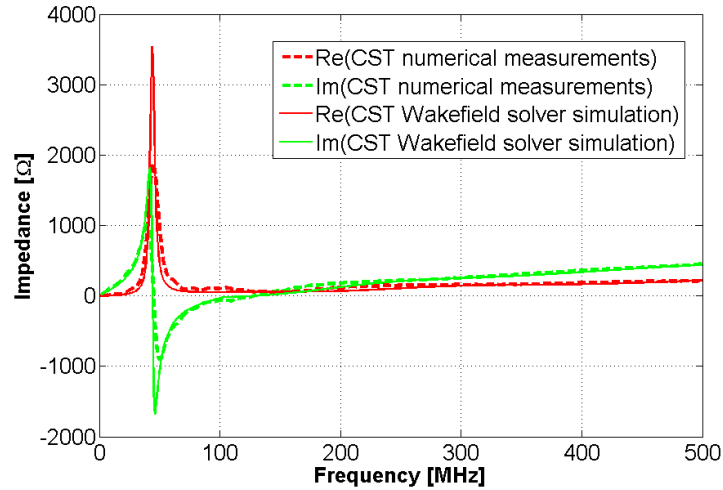


Figure 4.1: Longitudinal impedance of an MKE-L with serigraphy: comparing CST numerical measurements and Wakefield solver simulations.

#### 4.1.2 Comparing wire measurements and impedance models

The measurement setup and the procedures to obtain longitudinal and transverse impedances are outlined in [34, 37]. In this section we just show comparisons of coaxial wire measurements

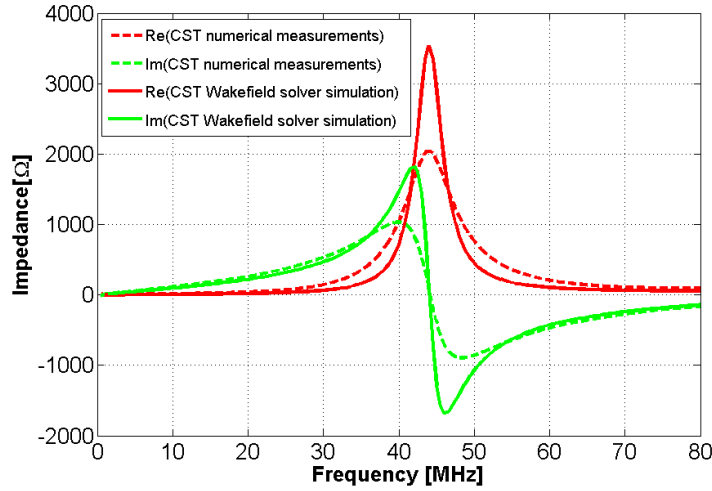


Figure 4.2: Low frequency behaviour of the longitudinal impedance for the MKE-L with serigraphy: comparing CST numerical measurements and Wakefield solver simulations.

and CST simulations. We obtain the longitudinal and the generalized transverse impedance from measurements of the scattering parameter  $S_{21,DUT}$  at different wire locations [33, 107] and the driving impedance from the two wire measurements [37, 99, 108].

A measurement campaign to measure the impedance of the SPS injection kickers MKP11955 (see Tab. 2.1) took place during July 2010. Figure 4.3 shows the longitudinal (left) and generalized vertical (right) impedance compared with the simulation model. Despite the limitations and uncertainty of the measurement method a good agreement is observed in both the longitudinal and transverse planes. The impedance of the SPS extraction kickers was also the object of several measurements performed during the campaign of the 2005-2007, focused on the reduction of the beam induced heating of these devices. New measurements have been performed during 2010 and 2011. From all the measurements data [34, 37] a good match with the advanced impedance model has been found. Figure 4.4 shows a comparison of the longitudinal impedance model for the SPS extraction kickers with the 2011 measurements carried out on both serigraphed and unserigraphed kicker. Despite a good agreement for the broadband impedance behavior, a clear difference is observed in the peak due to the serigraphy. Partly this difference can be explained by the additional losses introduced by the wire technique. Besides, the real setup is also affected by other loss mechanisms not modeled in the simulation (e.g. imperfect matching of the DUT to the network analyzer), which further changes amplitude and width of the resonance peak. A comparison of measurements and impedance model for the dipolar vertical impedance of an MKE with serigraphy is shown in Fig. 4.5. The measurements were performed by T. Kroyer with the two wire method [37]. Similarly to the longitudinal case we notice a good agreement in the broadband behaviour and some differences in the resonance due to the serigraphy.

#### 4.1. Bench measurements: the wire method

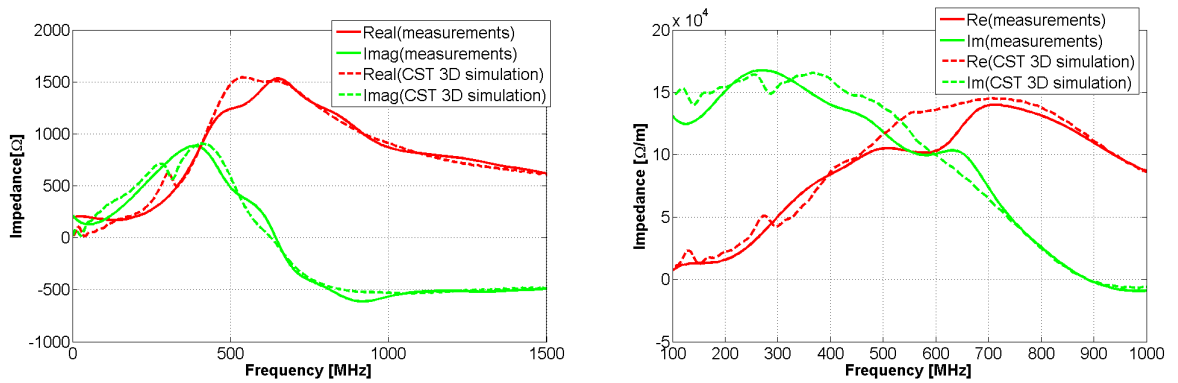


Figure 4.3: Comparing longitudinal (left) and generalized vertical (right) impedance for the MKP11955: coaxial wire measurements (full lines) and CST 3D simulations (dashed lines).

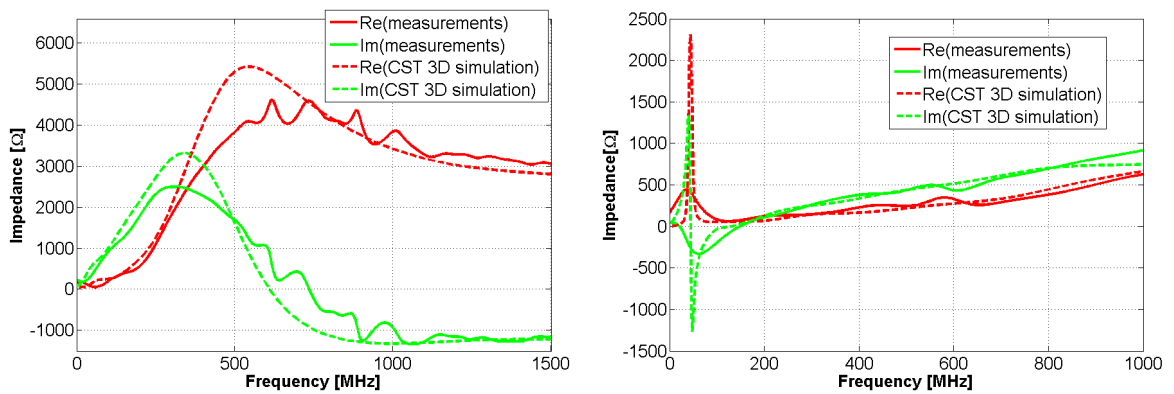


Figure 4.4: Comparison of coaxial wire measurements and CST 3D simulations for the longitudinal impedance of the unshielded MKE (left) and the shielded MKE (right).

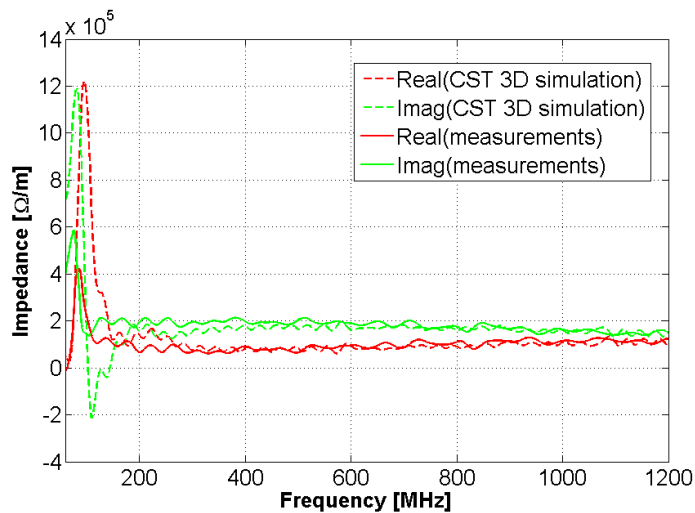


Figure 4.5: Comparison of coaxial wire measurements and CST 3D simulations for the vertical driving impedance of the shielded MKE.

### 4.2 Observations with beam

In the first section, we have dealt with a method used for bench measurement of the beam coupling impedance of individual vacuum chamber components (cavities, kicker etc.). A bunch of particles traveling in a real machine experiences the integrated effect of its electromagnetic interaction with all the vacuum chamber components. Coherent tune shift, instability thresholds and growth rates depend on the effective impedance of the machine (Eq. (1.24) and Eq. (1.25)). In particular one finds that its resistive part is responsible for the growth rate of the instabilities, while its imaginary part causes tune shift [8, 9, 10, 11]. The direct measurement of these effects is a powerful means to deduce information on the global effective impedance of a machine. In the first subsection, based on transverse tune shift measurements, we will focus the attention on the evaluation of the imaginary part of the transverse effective impedance of the SPS.

The second subsection will focus on the estimation of the longitudinal impedance of the MKE kickers based on the direct measurement of the beam induced heating in different beam conditions. This is possible because, as was shown in Chapter 2, the real part of the longitudinal impedance is directly related to the beam power loss  $\Delta W = \Delta E f_0$  (see Eq. (1.10)).

#### 4.2.1 Tune shifts measurements

Tune shift measurements give integrated information about the effective impedance of a machine, which depends on both its full impedance and the length/shape of the bunch used for the measurements (see Eq. (1.25)). The full impedance of a machine can be constructed by adding the impedances of all its components adequately weighted.

The first attempt to construct an impedance model for the SPS ring was addressed in the PhD thesis of B. Salvant [109]. This project is presently still ongoing and the model is continuously updated due to modification of some elements or the identification of new sources of impedance and their inclusion in the model. The present transverse impedance model of the SPS includes kickers, wall, beam position monitors (BPMs) and RF cavities. The SPS kicker and wall impedance model has been obtained as described in chapters 3 and 4 and represents the dominant part of the SPS effective impedance model. The impedance model of BPMs and RF cavities has been obtained from CST 3D simulations [110, 111].

The effective impedance [6, 7, 8] is calculated for the mode  $l = 0$  assuming a Gaussian bunch (Eq. (1.25)) using the impedance models of Figs. 2.42 and 2.43 for the kicker contribution and Figs. 3.9 and 3.10 for the resistive wall contribution. The effective impedance is directly related to the tune shift (e.g. see Eq. (6.207) of Ref. [8]). Tune shift measurements can be performed with high precision in SPS thanks to the Q meter system. The measurements are performed on a single circulating bunch of particles. The tune is measured as a function of the bunch intensity. The bunch length is also measured and recorded for each intensity.

For the Q20 optics the measured vertical tune shift during the 2012 [112] leads to a total SPS vertical effective impedance of  $18.3 \pm 0.7 \text{ M}\Omega/\text{m}$ . The uncertainty on the impedance has been calculated propagating in Eq. (6.207) of Ref. [8] the uncertainty of the tune shift measurements. The advanced model of the SPS kickers in the same conditions of the measurements predicts an effective vertical impedance of  $7.0 \text{ M}\Omega/\text{m}$ . Adding also the resistive wall contribution we

obtain  $(Z_y)_{\text{eff}} = 11.5 \text{ M}\Omega/\text{m}$ . Finally adding the contributions for RF cavities and BPMs we end up to  $(Z_y)_{\text{eff}} = 12.7 \text{ M}\Omega/\text{m}$  (about 70% of the measured effective impedance). The agreement is considered satisfactory, since a more detailed model including also other SPS impedance sources (e.g. pumping ports and septa) should explain at least part of this difference. Moreover, since the extrapolation of the effective impedance from the tune shift requires the knowledge of the bunch intensity and bunch length, it is very difficult to guarantee an uncertainty lower than 10-20% [42, 113].

A direct comparison between measurements and the impedance model is showed in Fig. 4.6 where we compare the vertical tune measurements with the tune obtained from Eq. (6.207) of Ref. [8] using as input the effective impedances of the SPS impedance model and the measured bunch intensity and bunch length for each point.

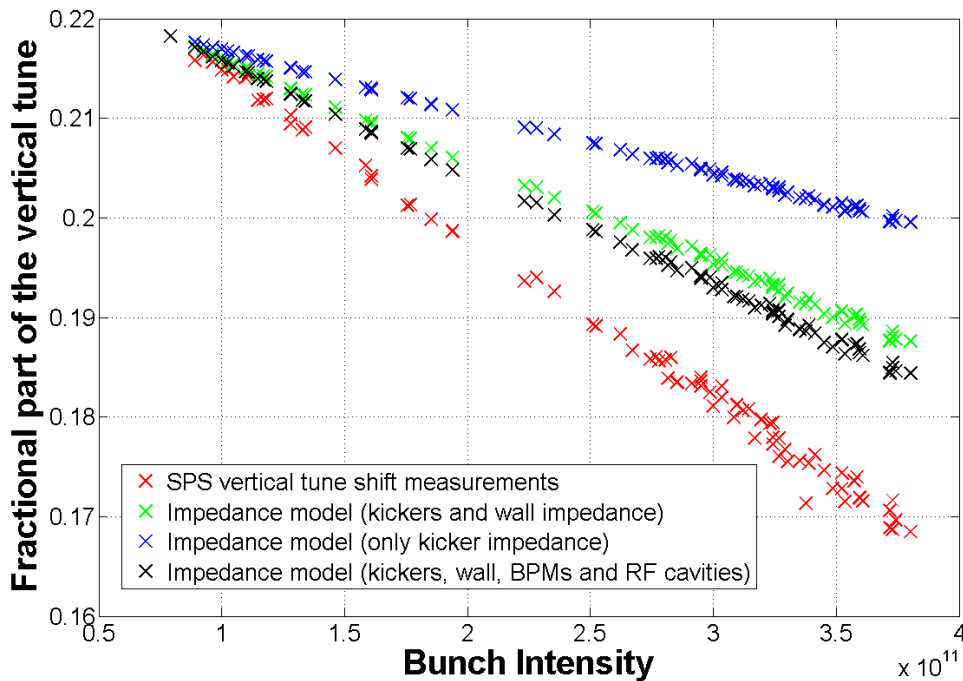


Figure 4.6: Vertical tune shift as a function of the bunch intensity. The measurement uncertainty is in the order of  $10^{-4}$ .

From 2001 the main modifications in the SPS complex concern the extraction kickers. Table 4.1 summarizes the total number of MKEs in the SPS year by year, specifying how many of them were serigraphed at the different stages. The SPS transverse impedance was well monitored by means of beam based measurements over the years. Several tune shift measurements were performed to keep track of its evolution [88, 114, 115, 116, 117, 118, 119, 120]. In Fig.4.7 we compare the relative change of the measured tune shift with the relative change of the SPS kicker impedance model due to the MKEs between 2001 and 2011. When comparing impedance values extrapolated from the tune shift measurements from different MD sessions

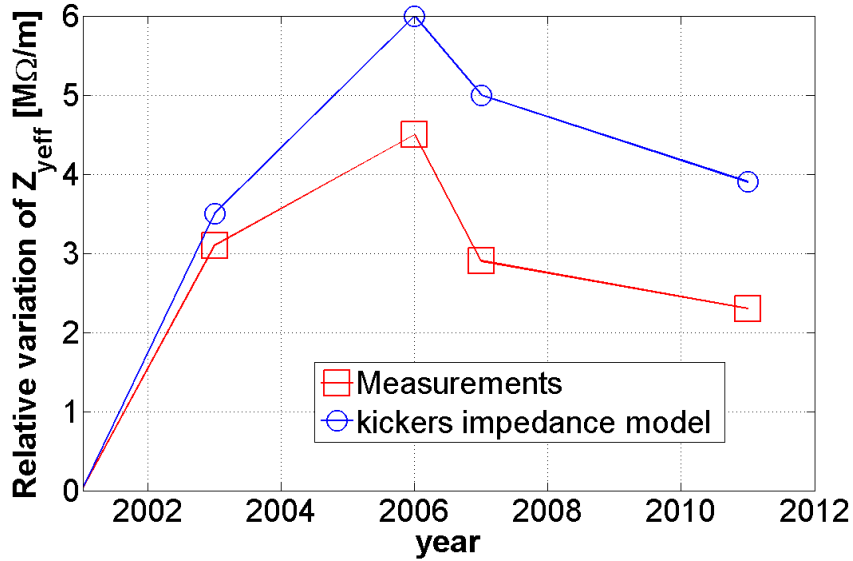


Figure 4.7: Comparison between the relative change of the measured SPS vertical effective impedance and the relative change of the SPS kickers vertical effective impedance model between 2001 and 2011. See Table 4.1 for installation and serigraphy data.

over the years, a certain level of uncertainty must be taken into account, due to the reproducibility of the beam conditions (e.g. bunch length, beam production in the pre-injectors) and the SPS machine settings (e.g. working point, chromaticity, magnetic status of the machine due to the position of the MD cycle in the supercycle).

Despite that, it is evident that the trend of the measured effective impedance follows quite closely the one that could have been expected based on the evolution of the kicker situation. This is an important confirmation that from 2001 onwards, the change in the SPS impedance has been largely dominated by the installation and serigraphy of the MKE's.

In the horizontal plane all the tune shift measurements exhibit a positive slope, which translates into a negative total SPS horizontal effective impedance [109, 120, 121]. The SPS impedance model predicts an effective horizontal impedance of  $-0.9\text{M}\Omega$  in agreement with the flat or slightly positive slope observed in tune shift measurements. A negative impedance (positive slope of the tune shift) can appear only if the detuning term is larger than the driving term. This is exactly compatible with the flatness of most of the SPS chambers, as well as with the features of the C-magnet kicker impedance model. This observation also suggests that the contribution of other elements of the SPS to the generalized horizontal impedance should be negligible. In Fig. 4.8 we compare measurements of the horizontal tune shift with the SPS impedance model. Finally, as for the vertical plane, we compare the relative change of the effective impedance with the relative change predicted by the kicker impedance model (see Fig.4.9). Also in this case the trend of the measured effective impedance is in good agreement with the relative change predicted by the kicker impedance model.

year	MKE (incl. MKESer)	MKESer
2001	0	0
2003	5	0
2006	9	0.5
2007	8	1.5
2009	8	3
2011	8	5
2012	8	7

Table 4.1: Total number of extraction kickers in SPS and the part of them serigraphed.

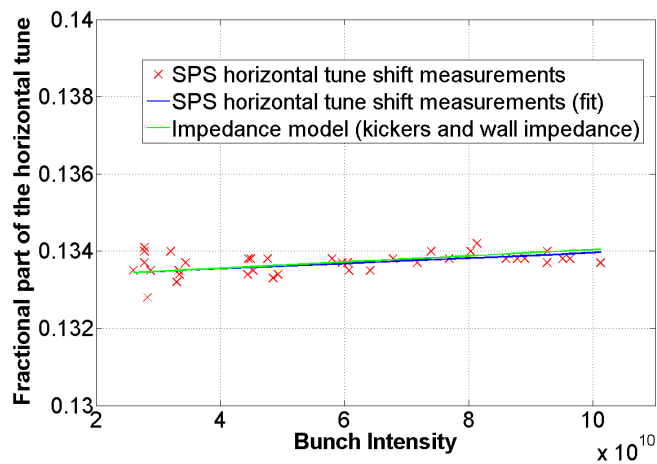


Figure 4.8: Fractional part of the horizontal tune shift as function of the bunch intensity. The measurement uncertainty is in the order of  $10^{-4}$ .

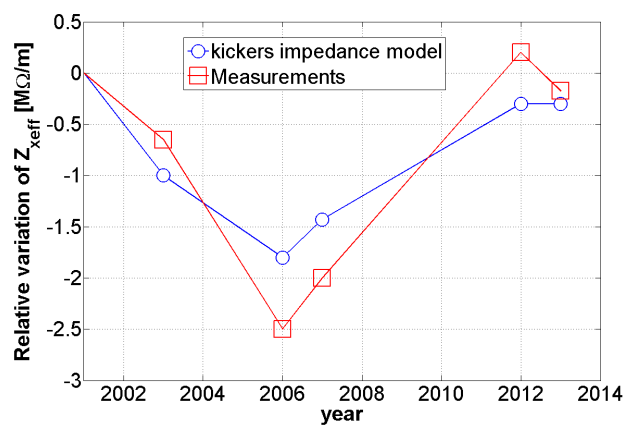


Figure 4.9: Comparison between the relative changing of the measured SPS horizontal effective impedance and the relative changing of the SPS kickers horizontal effective impedance model between 2001 and 2013.

### 4.2.2 MKE heating

#### Power loss calculation method

The power lost by a beam passing with revolution frequency  $f_0 = \frac{\omega_0}{2\pi}$  through a device having longitudinal impedance  $Z_{\parallel}(\omega)$  can be expressed as (cfr. (1.10)):

$$\Delta W = (f_0 e N_{\text{beam}})^2 \sum_{p=-\infty}^{p=\infty} \left( |\bar{\Lambda}(p\omega_0)|^2 \text{Re} [Z_{\parallel}(p\omega_0)] \right) \quad (4.3)$$

If  $Z_{\parallel}(\omega)$  can be expressed as a resonator impedance (or sum of resonators) and the following condition is satisfied:

$$f_s \ll \frac{f_r}{Q} \quad (4.4)$$

where  $f_s = \frac{1}{T_s}$ , with  $T_s$  being the bunch spacing,  $f_r$  is the frequency of the impedance resonance and  $Q$  is the quality factor of the resonances, the coupling between bunches can be neglected and the power loss can be calculated by resorting to the single bunch approximation:

$$\Delta W_{\text{SBA}} = n_{\text{bunches}} (f_0 e N_{\text{bunch}})^2 \sum_{p=-\infty}^{p=\infty} \left( |\bar{\lambda}(p\omega_0)|^2 \text{Re} [Z_{\parallel}(p\omega_0)] \right) \quad (4.5)$$

It is worth highlighting that the condition of Eq. (4.4) simply means that the coupling between

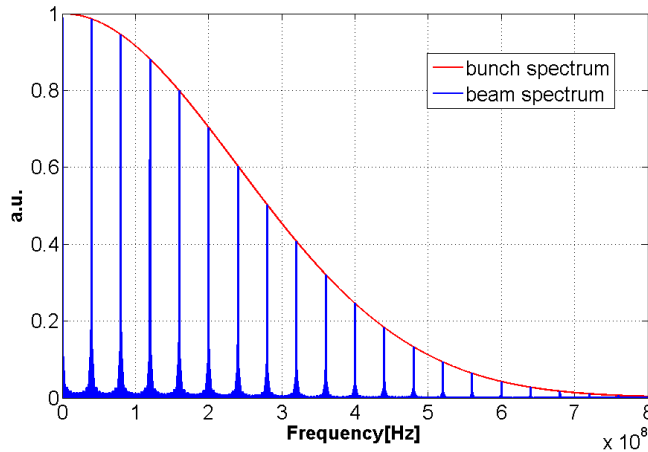


Figure 4.10: Bunch and beam spectrum assuming a Gaussian bunch profile for the 25ns SPS beam.

bunches is negligible because the wake induced by a bunch vanishes before the passage of the next bunch. Being  $N_{\text{beam}} = n_{\text{bunches}} N_{\text{bunch}}$ , the following relation can be found comparing



Eqs. 4.3 and 4.5:

$$\Delta W \leq n_{\text{bunch}} \Delta W_{\text{SBA}} \quad (4.6)$$

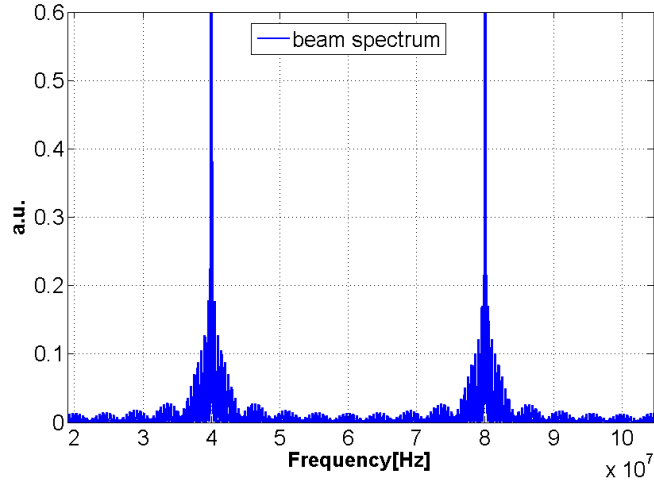


Figure 4.11: Zoom of the 25ns SPS beam spectrum.

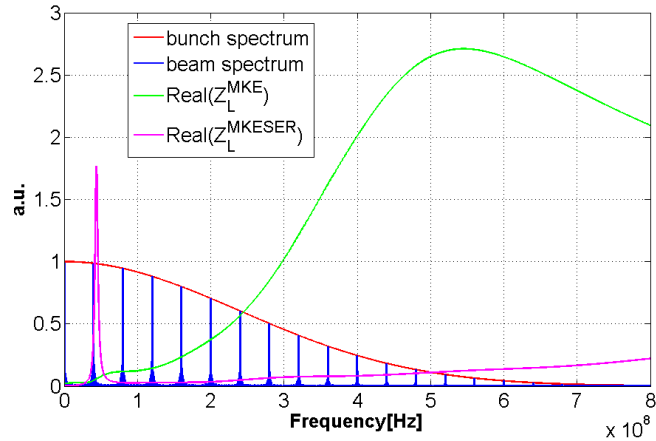


Figure 4.12: SPS beam and bunch spectrum together with the real part of the longitudinal impedance for an L-type MKE with and without serigraphy.

The SPS beam consists of 4 trains (also called batches) of bunches with bunch spacing typically of 25 ns or 50 ns and train spacing of 225 ns. Figure 4.10 shows the relative beam spectrum for the case of 25 ns and having assumed perfectly Gaussian bunches with  $\sigma_z = 0.2$  m. The envelope of the pulse train obviously corresponds to the single bunch spectrum, with Gaussian tails extending to  $\approx 1$  GHz. Figure 4.11 shows an arbitrary zoom of the beam spectrum for the 25 ns SPS beam, in which the finer structure of the line spectrum becomes more evident. The

main frequency lines are spaced by 40 MHz (associated with the bunch spacing), while other lines cluster around them, due to the train period and train spacing.

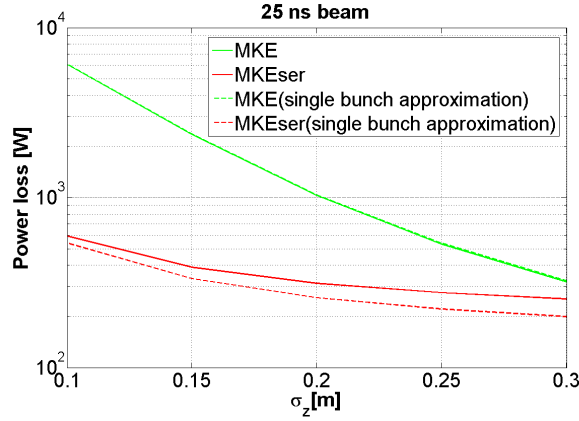


Figure 4.13: Power loss of an L-type MKE as function of the rms bunch-length for the SPS 25 ns beam with an intensity  $N_{\text{bunch}} = 1.1 \times 10^{11}$  performing the full calculation of Eq. (4.3) (full lines) and the single bunch approximation of Eq. (4.5) (dashed lines).

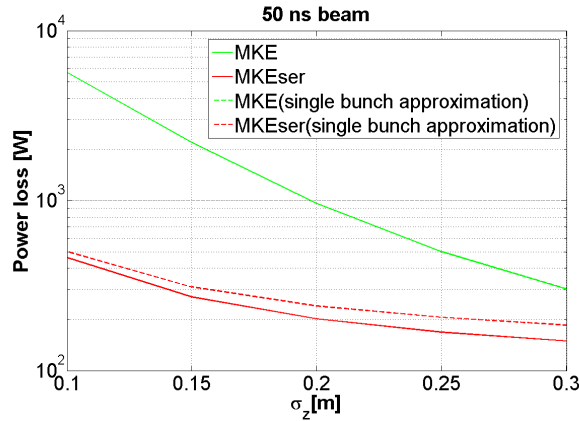


Figure 4.14: Power loss of an L-type MKE as function of the rms bunch-length for the SPS 50 ns beam with an intensity  $N_{\text{bunch}} = 1.5 \times 10^{11}$  performing the full calculation of Eq. (4.3) (full lines) and the single bunch approximation of Eq. (4.5) (dashed lines).

#### Application to the SPS extraction kickers

Figure 4.12 shows the beam spectrum together with the real part of the longitudinal impedance for an L-type MKE with and without serigraphy. Applying now Eqs. (4.3) and (4.5) with the impedance model shown in Fig. 2.37, we can calculate the power loss for an SPS extraction kicker. The calculation can be carried out for several values of bunch length, covering the range swept over a typical 25 ns or 50 ns beam production cycle. The results of these calculations are displayed in Figs. 4.13, 4.14, 4.15 and 4.16. Unlike an MKE without serigraphy, which has a clearly broadband behaviour, the impedance model of an MKE with serigraphy has a quite

narrow resonant peak in low frequency and thus does not fully satisfy the condition for single bunch approximation for either 25 ns or 50 ns beam, Eq. (4.4). For this reason the power loss calculated resorting to the single bunch approximation ((Eq. (4.5)) yields a different result with respect to that obtained by means of the Eq. (4.3), as appears from Figs. 4.13 and 4.14. Furthermore, it is worthwhile to observe the following points:

- Figures 4.13 and 4.14 show the clear difference between the power loss for kickers with serigraphy and that for kickers not serigraphed, for both 25 ns and 50 ns beams.
- The difference between 25 and 50 ns is expected to be less significant for non-serigraphed kicker (Fig. 4.15).
- The power loss ratio is a monotonic decreasing function of bunch length, as displayed in Fig. 4.16.

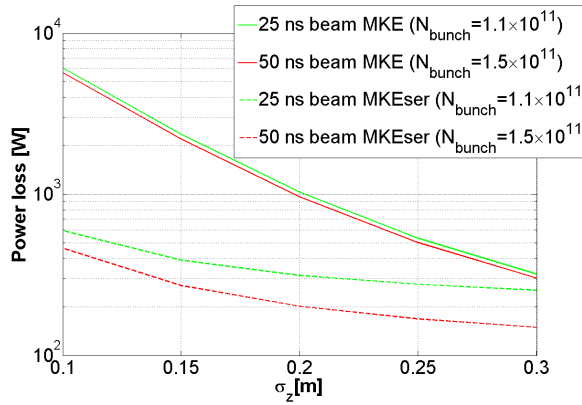


Figure 4.15: Power loss as function of the rms bunch-length for the SPS 25ns and 50ns beam with typical values of intensity per bunch.

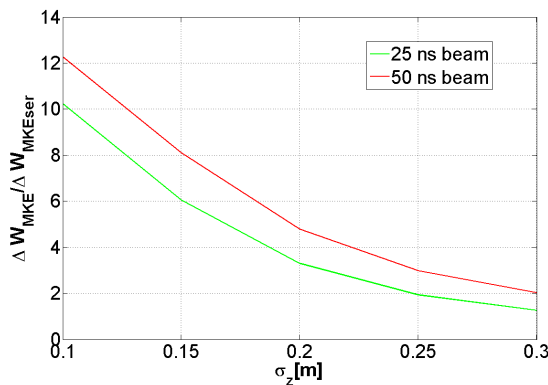


Figure 4.16: Power loss ratio between MKE with and without serigraphy for the 25ns and 50ns beam.

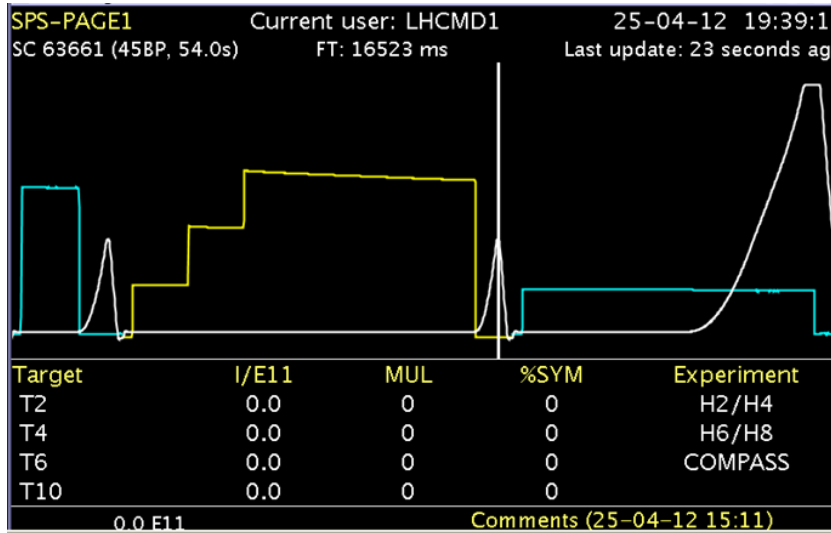


Figure 4.17: SPS supercycle during the MD on April 25th, 2012.

### Comparison with heating observations

In the previous subsection we calculated the power loss caused by four batches circulating in the SPS for a few different bunch length values. In order to compare it with direct heating observations, we need to consider the dynamics of the beam with the time. Typically, the SPS has a supercycle whose composition depends on the ongoing Machine Development (MD) activities and the beam requests from fixed target physics as well as from LHC. For instance, Fig. 4.17 shows the supercycle on a dedicated MD day (25/04/2012), in which a short 6 s cycle with a single bunch is followed by a long low energy cycle with three trains of 25 ns beam and a 21 s cycle with acceleration to 450 Gev with a lower intensity single bunch. To calculate the MKE heating from the power loss due to the 25ns beam, it is necessary to consider the fraction of time in which this beam is effectively circulating in the SPS (duty cycle), i.e. the ratio between the 25ns beam store time and the whole duration of the supercycle. Besides, two more aspects need to be taken into account: the beam intensity is changing while the beam is being injected and the bunch length changes along the energy ramp as illustrated in Fig. 4.18 for the case of the LHC 50ns filling cycle. The first aspect is considered by introducing an average beam intensity calculated as follow:

$$\langle N_{\text{beam}} \rangle = \frac{1}{t_2 - t_1} \sum_i \int_{\text{cycle}[i]} N_{\text{beam}}(t) dt \quad (4.7)$$

This analysis assumes that intensity per bunch and the beam spectrum are considered unchanged. In reality the beam spectrum changes according to the beam profile. A beam with only one batch will not exhibit the same frequency structure related to the batch spacing and batch period. However, Fig. 4.19 demonstrates that the power loss on both serigraphed and non-serigraphed MKEs normalized to the intensity remains unchanged for 1, 2 and 4 batches.

This means that the effect of the change in the beam spectrum is negligible and thus the effect of the multiple injections can be accounted for by simply rescaling by the beam total intensity. The time evolution of the bunch length leads to a time dependent power loss along the ramp. To take this aspect into account we can integrate the instantaneous power loss along the cycle:

$$\Delta W = \frac{1}{t_2 - t_1} \int_{t_1}^{t_2} \Delta W(t) dt \quad (4.8)$$

Neglecting the thermal radiation according to [66] and considering the power loss uniformly distributed on the ferrite block, simple application of the first law of the thermodynamics yields:

$$\frac{\Delta T}{\Delta t} = \frac{\Delta W}{C_{th}} \quad (4.9)$$

where  $\Delta T$  is the increase of temperature in the time window  $\Delta t$  and  $C_{th}$  is the thermal capacitance. In Eq.(4.9) the cooling is not included in the balance. The approximation of considering the power loss uniformly distributed on the ferrite is based on the observation made in [66] that the probe as installed on the kickers approximately measures the average temperature of the ferrite (see Fig. 4.20). Moreover, since the radiation is negligible, the cooling power can be assumed to be linear with the power loss, and can be included as follows:

$$\frac{\Delta T}{\Delta t} = \frac{\Delta W - P_{cooling}}{C_{th}} = \frac{\Delta W}{F_{cooling} C_{th}} \quad (4.10)$$

where  $P_{cooling} = G_{cooling} \Delta W$  is the cooled power and  $F_{cooling} = \frac{1}{1 - G_{cooling}}$  is the cooling factor. According to experimental estimations, the cooling system allows doubling the power loss on the ferrite [66, 122] ( $G_{cooling} > 0.5$ ,  $F_{cooling} > 2$ ). From Eq. (4.10) it can be deduced that the ratio between the power loss on a non-serigraphed MKE and that on a serigraphed MKE is equal to the ratio between their temperature rises:

$$\frac{\Delta T_{MKE}}{\Delta T_{MKEser}} = \frac{\Delta W_{MKE}}{\Delta W_{MKEser}} \quad (4.11)$$

Equation (4.11) provides an important instrument to benchmark the impedance model of the SPS extraction kickers with beam observations. As an example we analyzed the heating during the 25ns Machine development (MD) on April 25th 2012.

The MD was performed at the injection energy of 26 GeV and the RMS bunch length  $\sigma_z$  from the Gaussian fit of the bunch profile was estimated to be about 18 cm (2.4 ns). Direct measurements of the bunch length during the experiment are depicted in Fig. 4.21 with their relative error bars. We chose this experiment for our analysis, since it took place just after a technical stop of the machine operation, therefore the kickers had the time to cool down to

LHC fill	$\Delta T_{\text{MKE}} / \Delta T_{\text{MKEser}}$
2728	4.5
2729	6
2732	4.5
2816 -2817	5
2818	5
2836	6
2838 - 2839	5
2845	5
2847	5

Table 4.2: Heating ratio between the MKE with and without serigraphy during a selection of LHC fills.

the room temperature. In fact the application of Eq. (4.11) is more correct when the kickers have the same initial temperature. Figure 4.22 shows that a factor four was measured between the heating in the MKE with and that without serigraphy (both the MKE with and without serigraphy starts from the environment temperature of 23 °C and at the end of the MD reach respectively the temperature of 28 and 43 °C). This is in good agreement with that predicted by Eq. (4.11) using the SPS extraction kicker impedance model (see Fig. 4.16 for the 25ns beam with  $\sigma_z = 0.18$  m).

In order to compare the absolute value of the measured heating with our predictions we need to account for the beam intensity changing. The power loss is calculated with Eq. (4.3) using the average intensity value in the time period from Eq. (4.7). Figure 4.23 shows the integral of the intensity along each cycle, obtained by post-processing the intensity measurements performed with the beam current transformer (BCT) system of the SPS. The bunch length is considered constant, since the experiment was performed at injection energy (no acceleration). Along the 14 hours of the MD we calculated an integrated power loss on the MKE without serigraphy of about 144 W, which from Eq. (4.9) corresponds to an expected heating without cooling system of 42 °C. Including also the effect of the cooling system, this value has to be divided by about a factor 2, resulting in good agreement with the heating  $\Delta T = 20^\circ\text{C}$  observed during the MD.

A similar study has been performed also for the 50ns beam. Looking at the heating ratio between the MKE with and without serigraphy during a typical LHC fill, statistics based on a few fills has been done (see Tab. 4.2). From this statistics it is found that  $\left\langle \frac{\Delta T_{\text{MKE}}}{\Delta T_{\text{MKEser}}} \right\rangle \cong 5$  with a standard deviation of about 0.5. The fill 2818 has been analyzed into details as was done for the 25ns MD of April 25th. Figure 4.24 and 4.25 show respectively the measured heating during the fill and the integral of the intensity along the 50ns cycle during the time of the fill. In this case of study, since the beam is accelerated, for a correct estimation of the power loss also the evolution of the bunch length during the energy ramp needs to be considered (see Fig. 4.18). Accounting for both the intensity and bunch length changing with time (Eqs. (4.7) and (4.8)) during the 8 hours of the fill (Fig. 4.24, from 11.5 to 19.5), the integrated power loss

## 4.2. Observations with beam

should add up to 101 W. Using Eq. (4.9) this corresponds to a heating of 17 °C. As previously applied due to the cooling system, this value has to be divided by about a factor  $F_{\text{cooling}} = 2$  (see Eq. 4.10), which again is found in a very good agreement with the heating  $\Delta T = 7.5^\circ\text{C}$  observed during the experiment.

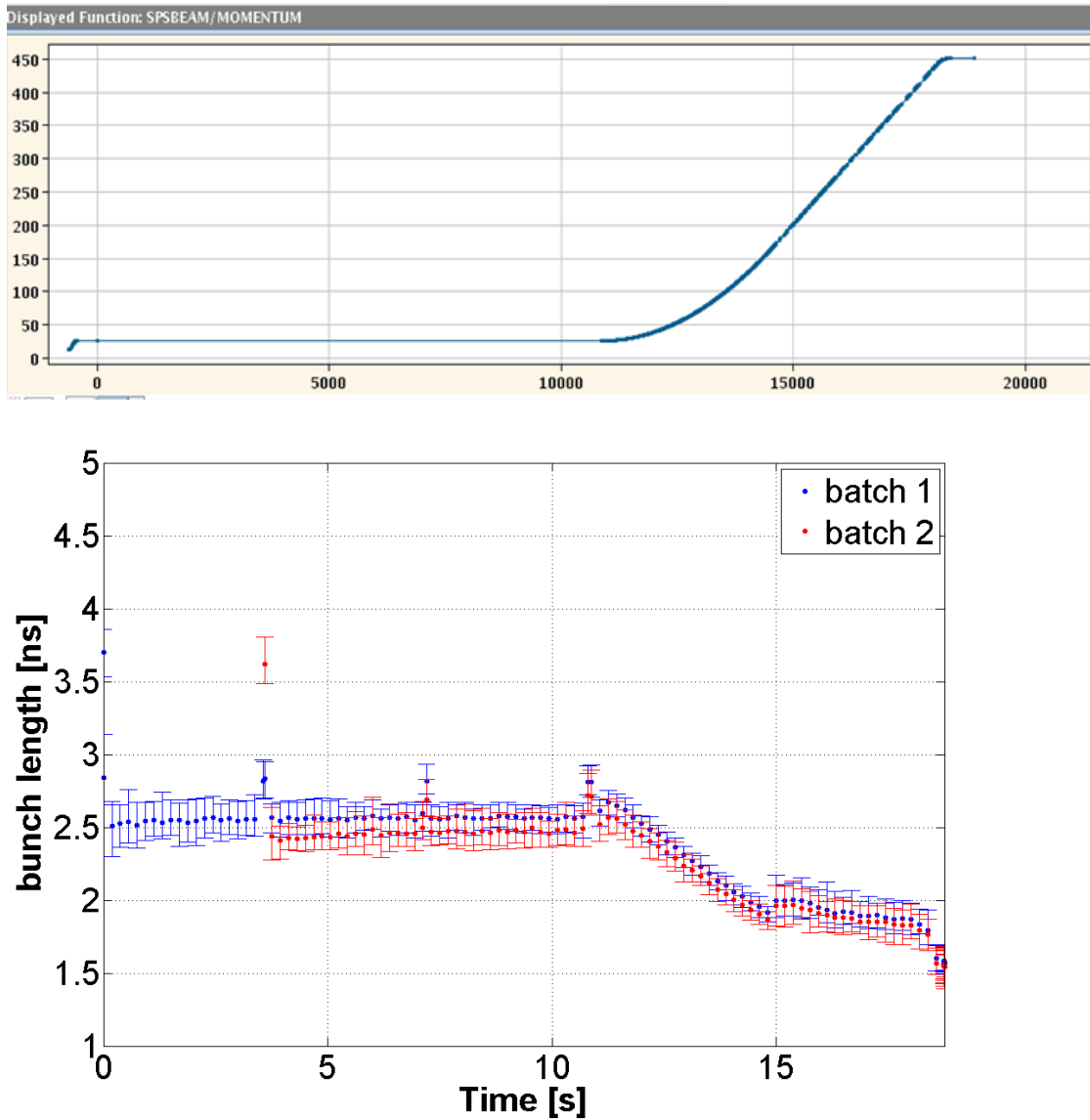


Figure 4.18: Typical evolution of the bunch length ( $4\sigma_z$ ) during the 50ns cycle. In the top picture the energy along the cycle is also depicted. Courtesy T. Argyropoulos.

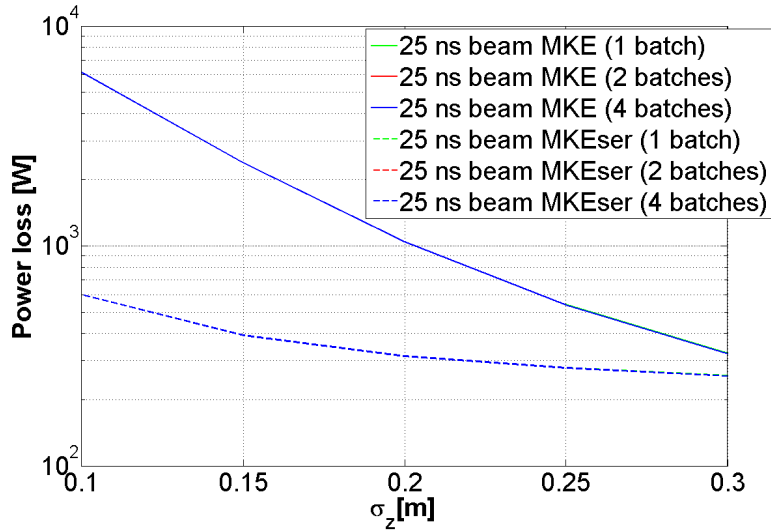


Figure 4.19: Power loss normalized to the intensity for the 25ns SPS beam with 1, 2 and 4 batches. The curves are perfectly superimposed.

- 1 - Pt100 probe
- 2 - Probed area
- 3 - Ceramic spacer
- 4 - Hottest area

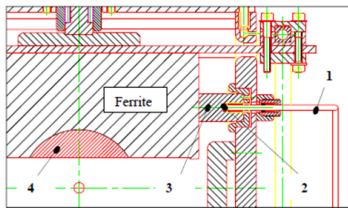


Figure 8 PT100 probe installation

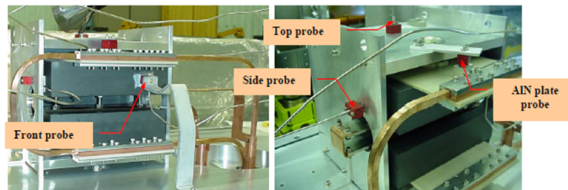


Figure 11 Photos of the cooling test bench and the probe's position

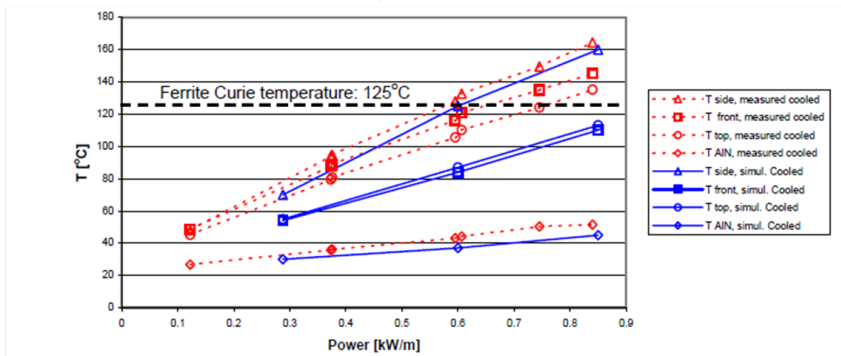


Figure 4.20: At the top left, temperature probe position as installed in the kicker. At the top right, probe positions on the test-bench. At the bottom, measured heating in the test bench as a function of the probe position ("front probe" corresponds to the probe position as installed on the kicker). Courtesy M. Timmins.



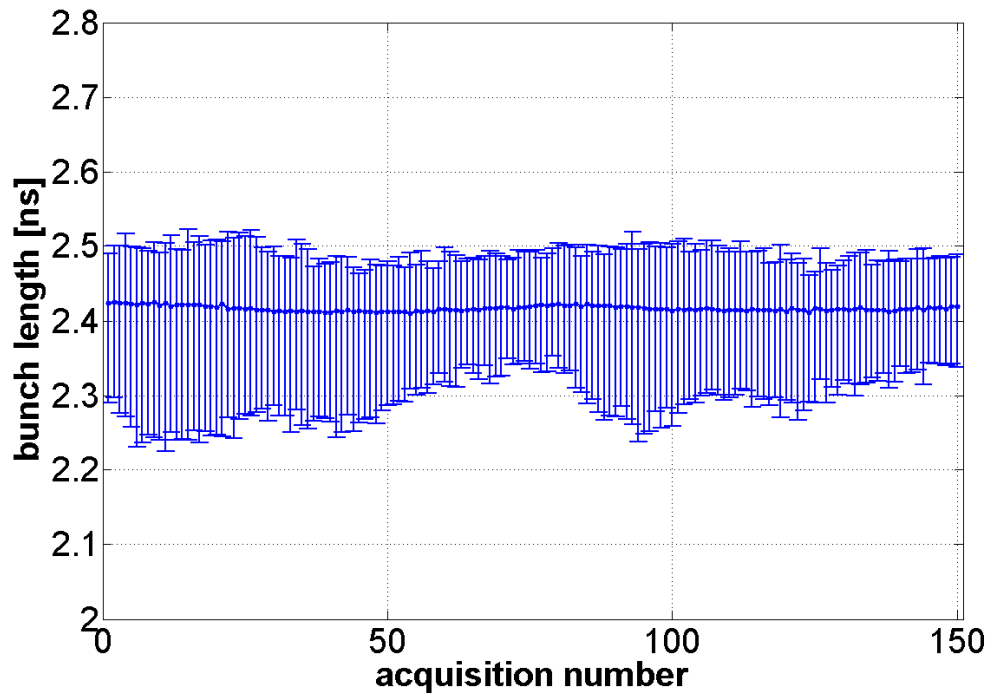


Figure 4.21: Bunch length acquisitions ( $4\sigma_z$ ) during the 25ns MD on April 25th 2012. Courtesy T. Argyropoulos.

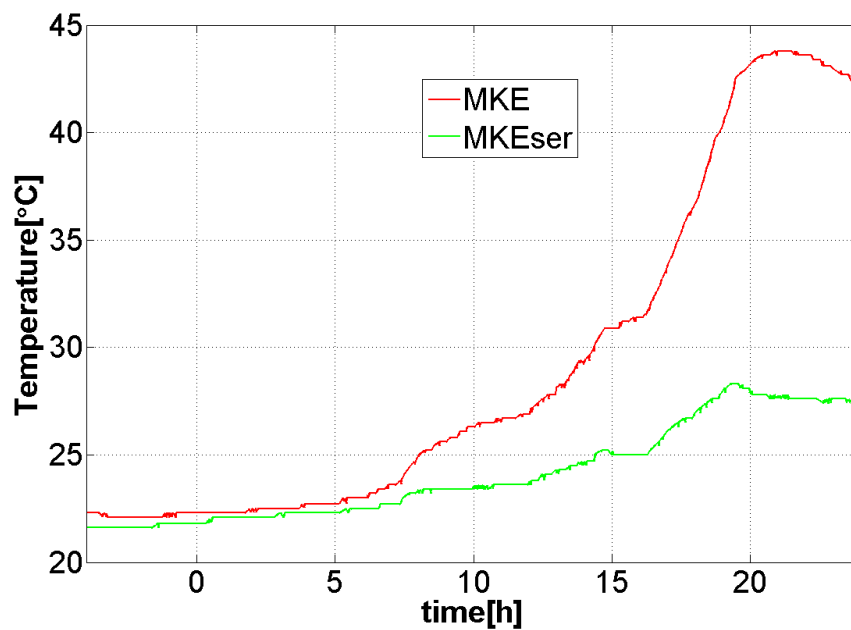


Figure 4.22: Measured heating during the MD on April 25th 2012 on the MKE with and without serigraphy.

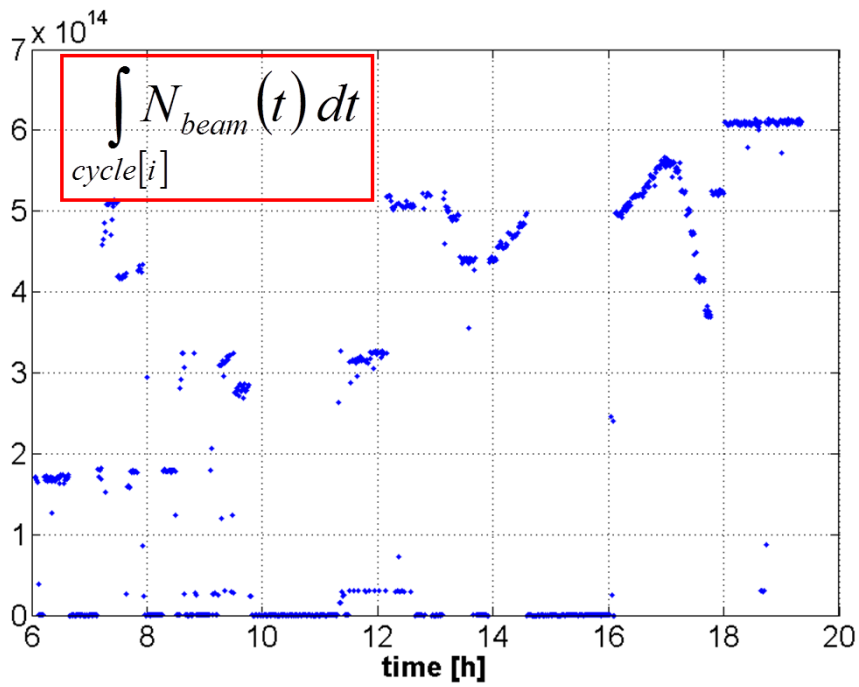


Figure 4.23: Integrated intensity along the 25ns cycle as a function of time during the MD on April 25th 2012.

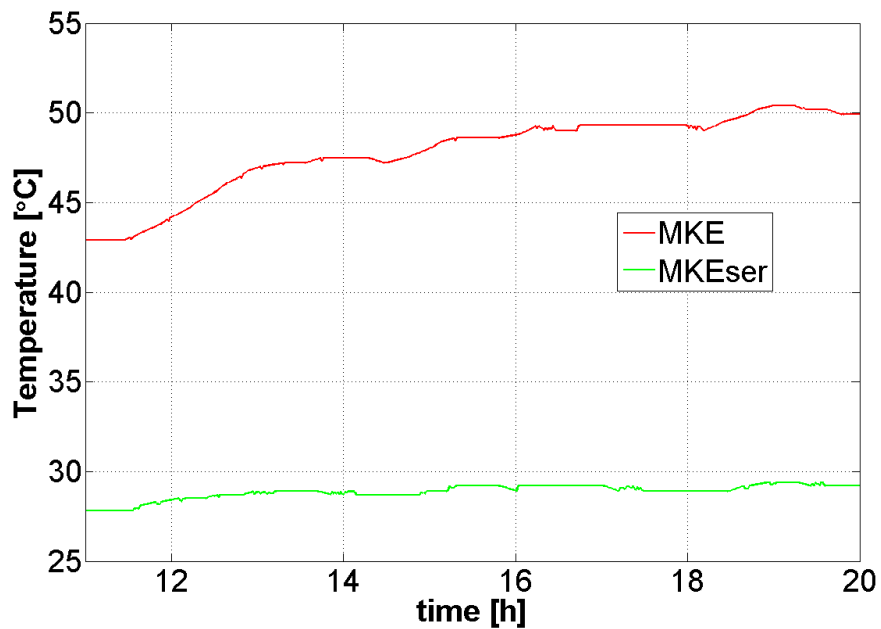


Figure 4.24: Measured temperature on the MKE kicker with and without serigraphy during the LHC fill 2818 (50 ns beam, accelerated to 450 GeV).

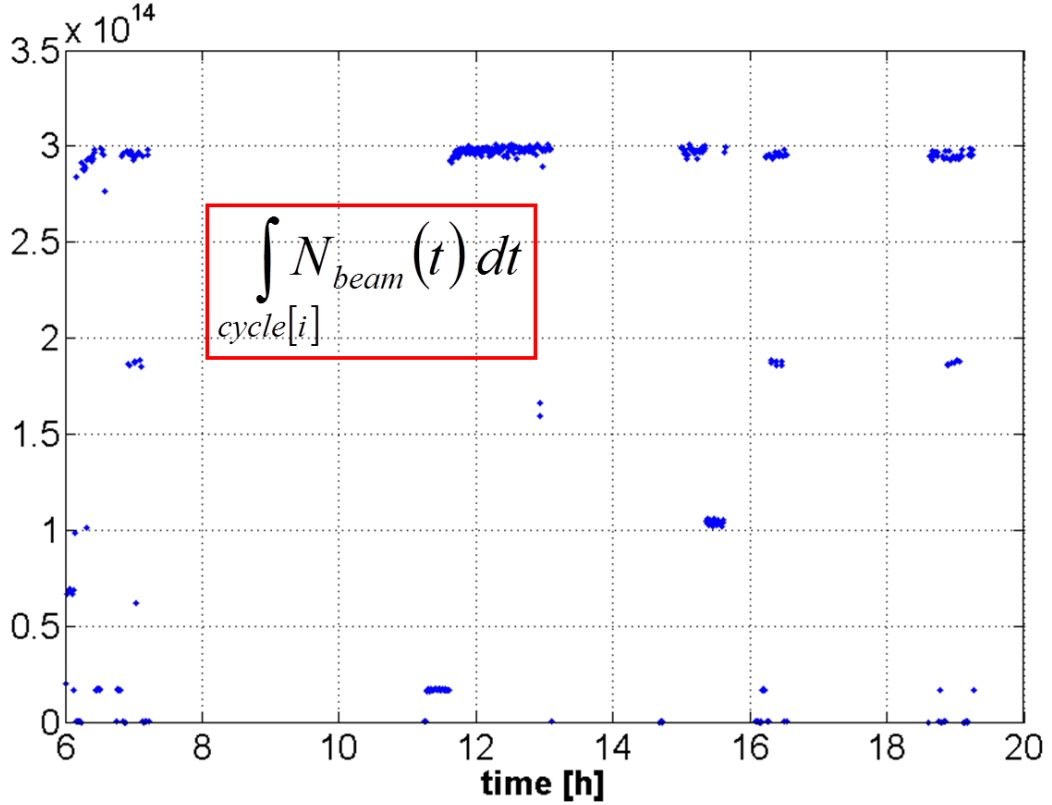


Figure 4.25: Integrated intensity along the 50ns cycle as a function of time during the LHC fill 2818 (50 ns beam).

#### Effect of the bunch distribution

In this section we will present a study of the sensitivity of the power loss estimation to the bunch distribution. A Gaussian profile is assumed when measuring the bunch length [123]. Nevertheless, also a parabolic or a cosine square distribution are considered appropriate to fit the bunch profile [124]. Up to now, in the analysis we assumed a Gaussian bunch profile. In the following we will analyze the uncertainty due to this choice, comparing the power loss obtained with the Gaussian profile with that obtained using different bunch distributions.

First, in order to study the effect of tails, we consider the case of a truncated Gaussian. A Gaussian profile cut with a rectangular function (see Fig. 4.26) is given by the following equation:

$$f(z) = \frac{1}{\sqrt{2\pi}\sigma_z} e^{-\frac{z^2}{2\sigma_z^2}} \left( \frac{\text{Sign}[b\sigma_z - z] + \text{Sign}[b\sigma_z + z]}{2} \right) \quad (4.12)$$

The bunch spectrum of a Gaussian truncated at  $2\sigma_z$  is showed in Fig. 4.27. Lobes due to the truncation appear. The truncation with a rectangular window is unrealistic (a smooth windowing should be used) but represents the worst case for the lobe formation, since their

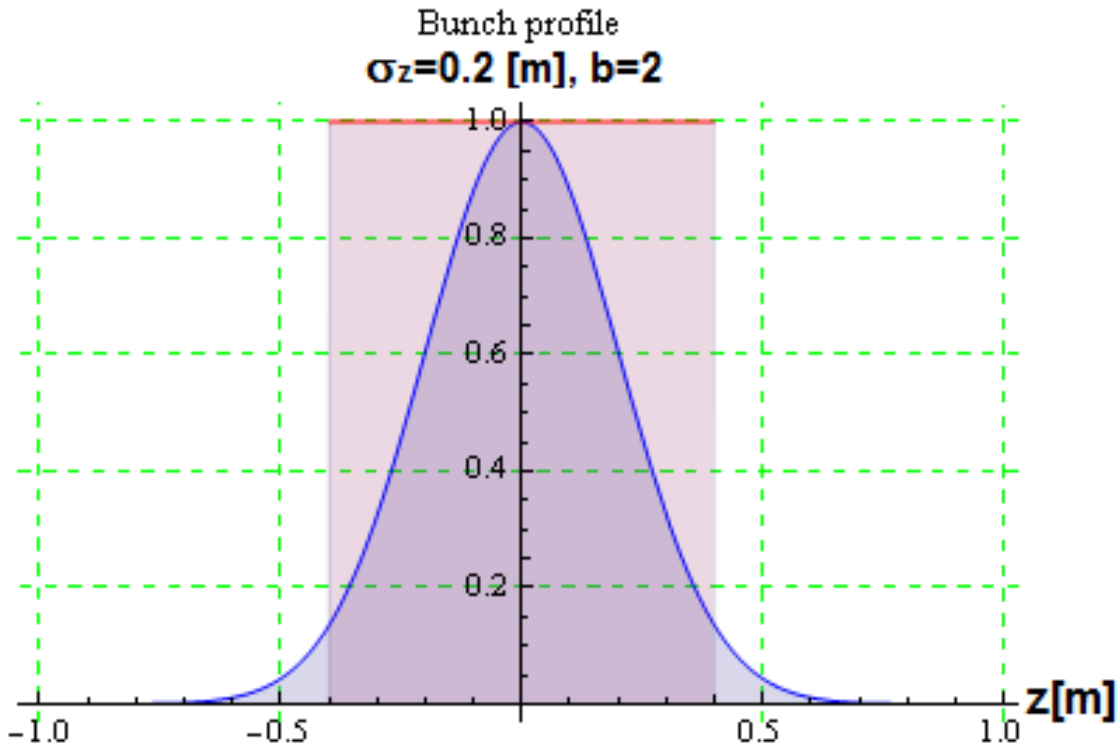


Figure 4.26: Gaussian bunch profile and truncation at  $\pm 2\sigma_z$ .

decay in frequency is very slow. Using Eq. (4.3) we calculated the power loss for a truncated Gaussian profile. The small differences observed with respect to the power loss obtained with a fully Gaussian profile (see Fig. 4.28) proves that for an MKE-type impedance the effect of the tails on the estimated power loss is negligible. Significant differences between the power loss calculated for an MKE with or without serigraphy start appearing when the Gaussian profile is truncated below  $2.5\sigma_z$ .

In order to assess the impact on the power loss of the core profile, we have studied two different bunch distributions other than Gaussian: parabolic and cosine square (see Fig. 4.29). Figure 4.30 shows a comparison of the power loss calculated from Eq. 4.3 for the profiles investigated having assumed the same standard deviation. From this comparison the Gaussian distribution turns out to be the most pessimistic one to estimate the power loss.

It would be more realistic to do these comparisons considering that the measurements of the bunch length are performed assuming a Gaussian profile with the FWHM (Full With Half Maximum) algorithm [123]. Comparing different distributions with the same FWHM, it turns out that the Gaussian distribution predicts the lowest power loss while the parabolic one can lead to a power loss up to a factor 2 larger, and the cosine square leads to a 20-30% larger heat load (see Fig. 4.31).

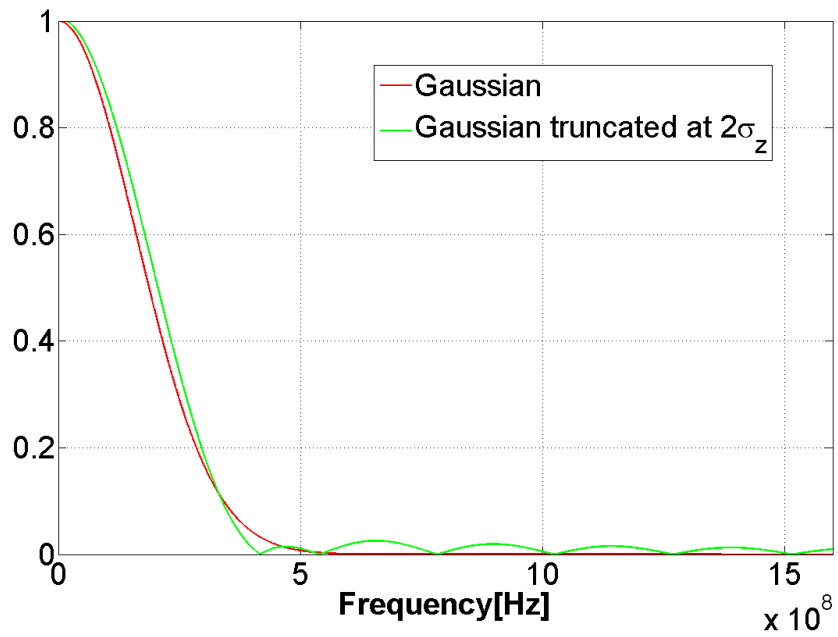


Figure 4.27: Comparison between the spectra of a Gaussian and a truncated Gaussian bunch profile.

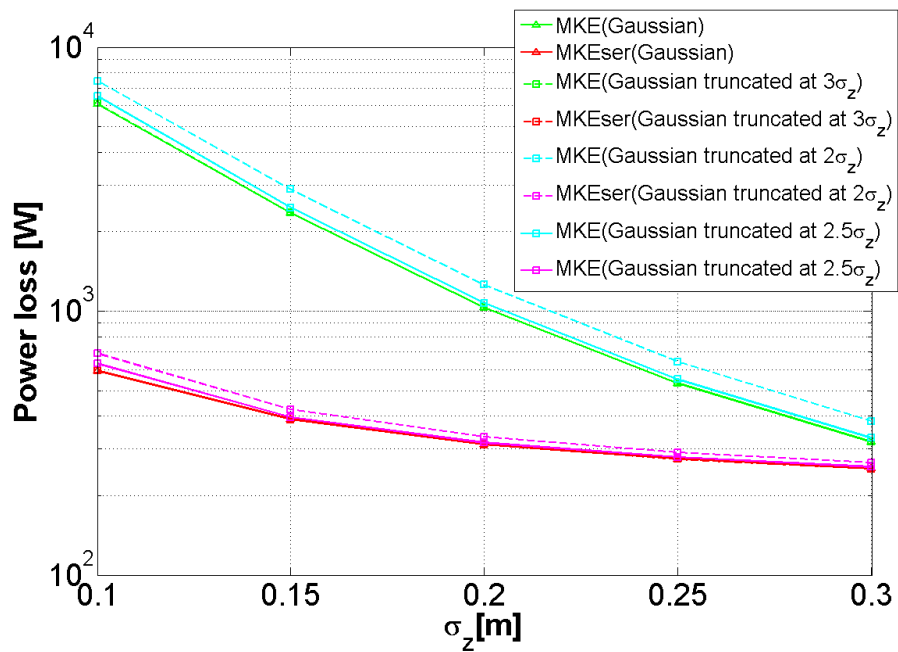


Figure 4.28: Comparison between the power loss of the MKE with and without serigraphy using Gaussian and truncated Gaussian bunch profiles (with different truncations).

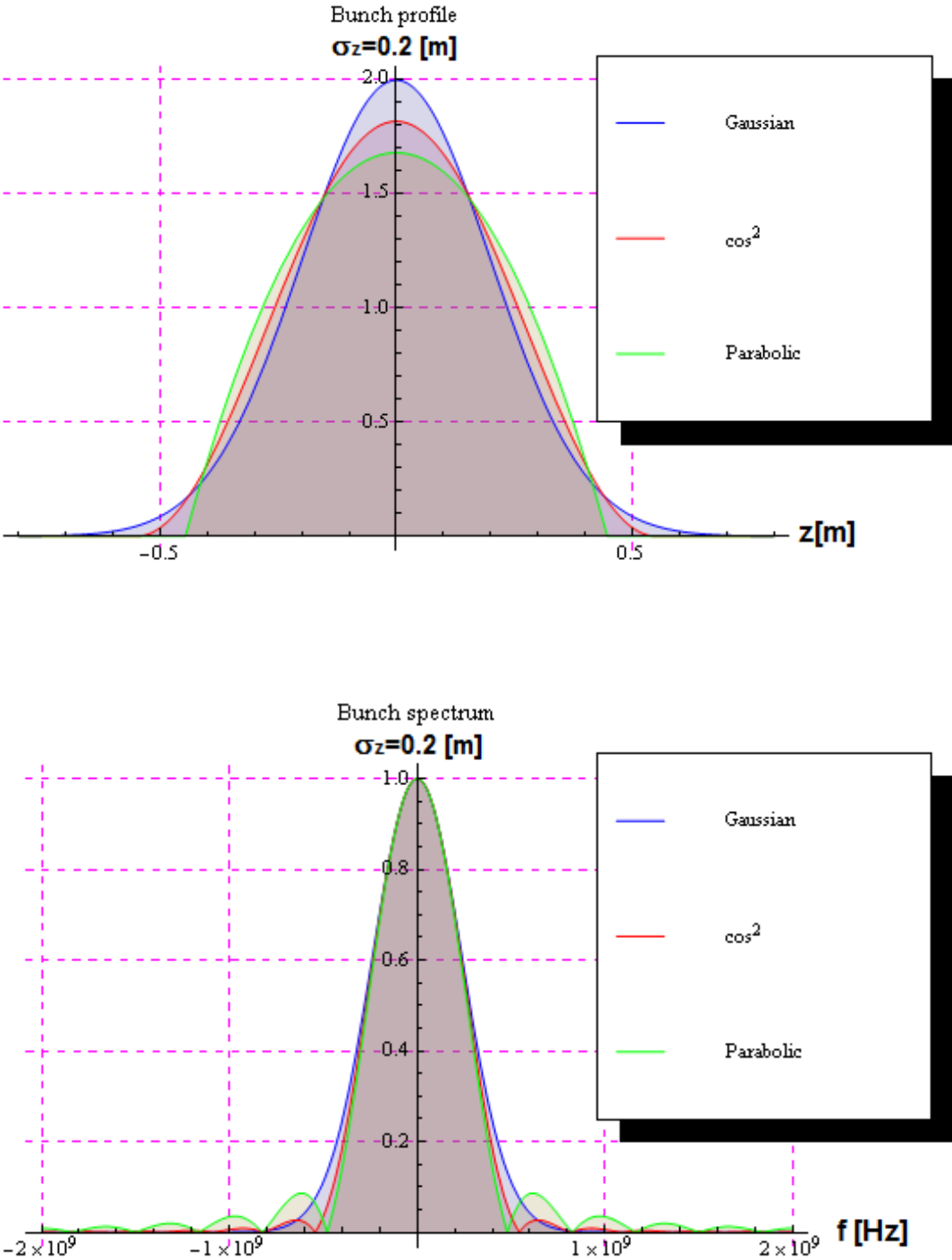


Figure 4.29: Some possible bunch profiles (top) and their corresponding spectra (bottom). The distributions are compared assuming that they have the same standard deviation.

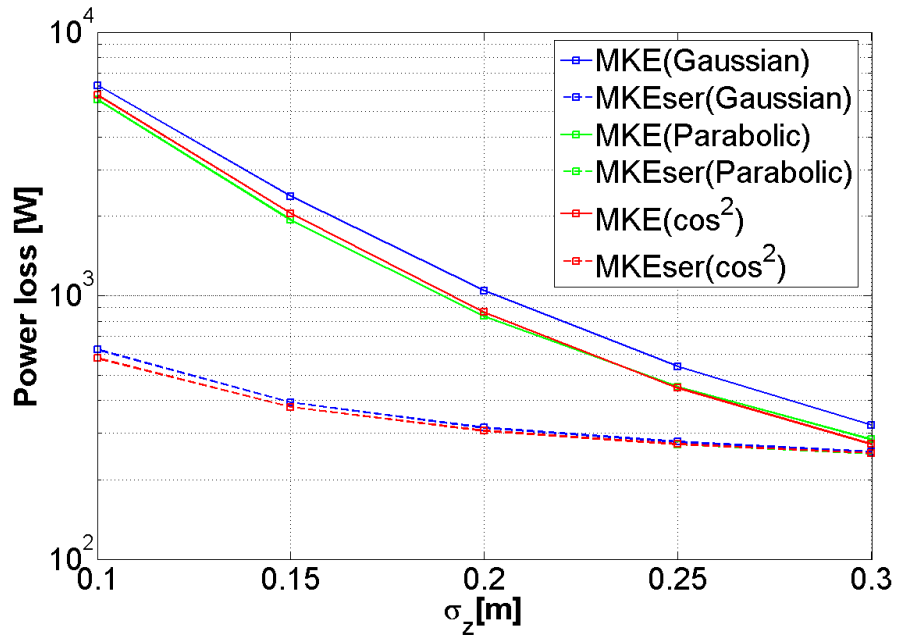


Figure 4.30: Comparison of the power loss obtained with different bunch profiles having the same standard deviation.

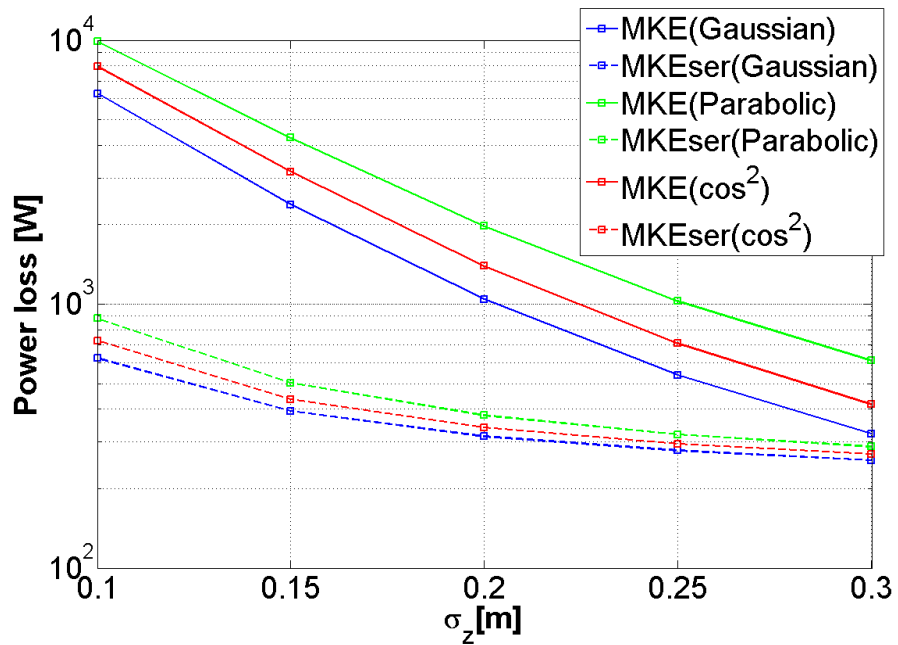


Figure 4.31: Comparison of the power loss obtained with different bunch profiles assuming the FWHM algorithm for the fit of the Gaussian profile.

### 4.3 EM characterization of materials

The EM characterization of materials up to high frequencies is a major requirement for the correct modeling of many accelerator components, e.g. collimators, kickers and high order mode damping devices for accelerating cavities. In some cases data are available from the supplier or can easily be found in the literature. Measuring complex permeability and permittivity is a critical task for a correct impedance modeling and its determination is not trivial. The knowledge of the method used for the measurement is fundamental for a correct interpretation of the results. In this frame we developed a measurement setup in order to have a valid instrument to verify the available data and possibly extend the model to a broader frequency range. Throughout this section we will illustrate the measurement technique, giving examples of application. In particular the method was used to confirm the model for the ferrite 8C11, which has been widely used for constructing the kicker impedance model.

#### 4.3.1 Methods for measuring the material properties

EM material characterization at microwave frequencies has a long history, dating back from the early 1940s. Over the past few decades, significant progress has been made in this field and a variety of new measurement techniques have been developed. Broadband EM material characterization is a major requirement in many applications (military, industry, research etc.). The coaxial line method, which will be explained in the following, has gained much importance in comparison with other methods because of its applicability over a wide range of frequencies. A coaxial cable fed at one side is filled with the material under test and closed on a well known load on the other side. The measured reflection coefficient can then be used as an input for a transmission line (TL) model or for a 3D EM simulation, which describes the measurements setup. The electromagnetic properties of the materials can thus be extrapolated. We have applied this method to characterize samples of SiC (Silicon Carbide), which could be used for LHC collimators as well as for CLIC accelerating structures, and NiZn ferrite used for kicker magnets or to damp HOM.

In all the methods, the basic idea is to measure a quantity (reflection or transmission S-parameters) that directly depends on the material properties. If the relation between the measured and the desired quantities is known by means of a theoretical or numerical model, it is possible to infer the properties of the material. Two main branches could be distinguished in the use of guided propagation for this purpose: waveguide methods [125, 126, 127, 128] and transmission line methods [129, 130, 131, 132, 133, 134]. Regarding the second branch the two main techniques are the coaxial line method and the strip-line method. The waveguide methods are intrinsically limited in frequency and do not allow for a broad band characterization. The stripline method has the advantages of permitting the characterization in a wide range of frequency, while at the same time the machining of the sample does not require special efforts (square sample). The coaxial line method has the great advantage of having a simple theoretical model for the dependence between the quantity measured and the EM properties. Moreover, the connection to the network analyzer can be easily done through commercial coaxial cable transitions. Consequently coaxial line methods have gained much importance as compared to other methods [135, 136]. The main drawback of this method is



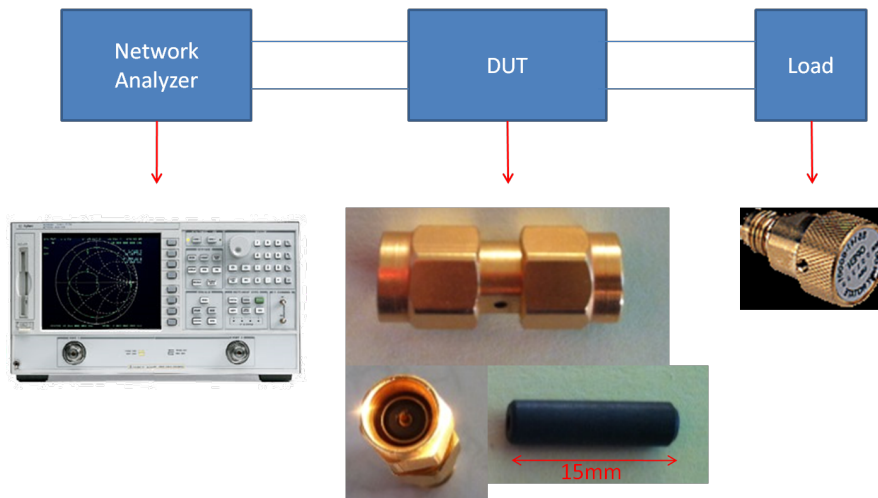


Figure 4.32: Measurements setup (DUT stands for device under test).

only technological: due to the machining of the sample, it is important to avoid the presence of an air gap between the inner conductor and the sample.

The electromagnetic (EM) characterization of materials plays a crucial role in the impedance modeling for the SPS accelerator complex at CERN or for damping materials in CLIC accelerating structures.

Up to now the characterization of dielectric materials for CLIC was based on the waveguide method [125, 137]. A sample of material is inserted in a waveguide of dimensions depending on the range of frequencies to be characterized. Therefore, the complex transmission coefficient  $S_{21}$  is measured in a certain range of frequencies. This quantity is related to the propagation constant and then to the electromagnetic material properties (permittivity and permeability). Therefore from the knowledge and inversion of this function (numerically calculated), it is possible to infer the EM characteristics of the material [125, 137]. This method needs different setups to investigate a wide range of frequencies and is not easy to treat analytically.

### 4.3.2 The Coaxial line method

The coaxial line method allows using only one measurement setup to characterize the material in a wide range of frequency. Since the propagation is TEM, there is no lower limit in frequency. The upper limit in the frequency range is given by the cutoff frequency of the first high order mode that can propagate in the structure. The mode with the lowest cutoff frequency is the  $TE_{11}$  mode. This mode has one 'period' around the circumference of the cable. To a good approximation, the condition for the  $TE_{11}$  mode to propagate is that its wavelength in the material is not longer than the average circumference of the filling material:

$$f_{TE_{11}} = \frac{2c}{\pi(D+d)\text{Re}[\sqrt{\epsilon_r\mu_r}]} \quad (4.13)$$

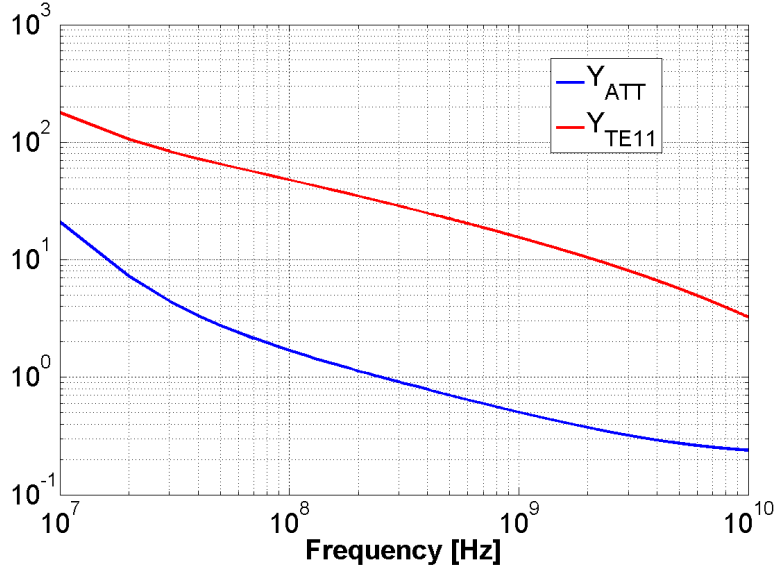


Figure 4.33: Factors  $Y_{ATT}$  and  $Y_{TE11}$  as function of the frequency.

where  $d$  and  $D$  are the diameter of inner and outer conductor of the coaxial line, respectively. Another parameter that determines the maximum frequency that can be analyzed is the attenuation along the line. As a criterion we consider to have a good resolution if the attenuation along the line is below 90%. Since the reflection coefficient is usually measured, the length of the line is twice the length of the sample, i.e.  $2l$ . If the penetration depth  $\delta$  is larger than  $l$ , we guarantee an attenuation lower than 90% ( $(1 - e^{-\frac{2l}{\delta}}) \times 100 = 86.5\%$ ) for frequencies below:

$$f_{ATT} = -\frac{c}{2\pi l \operatorname{Im}[\sqrt{\epsilon_r \mu_r}]} \quad (4.14)$$

A short standard coaxial line filled with the material to characterize is closed on a well-known load. Using a network analyzer the reflection coefficient is measured (see Fig. 4.32). Similarly to the waveguide, also in this case the measured parameter is related to the unknown material properties. This function can be obtained numerically (from 3D finite elements simulations) or from basic TL theory. Both frequencies  $f_{TE11}$  and  $f_{ATT}$  depend on the properties of the filling material according to the relation (4.13) and (4.14). Since in our setup,  $l = 15$  mm,  $d = 1.3$  mm and  $D = 4.1$  mm, we easily obtain that, for a dielectric material with  $\epsilon_r = 10 - 2j$ ,  $f_{ATT} = 10$  GHz and  $f_{TE11} = 11.2$  GHz. The limitation in frequency would be given in this case by the attenuation along the line.

In general, since permittivity and permeability are frequency dependent, Eqs. (4.13) and (4.14) become implicit equations in the unknowns  $f_{TE11}$  and  $f_{ATT}$ . The coverable range of frequencies cannot be determined a priori when the material in the coaxial cable is being characterized. Introducing the quantities  $Y_{TE11} = \frac{f_{TE11}}{f}$  and  $Y_{ATT} = \frac{f_{ATT}}{f}$ , the solutions will be provided by the conditions  $Y_{TE11} = 1$  and  $Y_{ATT} = 1$ . For example, for a ferrite 4A4, the curves

$Y_{TE11}(f)$  and  $Y_{ATT}(f)$  are plotted in Fig. 4.33, showing that, due to the attenuation on the line the measurements can reliably cover a range of frequency up to  $\approx 200$  MHz.

**The measurement procedure**

The feasibility of the adopted method was studied using a 3D EM simulator as the environment for ideal measurements and a TL model to obtain the reflection coefficient as a function of the material properties. The same function is obtained also numerically from the 3D EM code CST Microwave Studio. The flowchart of Fig. 4.34 explains the procedure with these two different methods.

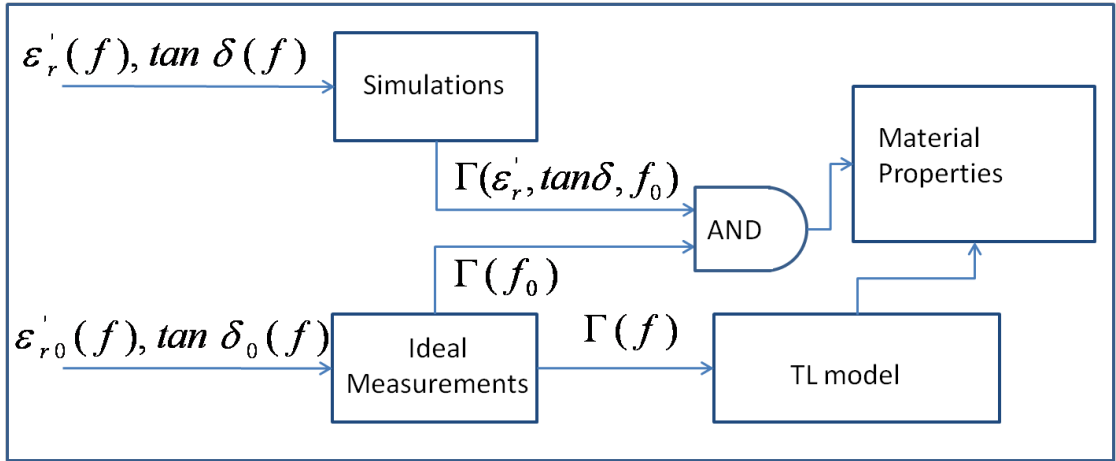


Figure 4.34: Flowchart for simulations and TL model techniques.

For the case of a dielectric material, the measurement system is simulated using the material properties (real permittivity  $\epsilon'_r(f)$  and dielectric loss tangent  $\tan \delta(f)$ ) as free parameters. The output of the simulations is always the reflection coefficient in a certain range of frequencies  $\Gamma(f)$ . From simulations we extrapolate 3D surfaces that display the complex reflection coefficient as a function of real permittivity and loss tangent at a given frequency  $f_0$ ,  $\Gamma(\epsilon'_r, \tan \delta, f_0)$  (or analogously for real and imaginary part of the complex permeability). The same function can be easily obtained analytically by modeling the measurement system with the TL theory (see Fig. 4.35):

$$\Gamma(z) = \frac{Z(z) - Z_0}{Z(z) + Z_0} \tag{4.15}$$

where  $Z(z)$  is obtained by transporting the known  $Z_{load}$  along the coaxial line of length  $l$ , propagation constant  $k_{DUT} = k_0 \sqrt{\epsilon_r \mu_r}$  and characteristic impedance  $Z_{DUT} = \sqrt{\frac{L_{DUT}}{C_{DUT}}} = 60 \sqrt{\frac{\mu_r}{\epsilon_r}} \ln(\frac{D}{d})$  where  $D$  and  $d$  are respectively the outer and inner radius of the coaxial line [56]. In a general circuital representation a transmission line can be modeled as illustrated in Fig.4.36. The characteristic quantities of the equivalent transmission line  $K_{DUT}$  and  $Z_{DUT}$  have been calculated neglecting the resistance and conductance per unit length  $R_{DUT}$  and

$G_{DUT}$ . This assumption requires the conditions  $\omega L_{DUT} \gg R_{DUT}$  and  $\omega C_{DUT} \gg G_{DUT}$ . The latter becomes critical for dielectric with high loss tangent ( $\tan \delta > 0.2$ ).

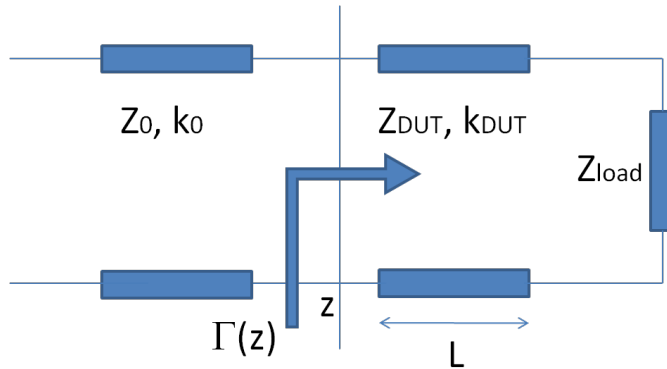


Figure 4.35: Transmission line model.

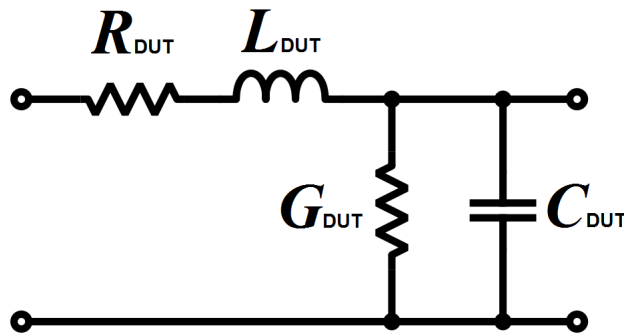


Figure 4.36: Schematic representation of the elementary components of a transmission line.

By using the function as calculated numerically or analytically, we found the possible solutions of real permittivity and loss tangent from the contour plot resulting from the intersection between the surfaces,  $\Gamma(\epsilon'_r, \tan \delta, f_0)$ , and the ideal measurements (i.e. the simulation of the reflection coefficient at one single frequency  $\Gamma(f_0)$  for given material properties  $(\epsilon'_{r0}, \tan \delta_0)$ ). Figure 4.37 shows the intersection of a surface with the ideal measurements at a certain frequency. Figure 4.38 shows contour plots for different surfaces and points from the TL model. Different contour plots are displayed for different terminations of the transmission line (open ended and short ended) and for the real part and the imaginary part of  $\Gamma$ . The solution is the confluence point of all configurations. In this example the solution gives 10 for the real part of the complex permittivity and 0.2 for the loss tangent. These results are confirmed by the TL model and in fact the solutions for the short and the open end lie exactly on the intersection of all contour plots. The encouraging simulation results, even in the limitation of the non-ideal world, encouraged us to proceed in the realization of the measurement set-up.

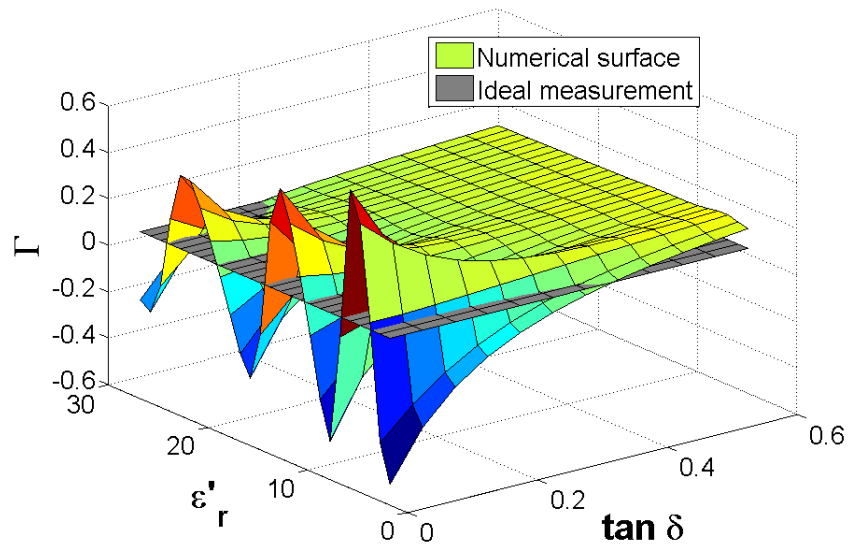


Figure 4.37: Reflection parameter as function of loss tangent and real permittivity.

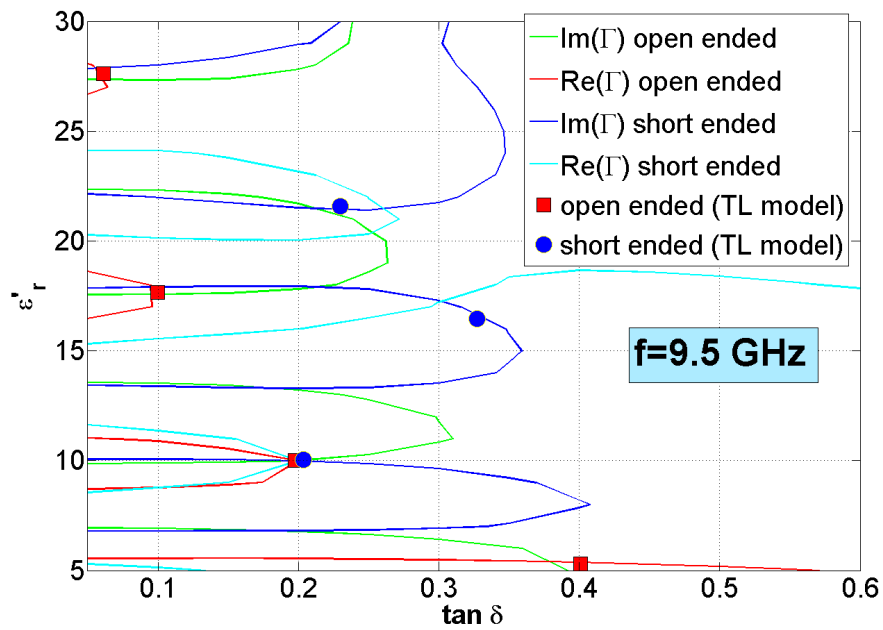


Figure 4.38: Contour plots for different 3D surfaces. The squared and round dots are calculated from the transmission line model.

### 4.3.3 Air gap

One complication of the coaxial method is the presence of an air gap in the fabrication process for the sample under test. Because of limitations in our machining tools we accepted to have an air gap between the inner conductor of the coaxial line and the material under test (see Fig. 4.39). The size of the air gap was measured by means of a digital microscope. A correction to the characteristic impedance was introduced to take into account the air-gap effect [138]. Due to the air gap the capacitance and the inductance have the following expression:

$$\frac{1}{C} = \frac{1}{C_{\text{sample}}} + \frac{1}{C_{\text{gap}}} \quad (4.16)$$

$$L = L_{\text{sample}} + L_{\text{gap}}$$

where  $C_{\text{sample}}$  and  $L_{\text{sample}}$  are the capacitance and inductance of the sample per m length:

$$C_{\text{sample}} = \frac{2\pi\epsilon_0\epsilon_r}{\ln\left(\frac{D}{d+\text{gap}}\right)} \quad (4.17)$$

$$L_{\text{sample}} = \frac{\mu_0\mu_r}{2\pi} \ln\left(\frac{D}{d+\text{gap}}\right)$$

and  $C_{\text{gap}}$  and  $L_{\text{gap}}$  are the additional capacitance and inductance per m length caused by the air gap:

$$C_{\text{gap}} = \frac{2\pi\epsilon_0\epsilon_r}{\ln\left(\frac{d+\text{gap}}{d}\right)} \quad (4.18)$$

$$L_{\text{gap}} = \frac{\mu_0\mu_r}{2\pi} \ln\left(\frac{d+\text{gap}}{d}\right)$$

The characteristic impedance of the line, taking into account also the air gap effect, has then been calculated.

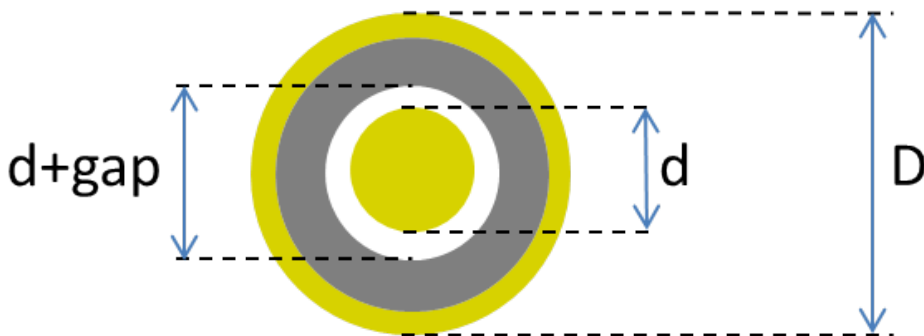


Figure 4.39: Transverse section of the DUT: in yellow the inner and outer conductor; in white the air gap and in gray the material to characterize.

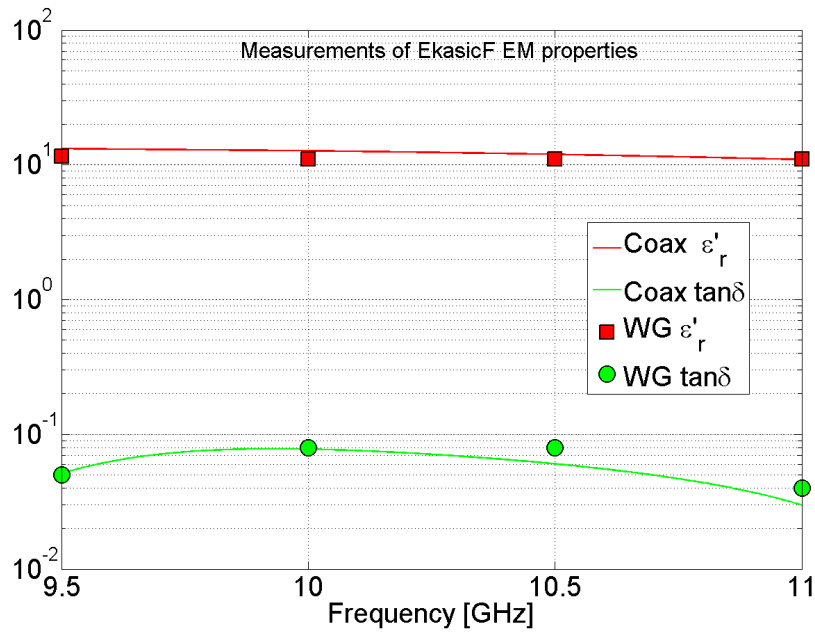


Figure 4.40: Measurements of real permittivity and loss tangent for SiC EkasicF.

#### 4.3.4 Measurement results

In this section we present a few examples of application of the coaxial line method described above. First, we show an example of dielectric material. Then, we will show measurements results for the ferrite 8C11 and TT2-111R. The EM properties have been measured by means of the reflection parameter in the coaxial line setup. Both EM simulations and TL model have been used to invert the functional relations. Figure 4.40 shows the properties of SiC EkasicF in the range 9.5 ÷ 11 GHz performed with the TL model. The dots are measurements with the waveguide method at different discrete frequencies. Figure 4.41 shows the contour plots for EkasicF at 9 GHz. Furthermore a measured point with the waveguide method is displayed at the same frequency.

Concerning the magnetic materials the model for the permeability of the ferrite 8C11, used in the SPS kicker magnets (see Fig. 2.3), was obtained from a first order dispersion fit on measured data by the supplier. In order to have a confirmation of the model, the complex permeability of the ferrite 8C11 has been measured by using the coaxial line method with the complex permittivity model of Eq. (2.2) with measurements of  $\epsilon'_r$  and  $\sigma_{el}$  provided by the supplier [25]. The measured ferrite properties have been found in good agreement with the ferrite model used up to now (see Fig. 4.42).

Finally, as a further confirmation of the measurement method, Fig. 4.43 shows the results of the measurements of the complex permeability of ferrite TT2-111R. The permittivity model (Eq. 2.2 with  $\epsilon'_r = 12$  and  $\sigma_{el} = 10^{-4}$  S/m) has been extrapolated from published results [127, 130]. The model of complex permeability is in reasonable agreement with published data [126, 130] and supplier data on the TT2-111R [139] obtained with the Agilent fixture [131].

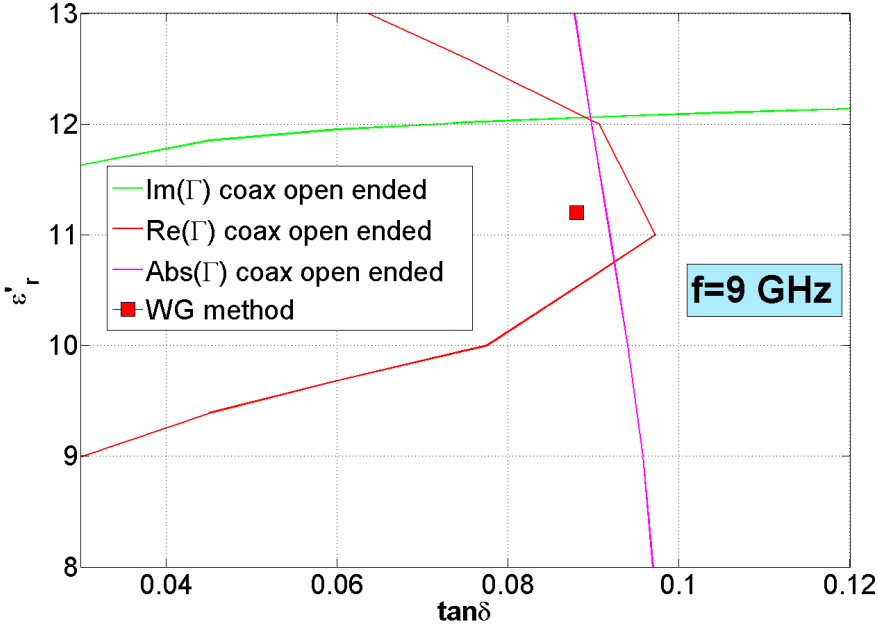


Figure 4.41: Contour plot for SiC EkasicF at 9 GHz.

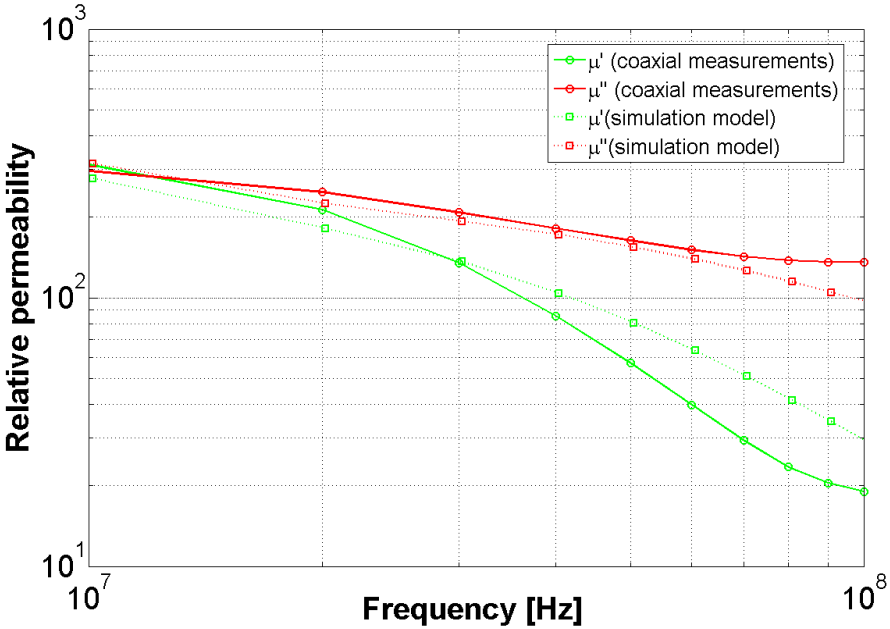


Figure 4.42: Measurements of complex permeability for the ferrite 8C11.



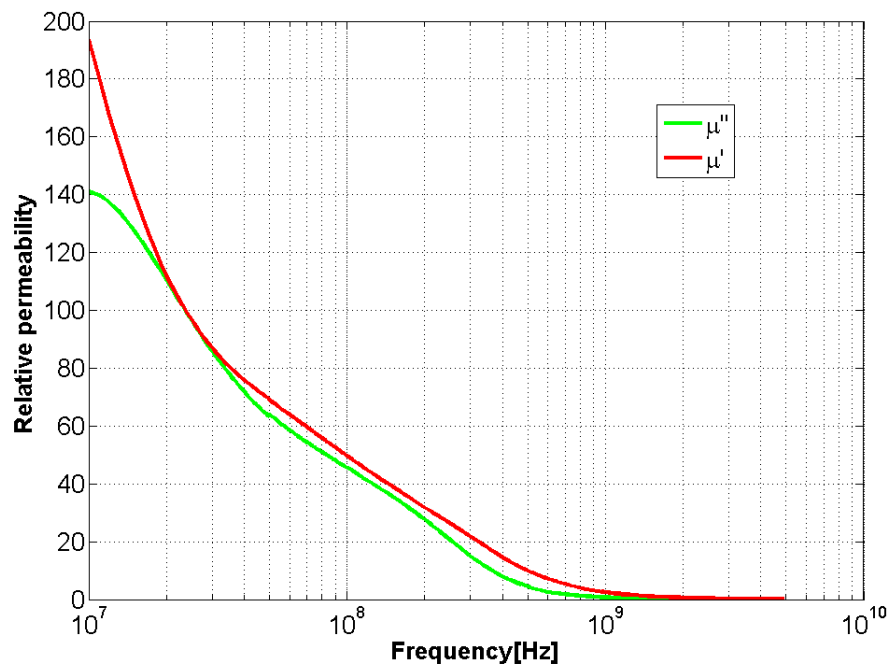


Figure 4.43: Measurements of complex permeability for the ferrite TT2-111R.



## Conclusions

In this PhD thesis we discussed the use of time domain 3D CST Particle Studio EM simulations to calculate wakes and/or impedances. As first steps, we compared their results with the known analytical solutions for circular and rectangular resistive chambers (see Figs. 1.7, 1.8 and 1.9) successfully recovering the theoretical Yokoya form factors [15] (see Fig. 1.11), and defining, in the transverse plane, the constant, driving and detuning terms of the wakes/impedances for both symmetric and asymmetric geometries (e.g see Fig. 1.6). The sensitivity of the simulations results to the numerical parameters has been discussed in detail, as well as the limits of validity of the wake formalism and its extension to the nonlinear regime (see Figs. 1.13 and 1.14). Secondly, we have simulated pillbox cavities and step transitions to further benchmark the EM simulations. CST-Particle Studio simulations of step-in and step-out transitions and PEC pillbox were successfully benchmarked with ABCI (see Figs. 1.18, 1.19, 1.25 and 1.28). The peaks below the pipe cut-off observed in the PEC pillbox tend to Dirac delta (see Figs. 1.16 and 1.17), and their appearance was explained. Moreover, through the analysis of a lossy pillbox in frequency domain, we gave methods to extrapolate typical frequency domain quantities (e.g.  $R_s$  and  $Q$  of resonant peaks) from time domain codes (see Fig. 1.23). We also showed that the impedance of a step-out and a symmetric step-in transitions are related by the relations of Eq. 1.37 (see Fig. 1.29) and gave a physical interpretation for it.

Using the CST Wakefield Solver an advanced model for the global SPS kicker impedance has been provided. The simulation model was improved step by step and successfully benchmarked with existing and new theoretical models, giving confidence in the numerical results and allowing for a better understanding of the EM problem. We found a very good agreement between CST time domain simulations for the simplified model of kicker proposed by Tsutsui and the theoretical results based on Tsutsui's formalism (e.g. see Figs. 2.13, 2.14 and 2.15). The ferrite permeability model is a very important input of theoretical and numerical calculations. We showed that using ferrites 4A4 or 8C11 does not lead to significant differences in the frequency range of interest (few tens of MHz up to few GHz) (see Fig. 2.8). The Tsutsui model approximates the C-shaped ferrite loaded kicker with two parallel plates of ferrite. We showed that the connection between the two blocks of ferrite needs to be taken into account below a few hundreds of MHz for the SPS kickers (see Fig. 2.22). For these reasons we developed an analytical approach for the impedance calculation of a C-magnet model. A theoretical model based on the separation of the two different contributions (coupling with the external circuit and core losses) to the coupling impedance has been presented. The model has been successfully benchmarked with CST-3D TD simulations (see Figs. 2.27 and 2.28) and has been

## Conclusions

---

used to include the contribution of the external circuits in the model of the ejection kicker of the PSB (see Fig. 2.29). A simulation technique, in order to account for external cable connections in CST particle Studio simulations has been also developed.

Next, some new aspects of the resistive wall impedance have been studied. In some cases of interest, the theoretical calculation applies very well. This is the case of the resistive wall impedance of simple chamber geometries. A theoretical approach based on the TL theory to calculate the resistive wall impedance of round chambers has been proposed. By means of form factor the method can be applied to rectangular or elliptical chambers. The model was successfully benchmarked with ReWall, a code based on the field matching technique (see Figs. 3.2, 3.3 and 3.5), and was used to construct the SPS wall impedance model. However, for more complicated geometries (asymmetries, small insert, holes etc.), a theoretical estimation without involving EM simulations becomes nonviable. An example of interest in this sense is the LHC beam-screen where CST 3D simulations were used for the impedance estimation (see Fig. 3.15). In order to perform this simulation in the frequency range of interest (few kHz to several tens of MHz) we developed a novel simulation technique, which we named the scaling technique (see Fig. 3.13).

The models were also successfully benchmarked with bench measurements based on the wire method (e.g. see Figs. 4.3, 4.4 and 4.5) and observations of beam induced heating and tune shift measurements (see Fig. 4.6). The longitudinal impedance model of the SPS extraction kicker shown in Fig. 2.37 can explain the ratio observed during the SPS operation between the beam induced heating of the MKE with and without serigraphy (see Fig. 4.16). Moreover, in order to further benchmark the impedance model of Fig. 2.37 we presented a simple thermal model to estimate the heating from the power loss, in order to attempt an absolute comparison with the measured heating. Considering that the model is a strong simplification of much more complex dynamics the agreement found was very encouraging. Concerning the bench measurements a numerical investigation of coaxial wire measurements has been presented. In order to verify the adopted EM models of the materials in theoretical calculation and 3D simulations an experimental setup for measuring EM properties (permittivity and permeability) of materials has been presented. The method was applied for measuring NiZn ferrites (see Figs. 4.42 and 4.43) and dielectric material (e.g. SiC) (e.g. see Fig. 4.40).

Through the research path described above, new contributions to the theory, simulation and measurement of wakes/impedances have been brought. The main contributions can be summarized as follows:

- **theory:**
  - A spectral method based on the field matching technique for the calculation of the longitudinal and transverse (driving, detuning and constant) impedances of an asymmetric ferrite loaded round chamber;
  - A theoretical model to account for the effect of the TEM mode on the kicker impedance
  - A theoretical model for resistive wall calculation based on the transmission line (TL) theory.

- **simulation:**

- Separating driving and detuning impedance in both symmetric and asymmetric chambers
- Benchmarks between 3D EM simulations with theories for different accelerator devices (resistive chambers, pill-box cavities, step-transitions, ferrite loaded kicker).
- Construction of an advanced model for the SPS kicker impedance
- Broad-band simulation of the beam coupling impedances (longitudinal and transverse) of the LHC beam screen (1 KHz-100 MHz) by using the scaling technique for resistive wall.

- **experiment:**

- Numerical investigation on the validity of bench measurements (numerical measurements)
- Comparison between bench measurements and simulations of SPS kickers
- Benchmark of beam observations with simulations
- Coaxial line method for measuring EM properties of materials (permittivity and permeability) in a wide range of frequencies (from few MHz up to several GHz).



# A EM simulations of CLIC components

In the frame of the CLIC studies, the main activities are EM simulation of the waveguide setup for measuring EM properties of materials [137] and preliminary studies on the CLIC crab cavities. Moreover, we also studied the beam coupling impedance of the CLIC stripline kicker benchmarking the 3D simulations with theoretical results [140] and giving guidelines for the reduction of the beam coupling impedance of these elements.

Here we shortly present the simulation studies performed for the CLIC crab cavities.

## A.1 EM simulations of CLIC crab cavities

### A.1.1 Introduction and motivation

In the study, reported in detail in Ref. [141], the impact of the resistive wall effect in the Beam Delivery System (BDS) of the future Compact Linear Collider (CLIC) has been computed. The aim of this study was to determine the thresholds of resistive wall multi-bunch instability in terms of pipe radius by means of numerical simulations, using a particle tracking code and assuming copper pipes. Considering the geometric apertures of the magnets and of the collimators, it was found out that at 3 TeV center of mass energy, a minimum pipe radius of 10 mm was necessary to completely suppress the effect. This study only focused on the multi-bunch resistive wall effect from transverse driving wake fields on the beam. Nevertheless, the effect of the geometric wake fields has also to be included for completeness of the study, since the addition of both effects can have a large impact on the beam. There are two main geometric wake field contributors in the BDS:

- the tapered parts of the collimators and step transitions which generate usually short-lived wake fields. This effect has a large importance on the single-bunch instabilities and has already been studied [142].
- the crab cavities which can trap modes excited by the beam. Those wake fields are usually long-lived and important for multi-bunch instabilities.

Both future electron-positron collider CLIC and International Linear Collider (ILC) require a crab cavity to align the bunches prior to collision. Initial studies have been conducted in order to optimize the shape of the CLIC crab cavities [143]. A normal conducting cavity, operating at the main linac frequency of 11.9942 GHz has been chosen for CLIC [144], whereas

## Appendix A. EM simulations of CLIC components

---

a superconducting design operating at 3.9 GHz was chosen for the ILC. In both cases, Higher Order Modes (HOM), Lower Order Modes (LOM) and Same Order Mode (SOM) can be excited, and therefore strong damping requirements must be imposed on those modes [145]. The aim of this study is to compute the transverse dipolar wake potentials in time domain with CST Particle Studio for one single crab cavity, at distances corresponding to the scale of the CLIC bunch train. The damping of the modes is not included in this analysis. Once we obtain the wake functions, their tabulated values can be imported in the particle tracking code. Since the wake fields generated by the tapered parts of the collimators are usually short-lived, we do not include them in the multi-bunch instabilities. The study of the multi-bunch stability of the beam under the effect of these wakes will also dimension the damping required by the absorbers.

### A.1.2 CST 3D EM simulation studies

For the ILC, simulations of the beam dynamics have been carried out with calculated wake field on the multi-bunch scale [146], taking into account the influence of the 14 dominant HOM's along 4 cavities. The bunch train of ILC is composed by 2820 bunches, each  $300 \mu\text{m}$  long and separated by roughly 20 ns. For CLIC, the parameters are tighter, with 312 bunches, each  $44 \mu\text{m}$  long, separated by 0.5 ns. With the current design of the CLIC cavity, found on [143], the cell is almost 8 cm long, see Fig. A.1.

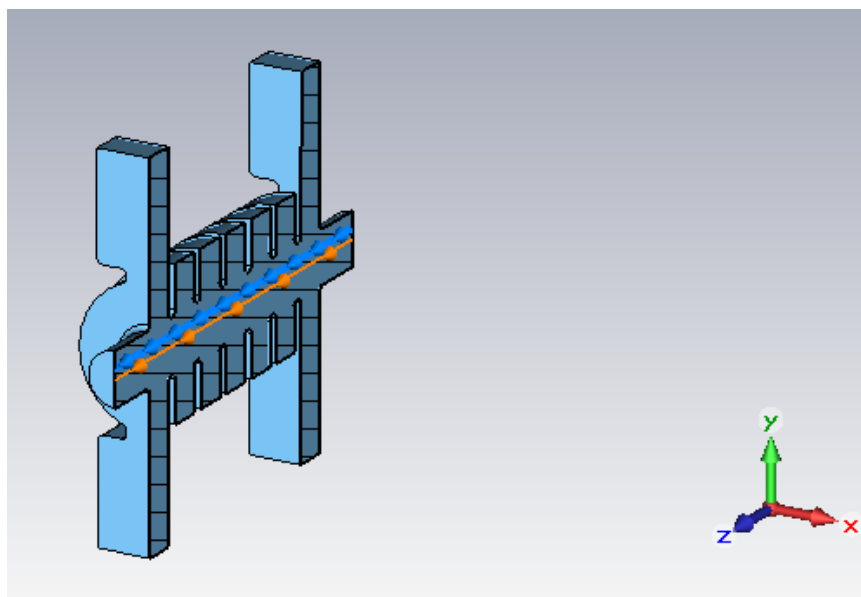


Figure A.1: Actual proposed Crab Cavity for CLIC.

The size of the beam clearly imposes some computational challenges for the wake field study, since we are limited by the virtual memory of today's computers. With CST Particle Studio, it is nowadays not possible to fulfil an accurate wake field study with  $44 \mu\text{m}$  long bunches and a reasonable number of mesh-lines per bunch. For instance, using 10 meshes per wavelength



and  $\sigma_z = 44\mu\text{m}$ , the number of meshes is larger than  $10^9$  for wake field calculations, which is clearly not affordable due to the limiting virtual memory of a domestic computer. Therefore, we will try to find a compromise between the number of meshes to use and the size of the bunch to model in the simulations.

In a first part, we try to find a reasonable number of mesh per electromagnetic wavelength which enables us to compute the wake potentials with an acceptable amount of meshes without losing accuracy. We carried out several simulations where we changed both the bunch length  $\sigma_z$  and the number of lines of mesh per wavelength (LW).

After having assessed a reasonable parameter for the cavity meshing, we carried out several simulations with different lengths of the bunch, scanning sizes from 6 mm down to  $880\mu\text{m}$  (still 20 times larger than the nominal size of the CLIC bunch). The wake potentials have been evaluated at a distance corresponding to 0.52 ns from the source particle. This separation time corresponds to the distance between two subsequent bunches in the CLIC. Results, presented in Fig. A.2, show a linear relation between the computed transverse dipolar wake potential and the length of the source bunch. Therefore, we decide it is realistic to assume a larger bunch length than what we need, and to extrapolate the wake to the  $44\mu\text{m}$  bunch length.

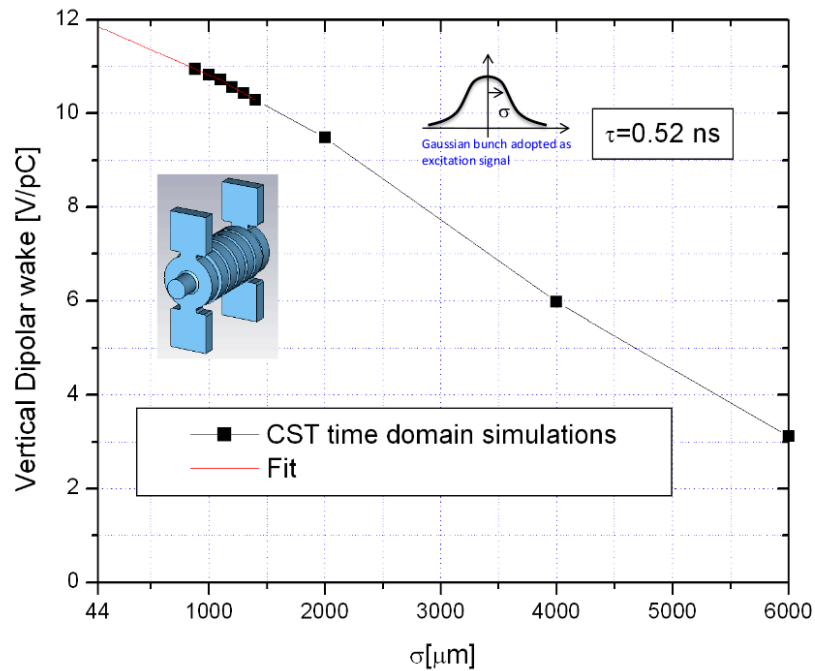


Figure A.2: Simulations with different bunch lengths.

In the following, we used the previous assessed parameters in order to compute the wake potentials over the whole bunch train of CLIC. Results are shown in Fig. A.3, where we used a driving bunch with  $\sigma_z = 6\text{ mm}$ . The envelope of the wake potential shows an oscillatory behaviour with a very low frequency of roughly 65 MHz. On the other hand, we can see a high-frequency behaviour in Fig. A.4(a) and Fig. A.4(b), where we plot the wake potential obtained between 1 ns and 6 ns,  $\approx 2.3\text{ ns}$  and  $\approx 2.6\text{ ns}$ , respectively. The frequency of this signal

## Appendix A. EM simulations of CLIC components

is about 12 GHz, see Fig. A.4(b), which clearly corresponds to the frequency of the cavity's principal dipolar mode [144]. Moreover, in Fig. A.3, we can see that the oscillations are not perfect, there are some small irregularities on the maximum of each oscillation. In order to understand the low-frequency modulation observed in Fig. A.3, we made an eigenmode study of the crab cavity with CST Microwave Studio. It was found that several modes were existing at frequencies close to the principal one (around 12 GHz), in a range of more or less 200 MHz. In particular, we could observe the Same Order Mode (SOM) with the opposite polarization of both operating and crabbing mode (see Tab. A.1). Those modes, which are not damped in the structure, could be excited by the beam.

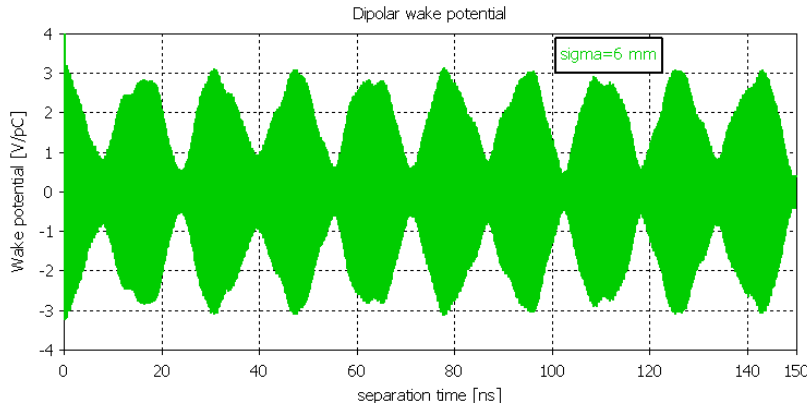


Figure A.3: Wake potentials over the CLIC bunch-train.

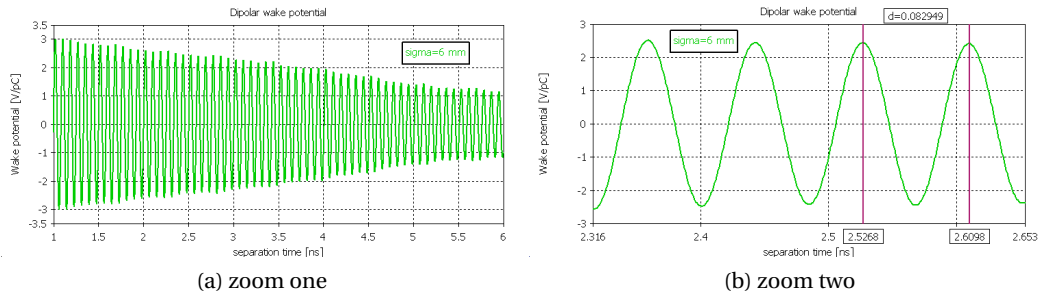


Figure A.4: Wake potentials close to the source bunch.

The low frequency oscillation (60-65 MHz) observed over CLIC's bunch train of Fig. A.3 does not change if we simulate the full structure (without electromagnetic symmetry) or the half structure with vertical magnetic symmetry ( $H_{tangential} = 0$  in the plane YZ). In the second case we are suppressing the horizontal polarization of the TE111-like hybrid dipole mode and the vertical polarization of the TM110-like hybrid dipole mode. Then probably the low frequency oscillation is generated from a beating between the TE111v and the TM110h separated in frequency exactly by 65 MHz. Indeed, simulating the half structure with horizontal magnetic symmetry ( $H_{tangential} = 0$  in the plane XZ) the low frequency oscillation disappears (we are suppressing the horizontal polarization of the TM110-like hybrid dipole mode and the vertical

polarization of the TE<sub>110</sub>-like hybrid dipole mode). Anyway a low frequency component at about 110-120 MHz turns out probably from a beating between the TE<sub>111h</sub> and the TM<sub>110v</sub> separated in frequency by 117 MHz (see Fig. A.5).

Mode	Frequency
TE <sub>111v</sub>	11.963 GHz
TE <sub>111h</sub>	11.989 GHz
TM <sub>110h</sub> (crab mode)	12.028 GHz
TM <sub>110v</sub>	12.106 GHz

Table A.1: SOM of the CLIC crab cavity.

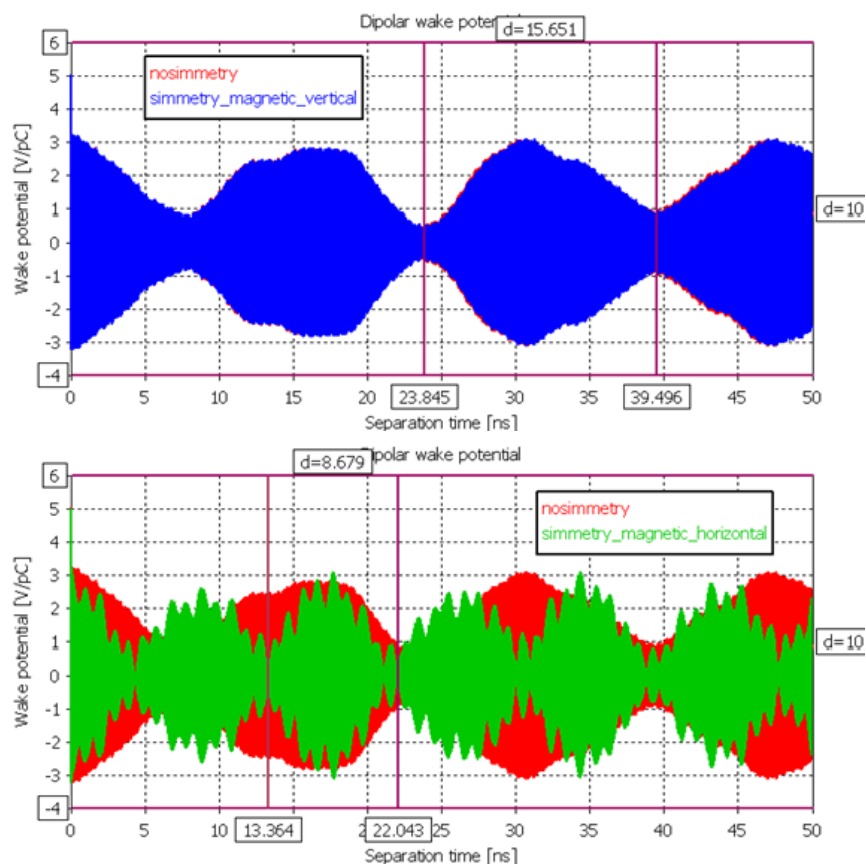


Figure A.5: Wake potentials over the CLIC bunch-train without symmetry (nosimmetry) and with horizontal and vertical magnetic simmetry.



# B Spectral model for the calculation of the transverse impedance of an abrupt transition

This work was done in close collaboration with V. G. Vaccaro. The calculation of the classical transverse dipolar impedance of an abrupt transition is something very critical. The classical time domain codes for the computation of wake potentials usually failed due to numerical issues (e.g. the Napoly integration method [147, 148] cannot be applied [19]). For this reasons we developed a spectral method for the calculation of the transverse impedance of an abrupt transition [149]. As case of example we studied the step-out transition of Fig. 1.27.

## B.1 The analytical approach

First, we write the longitudinal components of the primary (source) and scattered (modes in the guide) field. The longitudinal electric source field have the following expression:

$$\begin{aligned} E_z^{SC-}(r, \varphi, s) &= j \frac{Qk_0}{\beta\gamma^2} \cos\varphi [K_1(k_0 r / \beta\gamma) - \frac{K_1(k_0 b / \beta\gamma)}{I_1(k_0 b / \beta\gamma)} I_1(k_0 r / \beta\gamma)] e^{-jk_0 s / \beta} \\ E_z^{SC+}(r, \varphi, s) &= j \frac{Qk_0}{\beta\gamma^2} \cos\varphi [K_1(k_0 r / \beta\gamma) - \frac{K_1(k_0 d / \beta\gamma)}{I_1(k_0 d / \beta\gamma)} I_1(k_0 r / \beta\gamma)] e^{-jk_0 s / \beta} \end{aligned} \quad (B.1)$$

where:

$$Q = \frac{\omega P_y}{2\pi\gamma\epsilon_0 v^2} \quad (B.2)$$

and  $k_0 = \frac{\omega}{\beta c}$  is the propagation constant,  $P_y \vec{y}$  is the source momentum vector,  $K_1$ ,  $I_1$  are the modified Bessel functions of the first order. Moreover, the apex - indicates the field for  $z < 0$  and the apex + the field for  $z > 0$ . The longitudinal magnetic source field is zero. The

## Appendix B. Spectral model for the calculation of the transverse impedance of an abrupt transition

---

longitudinal electric and magnetic scattered fields are written as follows:

$$\begin{aligned}
 E_z^-(r, \varphi, s) &= \cos\varphi \sum_p C_p^E \frac{\Phi_p(r/b)}{b} \exp\left[j\left(\sqrt{k_0^2 b^2 - \alpha_p^2}\right) \frac{s}{b}\right] \\
 E_z^+(r, \varphi, s) &= \cos\varphi \sum_p D_p^E \frac{\Phi_p(r/d)}{d} \exp\left[-j\left(\sqrt{k_0^2 d^2 - \alpha_p^2}\right) \frac{z}{d}\right] \\
 Z_0 H_z^-(r, \varphi, s) &= \sin\varphi \sum_p C_p^H \frac{\Psi_p(r/b)}{b} \exp\left[j\left(\sqrt{k_0^2 b^2 - \alpha_p'^2}\right) \frac{z}{b}\right] \\
 Z_0 H_z^+(r, \varphi, s) &= \sin\varphi \sum_p D_p^H \frac{\Psi_p(r/d)}{d} \exp\left[-j\left(\sqrt{k_0^2 d^2 - \alpha_p'^2}\right) \frac{s}{d}\right]
 \end{aligned} \tag{B.3}$$

where:

$$\begin{aligned}
 \Phi_p(x) &= \sqrt{\frac{2}{\pi}} \frac{J_1(\alpha_p x)}{J_2(\alpha_p)} \\
 \Psi_p(x) &= \sqrt{\frac{2}{\pi}} \frac{\alpha_p' J_1(\alpha_p' x)}{\sqrt{\alpha_p'^2 - 1} J_1(\alpha_p')}
 \end{aligned} \tag{B.4}$$

and  $\alpha_p, \alpha_p'$  with  $p \in N$ , are respectively the zeros of the Bessel function  $J_1(x)$  and  $J_1'(x)$  and  $C^E, D^E, C^H$  and  $D^H$  are the unknown vectors.

### B.1.1 Projection of Maxwell equation in $r$ and $\varphi$

Writing the curl in cylindrical coordinates after some manipulation we obtained the following set of equation:

$$\begin{aligned}
 \left(jk_0 \frac{\partial}{\partial r} Z_0 H_s + \frac{1}{r} \frac{\partial}{\partial s} \frac{\partial}{\partial \varphi} E_s\right) &= \left(\frac{\partial^2}{\partial s^2} + k_0^2\right) E_\varphi \\
 \left(\frac{\partial}{\partial s} \frac{\partial}{\partial r} Z_0 H_s + \frac{jk_0}{r} \frac{\partial}{\partial \varphi} E_s\right) &= Z_0 \left(\frac{\partial^2}{\partial s^2} + k_0^2\right) H_r \\
 \left(-jk_0 \frac{\partial E_s}{\partial r} + \frac{Z_0}{r} \frac{\partial}{\partial s} \frac{\partial H_s}{\partial \varphi}\right) &= Z_0 \left(\frac{\partial^2}{\partial s^2} + k_0^2\right) H_\varphi \\
 \left(\frac{\partial}{\partial s} \frac{\partial}{\partial r} E_s - j \frac{k_0}{r} \frac{\partial}{\partial \varphi} Z_0 H_s\right) &= \left(\frac{\partial^2}{\partial s^2} + k_0^2\right) E_r
 \end{aligned} \tag{B.5}$$

The transverse field for the source and modes in the guide are then derived from Eq. (B.5).

### B.1.2 Field matching

The matching conditions are imposed at the transition ( $s = 0$ ) between the smaller and larger pipe from the continuity of azimuthal and normal fields:

$$\begin{aligned}
 \int_0^b \left( E_\varphi^{s-}(r,0) + E_\varphi^-(r,0) \right) \frac{\Phi_p(r/d)}{d} r^2 dr &= \int_0^d \left( E_\varphi^{s+}(r,0) + E_\varphi^+(r,0) \right) \frac{\Phi_p(r/d)}{d} r^2 dr \\
 \int_0^b \left( E_r^{s-}(r,0) + E_r^-(r,0) \right) \frac{\Psi_p(r/d)}{d} r^2 dr &= \int_0^d \left( E_r^{s+}(r,0) + E_r^+(r,0) \right) \frac{\Psi_p(r/d)}{d} r^2 dr \\
 \int_0^b \left( H_\varphi^{s-}(r,0) + H_\varphi^-(r,0) \right) \frac{\Psi_p(r/b)}{b} r^2 dr &= \int_0^b \left( H_\varphi^{s+}(r,0) + H_\varphi^+(r,0) \right) \frac{\Psi_p(r/b)}{b} r^2 dr \\
 \int_0^b \left( H_r^{s-}(r,0) + H_r^-(r,0) \right) \frac{\Phi_p(r/b)}{b} r^2 dr &= \int_0^b \left( H_r^{s+}(r,0) + H_r^+(r,0) \right) \frac{\Phi_p(r/b)}{b} r^2 dr
 \end{aligned} \tag{B.6}$$

Resorting to the Ritz-Galerkin method, the functional equations are transformed into an infinite set of linear equations using the projection matrix obtained from the previous system. We have the following system:

$$\begin{aligned}
 G_{11}C^H + G_{12}C^E &= G_{13}D^H + G_{14}D^E - S_1 \\
 G_{21}C^E + G_{22}C^H &= G_{23}D^E + G_{24}D^H - S_2 \\
 G_{31}C^E + G_{32}C^H &= G_{33}D^E + G_{34}D^H - S_3 \\
 G_{41}C^H + G_{42}C^E &= G_{43}D^H + G_{44}D^E - S_4
 \end{aligned} \tag{B.7}$$

where  $G_{nm}$  are the projection matrix of the  $n_{th}$  equation of the system (B.6).

The system (B.7) is solved in the following form:

$$\begin{aligned}
 M_{11}C^E + M_{12}D^E &= N_1 \\
 M_{21}C^E + M_{22}D^E &= N_2 \\
 \begin{pmatrix} M_{11} & M_{12} \\ M_{21} & M_{22} \end{pmatrix} \begin{pmatrix} C^E \\ D^E \end{pmatrix} &= \begin{pmatrix} N_1 \\ N_2 \end{pmatrix}
 \end{aligned} \tag{B.8}$$

where:

$$\begin{aligned}
 M_{11} &= G_{11}M_{HCD} - G_{13}M_{HDD} - G_{14} \\
 M_{12} &= G_{11}M_{HCC} - G_{13}M_{HDC} + G_{12} \\
 M_{21} &= G_{41}M_{HCD} - G_{43}M_{HDD} - G_{44} \\
 M_{22} &= G_{41}M_{HCC} - G_{43}M_{HDC} + G_{42} \\
 N_1 &= G_{13}M_{HDS} - G_{11}M_{HCS} - S_1 \\
 N_2 &= G_{43}M_{HDS} - G_{41}M_{HCS} - S_4
 \end{aligned} \tag{B.9}$$

## Appendix B. Spectral model for the calculation of the transverse impedance of an abrupt transition

---

with:

$$\begin{aligned}
M_{HCC} &= (G_{32})^{-1} (G_{34}M_{HDC} - G_{31}) \\
M_{HCD} &= (G_{32})^{-1} (G_{34}M_{HDD} + G_{33}) \\
M_{HCS} &= (G_{32})^{-1} (G_{34}M_{HDS} - S_3) \\
M_{HDC} &= (M_{HDI})^{-1} (G_{21} - G_{22}(G_{32})^{-1}G_{31}) \\
M_{HDD} &= (M_{HDI})^{-1} (G_{22}(G_{32})^{-1}G_{33} - G_{23}) \\
M_{HDS} &= (M_{HDI})^{-1} (S_2 - G_{22}(G_{32})^{-1}S_3) \\
M_{HDI} &= (G_{24} - G_{22}(G_{32})^{-1}G_{34})
\end{aligned} \tag{B.10}$$

From, the system (B.8) the unknown vectors are written as follows:

$$\begin{aligned}
D^E &= [M_{22} - M_{21}M_{11}^{-1}M_{12}]^{-1} [N_2 - M_{21}M_{11}^{-1}N_1] \\
C^E &= [M_{11} - M_{12}M_{22}^{-1}M_{21}]^{-1} [N_1 - M_{12}M_{22}^{-1}N_2]
\end{aligned} \tag{B.11}$$

From which  $C^H$  and  $D^H$  can be derived as follows:

$$\begin{aligned}
D^H &= M_{HDC}C^E + M_{HDD}D^E + M_{HDS} \\
C^H &= M_{HCC}C^E + M_{HCD}D^E + M_{HCS}
\end{aligned} \tag{B.12}$$

## B.2 Impedance derivation

The dipolar transverse impedance can be derived in two different ways. The first solution is to derive the transverse impedance from the longitudinal impedance of mode one (Eq. (1.3)) with the electric longitudinal field of Eq. (B.3) by using the Panofsky Wenzel theorem [55]. The other possibility is to calculate the impedance directly from the definition of Eq. (1.18):

$$-jZ_{\perp} = \frac{1}{p} \left[ E_r^v - \beta Z_0 H_{\phi}^v \right]_{\phi=0}^{r=0} \tag{B.13}$$

### B.2.1 Numerical results

The numerical implementation of the theory described above is a very critical task. Presently the matrices are truncated as described by Davino et al. in Ref. [150] (for the region with smaller radius we use a smaller number of zeros  $F_T b/d$  with respect to the region with larger radius). In his work Davino found an optimum in the convergence for  $F_T = 0.464$ . Work to optimize the numerical calculation is presently still underway. To be noticed that, out of the 16 matrices  $G$ , eight are rectangular and eight square (of which four are diagonal  $G_{14}$ ,  $G_{24}$ ,  $G_{32}$ ,  $G_{42}$ ) and that the system is solved to guarantee that only the square matrix has to be inverted. Figure B.1 shows a test example where we compared the results obtained with our model and ABCI simulation.



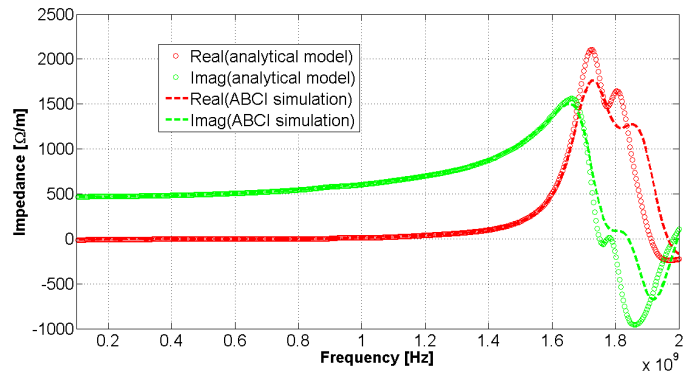


Figure B.1: Driving impedance of a step-out transition.



## C Calculation of $\zeta_m$ : transmission line model

Fig. C.1 show the transmission line model of the structure of Fig. 3.1. Each layer is modeled as a transmission line with propagation constant  $k_n$  and characteristic impedance  $\zeta_n$ . The line can be seen as closed on the characteristic impedance of the boundary layer since it is supposed to extend to infinity. The impedance  $\zeta_m$  is then calculated transporting recursively the intrinsic impedance of the boundary layer  $\zeta_{BC} = Z_{eq_n}$  along the line using the usual formula for the impedance transport:

$$Z_{eq_{n-1}} = \zeta_n \frac{Z_{eq_n} + j\zeta_n \tan(k_n s_n)}{\zeta_n + jZ_{eq_n} \tan(k_n s_n)} \quad (C.1)$$

It is evident that the model can be applied to an arbitrary number of layers.

As a very simple example of application we show the derivation of the classical thick wall formula. Considering one layer of infinite thickness we simply obtain  $\zeta_m = \zeta_{BC}$ . In general the intrinsic impedance of a layer can be written in the following form:

$$\zeta_n = \frac{1+j}{\sigma_{eq_n} \delta_{eq_n}} \quad (C.2)$$

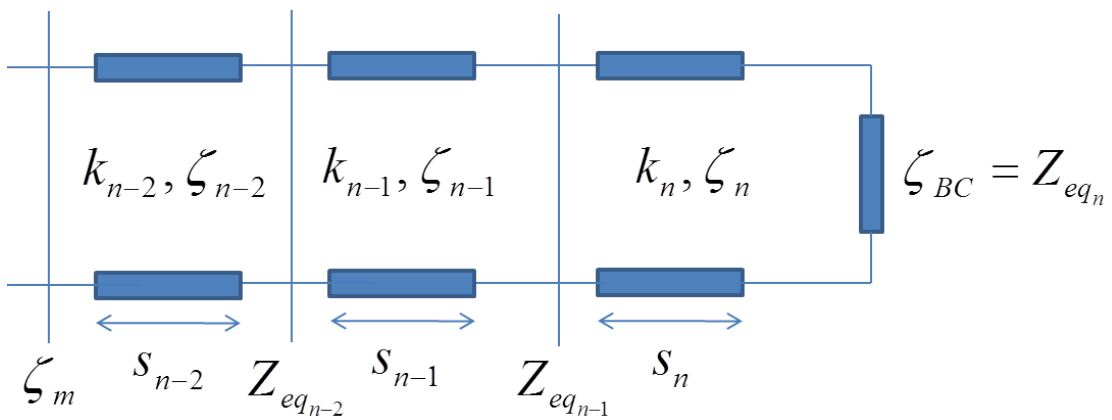


Figure C.1: TL model of the multilayer structure of Fig. 3.1 with  $n=3$ .

## Appendix C. Calculation of $\zeta_m$ : transmission line model

---

with:

$$\begin{aligned}\sigma_{eq_n} &= \sqrt{\omega^2 \epsilon_0 \epsilon' + \sigma_{el_n}^2} \\ \delta_{eq_n} &= \sqrt{\frac{2}{\omega \mu \sigma_{el_n} - j \omega^2 \mu \epsilon_0 \epsilon'}}\end{aligned}\tag{C.3}$$

For a good conductor ( $\sigma_{el} > 10^7$ ) up to frequencies of few hundreds of GHz, the following approximations hold:

$$\begin{aligned}\sigma_{eq_n} &= \sigma_{el_n} \\ \delta_{eq_n} &= \sqrt{\frac{2}{\omega \mu \sigma_{el_n}}}\end{aligned}\tag{C.4}$$

Writing the  $\zeta_{BC}$  in the form of Eq. (C.2) with the approximations of Eq. (C.4), from Eqs. (3.5) and (3.10) we obtain the classical thick wall formula for longitudinal and transverse impedance. It is worth noting that the thick wall formula not only requires the validity of the approximations of Eq. (C.4), but also that the attenuation due to propagation of cylindrical waves and the inductive bypass effect are negligible.

## D List of Publications

This list contains the contributions published during the course of the PhD thesis related to the subject of the PhD thesis

- **2010:**

- B. Salvant, E. Métral, N. Mounet, G. Rumolo, C. Zannini. "Quadrupolar Transverse Impedance of Simple Models of Kickers", IPAC10, Kyoto, Japan, May 2010.
- C. Zannini, E. Métral, G. Rumolo, B. Salvant. "Electromagnetic Simulations of Simple Models of Ferrite Loaded Kickers", CERN-BE-Note-2010-006, 2010.
- C. Zannini, E. Métral, N. Mounet, G. Rumolo, B. Salvant. "Electromagnetic Simulations of Simple Models of Ferrite Loaded Kickers", IPAC10, Kyoto, Japan, May 2010.
- B. Salvant, N. Mounet, C. Zannini, G. Arduini, O. Berrig, F. Caspers, A. Grudiev, E. Métral, G. Rumolo, E. Shaposhnikova, B. Zotter, M. Migliorati, B. Spataro. "Update of the SPS Impedance Model", IPAC10, Kyoto, Japan, May 2010.
- C. Zannini et al, Simulation of dipolar and quadrupolar wakes with CST Particle Studio, Presented at the CST European User Group Meeting, 21 April 2010.

- **2011:**

- G. De Michele, C. Zannini, A. Grudiev, E. Métral, T. Pieloni, G. Rumolo (CERN, Geneva). "Broadband electromagnetic characterization for accelerator component", IPAC11, San Sebastian, Spain, September 2011.
- C. Zannini, E. Métral, G. Rumolo, B. Salvant, V.G. Vaccaro. "Electromagnetic modeling of C shape ferrite loaded kickers", IPAC11, San Sebastian, Spain, September 2011.
- N. Biancacci, N. Wang, Q. Quin, E. Métral, N. Mounet, B. Salvant, C. Zannini, Migliorati, Mostacci, Palumbo. "Impedance calculations for simple models of kickers in the non-ultrarelativistic regime", IPAC11, San Sebastian, Spain, September 2011.
- H. Day, M.J. Barnes, F. Caspers, E. Métral, B. Salvant, C. Zannini, R. Jones. "Coaxial wire measurements of ferrite kicker magnets", IPAC11, San Sebastian, Spain, September 2011.

## Appendix D. List of Publications

---

- C. Belver, M.J. Barnes, A. Faus, G. Rumolo, F. Toral, C. Zannini. "Striplines for CLIC Pre-Damping and Damping Rings", IPAC11, San Sebastian, Spain, September 2011.
- **2012:**
  - C. Zannini, G. Rumolo, K. Li. "Effect of an asymmetric chamber on the beam coupling impedance", IPAC12, New Orleans, USA, May 2012.
  - C. Zannini, G. Rumolo, V.G. Vaccaro. "Effect of the TEM mode on the kicker impedance", IPAC12, New Orleans, USA, May 2012.
  - C. Zannini, G. Rumolo. "EM simulations in beam coupling impedance studies : some examples of application", ICAP12, Rostock, Germany, August 2012.
  - E.K. Platia, G. De Michele, G. Rumolo, C. Zannini. "Electromagnetic characterization of materials for the CLIC damping rings", ICAP12, Rostock, Germany, August 2012.

# List of acronyms

CAD	Computer Aided Design
DUT	Device Under Test
EM	ElectroMagnetic
FD	Frequency domain
FWHM	Full Width Half Maximum
HV	High Voltage
LHC	Large Hadron Collider
LW	Lines per Wavelength
MD	Machine Development
PEC	Perfectly Electrical Conducting
PML	Perfect Matching Layer
PS	Particle Studio
RMS	Root Mean Square
SPS	Super Proton Synchrotron
TD	Time Domain
TEM	Transverse ElectroMagnetic
TL	Transmission Line
WL	Wake Length
WM	Wire Method





## Bibliography

- [1] N. Mounet, *The LHC Transverse Coupled-Bunch Instability*. PhD thesis, Lausanne, EPFL, March 2012.
- [2] L. Palumbo and V. G. Vaccaro, “Wake field: impedances and Green’s function,” *CERN-87-03-V-1*, pp. 341–369, 1987.
- [3] S. Heifets, A. Wagner, and B. Zotter, “Generalized Impedances and Wakes in Asymmetric Structures,” *SLAC/AP110*, 1998.
- [4] V. G. Vaccaro, “Longitudinal instability of a coasting beam above transition, due to the action of lumped discontinuities,” *CERN-ISR-RF-66-35*, November 1966.
- [5] A. M. Sessler and V. G. Vaccaro, “Longitudinal instabilities of azimuthally uniform beams in circular vacuum chambers with walls of arbitrary electrical properties,” *CERN 67-2 ISR-Division*, 1967.
- [6] B. W. Zotter, “The effective coupling impedance for instabilities of Gaussian bunches,” *CERN-ISR-TH-80-03*, 1980.
- [7] B. W. Zotter, “The effective coupling impedance for bunched beam instabilities,” *CERN-ISR-TH-78-16*, 1978.
- [8] A. W. Chao, *Physics of collective beam instabilities in high energy accelerators*. New York: Wiley, 1993.
- [9] B. W. Zotter, “Collective effects: General description,” *CERN-85-19-V-2*, pp. 415–431, 1984.
- [10] J. L. Laclare, “Introduction to coherent instabilities: Coasting beam case,” *CERN-85-19-V-2*, pp. 377–414, 1985.
- [11] J. L. Laclare, “Bunched beam coherent instabilities,” *CERN-87-03-V-1*, pp. 264–326, 1987.
- [12] “<http://www.cst.com/>,”
- [13] G. Rumolo and F. Zimmermann, “Practical user guide for HEADTAIL,” *SL-Note-2002-036-AP*, November 2002.

## Bibliography

---

- [14] E. Koukovini-Platia, K. Li, N. Mounet, G. Rumolo, and B. Salvant, “Impedance effects in the clic damping rings,” Sep 2011.
- [15] K. Yokoya, “Resistive wall impedance of beam pipes of general cross section,” *Part. Accel.*, vol. 41, pp. 221–248, February 1993.
- [16] L. Palumbo, V. G. Vaccaro, and M. Zobov, “Wake fields and impedance,” *LNF-94-041-P*, September 1994.
- [17] C. Zannini, E. Métral, G. Rumolo, and B. Salvant, “Particle Studio simulations of the resistive wall impedance of copper cylindrical and rectangular beam pipes,” Presented at the SPS Impedance meeting (<http://sps-impedance.web.cern.ch/>), March 2009.
- [18] C. Zannini, “Status of Particle Studio simulations,” Presented at the SPS Impedance meeting (<http://sps-impedance.web.cern.ch/>), April 2009.
- [19] Y. H. Chin, “User’s guide for ABCI version 8.7: Azimuthal Beam Cavity,” *CERN-SL-94-02-AP*, February 1994.
- [20] K. Halbach and R. F. Holsinger, “SUPERFISH - a computer program for evaluation of rf cavities with cylindrical symmetry,” *Part. Accel.*, vol. 7, pp. 213–222, June 1976.
- [21] E. Métral, G. Arduini, T. Bohl, H. Burkhardt, R. Calaga, F. Caspers, H. Damerau, T. Kroyer, H. Medina, G. Rumolo, B. Salvant, M. Schokker, E. Shaposhnikova, B. Spataro, and J. Tückmantel, “CERN SPS Impedance in 2007,” *CERN-AB-2008-008*, August 2008.
- [22] H. Bartosik, G. Arduini, T. Argyropoulos, T. Bohl, S. Cettour-Cave, K. Cornelis, J. Esteban Muller, W. Hofle, Y. Papaphilippou, G. Rumolo, B. Salvant, and E. Shaposhnikova, “Increasing instability thresholds in the SPS by lowering transition energy,” *CERN-ATS-2012-177*, May 2012.
- [23] P. E. Faugeras, C. G. Harrison, M. Mayer, and G. Schröder, “A laminated-iron fast-pulsed magnet,” *CERN-SPS-ABT-77-16*, 1977.
- [24] L. Vos, “Longitudinal impedance from ferrite,” *CERN-SL-2000-010-AP*, March 2000.
- [25] “<http://www.ferroxcube.com/>,”
- [26] C. Zannini and B. Salvant, “Update on the impedance of the SPS kicker,” Presented at the SPS impedance meeting (<https://impedance.web.cern.ch>), October 2009.
- [27] B. W. Zotter, “New Results on the Impedance of Resistive Metal Walls of Finite Thickness,” *CERN-AB-2005-043*, August 2005.
- [28] E. Métral, “Transverse resistive-wall impedance from very low to very high frequencies,” *CERN-AB-2005-084*, August 2005.
- [29] H. Tsutsui, “Some Simplified Models of Ferrite Kicker Magnet for Calculation of Longitudinal Coupling Impedance,” *CERN-SL-2000-004-AP*, January 2000.

- 
- [30] H. Tsutsui, "Longitudinal impedances of some simplified ferrite kicker magnet models," *CERN-SL-2000-050-AP*, June 2000.
- [31] H. Tsutsui and L. Vos, "Transverse Coupling Impedance of a Simplified Ferrite Kicker Magnet Model," *LHC-PROJECT-NOTE-234*, September 2000.
- [32] F. Caspers, A. Mostacci, and H. Tsutsui, "Impedance Evaluation of the SPS MKE Kicker with Transition Pieces between Tank and Kicker Module," *CERN-SL-2000-071-AP*, October 2000.
- [33] E. Métral, F. Caspers, M. Giovannozzi, A. Grudiev, T. Kroyer, and L. Sermeus, "Kicker impedance measurements for the future multiturn extraction of the CERN Proton Synchrotron," *CERN-AB-2006-051*, July 2006.
- [34] M. J. Barnes, F. Caspers, T. Kroyer, E. Métral, F. Roncarolo, and B. Salvant, "Measurement of the longitudinal and transverse impedance of kicker magnets using the coaxial wire method," *CERN-ATS-2009-018*, July 2009.
- [35] B. Salvant, N. Mounet, C. Zannini, E. Metral, and G. Rumolo, "Quadrupolar Transverse Impedance of Simple Models of Kickers," *CERN-ATS-2010-076*, June 2010.
- [36] C. Zannini, "Simulations of the SPS kickers with CST Particle Studio," Presented at the SPS impedance meeting (<https://impedance.web.cern.ch>), August 2009.
- [37] T. Kroyer, F. Caspers, and E. Gaxiola, "Longitudinal and Transverse Wire Measurements for the Evaluation of Impedance Reduction Measures on the MKE Extraction Kickers," *CERN-AB-Note-2007-028*, July 2007.
- [38] R. L. Gluckstern and B. Zotter, "Transverse impedance of a resistive cylinder of finite length," *CERN-AB-Note-2008-045*, July 2008.
- [39] N. Biancacci, V. Vaccaro, E. Metral, B. Salvant, M. Migliorati, and L. Palumbo, "The mode matching method applied to beam coupling impedance calculations of finite length devices," *CERN-ATS-2012-187*, May 2012.
- [40] C. Zannini, "Simulations of simplified model of kickers in a large range of frequency," Presented at the SPS impedance meeting (<https://impedance.web.cern.ch>), May 2010.
- [41] C. Zannini, N. Mounet, B. Salvant, E. Metral, and G. Rumolo, "Electromagnetic simulations of simple models of ferrite loaded kickers," *CERN-ATS-2010-098*, June 2010.
- [42] H. Burkhardt, "SPS transverse impedance," Presented at the CERN Accelerator Performance Committee (APC) meeting (<http://ab-div.web.cern.ch/ab-div/Meetings/APC/>), 29 August 2003.
- [43] C. Zannini, B. Salvant, E. Metral, and G. Rumolo, "Electromagnetic simulations of simple models of ferrite loaded kickers," *CERN-BE-Note-2010-006*, June 2010.

## Bibliography

---

- [44] C. Zannini, "Update of the impedance model of the kicker: low frequency impedance," Presented at the CERN Impedance meeting (<https://impedance.web.cern.ch>), June 2010. 'https://impedance.web.cern.ch'.
- [45] C. Zannini and G. Rumolo, "Status of the EM simulations and modeling of ferrite loaded kickers," Presented at the CERN ICE section meeting (<https://emetral.web.cern.ch>), October 2010.
- [46] C. Zannini, K. Li, and G. Rumolo, "Effects of an Asymmetric Chamber on the Beam Coupling Impedance," *CERN-ATS-2012-081*, May 2012.
- [47] C. Zannini, V. G. Vaccaro, E. Metral, G. Rumolo, and B. Salvant, "Electromagnetic modeling of C-shaped ferrite loaded kickers," *CERN-ATS-2011-103*, September 2011.
- [48] V. Vaccaro, C. Zannini, and G. Rumolo, "Update on the kicker impedance model and measurements of material properties," Presented at the CERN Impedance meeting (<https://impedance.web.cern.ch>), 13 May 2011.
- [49] C. Zannini, "Simulation of dipolar and quadrupolar wakes with CST Particle Studio," Presented at the CST European User Group Meeting (<http://www.cst.com>), 21 April 2010.
- [50] C. Zannini and G. Rumolo, "Contributions of both constant and coupling terms to the wake fields," Presented at the CERN HEADTAIL meeting (<http://indico.cern.ch>), 16 May 2011.
- [51] J. D. Jackson, *Classical electrodynamics*; 3rd ed. New York: Wiley, 1999.
- [52] G. Nassibian and F. J. Sacherer, "Methods for measuring transverse coupling impedances in circular accelerators," *Nucl. Instrum. Methods*, vol. 159, no. 1, pp. 21–27, 1979.
- [53] L. J. Laslett, "Proceedings of the international symposium on electron and positron storage rings," vol. IV, pp. 5.1–5.9, September 1966.
- [54] D. Davino and A. Hahn, "Improved analytical model of the transverse coupling impedance of ferrite kicker magnets," *Phys. Rev. ST AB*, vol. 6, 2003.
- [55] W. K. H. Panofsky and W. A. Wenzel, "Some considerations concerning the transverse deflection of charged particles in radio-frequency fields," *Rev. Sci. Instrum.* 27, 1956.
- [56] D. M. Pozar, *Microwave engineering*; 3rd ed. Hoboken, NJ: Wiley, 2005.
- [57] D. Quatraro, A. Findlay, B. Mikulec, and G. Rumolo, "Head tail instability observation and studies at the proton synchrotron booster," *CERN-ATS-2010-071*, June 2010.
- [58] G. Rumolo, A. Findlay, B. Mikulec, M. Chanel, and D. Quatraro, "Beam instabilities in the PSB operation with high intensity beams," Presented at the CERN Machine Studies Working Group (MSWG), 27 August 2010.

- [59] C. Zannini, G. Rumolo, and V. G. Vaccaro, "Effect of the TEM Mode on the Kicker Impedance," *CERN-ATS-2012-082*, May 2012.
- [60] M. Timmins, "SPS extraction kicker magnet: thermal analysis," *TS-Note-2004-016*, July 2004.
- [61] L. Ducimetière, "Advances of Transmission line kicker magnets," *CERN-AB-2005-023*, June 2005.
- [62] M. J. Barnes, L. Ducimetière, T. Fowler, V. Senaj, and L. Sermeus, "Injection and extraction magnets: kicker magnets," *CERN-2010-004*, pp. 141–166, March 2011.
- [63] M. J. Barnes *Private communication*.
- [64] E. Gaxiola, A. Antoine, P. Burkel, E. Carlier, F. Castronuovo, L. Ducimetière, Y. Sillanoli, M. Timmins, and J. Uythoven, "Upgrade and tests of the sps fast extraction kicker system for lhc and cngs," no. *CERN-AB-2004-037*, 2004.
- [65] J. Uythoven, "Status report on beam induced heating of the MKE magnet," Presented at the CERN Accelerator Performance Committee (APC) meeting (<http://ab-div.web.cern.ch/ab-div/Meetings/APC/>), 24 June 2003.
- [66] M. Timmins, A. Bertarelli, E. Gaxiola, and J. Uythoven, "SPS extraction kicker magnet cooling design," *CERN-AB-Note-2004-005-BT*, May 2006.
- [67] B. L. Butler and M. Featherby, "Metallized Ceramic Vacuum Pipe for Particle Beams," *IEEE*, 1987.
- [68] E. Gaxiola, J. Bertin, F. Caspers, L. Ducimetière, and T. Kroyer, "Experience with Kicker Beam Coupling Reduction Techniques," *CERN-AB-2005-024*, June 2005.
- [69] F. Caspers, E. Gaxiola, T. Kroyer, M. Timmins, J. Uythoven, and S. Kurennoy, "A Retrofit Technique for Kicker Beam-Coupling Impedance Reduction," *CERN-AB-2004-048*, August 2004.
- [70] C. Zannini and G. Rumolo, "MKE heating with and without serigraphy," Presented at the CERN SPS upgrade meeting (<http://paf-spsu.web.cern.ch/paf-spsu/>), 2 August 2012.
- [71] C. Zannini, "EM simulations of the LHC beam screens including the weld," Presented at the CERN Impedance meeting (<http://impedance.web.cern.ch/>), March 2010.
- [72] C. Zannini, "News from the transverse impedances of the weld from the LHC beam screen," Presented at the CERN Impedance meeting (<http://impedance.web.cern.ch/>), March 2010.
- [73] N. Mounet and E. Metral, "Impedances of an Infinitely Long and Axisymmetric Multilayer Beam Pipe: Matrix Formalism and Multimode Analysis," *CERN-ATS-2010-065*, June 2010.

## Bibliography

---

- [74] A. Burov and V. Lebedev, "Transverse Resistive Wall Impedance for Multi-layer Round Chambers," *FERMILAB-CONF-2002-100-T*, 2002.
- [75] A. Burov and V. Lebedev, "Transverse Resistive Wall Impedance for Multi-Layer Flat Chambers," *FERMILAB-CONF-2002-101-T*, 2002.
- [76] E. Métral, B. Salvant, and B. Zotter, "Resistive-Wall Impedance of an Infinitely long Multi-Layer Cylindrical Beam Pipe," *CERN-LHC-PROJECT-Report-1014*, 2007.
- [77] L. Vos, "The Impedance of Multi-layer Vacuum Chambers," *CERN-AB-2003-093-ABP*, October 2003.
- [78] L. Vos, "The Transverse impedance of a cylindrical pipe with arbitrary surface impedance. oai:cds.cern.ch:604828," *CERN-AB-2003-005-ABP*, February 2003.
- [79] A. Koschik, F. Caspers, E. Métral, L. Vos, and B. W. Zotter, "Transverse Resistive Wall Impedance and Wake Function with Inductive Bypass," *CERN-AB-2004-065*, August 2004.
- [80] N. Mounet and E. Metral, "Generalized Form Factors for the Beam Coupling Impedances in a Flat Chamber," *CERN-ATS-2010-064*, June 2010.
- [81] R. L. Gluckstern, J. Van Zeijts, and B. W. Zotter, "Coupling impedance of beam pipes of general cross section.," *Phys. Rev. E*, vol. 47, pp. 656–663, June 1992.
- [82] M. A. Leontovich, "Investigations on radiowave propagation, part II," *Academy of Sciences, Moscow*, 1948.
- [83] T. B. A. Senior and J. L. Volakis, *Approximate boundary conditions in electromagnetics*. 1995.
- [84] A. Koschik, "Transverse Resistive Wall Wakefunction with Inductive Bypass," *AB-Note-2003-088-ABP*, November 2003.
- [85] P. Cruikshank, K. Artoos, F. Bertinelli, J. C. Brunet, R. Calder, C. Campedel, I. R. Collins, J. M. Dalin, B. Feral, O. Gröbner, N. Kos, A. G. Mathewson, L. I. Nikitina, I. N. Nikitin, A. Poncet, C. Reymermier, G. Schneider, J. C. Sexton, S. Sgobba, R. Valbuena, and R. J. M. Veness, "Mechanical Design Aspects of The LHC Beam screen," *CERN-LHC-Project-Report-128*, July 1997.
- [86] J. Bauche *Private communication*.
- [87] K. G. Nilanga, A. Abeywickrama, T. Daszczyński, Y. V. Serdyuk, and G. S. M, "Determination of Complex Permeability of Silicon Steel for Use in High-Frequency Modeling of Power Transformers," *IEEE TRANSACTIONS ON MAGNETICS*, vol. 44, April 2008.

- 
- [88] N. Biancacci and C. Zannini, "Update of the SPS impedance model," Presented at the CERN Machine Studies Working Group (MSWG) (<http://impedance.web.cern.ch/>), February 2012.
- [89] F. Caspers, M. Morvillo, and F. Ruggiero, "Surface Resistance Measurements for the LHC Beam Screen," *CERN-LHC-Project-Report-115*, June 1997.
- [90] Y. Baconnier, J. B. Jeanneret, and A. Poncet, "LHC beam aperture and beam screen geometry," *LHC-NOTE-326*, June 1995.
- [91] F. Ruggiero, "Single-beam collective effects in the LHC," *Part. Accel.*, vol. 50, pp. 83–104, February 1995.
- [92] A. Mostacci, *Beam-Wall interaction in the LHC liner*. PhD thesis, University of Rome, Geneva, 2001.
- [93] F. J. Sacherer, "Transverse resistive-wall instabilities of the bunched beam in the SPS," *CERN-SI-NOTE-BR-72-1*, May 1972.
- [94] L. Palumbo and V. G. Vaccaro, "Wake fields measurements," *LNf-89-035-P*, May 1989.
- [95] A. Faltens, C. Hartwig, E. D. Mohl, and M. Sessler, A, "An analog method for measuring the longitudinal coupling impedance of a relativistic particle beam with its environment," *8th International Conference on High Energy Accelerator*, 1971.
- [96] M. Sands and J. Rees, "A Bench Measurement of the Energy Loss of a Stored Beam to a Cavity," *LBL-PEP-NOTE-95.*, August 1974.
- [97] L. Hahn and F. Pedersen, "On a coaxial wire measurements of the Longitudinal Beam Coupling Impedance," *BNL-50870*, April 1978.
- [98] V. G. Vaccaro, "Coupling impedance measurements: an improved wire method," *INFN-TC-94-023*, November 1994.
- [99] F. Caspers, C. González, M. Dyachkov, E. Shaposhnikova, and H. Tsutsui, "Impedance measurement of the SPS MKE kicker by means of the coaxial wire method," *CERN-PS-RF-NOTE-2000-04*, February 2000.
- [100] E. Jensen, "An improved log-formula for homogeneously distributed impedance," *CERN-PS-RF-NOTE-2000-001*, January 2000.
- [101] J. N. Weaver, J. B. Styles, and P. B. Wilson, "Bench Measurements of the Loss Impedance for PEP Beam Line Components," *IEEE Trans. Nucl. Sci.* 26, 1979.
- [102] G. Di Massa and M. R. Masullo, "Beam Impedance Measurement Using a Synthetic Pulse Technique," *2nd European Particle Accelerator Conference*, 1990.
- [103] H. Day, M. Barnes, F. Caspers, E. Metral, B. Salvant, C. Zannini, and R. Jones, "Coaxial wire measurements of ferrite kicker magnets," *CERN-ATS-2011-275*, October 2011.

## Bibliography

---

- [104] A. Argan, L. Palumbo, M. R. Masullo, and V. G. Vaccaro, "On the Sands and Rees Measurement Method of the Longitudinal Coupling Impedance," IEEE Particle Accelerator Conference PAC 99.
- [105] M. Migliorati, L. Palumbo, A. Argan, F. Console, and S. De Santis, "Measurements of the Longitudinal Impedance of a Coaxial Cavity coupled with a Circular Pipe through Slots," *7th European Particle Accelerator Conference*, 2000.
- [106] R. Masullo, M. G. Vaccaro, V. and Paniello, "The stretched wire method: a comparative analysis performed by means of the mode matching technique," *LINAC10*, 2010.
- [107] H. Tsutsui, "On single wire technique for transverse coupling impedance measurement," *SL-Note-2002-034-AP*, October 2002.
- [108] M. Cardito, G. Di Massa, F. Galluccio, R. Losito, M. R. Masullo, and V. G. Vaccaro, "Transverse beam impedance measurement: a new coaxial method," *INFN-TC-93-10*, June 1993.
- [109] B. Salvant, *Impedance model of the CERN SPS and aspects of LHC single-bunch stability*. PhD thesis, Lausanne, EPFL, Switzerland, 2010.
- [110] B. Salvant, G. Arduini, C. Boccard, F. Caspers, A. Grudiev, R. Jones, E. Métral, G. Rumolo, C. Zannini, B. Spataro, D. Alesini, M. Migliorati, F. Roncarolo, and R. Calaga, "Coupling Impedance of the CERN SPS beam position monitors," *CERN-ATS-2009-046*, September 2009.
- [111] B. Salvant, N. Mounet, C. Zannini, G. Arduini, O. Berrig, F. Caspers, A. Grudiev, E. Métral, G. Rumolo, E. Shaposhnikova, B. Zotter, M. Migliorati, and B. Spataro, "Update of the SPS Impedance Model," *CERN-ATS-2010-077*, June 2010.
- [112] H. Bartosik, G. Arduini, T. Argyropoulos, T. Bohl, K. Cornelis, J. Esteban Muller, K. Li, A. Y. Molodozhentsev, Y. Papaphilippou, G. Rumolo, B. Salvant, F. Schmidt, E. Shaposhnikova, and H. Timko, "Low Gamma Transition Optics for the SPS: Simulation and Experimental Results For High Brightness Beams," *HB2012 Proc.*, September 2012.
- [113] H. Burkhardt, "Single Bunch Transverse Intensity Limitations in the SPS," *AIP Conf. Proc.*, vol. 773, pp. 368–370, January 2005.
- [114] H. Burkhardt, G. Rumolo, and F. Zimmermann, "Measurements of SPS Single-Bunch Coherent Tune Shifts and Head-Tail Growth Rates in the Year 2001," *SL-Note-2001-043-MD*, December 2001.
- [115] H. Burkhardt, "SPS transverse impedance and losses at injection," Presented at the CERN Accelerator Performance Committee (APC) meeting (<http://ab-div.web.cern.ch/ab-div/Meetings/APC/>), 3 October 2003.



- [116] H. Burkhardt, "First results on SPS transverse impedance measurements," Presented at the CERN Accelerator Performance Committee (APC) meeting (<http://ab-div.web.cern.ch/ab-div/Meetings/APC/>), 10 November 2006.
- [117] H. Burkhardt, "MDs on the SPS transverse impedance: preliminary results," Presented at the CERN Accelerator Performance Committee (APC) meeting (<http://ab-div.web.cern.ch/ab-div/Meetings/APC/>), 17 August 2007.
- [118] E. Métral, G. Arduini, T. Bohl, H. Burkhardt, R. Calaga, F. Caspers, H. Damerau, T. Kroyer, H. Medina, G. Rumolo, B. Salvant, M. Schokker, E. Shaposhnikova, B. Spataro, and J. Tückmantel, "CERN SPS Impedance in 2007," *CERN-AB-2008-008*, August 2008.
- [119] B. Salvant, "MDs on the SPS transverse impedance: preliminary results," Presented at the CERN Accelerator Performance Committee (APC) meeting (<http://ab-div.web.cern.ch/ab-div/Meetings/APC/>), 24 October 2008.
- [120] N. Biancacci, "SPS transverse impedance measurements," Presented at the CERN SPS upgrade meeting (<http://paf-spsu.web.cern.ch/paf-spsu/>), 26 April 2012.
- [121] H. Burkhardt, A. Koschik, G. Rumolo, F. Zimmermann, and B. W. Zotter, "Coherent tune shifts measured with few bunches in the SPS and comparison with resistive wall theory," *CERN-AB-2003-014-ABP*, May 2003.
- [122] G. Arduini, T. Bohl, F. Caspers, E. H. Gaxiola, T. Kroyer, M. Timmins, L. Vos, and J. Uythoven, "Beam Induced Heating of the SPS Fast Pulsed Magnets," *CERN-AB-2004-038*, 2004.
- [123] G. Papotti, "A Beam Quality Monitor for LHC Beams in the SPS," *CERN-LHC-PROJECT-Report-1154*, September 2008.
- [124] T. Bohl *Private communication*.
- [125] R. Fandos and W. Wuensch, "Estimation of the RF Characteristics of Absorbing Materials in Broad RF Frequency Ranges," *CLIC-Note-766*, June 2008.
- [126] M. Liepe, B. Barstow, and H. Padamsee, "First Studies for a Low Temperature Higher-Order-Mode Absorber for the Cornell ERL Prototype.," *SFR-2003-08*, May 2003.
- [127] V. D. Shemelin, M. Liepe, and H. Padamsee, "Measurements of Epsilon and Mu of Lossy Materials for the Cryogenic HOM Load," 21st IEEE Particle Accelerator Conference.
- [128] D. McGinnis, "Analysis of Microwave Properties for Various Absorbing Materials," *FERMILAB-PBAR-NOTE-594*, 1998.
- [129] F. Caspers, M. Morvillo, C. González, and M. Dyachkov, "Measurements of Complex Permeability and Permittivity of Ferrites for the LHC Injection Kicker," *LHC-PROJECT-NOTE-203*, October 1999.

## Bibliography

---

- [130] W. Barry, J. Byrd, J. Johnson, and J. Smithwick, "A collection of complex permittivity and permeability measurements," *LBL-33734*, February 1993.
- [131] Agilent, "Solutions for Measuring Permittivity and Permeability with LCR Meters and Impedance Analyzers," *Note 1369-1*, October 2008.
- [132] C. A. Jones, J. H. Grosvenor, and C. M. Weil, "RF material characterization using a large-diameter (76.8 mm) coaxial air line," NIST technical note-1517.
- [133] J. H. Grosvenor, "NIST measurement service for Electromagnetic characterization of materials," *IEEE TRANSACTIONS ON ELECTROMAGNETIC COMPATIBILITY*, vol. 53, no. 3, August 1993.
- [134] C. Zhao, Q. Jiang, and S. Jing, "Calibration-Independent and Position-Insensitive Transmission/Reflection Method for Permittivity Measurement With One Sample in Coaxial Line," *IEEE TRANSACTIONS ON ELECTROMAGNETIC COMPATIBILITY*, vol. 53, no. 3, August 2011.
- [135] J. Krupka, "Frequency domain complex permittivity measurements at microwave frequencies," *Meas. Sci. Technol.* 17 R55–R70, April 2006.
- [136] C. M. Weil, C. A. Jones, and J. H. Grosvenor, "On RF Material Characterization in the Stripline Cavity," *IEEE TRANSACTIONS ON MICROWAVE THEORY AND TECHNIQUES*, vol. 48, no. 2, February 2000.
- [137] T. Pieloni and R. Zennaro, "Absorbers Materials for HOM Damping in CLIC PETS and Accelerating Structures," Presented at the CERN Impedance meeting (<http://impedance.web.cern.ch>), 14 December 2009.
- [138] G. Fehlen, *Air gap error compensation for coaxial transmission line method of electromagnetic material characterization*. PhD thesis, Air Force Institute of technology, Ohio, 2006.
- [139] D. Chruishank *Private communication*.
- [140] C. Belver-Aguilar, A. Faus-Golfe, M. J. Barnes, G. Rumolo, C. Zannini, and F. Toral, "Striplines for CLIC Pre-damping and Damping Rings," *CERN-ATS-2011-269*, December 2011.
- [141] R. Mutzner, "Multi-Bunch effect of resistive wall in the beam delivery system of the Compact Linear Collider," Master's thesis, Lausanne, EPFL, Lausanne, 2010.
- [142] G. Rumolo, A. Latina, and D. Schulte, "Effects of Wake Fields in the CLIC BDS,"
- [143] P. K. Ambattu, G. Burt, R. G. Carter, A. C. Dexter, R. M. Jones, and P. McIntosh, "Initial study on the shape optimisation of the CLIC crab cavity," *arXiv:0810.2878*, October 2008.

- [144] G. Burt, P. K. Ambattu, A. C. Dexter, T. Abram, V. Dolgashev, S. Tantawi, and R. M. Jones, "X-band crab cavities for the CLIC beam delivery system," *arXiv:0903.2116*, March 2009.
- [145] G. Burt, R. M. Jones, and A. C. Dexter, "Analysis of damping requirements for dipole wake-fields in RF crab cavities," *Nuclear Science, IEEE Transactions on*, vol. 54, pp. 1728–1734, October 2007.
- [146] R. M. Jones, L. Bellantoni, G. Burt, A. Dexter, A. Latina, and D. Schulte, "Wake fields and beam dynamics simulations for the 3.9-GHz cavities of the ILC," *In Proceedings of LINAC06*, 2006.
- [147] O. Napoly, "The Wake Potentials From The Fields On The Cavity Boundary," *Part. Accel.*, vol. 36, pp. 15–24, June 1991.
- [148] O. Napoly, Y. H. Chin, and B. W. Zotter, "A generalized method for calculating wake potentials," *Nucl. Instrum. Methods Phys. Res., A*, vol. 334, pp. 255–265, March 1993.
- [149] V. G. Vaccaro, C. Zannini, and G. Rumolo, "An analytical derivation of the transverse impedance for a step-out transition," CERN-BE-Note (to be published).
- [150] D. Davino, G. Dome, G. Miano, G. Panariello, V. Vaccaro, and L. Verolino, "Longitudinal Coupling Impedance of an abrupt junction," *Nuovo Cimento 112A(12)*, 1999.



---

PERSONAL INFORMATION

---

Name	<b>Carlo Zannini</b>
Date of birth	September, 25 <sup>th</sup> 1982
Citizenship	Italian
Address	380, Rue des Vertes Campagnes, Gex, France
Phone (mobile)	+41 767040787
E-mail	carlo.zannini@cern.ch

---

EDUCATION

---

From March 2010	Ecole Polytechnique Fédérale de Lausanne (Lausanne, Switzerland), doctoral program in physics. Specialization in accelerator and beam physics, with emphasis on beam coupling impedance. PhD thesis entitled: 'EM simulations of CERN accelerator components and experimental applications'; defense expected the 15 April 2013
Mar 2006-Oct 2008	University of Naples Federico II (Naples, Italy), Laurea Magistrale in ingegneria elettronica. Master's thesis entitled: " <i>Il confinamento dei modi in cavità acceleratrici PBG periodiche e aperiodiche</i> "
Oct 2001-Jan 2006	University of Naples Federico II (Naples, Italy), Laurea in ingegneria elettronica. Thesis entitled: " <i>Processi di magnetizzazione nei materiali ferromagnetici dolci e perdite isteretiche</i> "
Jul 2001	High school diploma with final mark of 100/100 .

---

WORK EXPERIENCE

---

From Jan 2013	Fellow at CERN with Dr. Giovanni Rumolo in the beam physics department. Responsible for the beam coupling impedance model of SPS and PSB.
Jan 2010-Dec 2012	PhD student at CERN (Geneva, Switzerland) with Dr. Giovanni Rumolo in the beam physics department
Nov 2008-Dec 2009	Technical Student at CERN (Geneva, Switzerland) with Dr. Giovanni Rumolo in the beam physics department

---

LANGUAGES AND OTHER SKILLS

---

Italian	Mother tongue.
English	Good oral and written.
French	Good oral and written.
Computer science	Operating system: Linux and Microsoft. Programming languages C, C++, Assembler, VHDL, Matlab, Mathematica. Experience of computer modeling, finite element analysis and simulation software in various fields of application (P-Spice, Matlab, Mathematica, Origin, CodeComposerStudio, CST Studio Suite, HFSS etc.)

---

EXTRA-CURRICULAR ACTIVITIES

---

Music	Guitar
Sport	Tennis, ping-pong, football